

**ÇUKUROVA UNIVERSITY
INSTITUTE OF NATURAL AND APPLIED SCIENCES**

PhD. THESIS

Semiray GİRGİS

**INCLUSIVE FORWARD JET CROSS SECTION MEASUREMENT in
PROTON - PROTON COLLISIONS at $\sqrt{s} = 7$ TeV**

DEPARTMENT OF PHYSICS

ADANA, 2014

**ÇUKUROVA UNIVERSITY
INSTITUTE OF NATURAL AND APPLIED SCIENCES**

**INCLUSIVE FORWARD JET CROSS SECTION MEASUREMENT in
PROTON – PROTON COLLISIONS at $\sqrt{s} = 7$ TeV**

Semiray GİRGİS

PhD THESIS

DEPARTMENT OF PHYSICS

We certify that the thesis titled above was reviewed and approved for the award of degree of the Doctor of Philosophy by the board of jury on 19/06/2014.

.....
Prof. Dr. Eda EŞKUT
SUPERVISOR

.....
Assoc. Prof. Dr. Deniz SUNAR ÇERÇİ
CO-SUPERVISOR

.....
Prof. Dr. Ayşe POLATÖZ
MEMBER

.....
Prof. Dr. İsa DUMANOĞLU
MEMBER

.....
Asst. Prof. Dr. Salim ÇERÇİ
MEMBER

This PhD Thesis is performed in Department of Physics of Institute of Natural And Applied Sciences of Çukurova University.

Registration Number:

**Prof. Dr. Mustafa GÖK
Director
Institute of Natural and Applied Sciences**

**This Study was supported by Çukurova University Scientific Research Fund.
Project Number: FEF2011D3**

Not: The usage of the presented specific declarations, tables, figures, and photographs either in this thesis or in any other reference without citation is subject to "The law of Arts and Intellectual Products" number of 5846 of Turkish Republic.

ABSTRACT

PhD. THESIS

INCLUSIVE FORWARD JET CROSS SECTION MEASUREMENT in PROTON – PROTON COLLISIONS at $\sqrt{s} = 7$ TeV

Semiray GİRGİŞ

ÇUKUROVA UNIVERSITY
INSTITUTE OF NATURAL AND APPLIED SCIENCES
DEPARTMENT OF PHYSICS

Supervisor	: Prof. Dr. Eda EŞKUT
Co-Supervisor	: Assoc. Prof. Dr. Deniz SUNAR ÇERÇİ
	Year: 2014, Page: 168
Jury	: Prof. Dr. Eda EŞKUT
	: Assoc. Prof. Dr. Deniz SUNAR ÇERÇİ
	: Prof. Dr. Ayşe POLATÖZ
	: Prof. Dr. İsa DUMANOĞLU
	: Asst. Prof. Dr. Salim ÇERÇİ

Forward (di)jet studies provide an important testing ground for QCD predictions of the SM and give significant information for multiparton radiation, DGLAP and BFKL dynamics. This thesis presents measurement of cross section of inclusive forward jets and dijet events with at least one jet emitted at forward region in proton - proton collisions at $\sqrt{s} = 7$ TeV. The data for analysis are based on 3.14 pb^{-1} of luminosity events collected by the CMS detector in 2010. Jets are reconstructed with the anti- k_T jet algorithm ($R = 0.5$) in the Hadronic Forward (HF) calorimeter at pseudorapidities $3.2 < |\eta| < 4.7$, in the transverse momentum range $p_T = 35 - 150 \text{ GeV}/c$. The measurement is compared to next-to-leading order (NLO) perturbative Quantum Chromodynamics (pQCD) calculations, to PYTHIA and HERWIG parton shower event generators with different tunes as well as to the CASCADE and HEJ Monte Carlo within the experimental and theoretical uncertainties.

Key Words: CMS, QCD, Parton, Jets, PDF

ÖZ

DOKTORA TEZİ

**$\sqrt{s} = 7 \text{ TeV'lik PROTON – PROTON ÇARPIŞMASINDA İNKLÜSİF İLERİ}$
JET TESİR KESİTİ HESAPLAMASI**

Semiray GİRGİS

**ÇUKUROVA ÜNİVERSİTESİ
FEN BİLİMLERİ ENSTİTÜSÜ
FİZİK ANABİLİM DALI**

Danışman	: Prof. Dr. Eda EŞKUT
İkinci Danışman	: Doç. Dr. Deniz SUNAR ÇERÇİ
	Yıl: 2014, Sayfa: 168
Jüri	: Prof. Dr. Eda EŞKUT
	: Doç. Dr. Deniz SUNAR ÇERÇİ
	: Prof. Dr. Ayşe POLATÖZ
	: Prof. Dr. İsa DUMANOĞLU
	: Yrd. Doç. Dr. Salim ÇERÇİ

İleri bölgedeki jet ve iki jet çalışmaları, SM'in KRD tahminleri için önemli bir test alanı oluşturmaktır ve çoklu parton yayınımı, DGLAP ve BFKL dinamikleri için önemli bilgiler vermektedir. Bu tezde, $\sqrt{s} = 7 \text{ TeV}$ 'de pp çarpışmasında inklüsif ileri jetlerin ve en az biri ileri bölgede yayımlanan iki jet olaylarının tesir kesitleri ölçülmüştür. Analiz için, 2010 yılında CMS detektörü ile toplanan 3.14 pb^{-1} ışıklıklı veriler kullanılmıştır. Jetler ileri hadron kalorimetresinde, $3.2 < |\eta| < 4.7$ pseudorapiditede, $p_T = 35\text{--}150 \text{ GeV}/c$ enine momentum aralığında anti- k_T jet algoritması ($R = 0.5$) kullanılarak yeniden yapılandırılmıştır. Deneysel ve teorik belirsizlikler dahilinde ölçümler next-to-leading order (NLO) perturbatif kuantum renk dinamigi hesaplamalarıyla, CASCADE ve HEJ MC modellerinin yanısıra değişik ayarlı PYTHIA ve HERWIG olay üreteçleriyle karşılaştırılmıştır.

Anahtar Kelimeler: CMS, KRD, Parton, Jetler, PDF

ACKNOWLEDGMENTS

I would like to acknowledge everyone who helped me to bring this dissertation fruition.

First and foremost I would like to express my deep gratitude to my supervisor Prof. Dr. Eda EŞKUT for all words of encouragement, motivation and guidance during my PhD studies. She always showed me the best ways and it is indeed a privilege and pleasure to work with her.

I express my sincere thanks to my co-advisor Assoc. Dr. Deniz SUNAR ÇERÇİ and Asst. Dr. Salim ÇERÇİ, for their support during my studies, their contribution to this research work and also critical reading of the thesis. I would like to acknowledge the honourable members of my thesis committee, Prof. Dr. Ayşe POLATÖZ, Prof. Dr. İsa DUMANOĞLU. I wish to thank our Turkish group leader Prof. Dr. Gülsen ÖNENGÜT for her encouragement during my PhD. studies and I am especially grateful for her critical reading of the thesis. I would like to thank our high energy physics group member Prof. Dr. Aysel KAYIŞ TOPAKSU for her moral support and encouragement during my studies.

Prof. Dr. Hannes JUNG has helped me tremendously not only with reading and important criticism of the thesis but also he found time whenever I needed to discuss my analysis and for that I am very grateful. Additionally, I would like to thank Dr. Konstantinos KOUSOURIS for his help and excellent discussions relevant to various aspects of the analysis. I am grateful to Prof. Dr. Apostolos PANAGIOTOU for his reading, invaluable review and for giving me this great opportunity to work for the commissioning of the CASTOR detector to gain experience both on hardware and software issues and expand my knowledge of physics. I would like to thank to all collaborators from CERN on the Inclusive Forward Jet and Central-Forward Dijet Cross Section Analysis, they were many during the years. I would like to thank Prof. Dr. Suat ÖZKORUCUKLU for all the wonderful discussions we have had over the years.

My special and deepest thanks go to Murat ÇETİN for his support, encouragement and friendship. To Roman CHYLA, who has shown tremendous care to me in life. Thank you Roman, for being in my life, your wonderful care, encouragement and important criticism of the thesis. Glad you are...

Special gratitude goes to my best friends Gülşen AYAN, Oktay BAYSAL, Gülesen ÜSTÜNDAĞ, Alev MENGEN and Nuray MENGEN for their friendship and encouragement. I consider myself lucky to have such caring friends. I wish to thank my friends and colleagues Yalçın GÜLER, İlknur HOŞ, Aytül ADIGÜZEL, Çağlar ZORBİLMEZ and Kadri ÖZDEMİR. I always feel their friendship.

Special thanks are to TAEK (project code: 2012K120260) who sponsored me during the time I have spent at CERN.

Finally, I would like to thank all my family, and in particular my parents. If it was not for their unconditional love and support in my endeavors all these years would be too hard.

CONTENTS	PAGE
ABSTRACT	I
ÖZ	II
ACKNOWLEDGMENTS.....	III
CONTENTS	IV
LIST OF TABLES	VIII
LIST OF FIGURES.....	X
ABBREVIATIONS.....	XX
1. INTRODUCTION.....	1
2. THEORETICAL MOTIVATION.....	5
2.1. The Standart Model of Particle Physics	5
2.2. Quantum Chromodynamics	10
2.2.1. Perturbative QCD and Asymptotic Freedom	11
2.2.2. Quark Parton Model and Parton Density Function	13
2.2.3. Factorization Theorem	19
2.3. From Parton to Hadron.....	21
2.3.1. Parton Shower	22
2.3.2. Hadronization.....	22
2.4. Monte Carlo Generators.....	24
2.4.1. PYTHIA	25
2.4.2. HERWIG.....	25
2.4.3. CASCADE	26
2.4.4. HEJ	26
2.4.5. POWHEG.....	26
2.4.6. MC@NLO.....	27
2.4.7. NLOJET++.....	27
3. LHC and CMS EXPERIMENT	29
3.1. Large Hadron Collider	29
3.1.1. Proton Production and Linear Acceleration.....	32
3.1.2. Booster and Proton Synchrotron	32

3.1.3. Super Proton Synchrotron	32
3.1.4. Luminosity and Machine Parameters.....	33
3.1.5. The LHC Experiments	36
3.2. CMS	39
3.2.1. Tracker	42
3.2.1.1. Pixel Tracker	43
3.2.1.2. Inner Tracker	44
3.2.1.3. Outer Tracker	44
3.2.2. CMS Calorimeters.....	44
3.2.2.1. Electromagnetic Calorimeter	46
3.2.2.2. Hadron Calorimeter.....	48
3.2.3. Solenoid Magnet	54
3.2.4. Muon System	56
3.2.4.1. Muon Barrel System: Drift Tube Chambers	57
3.2.4.2. Muon Endcap System: Cathode Strip Chambers	58
3.2.4.3. Resistive Plate Chambers	60
3.2.5. The Data Acquisition and Trigger System.....	60
3.2.5.1. Level 1 Trigger.....	61
3.2.5.2. High Level Trigger.....	63
3.3. Forward Detectors	64
3.3.1. CASTOR Detector	64
3.3.2. ZDC Detector	65
4. JET RECONSTRUCTION at CMS	67
4.1. Jet Definitions and Kinematics	67
4.2. Jet Types at CMS	69
4.2.1. Calorimeter Jets.....	69
4.2.2. Jet-Plus-Track Jets	72
4.2.3. Particle-Flow Jets	72
4.2.4. Track Jets	73
4.3. Jet Reconstruction Algorithms.....	73
4.3.1. Iterative Cone Algorithm	76

4.3.2. Seedless Infrared Safe Cone Algorithm.....	76
4.3.3. Anti- k_T Algorithm	78
4.4. Jet Energy Corrections	80
4.4.1. Required Jet Energy Corrections	82
4.4.2. Optional Jet Energy Corrections	82
4.5. Jet Reconstruction and Performance in HF.....	84
4.5.1. Performance of the Forward Jet Reconstruction in Monte Carlo	84
4.5.2. Jet Energy Response	85
4.5.3. Jet Energy Resolution	89
4.5.4. Jet Position Resolution.....	90
5. INCLUSIVE FORWARD JET CROSS SECTION MEASUREMENT in PROTON- PROTON COLLISIONS at $\sqrt{s} = 7$ TeV	93
5.1. Forward Jet Production	93
5.2. Data and Monte Carlo Samples.....	96
5.3. Event Selection and Analysis Cuts	97
5.3.1. HF Noise Cut.....	97
5.3.2. Jet Quality Criteria Cut	97
5.4. Inclusive Forward Jet Cross Section Measurement	98
5.5. Jet Trigger and Trigger Efficiency	99
5.6. Luminosity Calculation.....	102
5.7. Unfolding Method.....	103
5.7.1. Bin-to-Bin Monte Carlo Method.....	103
5.7.2. Ansatz Method	108
5.7.3. Full Unfolding.....	110
5.7.4. RooUnfold Method	111
5.7.5. Bin Centre Correction	118
5.8. Systematic Uncertainties.....	121
5.8.1. Experimental Uncertainties	121
5.8.1.1. Jet Energy Scale	121
5.8.1.2. Jet p_T Resolution	123
5.8.1.3. Jet Quality Criteria	123

5.8.1.4. HF Cleaning	125
5.8.1.5. Primary Vertex Cut ($ z $)	127
5.8.1.6. Pile-Up Effect.....	127
5.8.1.7. Offset Correction.....	128
5.8.1.8. Summary of the Experimental Systematic Uncertainties.....	130
5.8.2. Theoretical Predictions.....	132
5.8.2.1. Next-to-Leading Order (NLO) Calculations.....	132
5.8.2.2. Non-Perturbative (NP) Corrections.....	133
5.8.3. Inclusive Forward Jet Spectrum.....	135
5.9 . Forward-Central Dijet Production.....	138
6. CONCLUSIONS	145
REFERENCES.....	149
CURRICULUM VITAE	157
APPENDIX	158
A. Unfolding to the Cross Section	160
B. Inclusive Forward Jet Cross Section	161
C. Bin-to-Bin Correction: Ansatz Method	165
D. Theoretical Uncertainties	167

LIST OF TABLES	PAGE
Table 2.1. Properties of the spin-1/2 particles, the fermions (Ralich, 2009)	6
Table 2.2. Fundamental forces with their mediator (Ralich, 2009)	7
Table 2.3. Properties of the spin-1 particles, the gauge bosons (Ralich, 2009)	7
Table 2.4. A possible representation of the color singlet and triplet of SU(3) symmetry	10
Table 3.1. Accelerator steps (Scheurer, 2008)	33
Table 3.2. Design specifications (except energy per proton beam and energy loss per turn) of the LHC for pp collision (Bruning et al., 2004)	34
Table 3.3. Main parameters of the CMS magnet (Bayatian et al., 1997c).....	55
Table 4.1. Calorimeter cell thresholds (Zielinski, 2010)	71
Table 4.2. Bin edges of GenJet p_T in GeV/c used for the studies of the jet response	85
Table 5.1. Resolution based binning in jet transverse momentum p_T , (GeV/c)....	99
Table 5.2. L1 and High Level Trigger jet descriptions.....	100
Table 5.3. Smeared Ansatz fits to the inclusive jet cross section	119
Table 5.4. Summary of the systematic uncertainties	131
Table 5.5. The measured, fully corrected p_T differential jet cross sections and their associated uncertainties	144
Table D.1. Theoretical Uncertainty	167
Table D.2. The unfolded data cross section values, fNLO and various MC models on hadron level	167
Table D.3. Difference of the unfolded data cross section values with various MC samples on hadron level	168
Table D.4. Difference of the unfolded data cross section values with fNLO and various MC samples on hadron level	168

LIST OF FIGURES	PAGE
Figure 2.1. Summary of interactions.....	8
Figure 2.2. The interaction vertices of the Feynman diagrams of QCD.....	9
Figure 2.3. Summary of measurements of α_s as a function of the energy scale Q . The respective degree of QCD perturbation theory used in the extraction of α_s is indicated in brackets.....	12
Figure 2.4. The Q^2 - x kinematic plane for the LHC and previous experiments, showing the mass ($M = Q$) and rapidity (y) dependence	15
Figure 2.5. Schematic phase space diagram for DIS	16
Figure 2.6. Examples of experimental measurements at various facilities providing information on the gluon PDF in the range $x \sim 10^{-5}$ - 0.8	17
Figure 2.7. The PDF distribution determined from the HERAPDF1.0 fit at $Q^2 = 10 \text{ GeV}^2$ for gluons, sea quarks, up (u_μ) and down (d_μ) valance quarks	18
Figure 2.8. Hard scattering process.....	19
Figure 2.9. SM cross sections for hard scattering versus \sqrt{s} at the Tevatron and LHC colliders.....	20
Figure 2.10. pp scattering processes	21
Figure 2.11. Hadronization using (a) string and (b) cluster models in Monte Carlo event generators	23
Figure 2.12. Working principle of a multi-purpose MC event generator	24
Figure 3.1. Overview of the Accelerator chain. The LHC is the last ring in a complex chain of particle accelerators	30
Figure 3.2. Official luminosity report 2010	31
Figure 3.3. The cross section and event rate in pp collisions as a function of center of mass energy	35
Figure 3.4. The LHC and experiments schema.....	36

Figure 3.5.	Schematic view of the CMS detector and its components	40
Figure 3.6.	Transverse slide of the CMS detector and particles traces in different subdetectors	41
Figure 3.7.	Schematic cross section through the CMS Tracker. Each line represents a detector module	42
Figure 3.8.	Geometrical layout of the Pixel detector	43
Figure 3.9.	Location of the ECAL and the HCAL detectors in and around the CMS magnet	45
Figure 3.10.	Longitudinal view of a quadrant of CMS electromagnetic calorimeter	46
Figure 3.11.	Longitudinal view of the four subsystems of the hadronic calorimeter	49
Figure 3.12.	Assembled HCAL half-barrel in SX5 (left), numbering scheme for the HB wedges. Wedge 1 is on the inside ($+x$ direction) of the LHC ring (right)	50
Figure 3.13.	HE Calorimeter (left), η segmentation and size increase in HE (right)	51
Figure 3.14.	Overview of the HF Calorimeter	52
Figure 3.15.	CMS HF Calorimeter production wedges (left), η segmentation and size increase in HF (right)	53
Figure 3.16.	The cross sectional view of the HF calorimer	53
Figure 3.17.	The CMS superconducting magnet	55
Figure 3.18.	Design overview of the outer CMS muon system	57
Figure 3.19.	Layout of the CMS barrel muon DT chambers in one of the 5 wheels	58
Figure 3.20.	Quarter view of the CMS detector. CSC of the Endcap Muon system are highlighted	59
Figure 3.21.	Resistive plate chamber layers	60
Figure 3.22.	CMS trigger and DAQ system	61
Figure 3.23.	Level-1 Trigger architecture	62
Figure 3.24.	Location of CASTOR in the CMS forward region	64

Figure 4.1.	A representation of the different stages of jet production and reconstruction: parton, particle and calorimeter level	67
Figure 4.2.	Sketch of calorimeter towers used for jet clustering. 5×5 ECAL-cells and one HCAL tower are logically combined to form a calorimeter tower in the barrel region.....	70
Figure 4.3.	Observed dijet event in the CMS calorimeters.....	71
Figure 4.4.	The Particle Flow algorithm. Particles in the CMS detector are seen as tracks and energy depositions and the algorithm attempts to fully reconstruct an event by combining information for all CMS subdetectors	73
Figure 4.5.	Configuration of Infrared (top) and Collinear (bottom) safe algorithm.....	75
Figure 4.6.	Cone-type Jet Algorithm: a) listing of initial four-vectors, b) and c) finding stable cones, d) splitting/merging algorithm applied, e) final jets	77
Figure 4.7.	Illustration of different jet algorithms in parton level	80
Figure 4.8.	Factorized Jet Energy Corrections in CMS	81
Figure 4.9.	ΔR distributions for the jet p_T bin 20-35 GeV/c for the anti- k_T ($R = 0.5$) algorithm	86
Figure 4.10.	ΔR distributions for the jet p_T bin 80-120 GeV/c for the anti- k_T ($R = 0.5$) algorithm	86
Figure 4.11.	Corrected jet response distributions for different p_T bins and for anti- k_T ($R = 0.5$) algorithm.....	87
Figure 4.12.	Corrected jet response as a function of p_T^{GenJet} for the anti- k_T ($R = 0.5$) algorithm	88
Figure 4.13.	Corrected jet response as a function of η^{GenJet} for the anti- k_T ($R = 0.5$) algorithm	88
Figure 4.14.	Energy resolution as a function of p_T^{GenJet} for the anti- k_T ($R = 0.5$) algorithm for jets reconstructed in $3.2 < \eta < 4.7$	89
Figure 4.15.	The $(\phi_{CaloJet} - \phi_{GenJet})$ distributions with Gaussian fits. Each histogram corresponds to different range in p_T^{GenJet}	91

Figure 4.16. HF jet ϕ resolutions as a function of p_T^{GenJet} for the anti- k_T ($R = 0.5$) algorithm	91
Figure 4.17. The $(\eta_{CaloJet} - \eta_{GenJet})$ distributions with Gaussian fits. Each histogram corresponds to different range in p_T^{GenJet}	92
Figure 4.18. HF jet η resolutions as a function of p_T^{GenJet} for the anti- k_T ($R = 0.5$) algorithm	92
Figure 5.1. $\text{Log}(x_{1,2})$ distribution of two partons producing at least one jet above $p_T = 20$ GeV/c at forward rapidities in pp collision	94
Figure 5.2. Feynman diagram for inclusive forward jet production	95
Figure 5.3. Jet Trigger Algorithm	100
Figure 5.4. Jet p_T spectrum (before applying JEC) of the trigger stream used for forward jet analysis (left), jet trigger turn-on of the HLTJet15U stream vs. corrected jet p_T (after applying JEC) (right) and Jet trigger efficiency vs. jet η (bottom)	101
Figure 5.5. Total luminosity shown run-by-run (left), effective luminosity obtained from the trigger HLTJet15U shown by run number (right). The prescale factors of HLT Jet15U trigger is shown by run number (bottom).....	102
Figure 5.6. Measured differential cross sections for jets as a function of p_T before unfolding the energy resolution (black dots), compared to detector-level MC simulations generated with PYTHIA 6 and HERWIG 6	104
Figure 5.7. The acceptance (left) and background (right) as a function of CaloJets p_T for PYTHIA 6.4.....	106
Figure 5.8. The purity (left) and stability (right) as a function of corrected CaloJets p_T for the bins in which cross section measurements are performed shown for PYTHIA 6.4.....	107
Figure 5.9. The bin-by-bin unfolding correction factors as a function of p_T for inclusive forward jets.....	107
Figure 5.10. Inclusive forward CaloJets p_T resolution with CMS MC simulation PYTHIA 6.4.....	109

Figure 5.11. Matrix element between CaloJets and Generated jets	111
Figure 5.12. Bin-by-Bin unfolding using RooUnfold. The measured, MC true and unfolded cross section (left). Ratio of unfolded to MC true cross section (right)	112
Figure 5.13. Bayes (D'Agostini with 1 st iteration) unfolding using RooUnfold. The measured, MC true and unfolded x-section (left). Ratio of unfolded to MC true x-section (right)	113
Figure 5.14. Bayes (D'Agostini with 2 nd iteration) unfolding using RooUnfold. The measured, MC true and unfolded x-section (left). Ratio of unfolded to MC true x-section (right)	113
Figure 5.15. Bayes (D'Agostini with 3 rd iteration) unfolding using RooUnfold. The measured, MC true and unfolded x-section (left). Ratio of unfolded to MC true x-section (right)	114
Figure 5.16. Bayes (D'Agostini with 4 th iteration) unfolding using RooUnfold. The measured, MC true and unfolded x-section (left). Ratio of unfolded to MC true x-section (right)	114
Figure 5.17. Bayes (D'Agostini with 5th iteration) unfolding using RooUnfold. The measured, MC true and unfolded x-section (left). Ratio of unfolded to MC true x-section (right)	115
Figure 5.18. SVD (with <i>kterm</i> = 1) unfolding using RooUnfold. The measured, MC true and unfolded cross section (left). Ratio of unfolded to MC true cross section (right).....	115
Figure 5.19. SVD (with <i>kterm</i> = 2) unfolding using RooUnfold. The measured, MC true and unfolded cross section (left). Ratio of unfolded to MC true cross section (right).....	116
Figure 5.20. SVD (with <i>kterm</i> = 3) unfolding using RooUnfold. The measured, MC true and unfolded cross section (left). Ratio of unfolded to MC true cross section (right).....	116
Figure 5.21. SVD (with <i>kterm</i> = 4) unfolding using RooUnfold. The measured, MC true and unfolded cross section (left). Ratio of unfolded to MC true cross section (right).....	117

Figure 5.22. SVD (with $kterm \geq 7$) unfolding using RooUnfold. The measured, MC true and unfolded cross section (left). Ratio of unfolded to MC true cross section (right).....	117
Figure 5.23. Smeared Ansatz fit to the jet p_T spectrum for DATA (left). Quality of the fit: fractional difference between the fitting curve and the "data" points. Error bars are statistical only (right).....	118
Figure 5.24. Smeared Ansatz fit to the jet p_T spectrum for MC (left), Quality of the fit: fractional difference between the fitting curve and the "data" points for MC (PYTHIA 6.4). Error bars are statistical only (right).....	118
Figure 5.25. The comparison of the correction factors obtained from MC method and Ansatz method	119
Figure 5.26. The final unsmeared cross sections obtained after the application of correction factors from MC method and Ansatz method and their ratio of cross sections obtained from both methods (bottom).....	120
Figure 5.27. Corrected jet p_T spectrum with JEC	122
Figure 5.28. The ratio between the p_T distribution obtained with the "LOOSE" and "TIGHT" Jet ID.....	124
Figure 5.29. The ratio between the p_T distribution obtained with the V1, V2 and V3 of the HF cleaning.....	126
Figure 5.30. The ratio between the p_T distribution obtained with the $ z < 24$ cm and $ z < 15$ cm	127
Figure 5.31. Average pile-up estimation obtained for the each run number used in the analysis (left). Average pile-up estimated per run with respect to number of primary vertices per run (right)	128

Figure 5.32. The p_T distributions for jets from events with exactly one vertex reconstructed and for jets from all events (left). The p_T distribution for jets from events with exactly one vertex reconstructed and the same distribution after applying to each jet a p_T shift of 0.5, 1, 2 and 3 GeV (right).....	130
Figure 5.33. Experimental uncertainties as a function of jet p_T for inclusive forward production	131
Figure 5.34. Non-perturbative corrections to NLO QCD calculations. The error bars correspond to half the spread between the predictions from PYTHIA 6.4 and HERWIG + JIMMY	133
Figure 5.35. Uncertainties on the predicted NLO inclusive forward jet spectrum	135
Figure 5.36. Inclusive jet cross section at forward pseudorapidities ($3.2 < \eta < 4.7$), fully corrected and unfolded, compared to particle-level predictions from PYTHIA 6, PYTHIA 8, HERWIG 6, NLOJET++ corrected for non-perturbative effects, POWHEG, CASCADE and HEJ (left). Ratio of theory/data for the forward jet spectrum (right)	136
Figure 5.37. The NLO predictions compared to the data	137
Figure 5.38. Feynman diagram for forward–central dijet production	138
Figure 5.39. Measured differential cross sections for forward jets in dijet events as a function of p_T , before unfolding the energy resolution (black dots), compared to detector-level MC simulations generated with different versions of PYTHIA and HERWIG for forward jets in dijet events.....	139
Figure 5.40. Systematic uncertainties as a function of jet p_T for forward jet spectra in dijet events	140
Figure 5.41. Differential cross sections as a function of jet p_T for dijet events with at least one forward jet for PYTHIA, POWHEG (+PYTHIA6), CASCADE	141

Figure 5.42. Differential cross sections as a function of jet p_T for dijet events with at least one forward jet for HERWIG, POWHEG (+HERWIG), HEJ	142
Figure 5.43. Ratio of theory to data for differential cross sections as a function of p_T , for forward jets produced in dijet events for PYTHIA, POWHEG (+PYTHIA6), CASCADE	143
Figure 5.44. Ratio of theory to data for differential cross sections as a function of p_T , for forward jets produced in dijet events for HERWIG, POWHEG (+HERWIG), HEJ	143
Figure A.1. The acceptance (left) and background (right) as a function of corrected PF jets p_T for PYTHIA 6.4	160
Figure A.2. The purity (left) and stability (right) as a function of corrected PF jets p_T for PYTHIA 6.4	160
Figure B.1. Inclusive Forward Calo jets p_T cross section on detector level for DATA and MC simulations PYTHIA 6.4 and HERWIG+JIMMY	161
Figure B.2. Inclusive Forward CaloJets η cross section on detector level for DATA and MC simulations, PYTHIA 6.4 and HERWIG+JIMMY	161
Figure B.3. Inclusive forward CaloJets vs. PF jets.....	162
Figure B.4. Lumi yield plot	162
Figure B.5. Detector level comparison between data and MC (PYTHIA) simulation	163
Figure B.6. Detector level comparison between data and MC (HERWIG) simulation	163
Figure B.7. Detector level comparison between PYTHIA and HERWIG	164
Figure B.8. Comparison between PYTHIA and DATA both detector level and hadron-level	164

Figure C.1. Comparison of MC correction factor obtained from PYTHIA 6.4 and HERWIG + JIMMY MCs for Calo jets for $3.2 < \eta < 4.7$ (left), and a comparison of correction factor obtained within the range of $3.2 < \eta < 4.6$ (right).....	165
Figure C.2. A comparison of correction factor obtained within the range of $3.2 < \eta < 4.7$ for PF jets (right)	165
Figure C.3. Correction factor obtained from Ansatz method for data (top) and for PYTHIA 6.4 MC (bottom).....	166

ABBREVIATIONS

ALICE	: A Large Ion Collider Experiment
ATLAS	: A Toroidal LHC Apparatus
BFKL	: Balitski-Fadin-Kuraev-Lipatov
CERN	: Conseil Europeenne pour la Recherche Nucleaire
CL	: Confidence Level
CMS	: Compact Muon Solenoid
CSC	: Cathode Strip Chamber
CTEQ	: Coordinated Theoretical-Experimental Project on QCD
DAQ	: Data AcQusition
DGALP	: Dokshitzer-Gribov-Lipatov-Altarelli-Parisi
DT	: Drift Tube
EB	: Barrel Electromagnetic Calorimeter
ECAL	: Electromagnetic CALorimeter
EE	: Endcap Electromagnetic Calorimeter
HB	: Barrel Hadronic Calorimeter
HCAL	: Hadronic CALorimeter
HF	: Hadronic Forward
HLT	: High Level Trigger
HO	: Outer Barrel Hadronic Calorimeter
JEC	: Jet Energy Correction
JER	: Jet Energy Resolution
JES	: Jet Energy Scale
LEP	: Large Electron Positron Collider
LHC	: Large Hadron Collider
LHCb	: Large Hadron Collider Beauty Experiment
MC	: Monte Carlo
PDF	: Parton Density Function
PS	: Proton Synchrotron
QCD	: Quantum Chromo Dynamics

QED	: Quantum Electro Dynamics
RBX	: Readout Box
RF	: Radio Frequency
RPC	: Resistive Plate Chamber
SM	: Standard Model
SPS	: Super Proton Synchrotron
TEC	: Tracker End Cap
TIB	: Tracker Inner Barrel
TID	: Tracker Inner Disks
TOB	: Tracker Outer Barrel

1. INTRODUCTION

Physics is the science that strives to understand the basic features of the world around us. Human desire for knowledge has led to deep insights into the mechanisms of nature and allowed for discovery of many amazing properties of the universe. In some cases this has only been possible because we strive to understand the fundamental components of matter and their interactions. It has been the accomplishment of particle physics to develop, with unprecedented accuracy a model of these interactions that we call Standard Model (SM) framework. This is currently the best theory for modeling the interactions and the behaviour of elementary particles and physical forces (except gravity). During the last 40 years the SM has been tested with success in many accelerators and particle physics detectors around the world. In the early 1980's, the discovery of particles such as the weak boson and more recently the Higgs boson, confirmed the SM's predictive power. In high precision searches only little deviation from the SM was observed, yet still, we do know that the SM cannot be the complete description of all particle interactions and because of several open questions it is not a complete theory. For example, the existence of neutrino oscillation, and thus neutrino mass, moreover the matter/anti-matter asymmetry in the universe and the problem of unifying the fundamental interactions show that there are still basic questions to be answered and all these unanswered questions suggest existence of new physics beyond the SM.

The SM contains twelve fundamental fermions (and their respective anti-particles) as constituents of matter and describes the strong, weak and electromagnetic interactions between them using mediating particles called gauge bosons. In this thesis particular emphasis is put on the theory of the strong interaction, Quantum Chromodynamics (QCD), as partons in the proton and their interactions are generally described in terms of QCD. For us it is important to understand what models are used by the Monte Carlo (MC) generators and what can be directly calculated within the framework of the SM, how the hard scatter partons are observed and what is the final state of hadrons. In Chapter 2 the most important concepts, such as interaction between quarks, gauge boson role of the mediator

application of perturbative theory to QCD, quark confinement and process of decay from hadron to parton are explained.

Chapter 3 provides an introduction to the Large Hadron Collider (LHC) and summarizes its experimental setup. It starts by describing the LHC and associated experiments at the Conseil Européen pour la Recherche Nucléaire (CERN), Switzerland. The main goal of the LHC is the search for physics beyond the SM and one of the major motivations for the current LHC operation was the discovery of the Higgs boson which was expected to be the origin of the elementary particle masses.

LHC has collided protons at a center of mass energy of 7 TeV in 2010 and 2011, and the colliding energy has been raised to 8 TeV in 2012. Two main LHC experiments (ATLAS and CMS) searching for Higgs presented their results on 4 July 2012, indicating the particle was discovered with a mass between 125 and 127 GeV/c^2 . By March 2013, the particle has been proven to behave, interact and decay in many of the ways predicted by the SM but more data is needed to know if it is indeed the Higgs boson or whether, as predicted by some theories, multiple Higgs bosons exist.

Section 3.2 describes the Compact Muon Solenoid (CMS) detector; one of the two multi-purpose experiments at the LHC (with ATLAS being the other one). It is designed for the discovery of new particles as well as for precise measurements of known processes within the SM. The main feature of CMS is the 4T superconducting solenoid that permits a compact design of the detector with a strong magnetic field. Starting from the closest to the interaction point, the individual subdetectors are the Tracker, the Electromagnetic Calorimeter (ECAL) and the Hadronic Calorimeter (HCAL) which are surrounded by the solenoid, followed by layers of muon detectors. The CMS detector is providing a calorimetric coverage to study jet production over a range of jet pseudorapidities as large as $\Delta\eta \approx 10$.

This thesis concentrates on the Hadronic Forward Calorimeter (HF), the subsystem of HCAL in CMS. The HF has two main purposes in CMS: to improve the measurement of the missing transverse energy (E_T^{miss}) and to enable identification and reconstruction of forward jets.

Chapter 4 focuses on jet definition, jet reconstruction and jet performance in the HF calorimeter. A jet is a narrow cone of hadrons and other particles produced by the hadronization of a quark or gluon and it can be classified by two main types of jet algorithms: cone algorithms and sequential recombination algorithms. The text will discuss what properties a successful jet algorithm needs to have to provide good correspondence between the parton level and the particle level search.

Chapter 5 presents the analysis of the main topic of the thesis: the measurement of inclusive forward jet cross section and dijet events with at least one jet emitted at central and the other at forward pseudorapidities in HF using 3.14 pb^{-1} of data from the CMS experiment in pp collision at $\sqrt{s} = 7 \text{ TeV}$. The jet cross section measurement is an important test to demonstrate the capabilities of the detector and it is the fundamental test of perturbative QCD (pQCD). This measurement also provides information on the parton distribution functions (PDFs) and the strong coupling and it is sensitive to the presence of new physics phenomena. The jet cross sections at large transverse momenta (p_T) measured at LHC are well described over several orders of magnitude by pQCD. In this analyses forward jets are measured within $3.2 < |\eta| < 4.7$ pseudorapidities, and central jets within the $|\eta| < 2.8$ range, in the transverse momentum range $p_T = 35 - 150 \text{ GeV}/c$ and only forward jet results are presented. The hadron level results are compared with predictions obtained from several Monte Carlo (MC) event generators, namely: PYTHIA 6 (version 6.422), PYTHIA 8 (version 8.135), HERWIG 6 (version 6.510.3 + JIMMY) and HERWIG++ (version 2.3) as well as to next-to-leading (NLO) pQCD predictions obtained either with NLOJET++ or with POWHEG package which implements a matching to PYTHIA or HERWIG parton showers. Additionally, data is compared to results from the CASCADE (version 2.2.04) which includes parton radiation from QCD evolution in $1/x$ and with the extra wide-angle gluon radiations included in the HEJ model.

All the analysis results and details presented in this thesis were published in CMS Analysis Notes (Cerci, Sunar Cerci et al., 2010), (Brona, Cerci et al., 2010), CMS Physics Analysis Summary (Chatrchyan et al., 2010a) and CMS Paper (Chatrchyan et al., 2012).

2. THEORETICAL MOTIVATION

In this chapter, the basic theoretical and phenomenological concepts related to the present analysis will be presented. First, an overview of the Standard Model (SM) of particles and forces, then Quantum Chromodynamics (QCD) and pp scattering processes will be discussed and finally Monte Carlo (MC) event generators used in this study will be covered.

2.1. The Standard Model of Particle Physics

The SM is so far the most successful theory describing the properties and interactions (electromagnetic, weak and strong) of the elementary particles. This model combines QCD and the electroweak theory. The gauge quantum field theory based on the symmetry group $SU(3)_C \times SU(2)_L \times U(1)_Y$, where the electroweak sector is in the $SU(2)_L \times U(1)_Y$ group and the strong sector is based in the $SU(3)_C$ group. Over the years the SM has been tested in different experiments and almost all the results obtained with high precision were in agreement with the predictions of the SM.

In the SM there are twelve fermions (and their anti fermions), twelve gauge bosons and one neutral Higgs particle. Fermions have half integer spin and obey Fermi-Dirac statistics and bosons have integer spin and obey Bose-Einstein statistics. The Higgs particle is a scalar and has spin 0. The fundamental fermions are further divided into leptons and quarks. Each of them consists of three generations with similar properties, e.g. electric charge q , spin J and third component of the weak isospin I_3 . Fundamental particles of the SM are shown in Table 2.1.

Leptons come in three lepton families: electron (ν_e , e), muon (ν_μ , μ) and tau (ν_τ , τ). They can also be classified according to their charge: the neutral neutrinos ν_e , ν_μ , ν_τ and the negatively charged e^- , μ^- and τ^- . Three of the leptons e , μ and τ carry a unit charge while neutrinos are chargeless and were initially believed to be massless. But, recent observations from neutrino experiments indicate neutrinos having nonzero mass (Karagiorgi et al., 2007).

The quarks come in six flavors and like the leptons, they can be grouped into three quark families: up (u) and down (d), charm (c) and strange (s), top (t) and bottom (b). The u , c , t quarks have electric charge $2e/3$ and the d , s , b quarks have charge $-e/3$, with e being the elementary electric charge. Leptons interact via the weak force while quarks carry an additional color charge and interact via the strong force.

Table 2.1. Properties of the spin-1/2 particles, the fermions (Ralich, 2009).

Generation	Name	Symbol	Charge (e)	Mass (GeV/c^2)
I	up quark	u	2/3	2.4×10^{-3}
	down quark	d	-1/3	4.8×10^{-3}
	electron	e	-1	0.5×10^{-3}
	electron-neutrino	ν_e	0	0
II	strange quark	s	-1/3	0.1
	charm quark	c	2/3	1.27
	muon	μ	-1	0.1
	muon-neutrino	ν_μ	0	0
III	bottom quark	b	-1/3	4.8
	top quark	t	2/3	172.6
	tau	τ	-1	1.7
	tau-neutrino	ν_τ	0	0

The particles and anti-particles in the SM interact via electromagnetic, weak and strong forces. The gravity is the fourth and the weakest amongst all. In Table 2.2 fundamental forces and their mediators are given. All these fundamental interactions can be characterized by gauge field theories.

Table 2.2. Fundamental forces with their mediator (Ralich, 2009).

Force	Strength	Theory	Mediator
Gravitational	10^{-42}	Gravitation	Graviton
Weak	10^{-13}	Flavordynamics	Massive Vector Bosons
Electromagnetic	10^{-2}	Electrodynamics	Photon
Strong	10	Chromodynamics	Gluon

The electromagnetic interaction occurs between two particles having electric charge. Quantum Electrodynamics (QED) is the quantum approach to the electromagnetic interaction and provides the mathematical theory associated with the gauge symmetry $U(1)$ and involves the exchange or production of photons. Hence photons are the mediators of electromagnetic interaction.

The weak interaction is very short ranged and is described by quantum flavor dynamics. The weak force mediating particles, W^\pm and Z^0 are massive. All elementary particles participate in the weak interaction, either via charged W or the Z^0 neutral interaction.

Table 2.3. Properties of the spin-1 particles, the gauge bosons (Ralich, 2009).

Force	Name	Symbol	Charge (e)	Mass (GeV/c ²)
Electromagnetic	photon	γ	0	0
Weak	W boson	W^\pm	1	80.4
Weak	Z boson	Z^0	0	91.2
Strong	gluon	g	0	0

The strong interaction is described by QCD with an underlying non-Abelian color symmetry $SU(3)$. The conserved quantity is the color charge. There are three types : red, green and blue and their anticolors.

Quarks are the only fermions carrying a color charge. The force is exchanged via massless gluons. They carry a color and anti-color, forming a color octet. In nature only colorless particles are observed as free objects. Thus, free quarks or gluons can not be observed. Quarks that form combined objects are called hadrons: Mesons consist of a quark and antiquark pair and baryons have three quarks (anti-quarks) (Ralich, 2009). A summary of interactions between particles described by the SM is shown in the Figure 2.1. The dashed line between the photon propagator and leptons indicates that photons couple only with charged leptons.

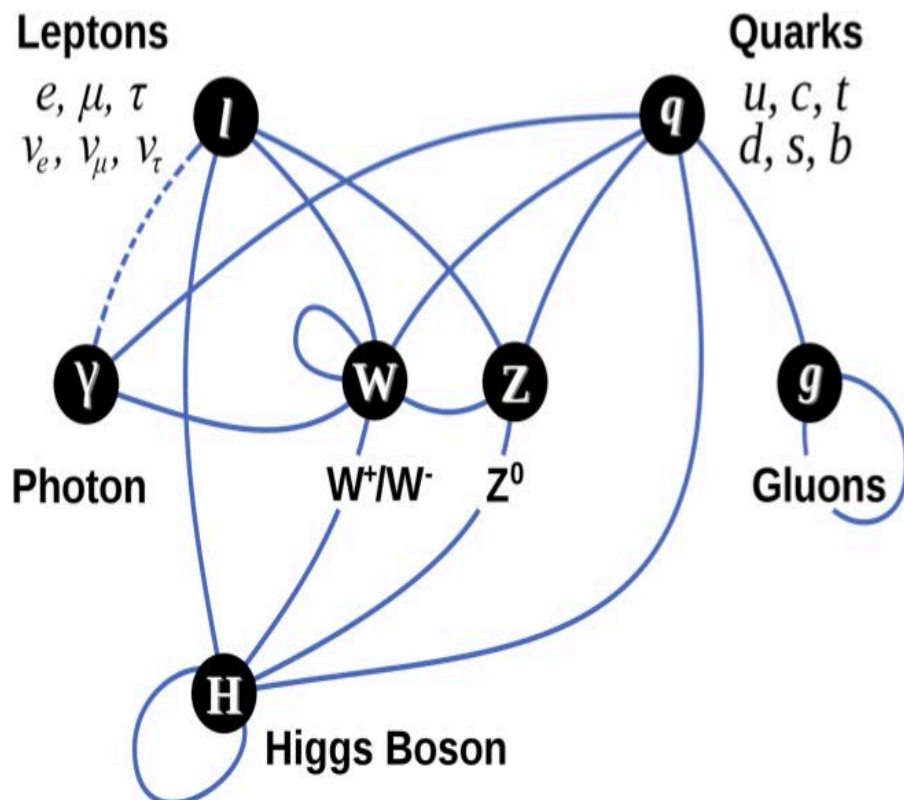


Figure 2.1. Summary of interactions (http://en.wikipedia.org/wiki/Higgs_boson).

The quark-gluon and gluon-gluon strong interaction vertices are shown in Figure 2.2.

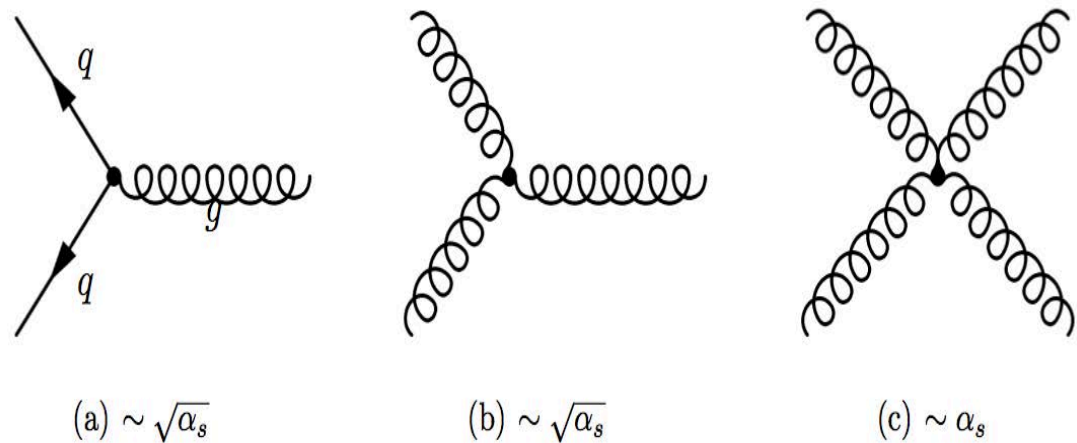


Figure 2.2. The interaction vertices of the Feynman diagrams of QCD.

The SM theory has been tested in various experiments and the agreement with experimental data is very high, but some questions are still unanswered. For example only massless gauge bosons are predicted, due to the local gauge invariance, hence, no explanation for the W and Z mass is given and the mass of the other particles is not explained either. One possible solution within the SM is the Higgs mechanism (Higgs, 1964). In this mechanism the scalar quantum field is called the Higgs field. Its introduction allowed to describe how mass arises from the interaction of particles with the Higgs field. The theory of particle physics is also strongly relevant to some fundamental cosmological questions. For instance to answer the question of matter-antimatter asymmetry in the universe and why there is still not a clear particle candidate for dark matter (Ralich, 2009). One another important question of particle physics is the unification of all four forces to one single force, which cannot be solved in the SM framework. Thus new theories like supersymmetry (Aitchison, 2007) or extra dimensions may provide an answer to the unification of gravity and the SM.

2.2. Quantum Chromodynamics

Quantum Chromodynamics (QCD) is a quantum field theory which describes the interaction between quarks and gluons through color charges. In the strong interactions the color charges of quarks have the same role as electric charges of particles in the electromagnetic interaction. So the color charge is the source of gluon field (Boyarkin, 2007). There are three color charges which are called red (r), green (g) and blue (b) and form a triplet under $SU(3)_C$.

$$R = \begin{pmatrix} 1 \\ 0 \\ 0 \end{pmatrix}, \quad G = \begin{pmatrix} 0 \\ 1 \\ 0 \end{pmatrix}, \quad B = \begin{pmatrix} 0 \\ 0 \\ 1 \end{pmatrix} \quad (2.1)$$

A possible representation of these color states as a singlet and an octet is given in Table 2.4. The singlet is colorless and for this reason it does not contribute to the interaction. The gluon has eight independent color states, which are linear combinations of a color and an anti-color charge, constituting a color octet.

Table 2.4. A possible representation of the color singlet and triplet of $SU(3)$ symmetry.

symmetry	representation							
octet	$r\bar{g}$	$r\bar{b}$	$g\bar{b}$	$g\bar{r}$	$b\bar{r}$	$b\bar{g}$	$\sqrt{1/2}(\bar{r}r - \bar{g}g)$	$\sqrt{1/6}(\bar{r}r + \bar{g}g - \bar{b}b)$
singlet	$\sqrt{1/3}(\bar{r}r + \bar{g}g - \bar{b}b)$							

The precision QCD calculations and their experimental tests at pp collider are very difficult. Basically, physics aspects of the LHC, from particle searches beyond SM to electroweak precision measurements and studies of heavy quarks are connected to the interactions of quarks and gluons at large transferred momentum. All of the processes to be investigated at the LHC involve QCD to some extent. It cannot be otherwise, since the colliding quarks and gluons carry the QCD color charge (Catani et al., 2000).

2.2.1. Perturbative QCD and Asymptotic Freedom

Perturbative QCD (pQCD) seeks to identify the structure of multi partonic systems which are produced by QCD cascades. pQCD wants to obtain the same real information about confinement using calculable characteristics of quark, gluon ensembles and measurable characteristics of final hadronic states in hard processes (Dokshitzer et al., 1991). Thus pQCD is very important for understanding of rates and characteristics of predictions for hard processes at the LHC both for signals and backgrounds. Interactions are described by their coupling and the coupling can be chosen to be dimensionless to make possible a comparison of the different couplings. pQCD is based on the strong coupling constant α_s given below:

$$\alpha_s(Q^2) = \frac{1}{b_0 \ln(Q^2/\Lambda_{QCD}^2)} \quad (2.2)$$

where $b_0 = (11N_c - 2n_f)/12\pi$, N_c and n_f are the numbers of colors and quark flavours, respectively. Λ_{QCD} is the scale parameter characterizing the energy scale at which the coupling escapes to infinity. For $Q^2 < \Lambda^2_{QCD}$, which corresponds to large distances, α_s increases, causing confinement of quarks and gluons. On the other hand α_s decreases with an increasing scale of the interaction Q^2 . The strong coupling α_s as a function of the energy scale Q is shown in Figure 2.3 (top). In this plot the current world average value of QCD coupling is $\alpha_s(M_Z^2) = 0.1184 \pm 0.0007$ (Beringer et al., 2012). The summary of values of $\alpha_s(M_Z^2)$ obtained for various sub-classes of measurements is also demonstrated in Figure 2.3 (bottom).

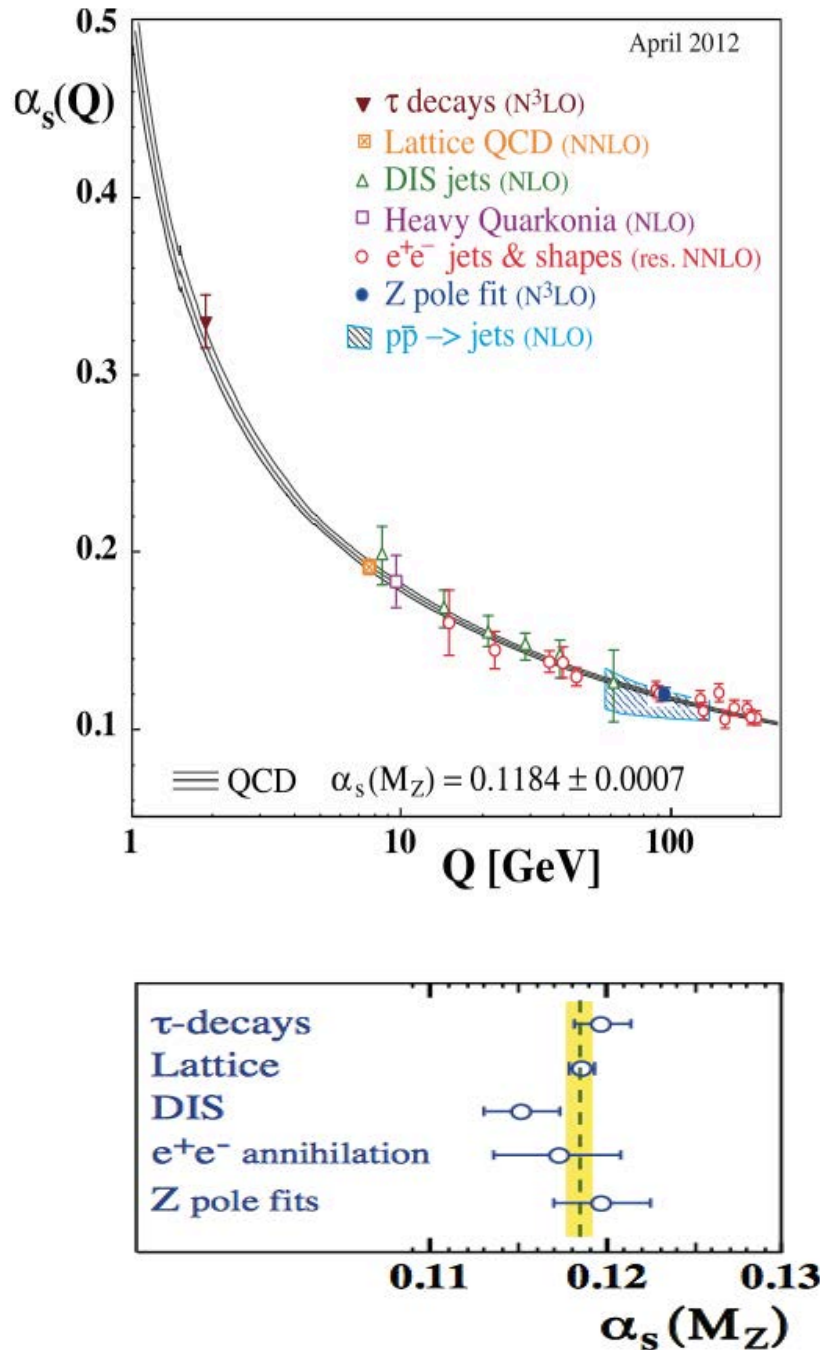


Figure 2.3. Summary of measurements of α_s as a function of the energy scale Q . The respective degree of QCD perturbation theory used in the extraction of α_s is indicated in brackets (NLO: next to leading order; NNLO: next-to-next-to leading order; res NNLO: NNLO matched with resummed next-to-leading logs; N³LO: next-to-NNLO) (top) and summary of values of $\alpha_s(M_Z^2)$ (bottom) (Beringer et al., 2012).

The property of color confinement can be used to identify qualitatively why free quarks and colored combinations of hadrons have not been observed in nature. At high $Q^2 > 1 \text{ GeV}^2$, α_s becomes small. In this case quarks are not influenced by the other partons in the proton and only interact very weakly with each other and can be treated as free particles. This behavior is called asymptotic freedom. It is the important characteristics of strong interaction which describes the behavior of quarks inside hadrons and hadron formation and is successfully applied in theory calculations, since it allows the application of perturbative techniques.

2.2.2. Quark Parton Model and Parton Density Function

The high energy interactions of hadrons are described by the QCD parton model. The main idea of this model is that the hard scattering between two hadrons can be understood as the interaction between the partons, quarks and gluons. The Quark Parton Model (QPM) was developed by Feynman in order to explain the scaling behaviour of the deep inelastic scattering (DIS) structure function F_2 as predicted by Bjorken (Bjorken, 1969). Bjorken suggested that the structure function of a proton is a function of variable x , parton momentum fraction. Bjorken scaling expects F_2 to be independent of Q^2 while depending only on x at high enough Q^2 . Deep inelastic scattering (DIS) is the name given to a process used to probe the insides of hadrons (such as protons and neutrons), using electrons, muons and neutrinos. The direct evidence for the existence of quarks inside the proton is provided by DIS. First DIS experiments at the Stanford Linear Accelerator Center (SLAC) proved this behaviour at $x \sim 0.25$ and it was explained by Feynman as a proton being made out of point like constituents which he himself called partons. In the QPM the structure functions F_2 can be written as;

$$F_2(x, Q^2) = 2x F_1(x, Q^2) = \sum_i e_i^2 x f_i(x) \quad (2.3)$$

where the function $f_i(x)$ is the Parton Distribution Function (PDF) of the proton.

The sum runs over all quarks and anti-quarks in the proton, which have electrical charge e_i . $f_i(x)$ gives the probability of finding a parton i carrying the momentum fraction x in the proton. $f_i(x)$ is independent of α_s and any scale and directly proportional to F_2 . The structure function F_1 is defined by the parton densities, while F_2 describes the momentum densities. The QPM predicts the longitudinal structure function $F_L(x, Q^2) = 0$, which is a consequence of the scattering from spin -1/2 partons in the absence of QCD radiation.

$$F_L = F_2 - 2xF_1 = 0 \quad (2.4)$$

It follows that $F_2 = 2xF_1$, which is known as the Callan-Gross relationship. From the equation 2.3, structure function of the proton can be written as:

$$F_2(x) = x \left(\frac{4}{9} [u(x) + \bar{u}(x)] + \frac{1}{9} [d(x) + \bar{d}(x) + s(x) + \bar{s}(x)] + \dots \right) \quad (2.5)$$

where $u(x)$ ($d(x), s(x)$) is the PDF for $u(d, s)$ quark in the proton while $\bar{u}(x)$ ($\bar{d}(x), \bar{s}(x)$) for $\bar{u}(\bar{d}, \bar{s})$ antiquark.

The momentum distribution functions of the partons within the proton are called Parton Distribution Functions (PDFs) when the spin direction of the partons is not considered. The PDF gives the probability densities for finding a parton carrying a momentum fraction x at Q^2 . The knowledge of proton PDFs mainly comes from the DIS (Soper, 1997), HERA (Dittmar et al., 2005), fixed target and TEVATRON (Bhatti and Lincoln, 2010) data. DIS experiments have shown that the number of partons grows at low x with Q^2 and falls at high x . At low Q^2 the three valence quarks become more and more dominant in the nucleon while at high Q^2 there are more and more quark-antiquark pairs which carry a low momentum fraction x . Assuming the factorization scale (Q) is equal to M , the mass of the final state, the relationship

between the parton (x, Q^2) values and the kinematic variables M and rapidity (y) is shown both for LHC and also previous experiments in Figure 2.4.

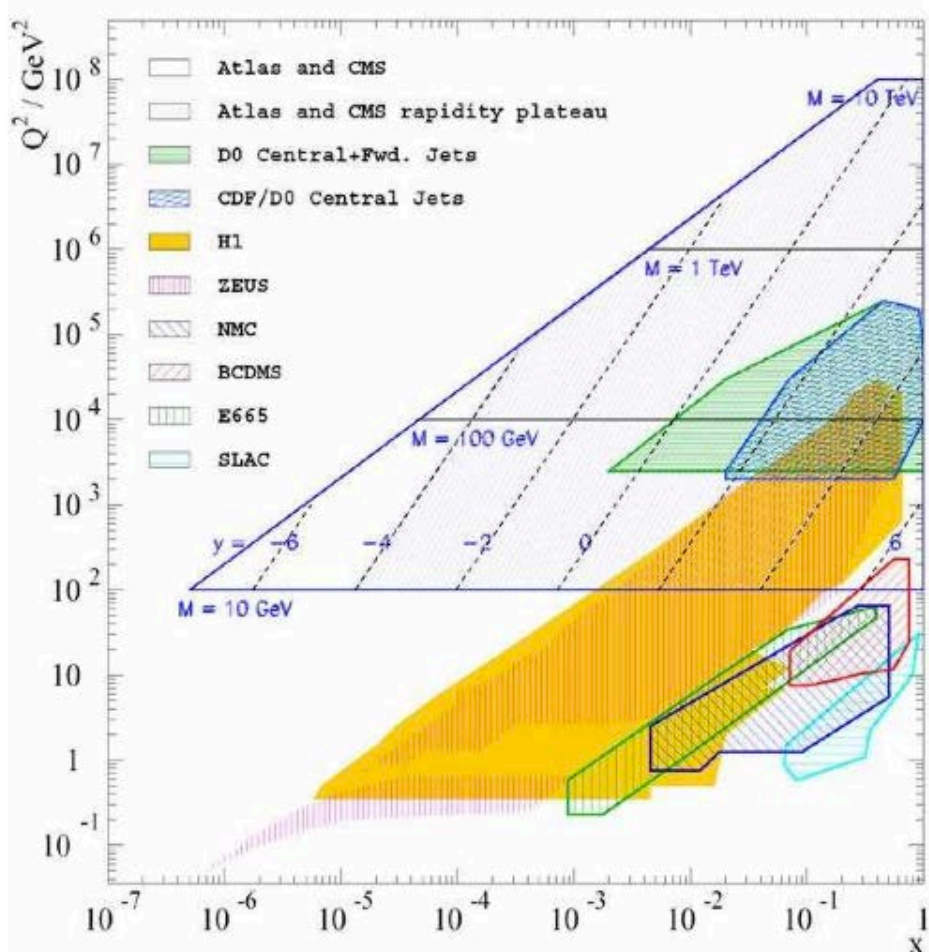


Figure 2.4. The Q^2 - x kinematic plane for the LHC and previous experiments, showing the mass ($M = Q$) and rapidity (y) dependence (Tricoli, 2006).

Some attempts to describe the evolution of the parton densities were made. When α_s is large, higher order corrections are important and need to be included to all orders. This can only be done in approximations like DGLAP (Dokshitzer, Gribov, Lipatov, Altarelli, Parisi), BFKL (Balitsky, Fadin, Kuraev, Lipatov) etc. DGLAP and BFKL describe the evolution of $F_2(x, Q^2)$ with Q^2 and x , respectively. DGLAP approximation is valid only at large enough x where α_s is small and $\ln(1/x)$ terms are not important. BFKL is expected to be a good approximation in a different region, in other words at very low x but at Q^2 large enough in order to work with

logically small values of $\alpha_s(Q^2)$. Another model is the CCFM (Catani et al., 1990) approximation. This model combines features from both the DGLAP and BFKL approximations and provides a convincing description of many data in a wide kinematic region. A schematic phase space diagram for DIS is shown in Figure 2.5 where the DGLAP and BFKL evolution directions are marked by arrows. In the non-perturbative (NP) region $Q^2 < \Lambda^2_{\text{QCD}}$ (blue area) the coupling is large and not much is known here from the point of pQCD. The saturation region (yellow area) can be understood by means of perturbative methods at low x (Lastovicka, 2004).

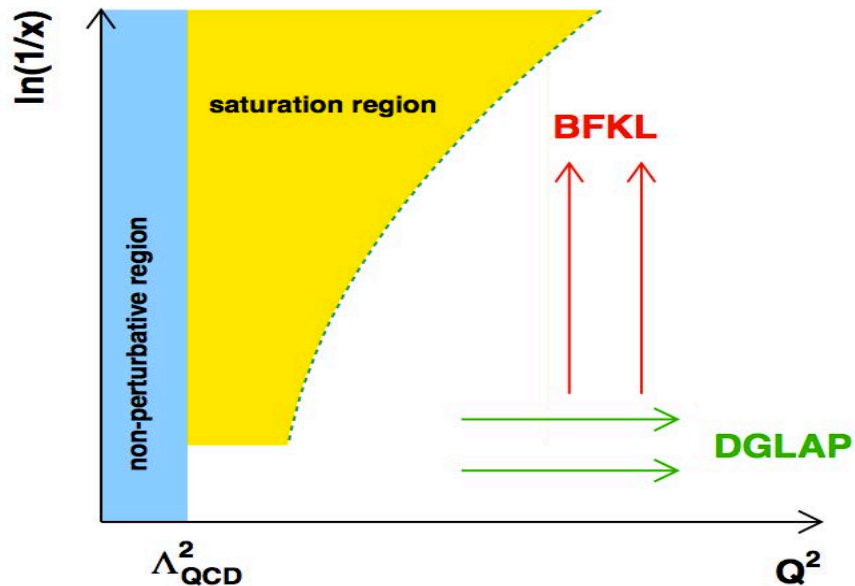


Figure 2.5. Schematic phase space diagram for DIS (Lastovicka, 2004).

Cross sections are calculated by convoluting the parton level cross section with the PDFs. QCD does not predict the parton content of the proton, for this reason the starting values of the PDFs are determined by fitting data from experimental observations in various processes using the DGLAP evolution equation and can not be calculated perturbatively (Placakyte, 2011). The resulting PDFs depend on the choice of the input data, the order in which the pQCD calculation is performed, the assumptions about the PDFs, the treatment of heavy quarks, the correlation between α_s , the PDFs and the treatment of the uncertainties. The determination of PDFs was carried out by several groups, namely MSTW (Martin et

al., 2009), CTEQ (Nadolsky et al., 2008), NNPDF (Ball et al., 2009), HERAPDF (Aaron et al., 2010), AB(K)M (Alekhin et al., 2010) and GJR (Glück et al., 2008). Figure 2.6 summarizes the variety of measurements at different experimental facilities which are sensitive to the gluon density and their approximate x coverage (d'Enterria, 2006).

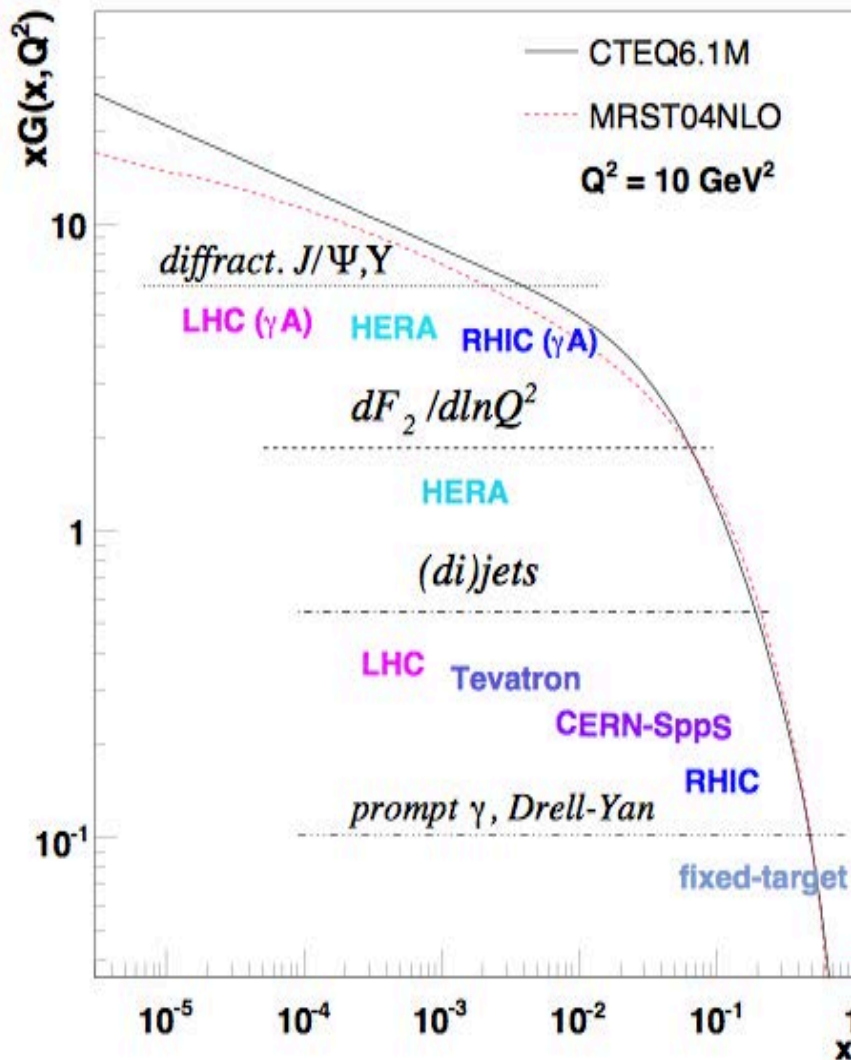


Figure 2.6. Examples of experimental measurements at various facilities providing information on the gluon PDF in the range $x \sim 10^{-5} - 0.8$ (d'Enterria, 2006).

The data from HERA and other experiments are calculated using the QCD evolution equations at next-to-leading order (NLO) and next-next-to-leading order

(NNLO) by several groups and all supply consistent predictions for the LHC processes. The fitted PDFs as determined by the HERAPDF1.0 fit is given in Figure 2.7. The distributions $xu_v(x)$, $xd_v(x)$, $xg(x)$, $xS(x)$, where $xS(x) = 2x(\bar{U}(x) + x\bar{D}(x))$ are shown at $Q^2 = 10 \text{ GeV}^2$. The gluon and sea quark distributions are scaled down by a factor of 20. At $Q^2 = 10 \text{ GeV}^2$ and $x = 0.01$ the valance contribution is about 5 % and goes over the magnitude limit of the PDFs uncertainties.

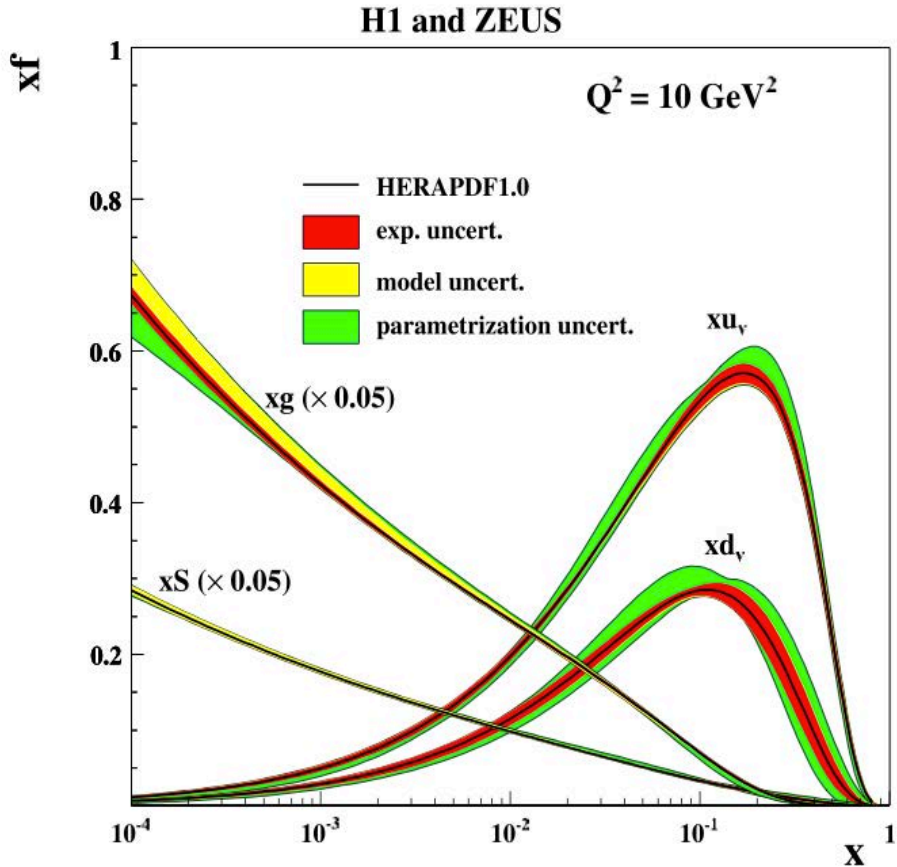


Figure 2.7. The PDF distribution determined from the HERAPDF1.0 fit at $Q^2 = 10 \text{ GeV}^2$ for gluons, sea quarks, up (u_μ) and down (d_μ) valance quarks (Petrushkin, 2010).

2.2.3. Factorization Theorem

The factorization theorem provides prescriptions to separate long and short-distance effects in hadronic cross sections. QCD factorization theorem can be used to calculate a wide variety of hard scattering cross sections in hadron-hadron collisions. Diagrammatic structure of a generic hard scattering process is shown in Figure 2.8.

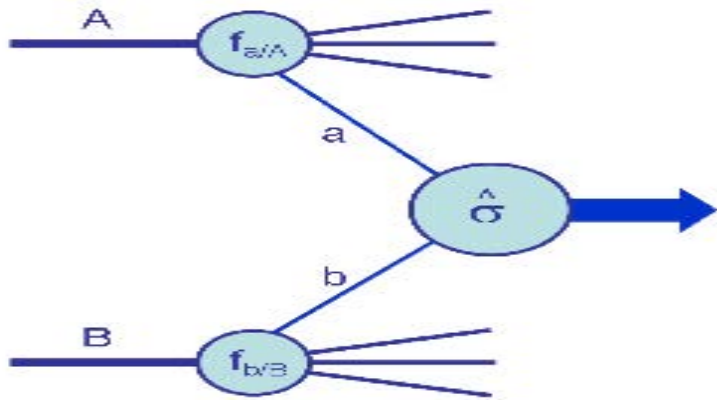


Figure 2.8. Hard scattering process (<https://inspirehep.net/record/1120513/plots>).

The QCD factorization theorem states that in the presence of a hard scale the cross section can be written as,

$$\sigma_{AB} = \int dx_a dx_b f_{a/A}(x_a, \mu_F^2) f_{b/B}(x_b, \mu_F^2) \times [\hat{\sigma}_0 + \alpha_s(\mu_R^2) \hat{\sigma}_1 + \dots]_{ab \rightarrow X} \quad (2.6)$$

where σ_{AB} gives the cross section of the hard subprocess which is calculated in pQCD. μ_F is the factorization scale which can be thought of as the scale which separates the hard and soft component of the interaction and μ_R renormalization scales for QCD coupling. To avoid unnaturally large logarithms reappearing in the perturbative series $\mu_F = \mu_R$ is often assumed. Formally, the cross section calculated to all orders in perturbation theory is invariant under changes in these parameters (Campbell, Huston and Stirling, 2006). The partonic cross section is computable as a power series expansion in the QCD coupling $\alpha_s(Q)$ as shown in equation 2.7.

$$\begin{aligned}
\hat{\sigma}_{ab}(p_1, p_2; Q, \dots; \alpha_s(Q)) = & \alpha_s^k(Q) \{ \hat{\sigma}_{ab}^{(LO)}(p_1, p_2; Q, \dots) \\
& + \alpha_s(Q) \hat{\alpha}_{ab}^{(NLO)}(p_1, p_2; Q, \dots) \\
& + \alpha_s^2(Q) \hat{\alpha}_{ab}^{(NNLO)}(p_1, p_2; Q, \dots) + \dots \}
\end{aligned} \quad (2.7)$$

The lowest (or leading) order (LO) term $\hat{\sigma}^{(LO)}$ gives only an estimate of the cross section. Thus one needs the NLO term, which is available for the most cases of interest (Catani et al., 2000). Some important SM cross sections prediction at $p\bar{p}$ and pp colliders are calculated using NLO in perturbation theory and are shown in Figure 2.9.

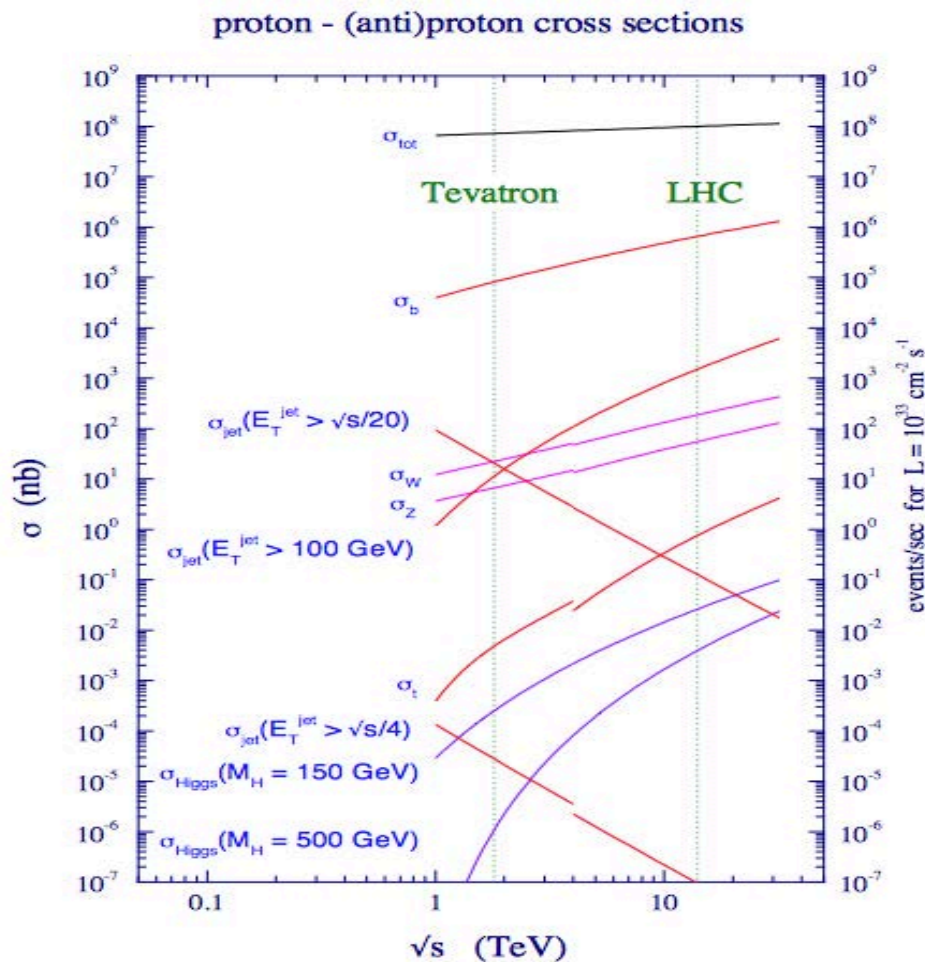


Figure 2.9. SM cross sections for hard scattering versus \sqrt{s} at the Tevatron and LHC colliders (Campbell, Huston and Stirling, 2006).

2.3. From Parton to Hadron

The hard interaction between two colliding fundamental particles can be described using the SM. The transition from the hard partons to hadrons can be factorized into Parton Shower and the Hadronization.

Proton-proton scattering process can be explained as a sequence of three stages shown heuristically in Figure 2.10.

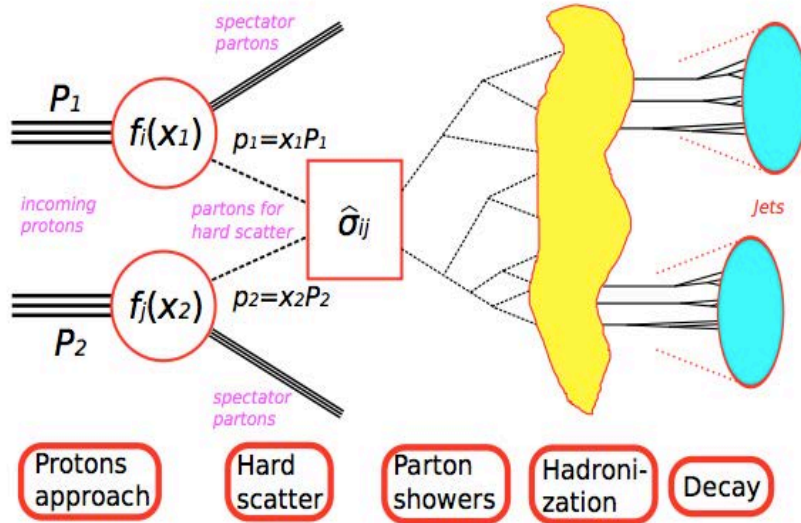


Figure 2.10. pp scattering processes (Cheung, 2011).

- The partons inside each of the two incoming protons P_1 and P_2 approach each other with some momentum fractions x_1, x_2 and their momentum distributions $f_i(x_1)$ and $f_j(x_2)$ are described by PDFs.
- One of the partons inside each of the incoming protons interact in a hard scattering. The hard scattering occurs between the pair of partons that behave as free particles. The cross section of this process can be calculated perturbatively. The remaining partons, called spectator partons do not influence the hard scattering.
- Outgoing partons are generated from the two scattered partons and after parton showering and hadronization, form jets (Cheung, 2011).

2.3.1. Parton Shower

The parton shower (PS) describes parton emission from the parton in the hard interaction and adds higher order QCD effects to the hard process. When the energy decreases α_s become larger and therefore the rate of the parton emission increases and consequently partons hadronize when approaching Λ_{QCD} . The evolution of the showering can be described by DGLAP equations and can be characterized by the momentum fraction z of the radiated particles, its azimuthal angle ϕ and the flavour of the emitted particles. The shower evolution depends to large extents on low energetic processes. Since these processes can not be calculated analytically they are modeled using PDFs. Radiation of partons in the initial and final state and to relate the few partons produced in the hard processes to the partons can be explained by parton showering. During parton showering, each of the final-state partons radiates additional partons, in the end the original outgoing partons are replaced by a number of low energy partons. The showering of one parton results in a jet of quarks and gluons, moving approximately in the initial parton direction.

2.3.2. Hadronization

The transition from partons to hadrons is called “hadronization”. Hadronization processes are responsible for the conversion of the color charged particle into colorless hadrons. Since hadronization processes happen in a region where α_s is large, these processes can not be calculated from perturbation theory but can only be described by phenomenological models like Lund String and Cluster Models.

Lund string model: The Lund string model is one of the most popular hadronization models. It is implemented in the multi purpose generator PYTHIA motivated by the properties of the color field between two colored particles. Two color charged objects are bound together by a color string with the string constant κ [GeV/fm]. As the two particles move apart the color string is stretched out causing the energy in the

string to increase. When enough energy is stored in the string it can break and new quarks are produced. In order to conserve quantum numbers the created particles must be either a quark-anti quark pair or a diquark-antidiquark pair. Each of the newly created quarks connects to the old quarks with the remaining parts of the color string. When no energy for further pair production is left, the process stops and the resulting string fragments are combined into hadrons. Figure 2.11 (a) shows the schematic picture of string model of hadronization.

Cluster Model: The cluster model is very different compared to the string model. This model is based on the color pre-confinement property of QCD. After the parton showering the remaining gluons split into either light quark-antiquark or diquark-antidiquark pairs. The nearest quark and antiquark then combine into a color singlet clusters. These clusters decay directly into two hadrons unless they are very heavy, in that case the clusters decay into two clusters; or if they are too light then into a single hadron. In Figure. 2.11 (b), schematic description of cluster model is shown for hadronization.

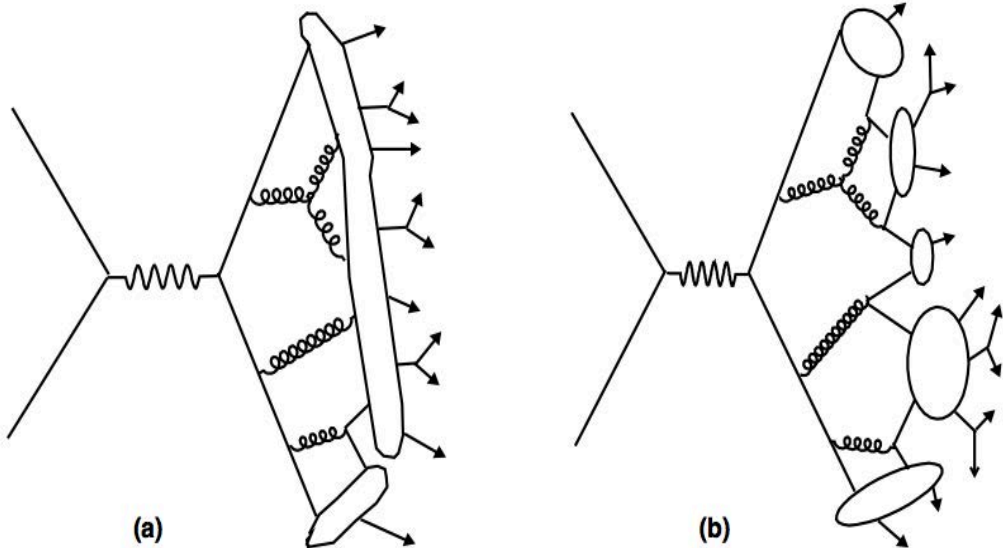


Figure 2.11. Hadronization using (a) string and (b) cluster models in Monte Carlo event generators.

2.4. Monte Carlo Generators

Multi purpose Monte Carlo (MC) event generators which allow to make predictions on distributions expected and measured in experiments, are very important tools in particle physics. The working principle of a hadron level MC generation is shown in Figure 2.12. The different steps can be executed by multiple generators, making it possible to use for example different parton shower algorithms on the same hard scattering. Two partons from the incoming protons interact according to the hard scattering. The outgoing hard partons together with the proton remnants are subject to the parton shower to form the partonic final state (PFS). These partons are then hadronized. Particles with a mean lifetime below a particular threshold are also decayed.

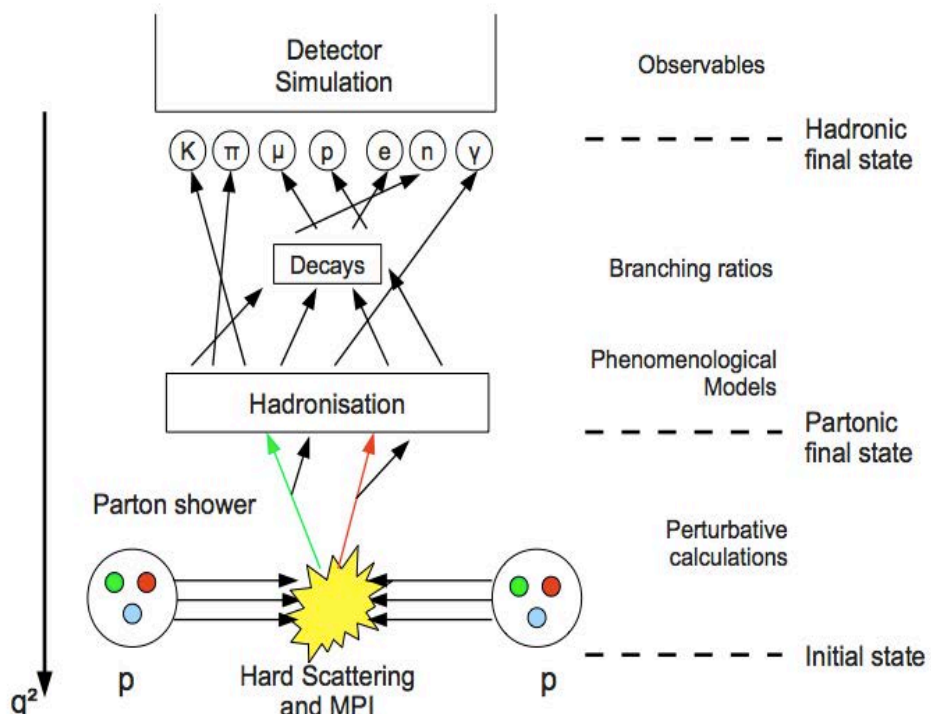


Figure 2.12. Working principle of a multi-purpose MC event generator (Heinrich, 2011).

2.4.1. PYTHIA

PYTHIA (Sjöstrand, Mrenna and Skands, 2006) is a MC event generator program which combines many theoretical and empirical models to describe parton remnants, initial and final state radiation, fragmentation and multiple interactions using the Lund string hadronization model and a p_T -ordered parton showering.

PYTHIA is currently available in both a Fortran and a C++ version. The Fortran version has been developed since 1977 (with the latest version is PYTHIA 6.4.28) and the latest C++ version is PYTHIA 8 (Sjöstrand, Mrenna and Skands, 2008). PYTHIA 6 consists of a large range of physics processes. All SM 2→1 and 2→2 matrix elements, soft and hard QCD processes, heavy flavor production, vector boson and SM Higgs production are included in this MC model. Furthermore, many non SM processes such as supersymmetry and technicolor are included. These processes can not be calculated using perturbation theory but phenomenological models have to be applied to reproduce observed distributions. The hadronisation and the multiparton interactions, as is the case for PYTHIA 6 contain a large number of free parameters. Combinations of certain values for all of these parameters are called tunes. It requires an underlying event model to describe the interactions between the proton remnants (Heinrich, 2011).

2.4.2. HERWIG

The HERWIG (Hadron Emission Reactions With Interfering Gluons) (Marchesini et al., 1992) is a general purpose MC event generator. It is based on a parton branching process and uses an angular ordered parton shower for initial and final state QCD radiation and a cluster model to reproduce the hadronization of the partons. In the hadronization process, three types of non-perturbative contributions have to be taken into account: the identification of the incoming partons as components of the incoming particles, the transformation of the outgoing partons into hadrons and the inclusion of multiparton interactions.

The HERWIG-JIMMY (Butterworth, Forshaw, Seymour, 1996) is the Fortran version of HERWIG for simulating multiple parton-parton interactions. HERWIG++ (Bahr et al., 2008) is the C++ version of HERWIG.

2.4.3. CASCADE

CASCADE (Jung et al., 2010) is a MC event generator which produces full hadron level events for ep , pp processes. It uses the Lund string model for hadronization and applies the CCFM evolution equation for the initial state cascade supplemented with off-shell matrix elements for the hard scattering (Jung, 2001).

2.4.4. HEJ

The High Energy Jet (HEJ) (Andersen and Smillie, 2011) is a MC generator for multijet analysis. It provides a perturbative approximation of the hard scattering matrix elements to jet production to any order in the coupling, Therefore it gives a description directed especially at hard, wide-angle QCD radiation and is developed to account for effects of many hard and radiative corrections. Such corrections become increasingly important, as the centre-of-mass energy at colliders increases (Andersen, Lonnblad and Smillie, 2011).

2.4.5. POWHEG

In the POWHEG (Positive Weight Hardest Emission Generator) (Nason and Webber, 2012) the main idea is to produce the hardest radiation first and then feed the event to any shower generator for subsequent, softer radiation. In shower generators ordered in transverse momenta, the hardest emission is always the first and in these circumstances POWHEG simply replaces the hardest emission with its own, NLO accurate emission. It generates events with positive (constant) weight and it does not depend on MC program used for subsequent showering. It can be interfaced to any modern ‘shower’ analyzer.

2.4.6. MC@NLO

MC@NLO (Nason and Webber, 2012) is a tool for combining a MC event generator with NLO calculations of rates for QCD processes. It can calculate the matrix element for many processes at NLO and includes dynamic properties that cannot be provided by standard MC generators. It makes use of either HERWIG or HERWIG++ event generator.

(<http://www.hep.phy.cam.ac.uk/theory/webber/MCatNLO/>).

2.4.7. NLOJet++

NLOJET++ (Nagy, 2003) is a C++ program to calculate LO and NLO order cross section in e^+e^- annihilations, DIS and hadron hadron collisions using the Catani-Seymour dipole subtraction method.

3. LHC and CMS EXPERIMENT

This chapter introduces the Large Hadron Collider (LHC) as well as its experiments. Particular attention is dedicated to CMS and its most important detector components.

3.1. Large Hadron Collider

The LHC is a proton-proton accelerator built at CERN. The accelerator complex is located on the border between Switzerland and France between the Geneva lake and the Jura mountains, 50-175 m underground in the 26.7 km long tunnel which used to hold the Large Electron Positron (LEP) Collider until 2000. The LHC is the world's biggest high energy particle accelerator. It was built in collaboration with over 10,000 scientists and engineers from over 100 countries, as well as hundreds of universities and laboratories throughout the world.

On 10 September 2008, the proton beams were successfully circulated in the main ring of the LHC for the first time, but nine days later operations were halted due to a magnet quench incident caused by an electrical circuit fault. The following helium gas explosion damaged over 50 superconducting magnets and their mountings, and contaminated the vacuum pipe. After extensive repairs, on 20 November 2009 proton beams were successfully circulated again. In March 2010, two proton beams collided for the first time at a center of mass energy of 7 TeV and the LHC began its planned research program.

The LHC is supplied with protons from an accelerator chain with step by step increases in proton energy. The protons are obtained by stripping electrons from hydrogen atoms, these are accelerated in a linear accelerator (LINAC2) to an energy of 50 MeV and subsequently fed to the booster which brings the protons to an energy of 1.4 GeV. The protons are then injected in the Proton Synchrotron (PS) that in turn accelerates them to an energy of 26 GeV. Then the proton beams are further accelerated up to 450 GeV in the Super Proton Synchrotron (SPS). In the end, proton beams are injected into the LHC and accelerated to the energy of 3.5 TeV as shown

in Figure 3.1. A brief description of a proton accelerated through the accelerator complex of CERN is given in the next chapter.

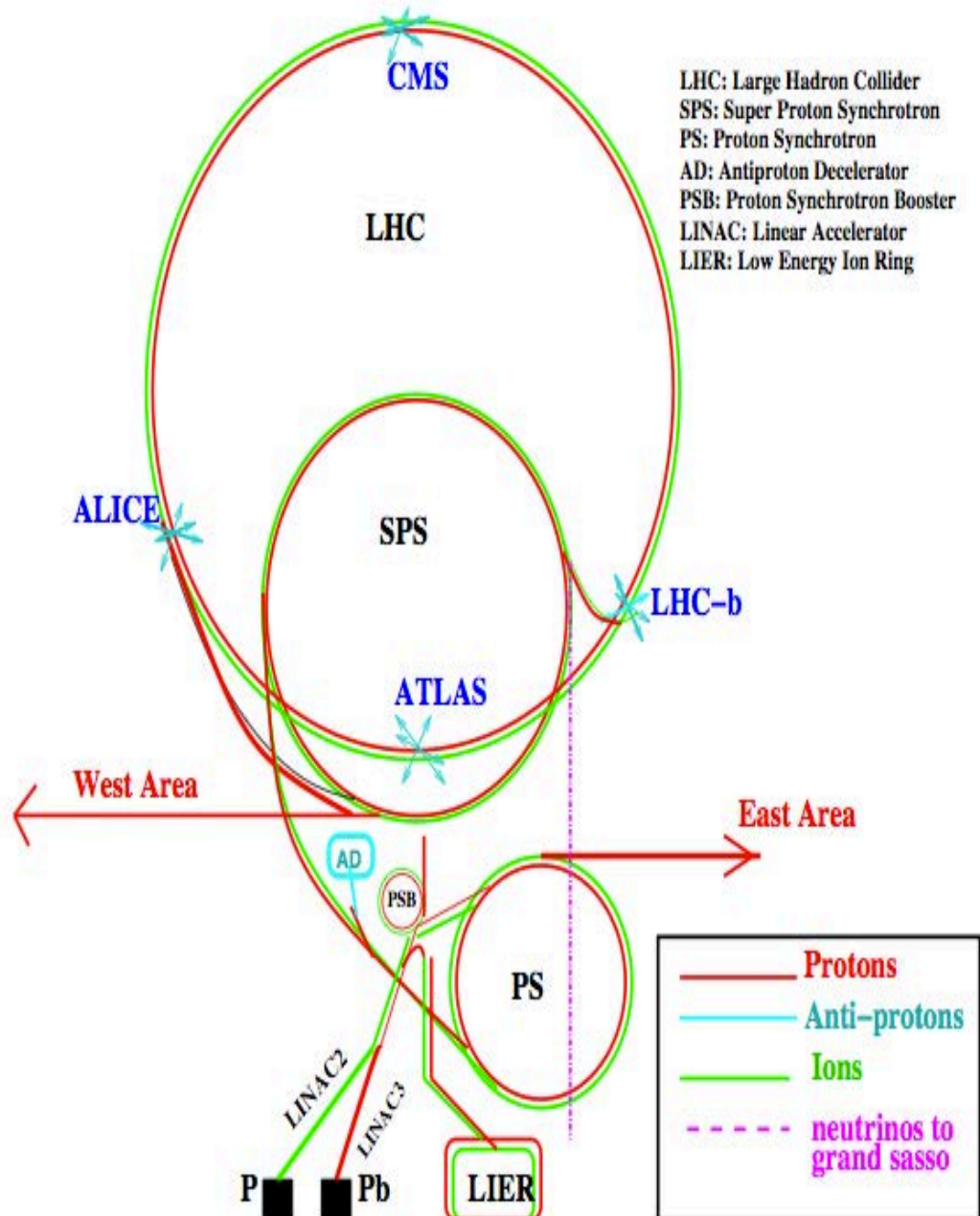


Figure 3.1. Overview of the Accelerator chain. The LHC is the last ring in a complex chain of particle accelerators. It is supplied with protons from the injector chain LINAC2 → Booster → PS → SPS (Bawa, 2007).

The LHC delivered 47 pb^{-1} of collision data during the 2010 run, 43 pb^{-1} of these were recorded by the CMS experiment and approximately 36 pb^{-1} of collision data passed quality tests and were approved for analyses. Official luminosity report is shown in Figure 3.2.

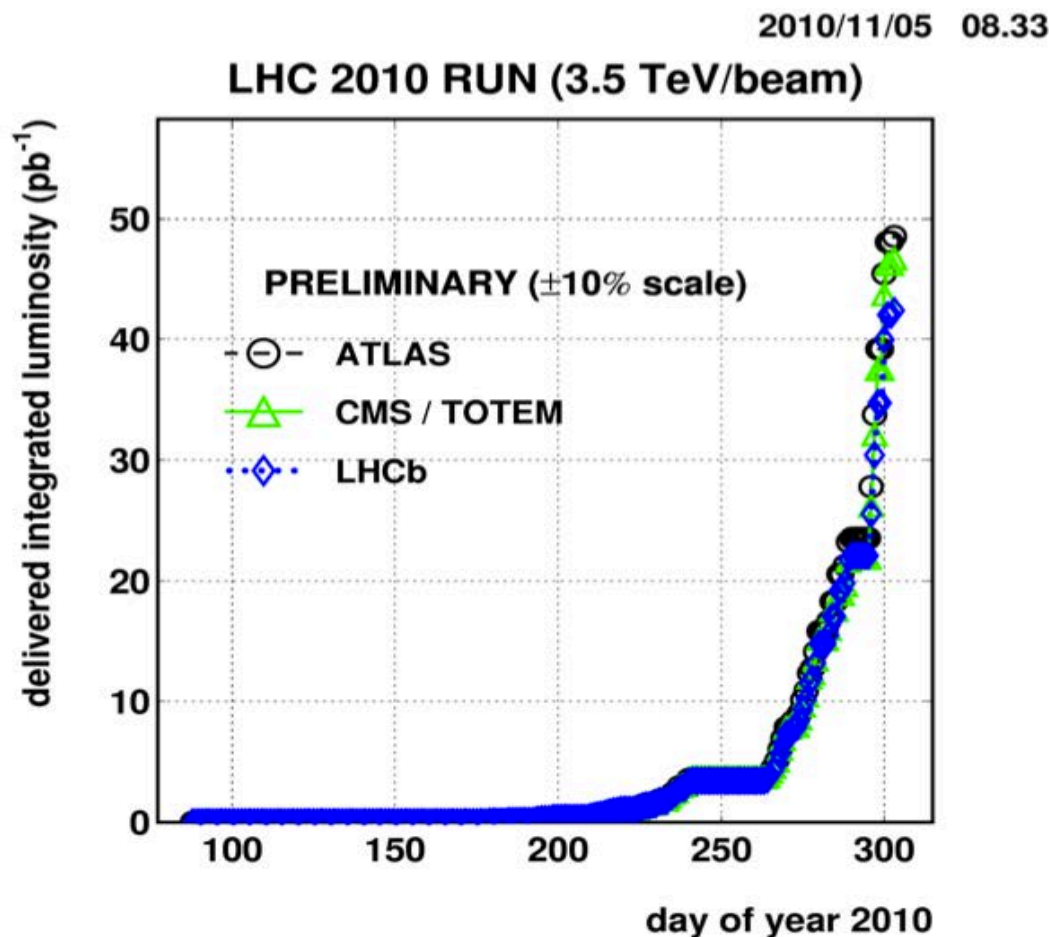


Figure 3.2. Official luminosity report 2010 (<http://lpc.web.cern.ch/lpc/>).

The LHC resumed its operation in March 2011 at 7 TeV center of mass energy and collected data until the end of 2012 at 4 TeV per beam. It is since then stopped for 18 months to allow for final work to be done to increase the center of mass energy to the design value of 13 TeV.

3.1.1. Proton Production and Linear Acceleration

The first step of the proton production is the ionisation of hydrogen gas by way of a Radio Frequency Quadrupole (RFQ) duoplasmatron creating a negatively charged ion beam of 750 keV. This beam is also accelerated by a LINAC2 and is released via a carbon foil at the end of the machine. The foil strips off all orbiting electrons to produce a pure proton beam at an energy of 50 MeV and a current of 180 mA which is essential for the next injection step (Scheurer, 2008).

3.1.2. Booster and Proton Synchrotron

The PS Booster, a synchrotron, is the first and smallest circular proton accelerator in the accelerator chain at the LHC. The accelerator was built in 1972, and contains four combined rings with a radius of 25 meters. It takes protons with an energy of 50 MeV from the LINAC2 and accelerates protons up to 1.4 GeV ready to be injected into the PS. The PS provides beam source for several CERN experiments. It has undergone several upgrade stages and is now capable of accelerating the protons to an energy of 26 GeV.

3.1.3. Super Proton Synchrotron

The SPS is a particle accelerator of the synchrotron type at CERN to accelerate electrons, positrons, protons, antiprotons and heavy ions for a variety of experiments. It is used as the final injector for high intensity proton beams for the LHC and is housed in a circular tunnel with circumference of 6.9 km. SPS speeds up the proton beam from the 26 GeV and accelerates it to a final energy of 450 GeV. Then, the beam is split and extracted via two transfer lines into the LHC main rings in opposite directions. The protons are finally transferred both in a clockwise and also anti-clockwise direction to the LHC where the protons are accelerated to their nominal 7 TeV. The beams will rotate for several hours before being steered into collisions at the different points where detectors, CMS, ALICE, ATLAS, LHCb are

positioned. Table 3.1 gives a short summary of the accelerator chain and shows the corresponding beam energies in each of the different acceleration steps.

Table 3.1. Accelerator steps (Scheurer, 2008).

Accelerator	Injection Energy	Final Energy
LINAC2	750 keV	50 MeV
PSB	50 MeV	1.4 GeV
PS	1.4 GeV	26 GeV
SPS	26 GeV	450 GeV
LHC	450 GeV	7 TeV

3.1.4. Luminosity and Machine Parameters

The design luminosity of the LHC is $10^{34} \text{ cm}^{-2} \text{ s}^{-1}$. This leads to arround 1 billion proton-proton interactions per second. The number of generated events per second for a particular process under study in the LHC is given by:

$$N = \sigma x L \quad (3.1)$$

where σ is the process cross section and L the luminosity of the machine. The production rate per second for a physical process is given by :

$$R = L\sigma \quad (3.2)$$

$$L = \frac{N_b^2 n_b f_{rev} \gamma F}{4\pi \epsilon_n \beta^*} \quad (3.3)$$

where N_b is the number of particles per bunch, n_b is the number of bunches per beam, f_{rev} the revolution frequency, γ the relativistic gamma factor, ϵ_n the normalized

transverse beam emittance a measure for the phase space area associated with the two transverse degrees of freedom. The variables describing the interaction point are the betatron function β^* and the geometric luminosity reduction factor F (Evans and P.B, 2008). The most important parameters of the LHC collider are summarized in Table 3.2.

Table 3.2. Design specifications (except energy per proton beam and energy loss per turn) of the LHC for pp collision (Bruning et al., 2004).

Parameter	Value
Energy per proton beam	3.5 TeV
Number of bunches	2808
Number of particles per bunch	1.15×10^{11}
Bunch spacing	25 ns
RMS of bunch length	7.55 cm
Bunch crossing rate	40 MHz
Peak luminosity	$10^{34} \text{ cm}^{-2} \text{ s}^{-1}$
Luminosity lifetime	14.9 h
Energy loss per turn	420 eV

Figure 3.3 demonstrates the expected energy dependence of the total cross section, left scale of some interesting physics processes which have much smaller cross sections, while the right scale is the event rate of the physics processes at a typical luminosity of $10^{34} \text{ cm}^{-2} \text{ s}^{-1}$.

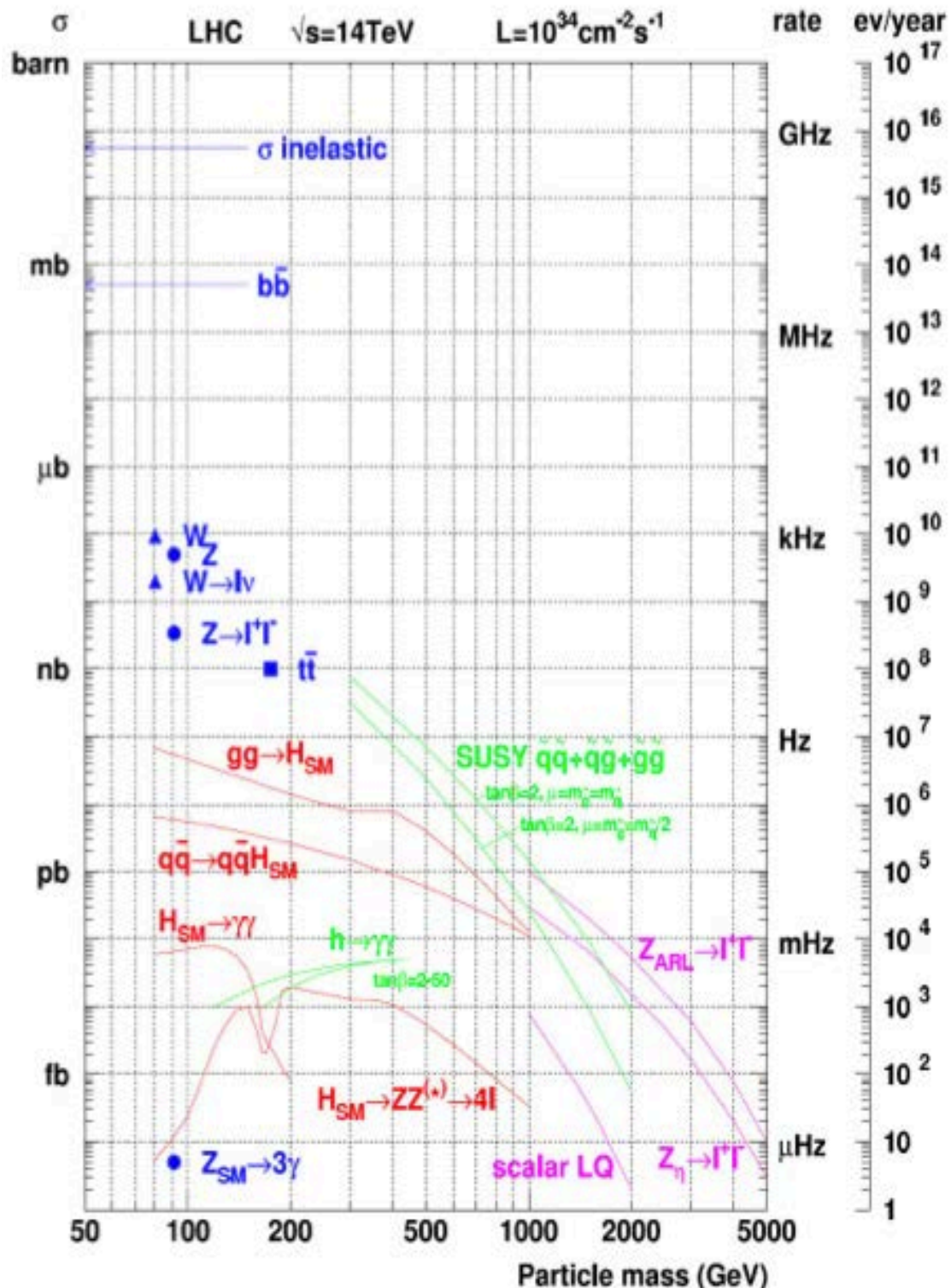


Figure 3.3. The cross section and event rate in pp collisions as a function of center of mass energy (Sanudo, 2009).

3.1.5. The LHC Experiments

Currently the LHC hosts seven experiments at its four underground caverns distributed around the main ring. A Toroidal LHC ApparatuS (ATLAS) and Compact Muon Solenoid (CMS) are two general purpose detectors. The CMS experiment will be described in more detail later in this chapter. The other five experiments namely A Large Ion Collider (ALICE), Large Hadron Collider beauty (LHCb), Large Hadron Collider forward (LHCf), TOTal Elastic and Diffractive Cross Section Measurement (TOTEM) and Monopole and Exotics Detector (MoEDAL) will be mentioned only briefly. Figure 3.4 shows LHC experiments schema.

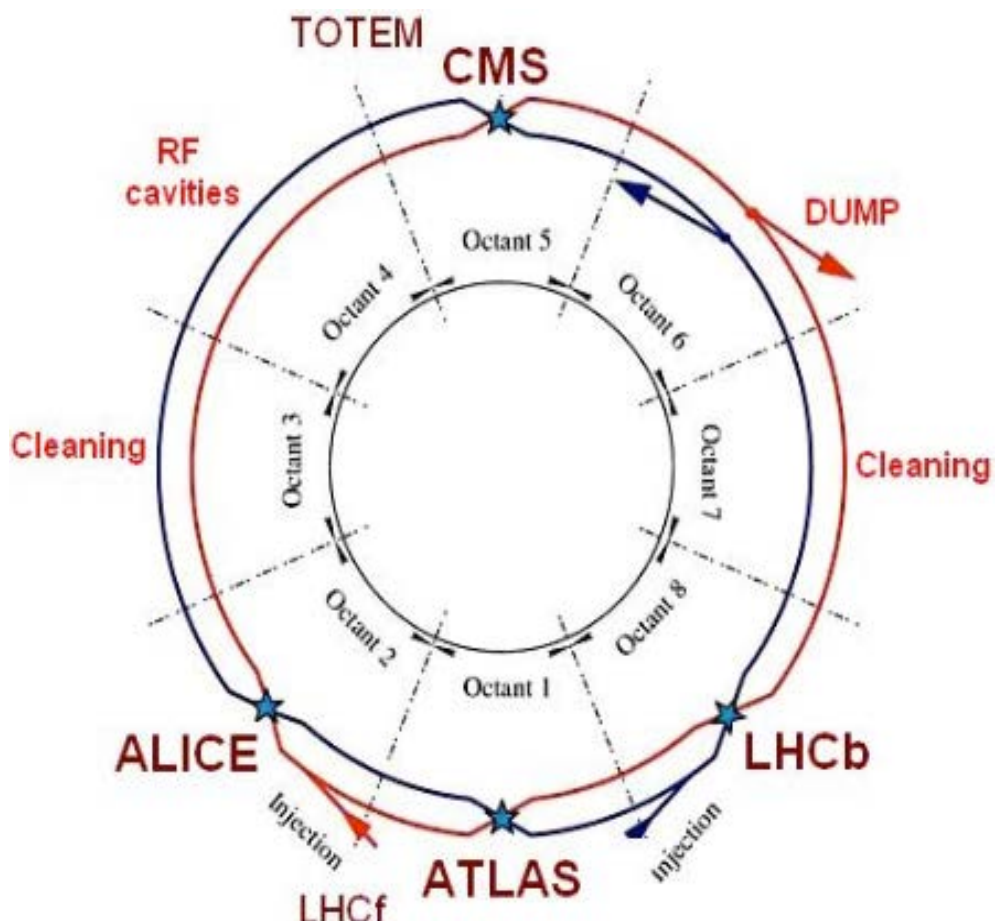


Figure 3.4. The LHC and experiments schema (<http://www.lhc-closer.es/1/3/4/0>).

ALICE : ALICE (Aamodt et al., 2008) is a general-purpose, heavy-ion detector which focuses on QCD, the strong-interaction sector of the SM. It is built to study the quark-gluon plasma at extreme values of energy density and temperature in nucleus-nucleus collisions. It also allows a comprehensive study of hadrons, electrons, muons, and photons produced in the collision of heavy nuclei (Pb- Pb), up to the highest multiplicities at the LHC. The detector consists of a central barrel and a single arm forward muon spectrometer. Its size adds up to 26 m in length, a diameter of 16 m and the weight of about 10 000 t.

ATLAS: ATLAS (Aad et al., 2008) is, together with CMS, one of the two general purpose experiments designed to investigate a wide range of SM phenomena and beyond SM (BSM) theories. It is the largest volume collider detector ever built with a total length of 46 m and a diameter of 25 m for the barrel and endcap system. Main property of the detector is the toroidal shaped magnet system. This system provides a homogeneous magnetic field inside the torus. Innermost detector is a tracker in a solenoid magnet field to measure the path and momenta of charged particles, followed by electromagnetic and hadronic calorimeters. ATLAS has an efficient tracking system, good electromagnetic calorimetry and near hermetic jet measurement capability. These properties make possible for the detector to effectuate certainty measurements on leptons, jets and photons and identify events with missing E_T . Muons, in the meantime can penetrate calorimeters and also is used to measure the momenta of the muons to help in triggering.

LHCb: LHCb (Augusto Alves Jr et al., 2008) is an experiment dedicated to heavy flavour physics at the LHC. Main goal of LHCb is to study a slight asymmetry between matter and anti-matter in interactions of particles with bottom quarks. It is designed to answer fundamental questions on the formation of universe. The detector is built to detect particles with a low transverse momentum going forward close to the beam line. It is composed of a forward spectrometer with planary detectors lined up one behind the other over a length of about 21 m (Scheurer, 2008).

LHCf: LHCf (Adriani et al., 2008) is a small experiment built inside the ATLAS underground cavern 140 m off the interaction point. The LHCf experiment measures the forward production of neutral particles in the proton collisions at low angles. The results are then used to model cosmic ray air showers within the Earth atmosphere.

TOTEM: The TOTEM (Anelli et al., 2008) experiment is designed to measure the total proton-proton cross section, elastic scattering and diffractive dissociation in the LHC. It is also used to monitor the actual luminosity of the LHC machine. The detector is hosted inside the CMS cavern. More specifically TOTEM measures :

- The total cross-section with an absolute error of 1mb using a luminosity independent method,
- Diffractive dissociation, including single, double and central diffraction topologies using forward inelastic detectors in combination with one of the large LHC detectors,
- Elastic proton scattering over a wide range in momentum transfer up to $-t \approx 10 \text{ GeV}^2$ (Berardi, 2004).

MoEDAL: MoEDAL (Pinfold et al., 2009) is the latest experiment at the LHC and shares its cavern with LHCb. The main motivation of MoEDAL is to directly search for the Magnetic Monopole and other highly ionizing Stable (or pseudo-stable) Massive Particles (SMPs) at the LHC.

3.2. CMS

The CMS (Chatrchyan et al., 2008) is a general goal detector designed to run at the highest luminosity and is located at Point 5 of the LHC near Cessy, France. At the design luminosity a average of 20 inelastic collisions are expected every 25 ns, the products of which need to be collected and processed. The detector must provide good positional and time resolution so that it is possible to distinguish interesting events from background noise. This necessitates a large number of detector channels, that must be well synchronized. The general requirements for such a detector are:

- Good charged particle momentum resolution and reconstruction efficiency in the inner tracker part and high granularity especially near the interaction point,
- Good electromagnetic energy resolution, wide geometric coverage, efficient photon and lepton isolation at high luminosities,
- Hadron calorimeters with hermetic coverage, with optimal missing transverse energy and dijet mass resolution,
- Good muon definition, charge determination and momentum resolution over a wide range of momenta and angles (Chatrchyan et al., 2008).

The main property of CMS is a large superconducting solenoid magnet which provides a 3.8 T field. Starting from the point closest to the interaction area, the individual subdetectors are the Tracker, the Electromagnetic Calorimeter (ECAL) and the Hadronic Calorimeter (HCAL) which are encircled by a solenoid, followed by layers of muon detectors. The overall dimensions of CMS are 28.7 m in length, a diameter of 15 m and a total weight of 14000 t. Figure 3.5 shows a schematic layout of the CMS detector. The detector consists of different subdetectors, each with a well defined set of properties to measure certain phenomena.

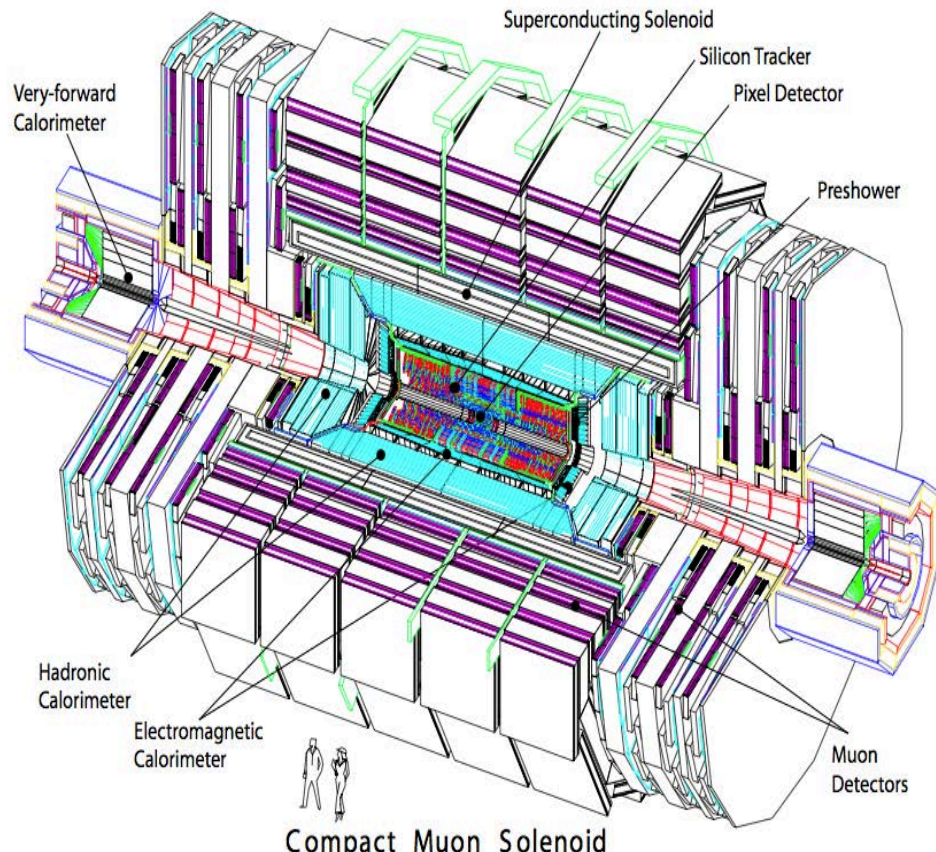


Figure 3.5. Schematic view of the CMS detector and its components (Bayatian et al., 2006).

The innermost part of CMS is the silicon tracking detector which measures the momentum of a charged particle in the magnetic field. The tracker is confined by the electromagnetic calorimeter measuring the energy of electrons and photons. Behind the electromagnetic calorimeter, the hadron calorimeter records energy of strongly interacting particles. And the coil of the superconducting solenoid magnet encloses the previous subdetectors. There are the four stations of muon chambers embedded in the iron yoke of the magnet. Each muon station includes several layers of aluminum drift tubes (DT) in the barrel region and cathode strip chambers (CSC) in the endcap region, complemented by resistive plate chambers (RPC). Figure 3.6 illustrates the trajectories of different particles as they pass through the detector.

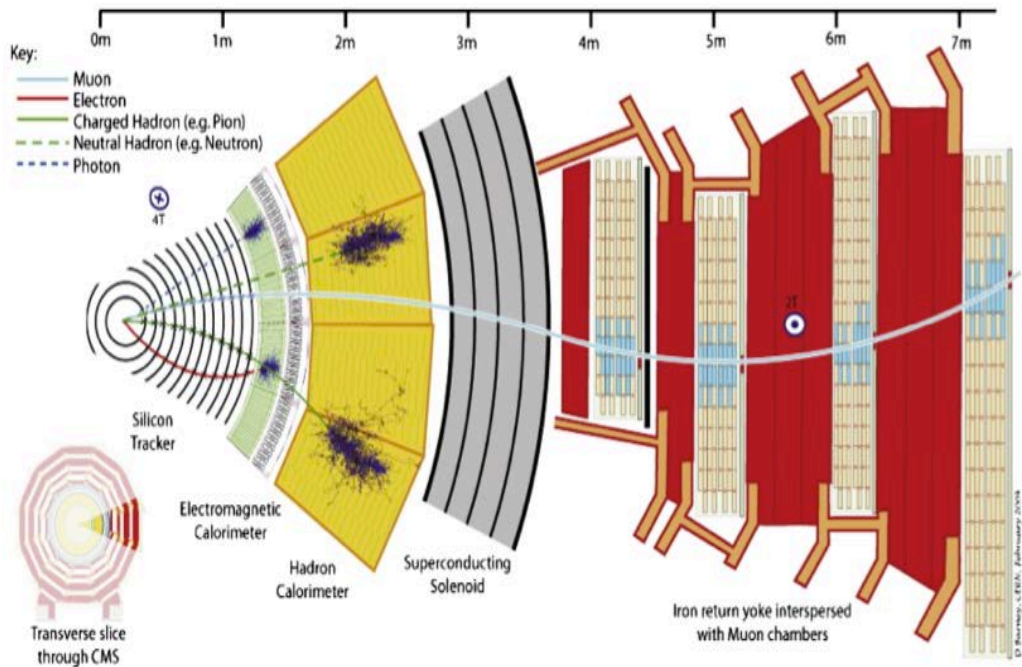


Figure 3.6. Transverse slice of the CMS detector and particles traces in different subdetectors (Lazaridis, 2011).

The CMS Coordinate Frame

CMS uses a right-handed coordinate system with the origin centered at the nominal collision point inside the experiment, the z -axis along the beam pipe, the y -axis points vertically upward and the x -axis pointing toward the center of the LHC ring. CMS is cylindrically symmetric around the beam line and the radial distance from the beam is defined as r , the azimuthal angle ϕ is measured from the x -axis in the x - y plane and the polar angle θ is measured from the z -axis. Pseudorapidity is identified as $\eta = -\ln \tan(\theta/2)$. Hence, the physical observables, momentum $p_T = |\vec{p}| \sin \theta$ and energy transverse (E_T) to the beam, are calculated directly from the x and y components (Chatrchyan et al., 2008).

3.2.1. Tracker

The CMS tracker (Bayatian et al., 1998) is cylindrical in shape and the detector lies closest to the beam interaction point. The design goal of the central tracking system is to reconstruct isolated high p_T tracks with an efficiency better than 95% and high p_T tracks within jets with an efficiency of more than 90% over the rapidity range $|\eta| < 2.6$. It provides absolute, efficient measurement of charged particles trajectories arising from the LHC collisions.

The inner tracking system consists of ten layers of silicon strip detector for the absolute track reconstruction, in addition to three layer of pixel detectors for the certain reconstruction of certain vertices in the barrel part and two pixel layers and three plus nine strip layers in each endcap section as shown in Figure 3.7.

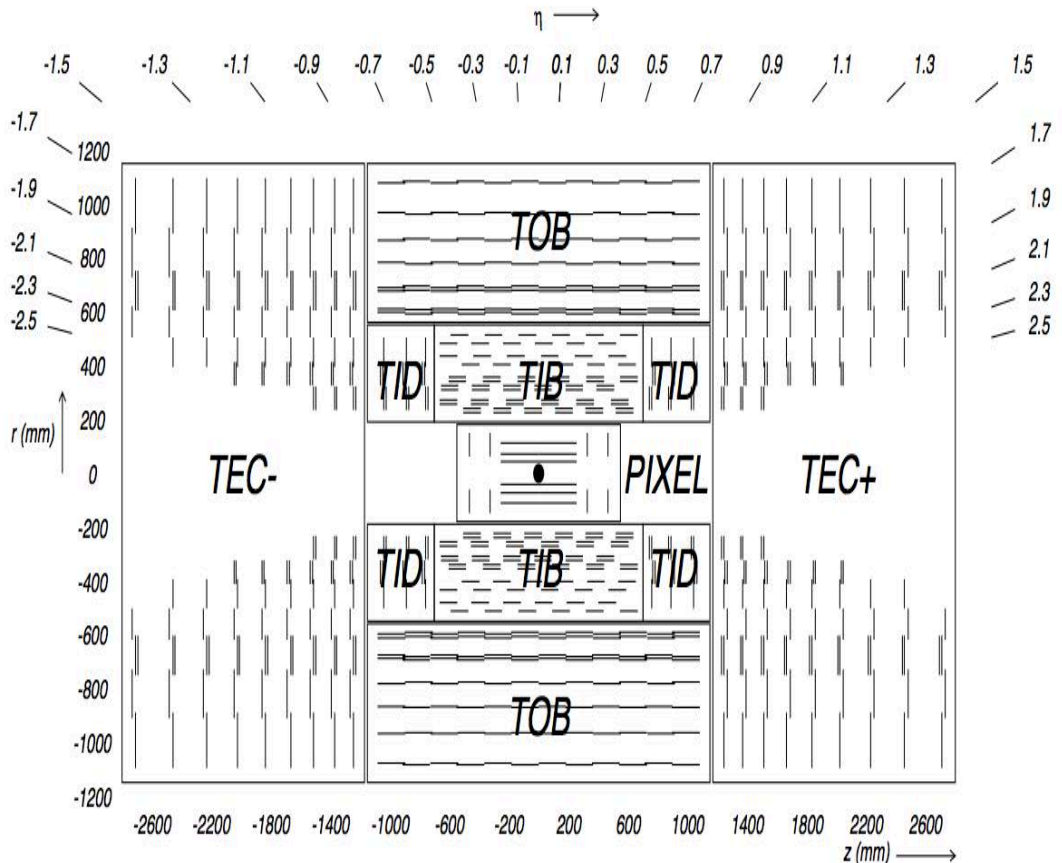


Figure 3.7. Schematic cross section through the CMS Tracker. Each line represents a detector module (Chatrchyan et al., 2008).

3.2.1.1. Pixel Tracker

Pixel tracker is the inner-most part of the tracking system designed to provide a supreme resolution for primary and secondary vertices and contribute three 2-dimensional measurements to the tracking for strong track seeding and resolution uncertainties. Pixel detector consists of three layers of pixel modules, positioned at radii of 4.4, 7.3 and 10.2 cm and two end disks extending from 6 to 15 cm in radius placed at 34.5 cm and 46.5 cm from the collision point. Each silicon sensor has a surface of $100 \mu\text{m} \times 150 \mu\text{m}$ and a thickness of 300 μm , with about 65 million such channels. The spatial resolution has been measured to be about 10 μm for the (r, ϕ) measurement and about 20 μm for the z measurement (Lazaridis, 2011). The pixel tracking system is divided into a pixel barrel and a pixel forward detector and covers the pseudorapidity region of $|\eta| < 2.5$.

The pixel forward section consists of four disks, two at each side of the vertex. The disks extend radially from ≈ 6 to 15 cm and are placed at $z = \pm 34.5$ cm and $z = \pm 46.5$ cm. Geometrical layout of the Pixel detector in the CMS Tracker is shown in Figure 3.8.

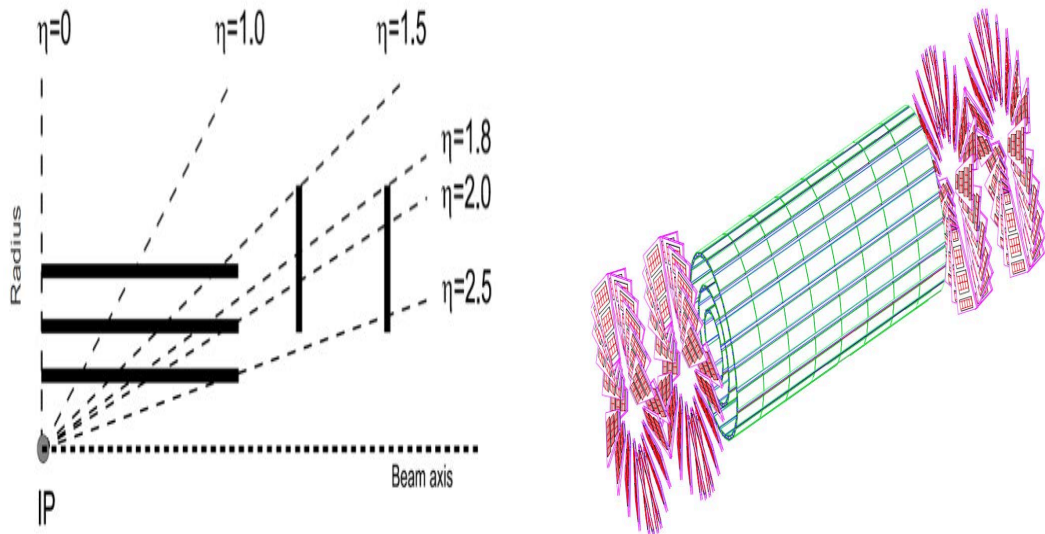


Figure 3.8. Geometrical layout of the Pixel detector (Bayatian et al., 2006).

3.2.1.2. Inner Tracker

Next to the pixel subdetector is the inner tracker ($20 < r < 55$ cm), consisting of the Tracker Inner Barrel (TIB) and of the Tracker Inner Disk (TID). TIB and TID are the strip subdetectors that are closest to the interaction region. The first two layers of the TIB and the inner two rings of the TID cover stereo modules for 2D measurements. The TIB is made of four layers located at radii of 25.5, 33.9, 41.85 and 49.8 cm. Each layer of the TIB extended to $|z| < 70$ cm is divided into four parts, an upper and a lower part on every side of the vertex. The TID has six identical disk structures, three on each side of the interaction point located at distances from the interaction point between ± 80 cm and ± 90 cm. On each disk the modules are placed in three rings alternatively in the forward and backward parts of the disk.

3.2.1.3. Outer Tracker

The outer tracker is subdivided into three parts, the Tracker Outer Barrel (TOB) and two Tracker End Caps (TEC) called TEC+ and TEC- with respect to their position in the CMS coordinate system. The Outer Tracker uses larger and thicker silicon strips than the Inner Tracker to limit the number of individual readout channels. Tracker Outer Barrel (TOB) contains six layers with $|z| < 110$ cm and contributes to track measurement up to a pseudorapidity of about $|\eta| < 1.3$. Each layer is made of rods, with six modules inside each rod. The TEC extends in the z -direction from ± 124 cm to ± 280 cm and radially from 22 cm to 113.5 cm (diameter 227 cm). Each endcap includes nine disks made of a Carbon Fiber Composite.

3.2.2. CMS Calorimeters

The CMS calorimeters design goal is to measure the energies of electrons, photons and hadrons that emerge from the collision. The calorimeter system is very important to the physics measurements for following reasons:

- Energy response resolution improves with energy (opposed to magnetic spectrometers),
- It allows for measurements of neutral hadrons that cannot be measured by the tracker system,
- It provides a trigger with quick detection of high p_T .

CMS has an electromagnetic calorimeter (ECAL) and a hadronic calorimeter (HCAL). The ECAL is used to measure electrons and photons through electromagnetic interactions while the HCAL is used to measure hadrons through the strong interaction. Figure 3.9 shows the locations of the ECAL and HCAL (quarter slice-longitudinal cross section) in and around the CMS magnet.

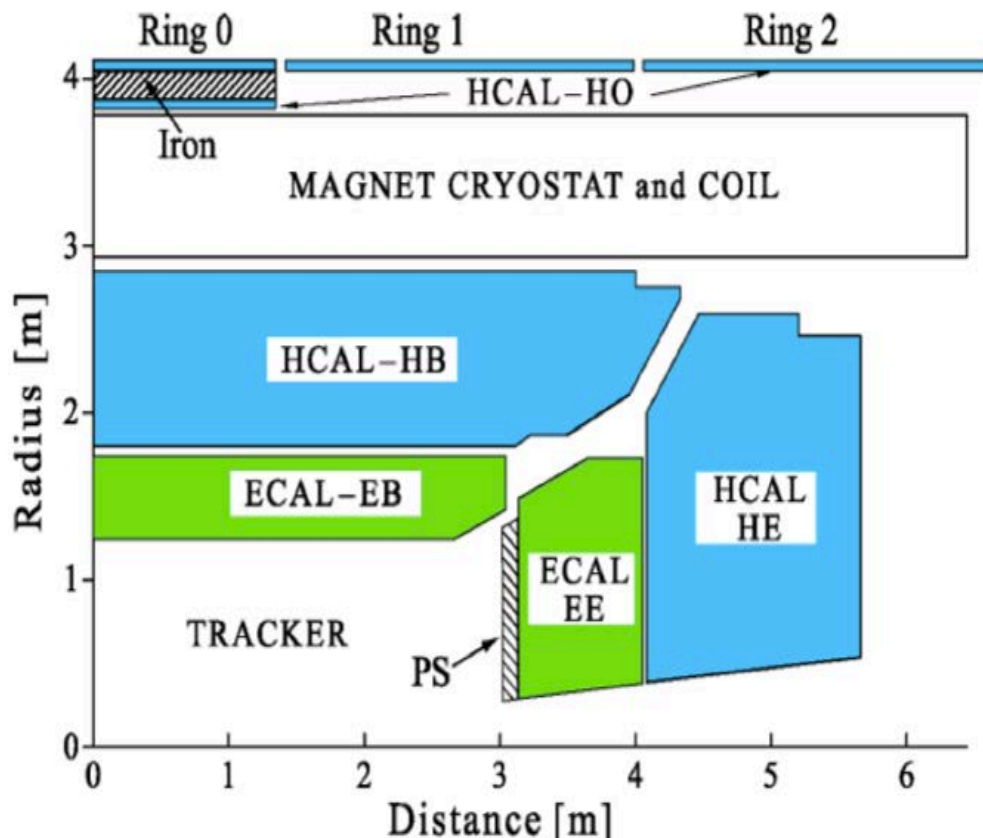


Figure 3.9. Location of the ECAL and the HCAL detectors in and around the CMS magnet (Abdullin et al., 2009).

3.2.2.1. Electromagnetic Calorimeter

The ECAL (Bayatian et al., 1997a) of CMS is a hermetic homogeneous calorimeter made of lead tungstate (PbWO_4) crystals as scintillating material. PbWO_4 crystals were chosen because of a very high density (8.28 g cm^{-3}), short radiation length ($X_0 = 0.89 \text{ cm}$) and small Moliere Radius ($r = 2.2 \text{ cm}$) and also they are fast (80% of the light is emitted within 25 ns) (Bayatian et al., 2006). These features allow for a compact calorimeter design where electrons, positrons and photons deposit their energy within a small depth. Aim of the ECAL is the definite energy measurement of electrons, photons and jets. It consists of three main parts: Barrel (EB), Endcap (EE) and Preshower (ES) as shown in Figure 3.10.

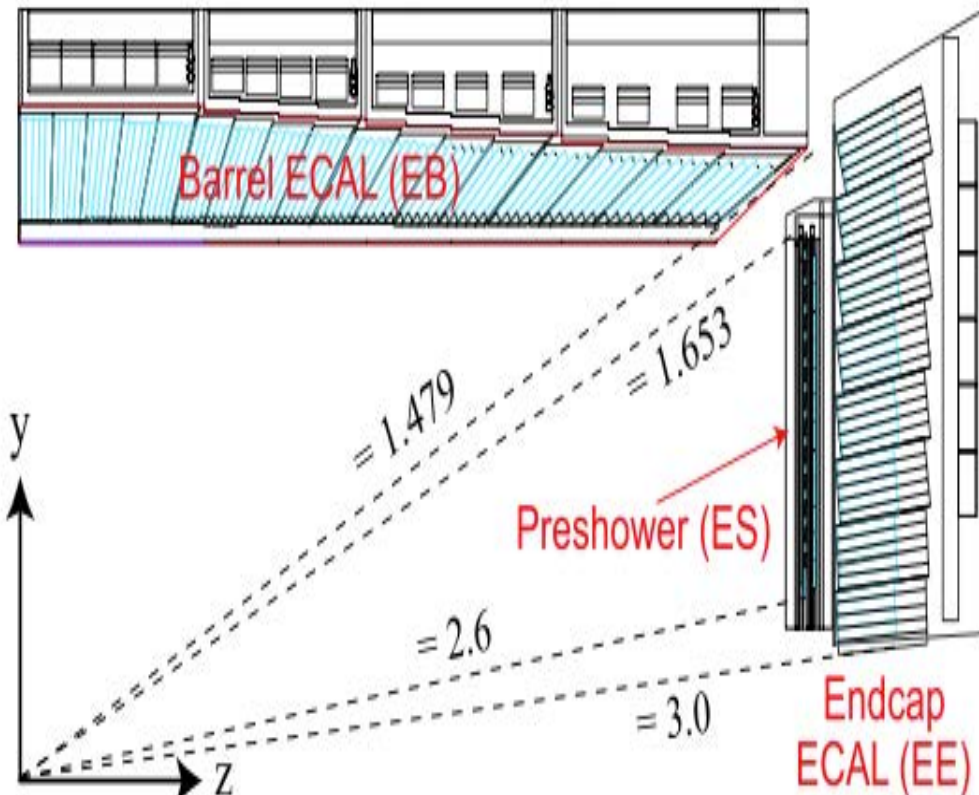


Figure 3.10. Longitudinal view of a quadrant of CMS electromagnetic calorimeter (Bayatian et al., 2006).

Electromagnetic Barrel Calorimeter: The Electromagnetic Barrel (EB) covers the pseudorapidity range $|\eta| < 1.479$ and consists of 61200 PbWO₄ crystals. They are positioned in such a way that the ECAL has a homogenous crystal distribution in η . The crystal cross section corresponds to approximately 0.0174×0.0174 in the $\eta - \phi$ plane or $22 \times 22 \text{ mm}^2$ at the front face of the crystal and $26 \times 26 \text{ mm}^2$ at the rear face. The crystal length is 230 mm corresponding to 25.8 X_0 . In the barrel, silicon avalanche photodiodes (APDs) are used. The ECAL barrel is organized into 36 so-called supermodules. Each supermodule covers an azimuthal angle of 20° and contains four modules with 500 crystals in the first module and 400 crystals in the remaining three. To purify construction and assembly, crystals have been grouped in arrays of 2×5 crystals which form a submodule. Avalanche photodiodes are integrated into each submodule as photodetectors (Stober, 2008).

Electromagnetic Endcap Calorimeter: The two ECAL endcaps (EE) of CMS cover the pseudorapidity range of $1.479 < |\eta| < 3.0$ and consists of 7324 crystals. The longitudinal distance between the interaction point and the endcap envelop is 3144 mm in the simulation even when the interaction points position changes when the 4T magnet field is switched on. Each endcap consists of two large substructures, so called Dees. Every Dee holds 3662 identical shaped crystals which are organized into mechanical units of 5×5 crystals, called SuperCrystals (SCs).

Electromagnetic Preshower Detector: Preshower detector (ES) covers most of the endcap surface. It includes two orthogonal planes of silicon strip sensors (so-called micro modules) interleaved with lead. Its principal aim is to enable a good identification of neutral pion and photon discrimination in the endcaps within $1.653 < |\eta| < 2.6$. It also helps the identification of electrons, against minimum ionizing particles and improves the position determination of electrons and photons with high granularity (Bayatian et al., 2006).

3.2.2.2. Hadron Calorimeter

The CMS hadron calorimeter (HCAL) (Bayatian et al., 1997b) is placed outside the electromagnetic calorimeter and covers the pseudorapidity region $|\eta| < 5.0$. It plays a role in identification and measurement of quarks, gluons and neutrinos by measuring the energy and direction of jets and also determines the missing transverse energy. Due to photons and electrons being totally absorbed in the ECAL, the HCAL indirectly allows for identification of these particles as well. The design of the HCAL assumes;

- good hermeticity,
- good transverse granularity,
- moderate energy resolution and sufficient depth for hadron shower containment.

HCAL consists of four main parts: barrel (HB), endcap (HE), outer (HO) and forward (HF). The central barrel and endcap HCAL subdetectors completely surround the ECAL and are fully immersed within the high magnetic field of the solenoid. The HB and HE are joined hermetically with the barrel extending out to $|\eta| = 1.4$ and the endcap covering the overlapping range $1.3 < |\eta| < 3.0$. HF is located 11.2 m from the interaction point and provides coverage of $3 < |\eta| < 5.0$, while HO procures additional coverage outside of the magnet coil (Bayatian et al., 2006).

In HCAL brass is chosen as absorbing material while for the active material about 70000 plastic scintillator tiles are used. Figure 3.11 shows subsystem of the HCAL.

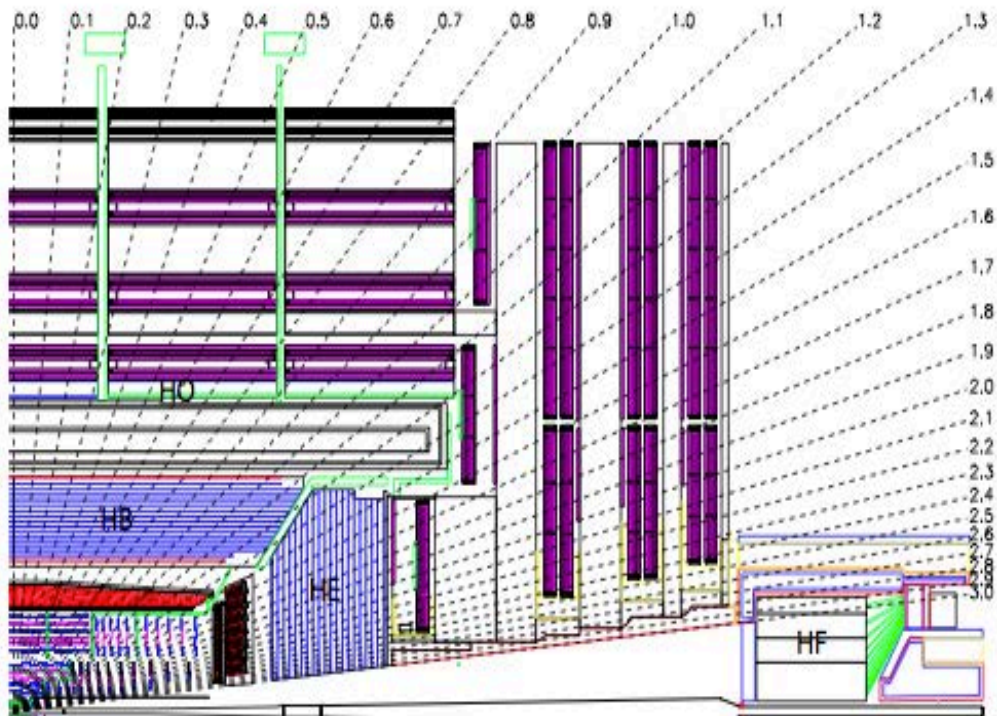


Figure 3.11. Longitudinal view of the four subsystems of the hadronic calorimeter (Chatrchyan et al., 2008).

Hadron Barrel Calorimeter: Hadron barrel (HB) as shown in Figure 3.12 (left) is located between EB and the CMS magnet and is composed of 64 segments covering the pseudorapidity region of $|\eta| < 1.3$. Each plane in the η segmentation is divided into a ring of 36 segments covering the complete ϕ -region. This results in 2304 towers with a segmentation of $\Delta\eta \times \Delta\phi = 0.087 \times 0.087$. The towers themselves consist of 15 brass plates of 5 cm thickness with 3.7 mm scintillator plates between them. The first scintillator plate has a thickness of 9 mm to produce better light output. The HB is divided into two halves barrel sections (HB+ and HB- depending on their z position) each composed of 18 identical wedges that cover 20° in ϕ . The numbering scheme of the wedges are shown in Figure 3.12 (right).

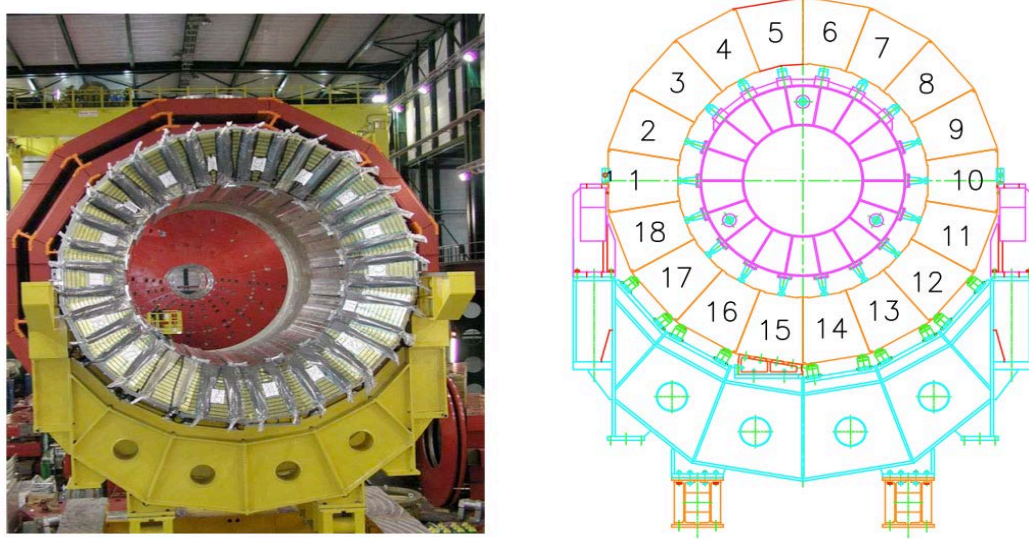


Figure 3.12. Assembled HCAL half-barrel in SX5 (left), numbering scheme for the HB wedges. Wedge 1 is on the inside (+x direction) of the LHC ring (right) (Chatrchyan et al., 2008).

Each wedge contains brass alloy absorber plates and 16 layers of active plastic scintillator tiles located in between the stainless steel and brass absorber plates. The innermost and outmost absorber layers are made of stainless steel (Bayatian et al., 2006).

Hadron Endcap Calorimeter: The Hadronic Endcap Calorimeter (HE) is a sampling calorimeter located inside the CMS magnet and consists entirely of brass absorber plates and overlaps with the HB in tower 16. HE subdetector's location at CMS is given in Figure 3.13 (left). The thickness of the plates is 78 mm and scintillator thickness is 3.7 mm. There are 19 plastic scintillation layers and $\Delta\eta \times \Delta\phi$ tower segmentation for pseudorapidity range $|\eta| < 1.74$ matches that of the barrel, while for higher η the size doubles. η segmentation in HE is given in Figure 3.13 (right). On the contrary the HB, the HE towers have a longitudinal segmentation. The reason for this is the radiation environment, hence offering the possibility to correct the calibration coefficients after scintillator degradation.

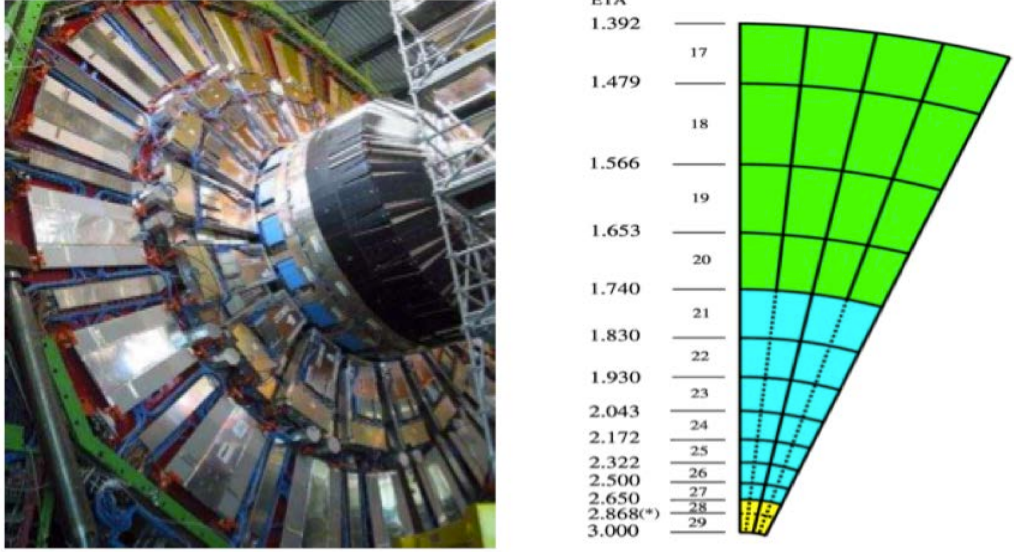


Figure 3.13. HE Calorimeter (left), η segmentation and size increase in HE (right)(Bayatian et al., 2006).

Hadron Outer Calorimeter: The Hadron Outer Calorimeter (HO) sits outside the CMS magnet and ensures that enough sampling depth is provided in the barrel region. HO consists of arrays of scintillator located outside the magnet coil and includes five rings 2.5 m wide along the z -axis. Each ring has 12 identical ϕ -sectors. The 12 sectors are separated by 75 mm thick stainless steel beams which hold successive layers of iron of the return yoke as well as the muon system. The rings are identified by the numbers $-2, -1, 0, +1, +2$ with increasing η . The HO covers the pseudorapidity region $|\eta| < 1.26$ and allows to recover shower leakage caused by the short interaction length and thus improves the missing E_T measurement (Chatrchyan et al., 2008).

Hadron Forward Calorimeter: The Hadron Forward Calorimeter (HF) as shown in Figure 3.14 is located 11.2 m from the interaction point and is made of steel absorbers and radiation hard quartz fibers with a fast collection of the emitted Cherenkov light within the fibres. There are two sets of fibres: Long (1.65 m) and short (1.43 m) quartz fibers placed separately and readout with phototubes. Each HF module has 18 wedges in a non-projective geometry, with quartz fibers running parallel to the beam axis along the length of the iron absorbers as shown in 3.15

(left). The detectors are divided into a tower geometry. There are 13 towers in η , all with a size given by $\Delta\eta \approx 0.175$, except for the lowest- η towers with $\Delta\eta \approx 0.1$ and the highest- η towers with $\Delta\eta \approx 0.3$. In Figure 3.15 (right), η segmentations are shown for HF. The ϕ segmentation of all towers is 10° , except for the highest- η one which has $\Delta\phi = 20^\circ$. This leads to 900 towers and 1800 channels in the two HF modules. Figure 3.16 presents a cross sectional view of the HF.

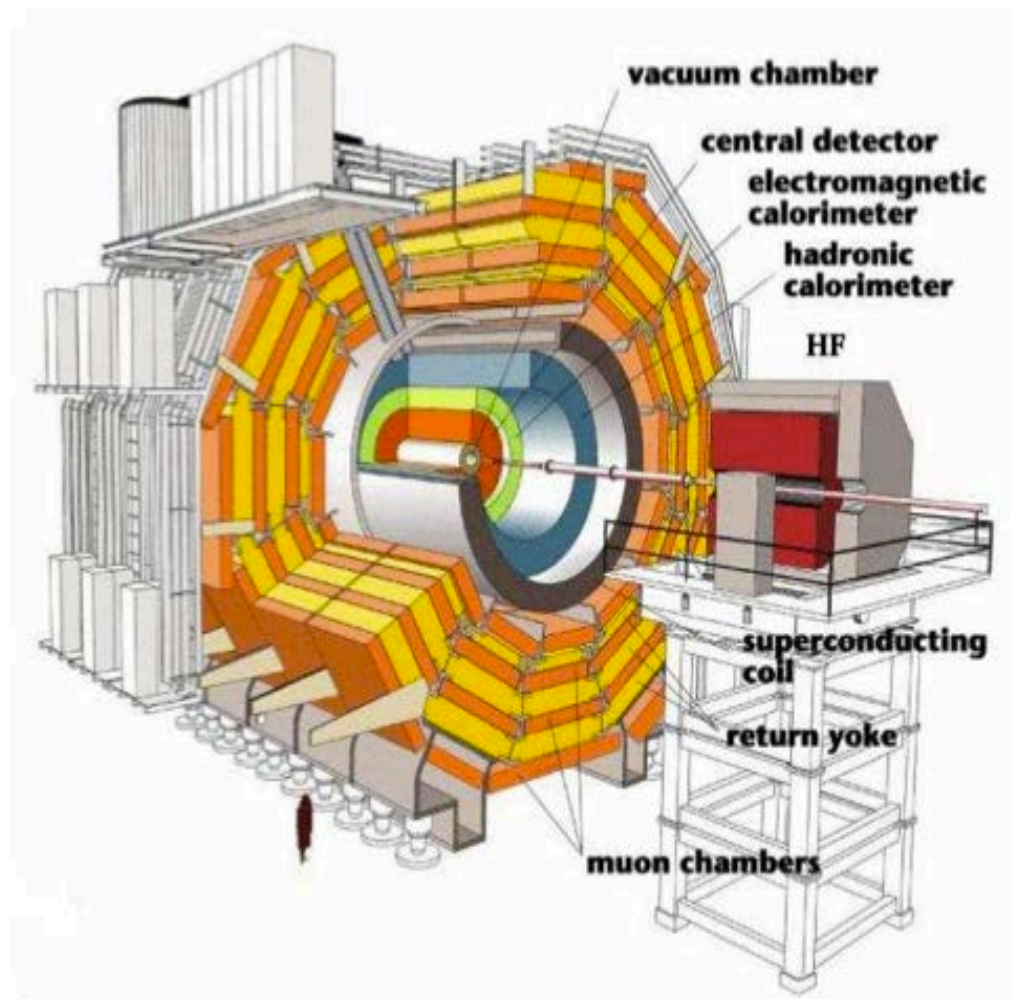


Figure 3.14. Overview of the HF Calorimeter (Akgün, 2003).

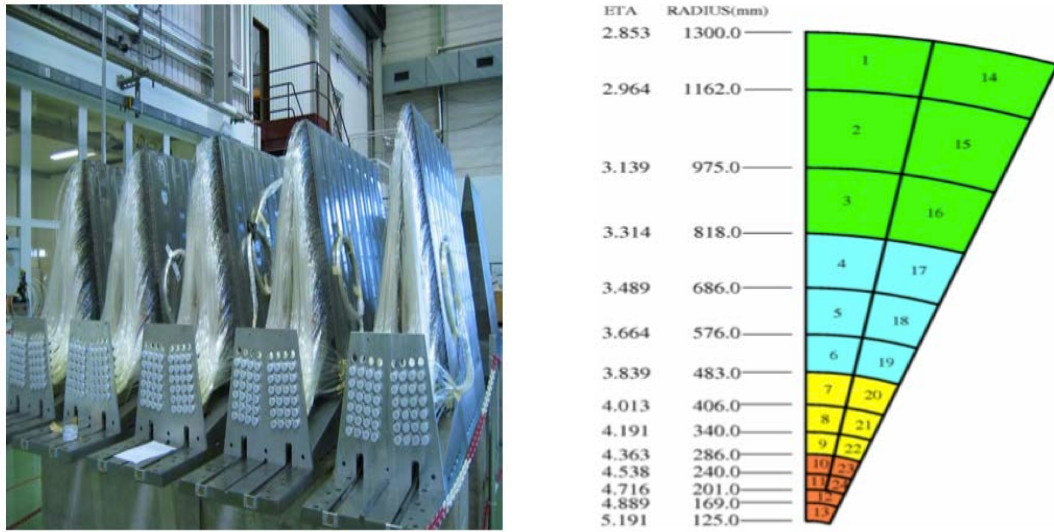


Figure 3.15. CMS HF Calorimeter production wedges (left), η segmentation and size increase in HF (right) (Bayatian et al., 2006).

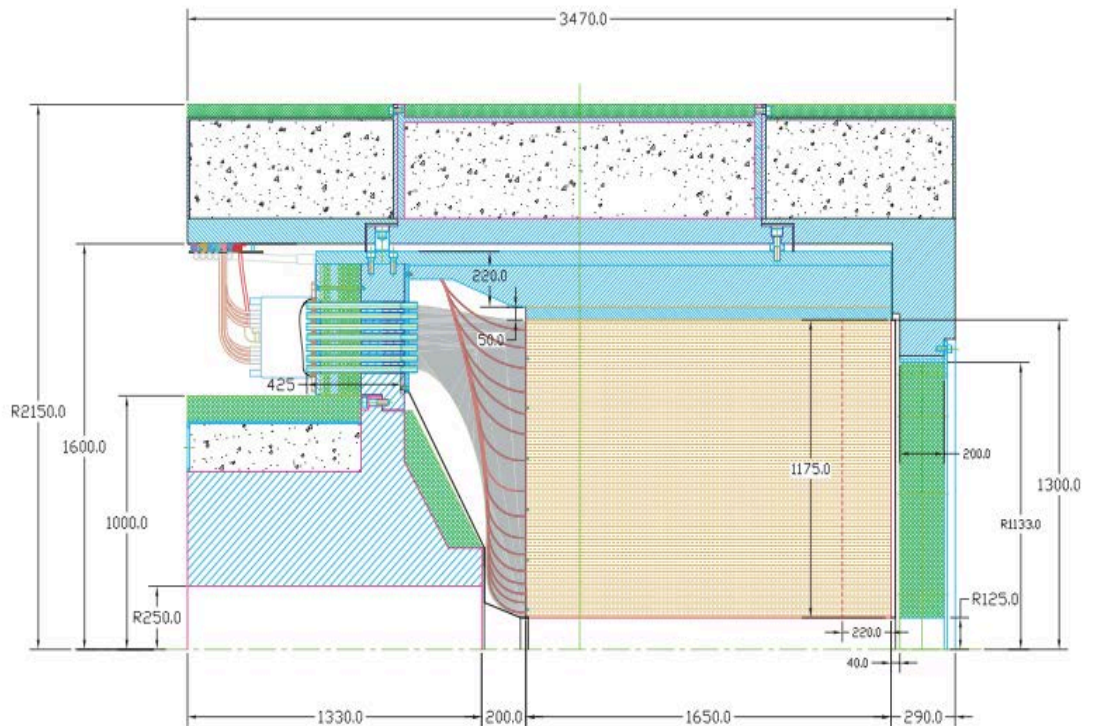


Figure 3.16. The cross sectional view of the HF calorimeter (Chatrchyan et al., 2008).

The signal is generated when charged shower particles above the Cherenkov threshold generate Cherenkov light. The Cerenkov light produced by the relativistic components of the shower is detected by an array of photomultipliers (PMT). In HF the PMTs operate in a temperature controlled environment, inside individual magnetic shields to protect PMTs from a moderate magnetic field. By measuring Cerenkov light, the HF is generally sensitive to the electromagnetic component of the shower. The neutral constituent of the hadron shower is favourably sampled in the HF technology. HF design causes narrower and shorter hadronic showers and therefore is ideally sufficient for the jammed environment in the forward region (Bayatian et al., 2006). The main physics purpose of the HF calorimeter is to tag high energy jets generated by vector-boson fusion events. The construction of the calorimeter, which will cover the pseudorapidity interval $2.8 < |\eta| < 5.2$ is driven by the requirements of a high radiation environment. This pseudorapidity region is very important for heavy Higgs, SUSY and low- x QCD effects in forward jet production searches.

3.2.3. Solenoid Magnet

CMS contains an enormous super conducting solenoidal magnet (Bayatian et al., 1997c) (Figure 3.17) which weighs 12000 t and has dimensions of 12.9 m in length and 5.9 m in diameter. A maximum energy of 2.7 GJ can be stored in the magnet. It is able to generate an inner uniform 4 T magnetic field whose properties, summarized in Table 3.3 allow certain measurements of charged particles transverse momentum. The magnetic field in the iron return yoke, which hosts several layers of muon chambers is saturated at about 2. The silicon tracking system and the electromagnetic and hadronic calorimeters are placed just inside the solenoid making the detector compact in order to decrease disturbing interactions of particles with the coil material (Ralich, 2009).

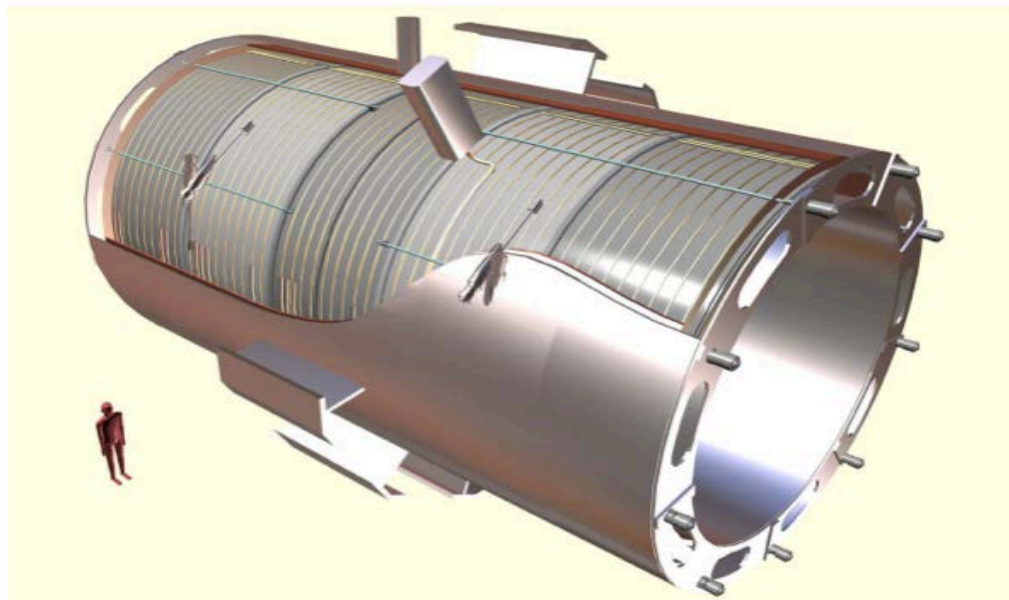


Figure 3.17. The CMS superconducting magnet (Chatrchyan et al., 2008).

Table 3.3. Main parameters of the CMS magnet (Bayatian et al., 1997c).

Magnetic induction at impact point	4.0 T
Peak magnetic induction on the conductor	4.6 T
Magnetic length	12.48 m
Stored energy	2.52×10^9 J
Magnetomotive force	42.24×10^6 At
Magnetic radial pressure	6.47×10^6 Pa
Axial compressive force at mid plane	122×10^6 N

3.2.4. Muon System

The muon detectors (Bayatian et al., 1997d) are placed outside the CMS magnet and have to provide robust muon identification and precise momentum measurement. Additionally it is necessary to have a quick response to the passage of muons so as to provide information to the CMS trigger system. It is the largest and one of the most important systems of the CMS detector that cover the pseudorapidity range of $|\eta| < 2.4$ and lie in the outermost region of the detector. The muon detector chambers have three functions: muon identification, momentum measurement, triggering and are designed to reconstruct momentum and charge of muons over the the entire kinematic range of the LHC (Chatrchyan et al., 2008). Because of the CMS geometry, the muon system has a cylindrical barrel section and two endcaps. The system also consists of three separate gaseous detector systems: Aluminum Drift Tubes (DT), Resistive Plate Chambers (RPC) and Cathode Strip Chambers (CSC).

In the barrel region $|\eta| < 1.2$ DT are used. In this part where the neutron induced background is small and the muon rate is low and magnetic field (4T) is uniform, drift chambers with standart rectangular drift cells are used. In the two CMS endcaps where muon rate and background levels are high, the magnetic field is large and non uniform, the muon system uses CSC (Chatrchyan et al., 2008). The CSCs cover the pseudorapidity range up to $|\eta| < 2.4$. In addition to those, RPCs are diffused in both the barrel and the endcap regions. The DT and CSC are used to provide good position measurement and the bending angle of a muon. The RPCs are useful for triggers due to their fast response with precise timing measurement. All muon detectors contribute to the L1 trigger system, satisfying independent and supplementary sources of information. The layout of the CMS muon system is shown in Figure 3.18.

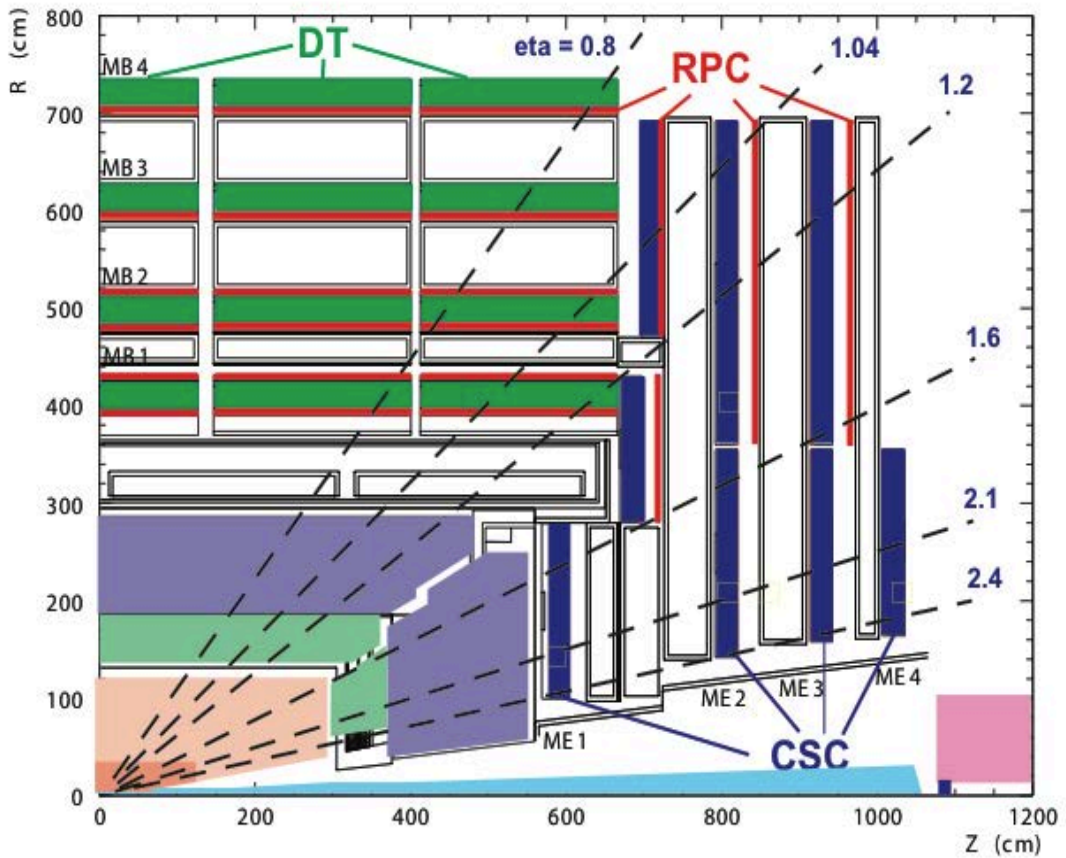


Figure 3.18. Design overview of the outer CMS muon system (Bayatian et al., 2006).

3.2.4.1. Muon Barrel System: Drift Tube Chambers

The barrel DT chambers cover the pseudorapidity region $|\eta| < 1.2$. The CMS barrel muon detector consists of four concentric cylinders around the beam line as shown in Figure. 3.19. The three inner cylinders have 60 drift chambers each. The outer cylinder has 70 chambers and about 172000 sensitive wires were used in this part of the detector. Each of the 12 sectors of the yoke have four muon stations per wheel, labeled MB1, MB2, MB3 and MB4. The yoke iron support between the station chambers creates unavoidable dead zones in ϕ coverage. To minimize their effect, the muon detection zones are set to no overlap in ϕ (Chatrchyan et al., 2008).



Figure 3.19. Layout of the CMS barrel muon DT chambers in one of the 5 wheels (Chatrchyan et al., 2008).

3.2.4.2. Muon Endcap System: Cathode Strip Chambers

The Muon Endcap Detector is made of 468 CSCs. Each Endcap consists of four stations with chambers, labeled ME1, ME2, ME3 and ME4, in the increasing order of distance from the interaction point as shown in Figure 3.20. The stations are inbuilt perpendicular to the direction of the beam on the disks enclosing the magnet. In each disk, the chambers are divided into rings around the beam axis (two for ME2-4 and three for ME1). Each of the rings has 36 chambers, except for the innermost rings of ME2-ME4, that have 18 chambers. Similar to the Muon Barrel, there are layers of the double gap RPCs in the Endcaps (Gleyzer, 2011).

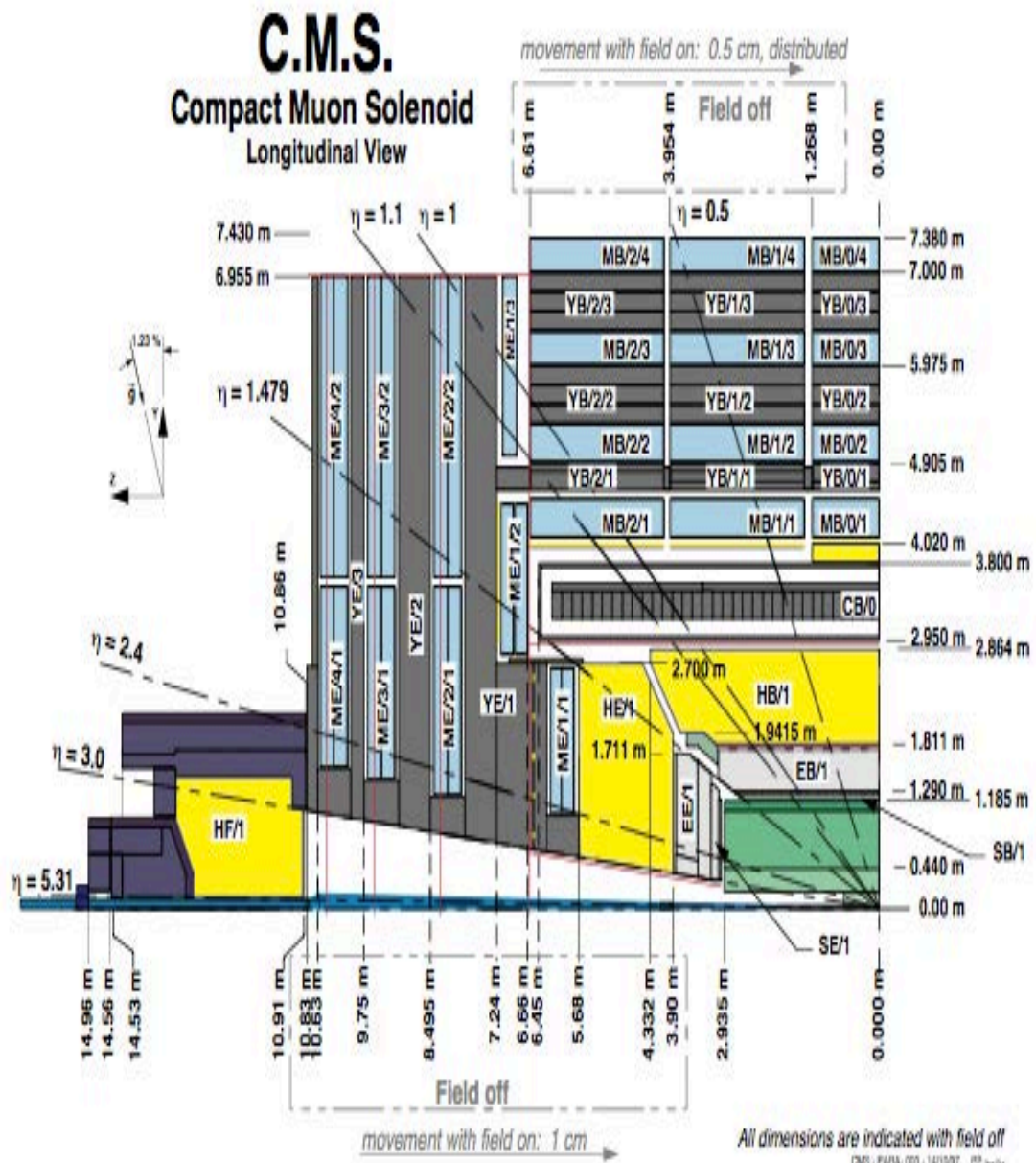


Figure 3.20. Quarter view of the CMS detector. CSC of the Endcap Muon system are highlighted (<http://inspirehep.net/record/837874/plots>).

3.2.4.3. Resistive Plate Chambers



Figure 3.21. Resistive plate chamber layers (<http://cms.web.cern.ch/news/resistive-plate-chambers>).

Resistive Plate Chambers (RPC) are gaseous parallel plate detectors that combine enough spatial resolution with a time resolution comparable to that of scintillators. The RPC basic double gap module comprises two gaps operated in avalanche mode. The width of the gap is 2 mm and length of the strip is 130 cm, except in MB2, where it can be either 85 cm. There are 480 RPCs in the barrel and 1020 total. RPC's time tagging capability is better than LHC bunch crossing time (25ns) and it provides fast response and an accurate timing measurement which is used in the muon trigger.

3.2.5. The Data Acquisition and Trigger System

The CMS Data Acquisition (DAQ) (Bayatian et al., 2000b) and Trigger system are designed to collect and analyse the detector information at the LHC bunch crossing frequency of 40 MHz. DAQ system operates the Detector Control System (DCS) for the operation, controls all detector components and general infrastructure of the experiment (Bayatian et al., 2000a). There is a bunch crossing every 25 ns at LHC and bunch crossing rate of the LHC leads to approximately 10^9 interactions per second. The nominal event size is about 1.5 MB in case of pp collisions and 100 TB of data results in per second. Since this amount is too large to store and process in

any tape or disk, a trigger system is used in CMS. CMS trigger system consists of two independent trigger levels:

- Level 1 Trigger (L1),
- High Level Trigger (HLT).

Schematic view of the CMS trigger and DAQ system is shown in Figure 3.22.

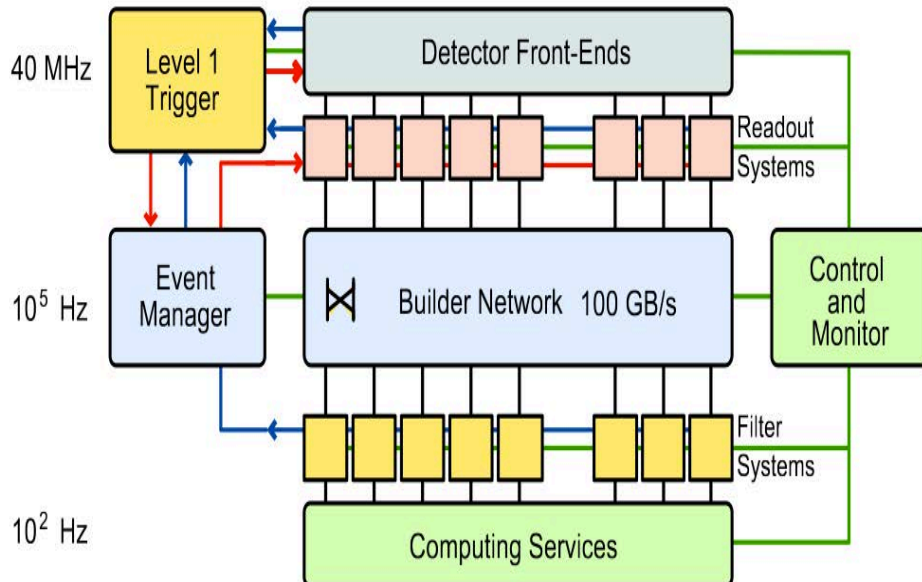


Figure 3.22. CMS trigger and DAQ system (Bayatian et al., 2006).

3.2.5.1. Level 1 Trigger

The Level-1 (L1) triggers contain the calorimetry and muon systems, as well as some correlation of information between these systems. The Level-1 decision depends on the subsistence of “trigger primitive” objects such as photons, electrons, muons and jets above set E_T or p_T thresholds. It also uses global sums of E_T and E_{miss}^{miss} (Chatrchyan et al., 2008). Calorimeter and muon system work in parallel and analyse the data locally. They combine the information and generate the output passed to the DAQ. As the L1 trigger system is located 90 m outside the detector,

has a latency of 3.2 μ s between the bunch crossing. L1 trigger goal is to analyse every 40 MHz pp collision and decrease the data rate passed on to the HLT to 100 kHz. It accepts signals and raw readout data are then buffered and sent to a computer farm for the HLT processing. Since L1 has to have a high and carefully understood efficiency it is arranged into three basic subsystems:

- L1 Calorimeter Trigger,
- L1 Muon Trigger,
- L1 Global Trigger.

The L1 Global Trigger combines the output of L1 Calorimeter Trigger and L1 Muon Trigger, as shown in Figure 3.23. L1 Muon Trigger consists of information from RPC, CSC and DT specific triggers are combined in so called L1 Global Muon Trigger.

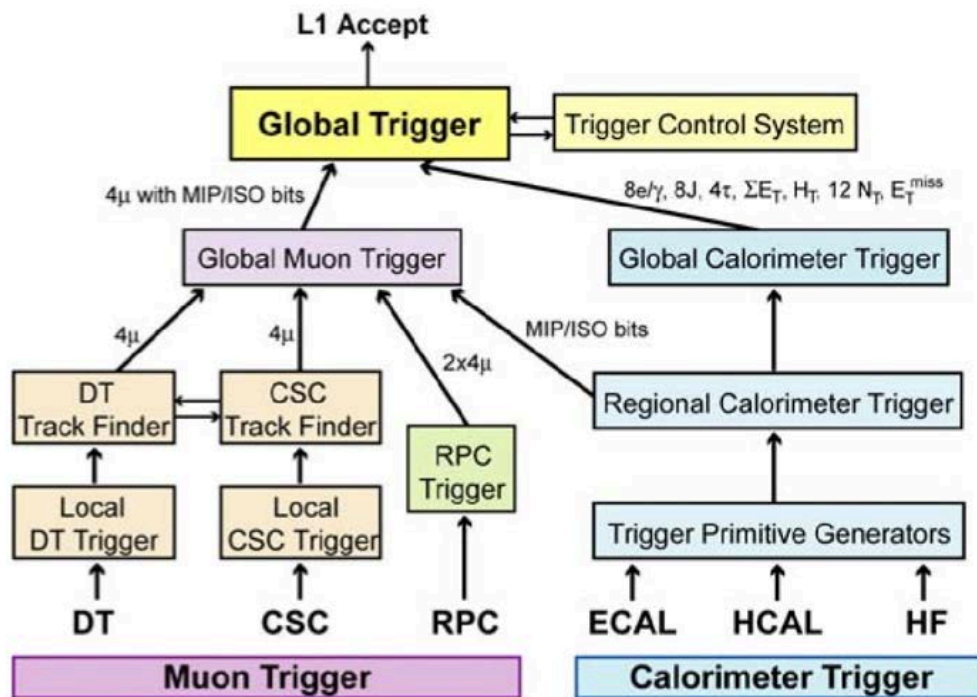


Figure 3.23. Level-1 Trigger architecture (Chatrchyan et al., 2008).

3.2.5.2. High Level Trigger

High Level Trigger (HLT) system is a software system and uses the detector signals that pass the L1 trigger. HLT is responsible for reducing the L1 output rate down to the target of 100 Hz. The HLTs have access to all the information used in L1 since this is stored locally in the L1 trigger crates. It can run on high resolution and provides a full reconstruction of the event. The HLT decisions are based on the informations from all subdetectors. This information includes data from the tracker and the full granularity of the calorimeters. In order to make efficient use of the allocated trigger decision time, the HLT code is divided in three virtual layers:

- Level-2,
- Level-2.5,
- Level-3.

Level-2 uses muon and calorimeter information, level-2.5 additionally uses hit information from the pixel detector and level-3 uses full detector information (Lazaridis, 2011).

3.3. Forward Detectors

3.3.1. CASTOR Detector

The CASTOR (Centauro And Strange Object Research) detector is an electromagnetic (EM) and hadronic (HAD) calorimeter of CMS. It is located at 14.39 m from the interaction point, covering the pseudorapidity range $5.2 < |\eta| < 6.6$. Figure 3.24 shows the location of CASTOR in the CMS forward region.

CASTOR is designed for the very forward rapidity region to search for strangelets and centauro events in heavy ion collisions, kinds of exotic matter potentially formed in the baryon dense region, and for diffractive and low- x physics in pp collisions at the LHC

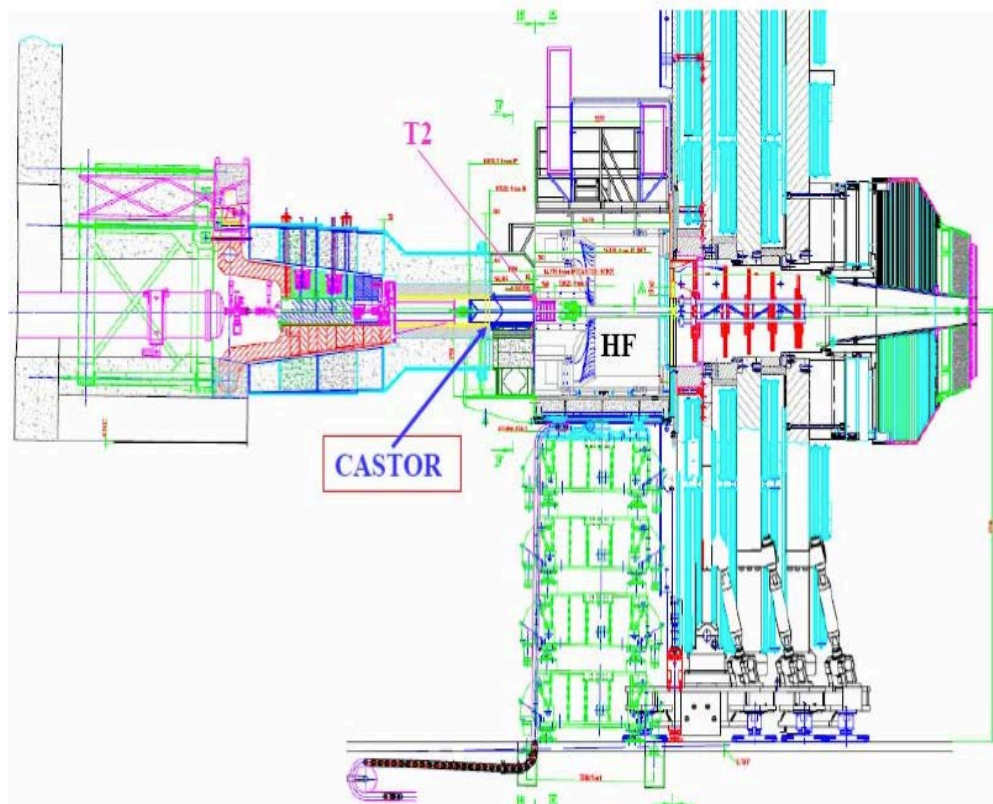


Figure 3.24. Location of CASTOR in the CMS forward region (Chatrchyan et al., 2008).

CASTOR is constructed from layers of tungsten (W) plates as absorber and fused silica quartz (Q) plates as active medium. The main advantages of quartz calorimeters are radiation hardness, fast response and compact detector dimensions, making them sufficient for the experimental conditions encountered in the very forward region (Chatrchyan et al., 2008). The CASTOR detector is a Cerenkov effect based calorimeter. A high energy particle will shower in the tungsten volume and will generate relativistic charged particles that emit Cerenkov light in the quartz plate. The Cerenkov light is then collected and transmitted to the photodetector devices through air-core light guides (Aslanoglu et al., 2007).

3.3.2. ZDC Detector

A set of two Zero Degree Calorimeters (ZDC) (Grachov et al., 2006) cover $|\eta| \geq 8.3$ pseudorapidity and are designed to complement the CMS very forward region, notably for heavy ion and pp diffractive research. Each ZDC has the EM and HAD sections. Two identical ZDCs are located between the two LHC beam pipes at ≈ 140 m on each side of the CMS interaction region at the detector slot of 1 m length, 96 mm width and 607 mm height inside the neutral particle absorber TAN (Hoyer, Turner, Mokhov, 1998). The TAN is located in front of the D2 separation dipole and was designed to protect magnets and detectors against debris generated in the pp collisions, and against beam halo and beam losses (Chatrchyan et al., 2008).

4. JET RECONSTRUCTION at CMS

In this chapter, properties of jets, jet types and basic information on the forward jet reconstruction algorithms are presented. Then the MC jet performance studies are shown in Section 4.5. Here the jet energy response and the jet reconstruction resolution in both energy and position are presented.

4.1. Jet Definition and Kinematics

In hadronic interactions the final state partons are quarks and gluons. Because of confinement, quarks carry a color charge and cannot exist in a free form. Therefore they fragment into hadrons before they can be directly detected, becoming jets. These jets can be measured in a particle detector and studied to define the properties of the quark. A jet is a cone of hadrons and other particles produced by the hadronization process of quarks and gluons. It is the experimental signature of a parton and is usually described at one of three levels: parton, particle and calorimeter jets as shown in Figure 4.1.

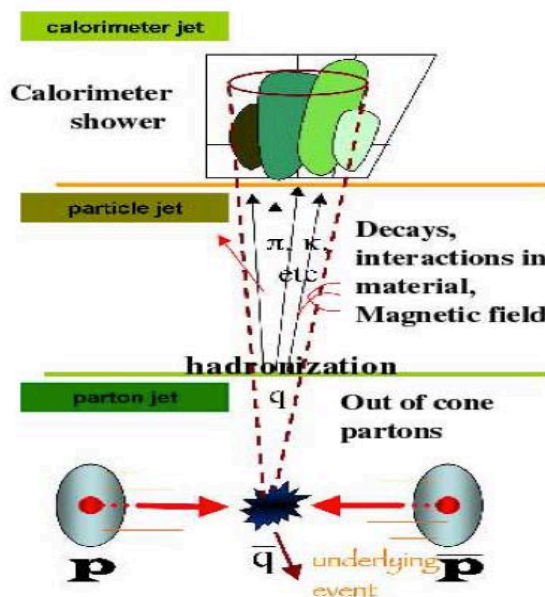


Figure 4.1. A representation of the different stages of jet production and reconstruction: parton, particle and calorimeter level (Ellis et al., 2007).

Partons produced after the collisions are called “parton jets” before they fragment into other particles. A parton materializes into many particles through hadronization or fragmentation. These particles are defined as “particle jets” and their number increases in a cone shape along the direction of the original quark or gluon. When we want to measure the energy of a jet, we need to use a calorimeter. The hadronized particles deposit their energy in an approximate circle on the calorimeter and we use this energy cluster to measure the energy of the jet and call it “calorimeter jet”.

A jet can also be described using p_T (transverse momentum), ϕ (azimuth angle), y (rapidity) and m (mass) variables. The four components of momenta are (Ellis et al., 1996) :

$$p^\mu = \left(\sqrt{p_T^2 + m^2} \cosh(y), p_T \sin \phi, p_T \cos \phi, \sqrt{p_T^2 + m^2} \sinh(y) \right) \quad (4.1)$$

where the rapidity is;

$$y = \frac{1}{2} \ln \left(\frac{E + p_z}{E - p_z} \right) \quad (4.2)$$

and p_z is the momentum along the beam direction. For $m \rightarrow 0$, the rapidity is equal to the pseudorapidity, η .

$$\eta = \ln \tan \left(\frac{\theta}{2} \right) \quad (4.3)$$

A jet is defined as a cluster of transverse energy E_T in a cone size ΔR which is given by;

$$\Delta R = \sqrt{(\Delta \eta)^2 + (\Delta \phi)^2} \quad (4.4)$$

Jet transverse energy (E_T), jet pseudorapidity (η) and jet azimuth (ϕ) are described as (Ellis et al., 2007);

$$E_{T_{jet}} = \sum_{i \in jet} E_{T_i} \quad (4.5)$$

$$\eta_{jet} = \frac{1}{E_{T_{jet}}} \sum_{i \in jet} E_{T_i} \eta_i \quad (4.6)$$

$$\phi_{jet} = \frac{1}{E_{T_{jet}}} \sum_{i \in jet} E_{T_i} \phi_i \quad (4.7)$$

where i is the protojet.

4.2. Jet Types at CMS

There are four types of reconstructed jets at CMS depending on the utilized subdetectors. These jet types are: Calorimeter jets, Jet-Plus-Track jets, Particle-Flow jets and Track Jets.

4.2.1. Calorimeter Jets

Calorimeter Jets (CaloJets) are reconstructed using the information from the ECAL as well as the HCAL calorimeters. The building blocks for CaloJets measurements are calotowers which are made of the HCAL towers and the corresponding ECAL crystals. A sketch of the so-called “calorimeter towers” is shown in Figure 4.2 for the barrel region.

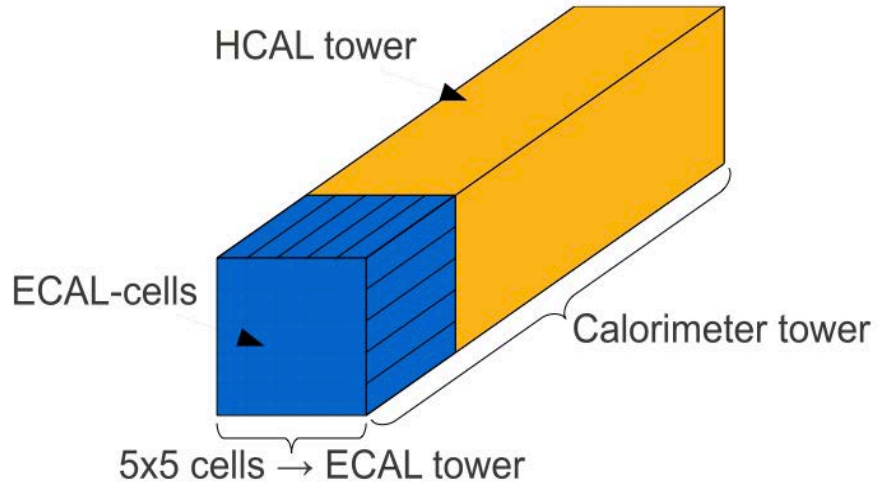


Figure 4.2. Sketch of calorimeter towers used for jet clustering. 5×5 ECAL-cells and one HCAL tower are logically combined to form a calorimeter tower in the barrel region (Kirschenmann, 2010).

CaloJets are simple objects which use only calorimeter information and are strongly affected by the non-linearity of the calorimeters. CaloJets are usually used by the trigger system since the readout of calorimeter measurements is fast (Schröder, 2012). In order to decrease noise in the HCAL towers and the amount of data transferred forward, zero suppression is applied. In order to suppress the contribution from extra pp interactions in the same bunch crossing (pileup) calorimeter towers with the transverse energy of $E^{tower} < 0.3$ GeV are not used in jet reconstruction. An application of a lower cut on the energy or the transverse energy of a calorimeter, readout cell or calorimeter tower built from a calorimeter cell. Towers and cells with energy that is below the cut are not used in jet reconstruction. These thresholds are listed in Table 4.1. The Figure 4.3 shows the calorimeter segmentation in η and ϕ with energy deposition in calorimeter towers in event display of a dijet event. While blue part shows energy deposition in HCAL, red part shows energy deposition in ECAL.

Table 4.1. Calorimeter cell thresholds (Zielinski, 2010).

Section	Threshold (GeV)
HB	0.7
HE	0.8
HO	1.1/3.5(Ring 0/Ring 1,2)
HF (Long)	0.5
HF (Short)	0.85
EB	0.07 (per crystal, double-sided)
EE	0.3 (per crystal, double-sided)
EBsum	0.2
EEsum	0.45

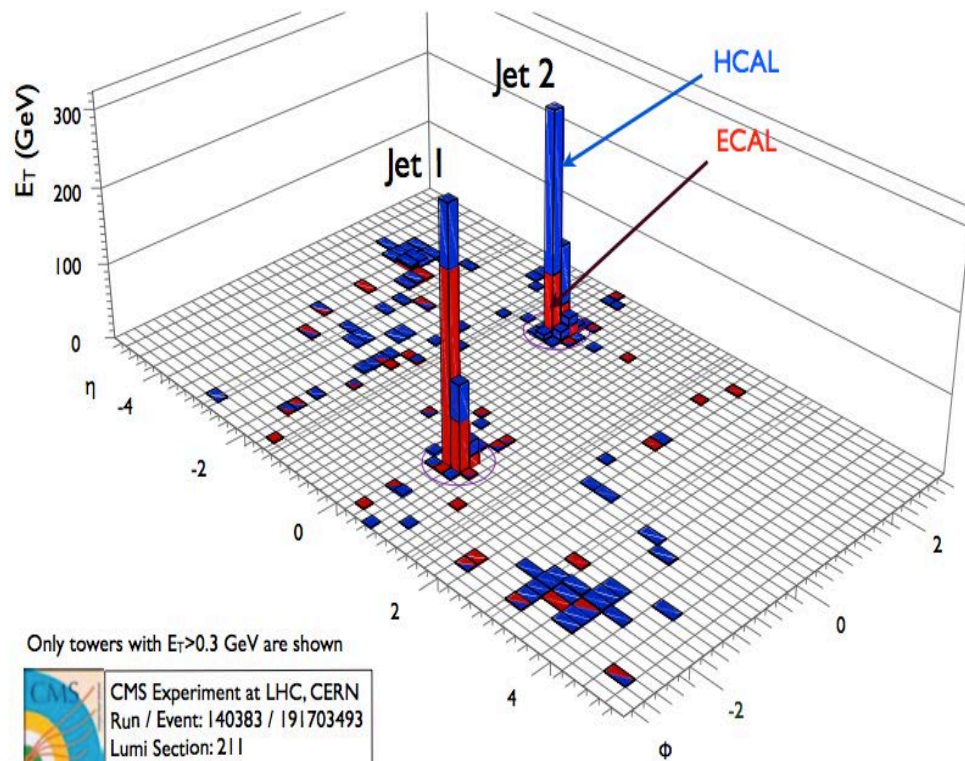


Figure 4.3. Observed dijet event in the CMS calorimeters.

4.2.2. Jet-Plus-Track Jets

Jet-plus-track jets (JPT), which are CaloJets complemented with tracking information use the momentum of charged particles measured in the tracker and the energy of a jet reconstructed from calorimetric energy depositions is corrected. The JPT algorithm requires inter-calibration between the calorimeter and tracker since it does not depend on cluster finding algorithms running on calorimeter cells. However the JPT is insensitive to the low energy clustering in the calorimeter and track-cluster matching while averaging the measurement capabilities of the two subsystems. The JPT algorithm and the associated data based calibration and correction methods improve the jet resolution and response by combining the calorimeter and tracking measurements.

4.2.3 Particle-Flow Jets

The Particle Flow (PF) algorithm reconstructs PF jets which are clustered from the four momenta of the particle candidates. It combines the information from all CMS subdetectors as shown in Figure 4.4 to identify and reconstruct all stable particles existing in an event namely electrons, muons, photons, charged hadrons and neutral hadrons, towards an optimal determination of their direction, energy and type. Electrons are reconstructed by a combination of a track and energy deposition in the ECAL while muons are reconstructed from a combination of the tracker and muon chamber. Charged and neutral hadrons deposit their energy in HCAL. Charged hadrons are reconstructed with the tracker in addition to the HCAL (Bernet et al., 2009). The resulting list of particles can be used to build different higher level objects and observables such as jets, missing transverse energy (MET), taus, lepton and photon isolation, b-jet tagging, etc. The PF building blocks are in the form of charged tracks, calorimeter clusters and muon tracks. The CMS tracker information improves the jet p_T resolution versus pure calorimetric jet reconstruction. PF jets provide more information with respect to the other types and are therefore used by most physics analyses within CMS.

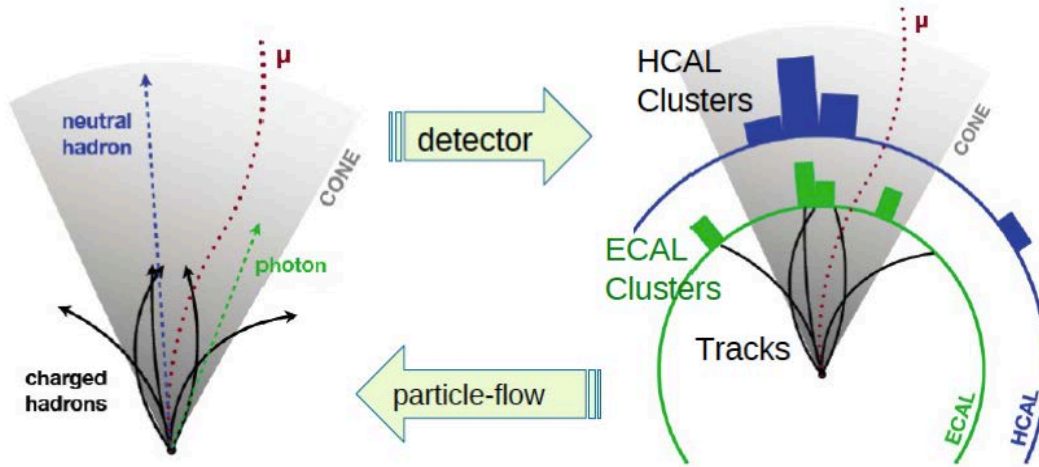


Figure 4.4. The Particle Flow algorithm. Particles in the CMS detector are seen as tracks and energy depositions and the algorithm attempts to fully reconstruct an event by combining information for all CMS subdetectors (Gleyzer, 2011).

4.2.4. Track Jets

Track jets are constructed from the reconstructed charged particle tracks in the tracker. The algorithm uses well-measured tracks correlated to the primary vertex. Track jets have very good angular resolution and are independent of calorimetric measurements. Track jets are similar to the charged component of PF jets. While PF jets are focused on the energy measurement and include very low momentum tracks with large impact parameters, in track jets the track selection is stricter and track jets are a very reliable way to find jets down to very low p_T .

4.3. Jet Reconstruction Algorithms

Observing jets provides information about the feature of the original partons produced after collisions. Jets have to be defined by an algorithm. There are many jet finding algorithms and the best choice often depends on the subject of interest. Jet finding algorithms can be classified into two major groups:

- Cone-based Algorithms (Midpoint Cone, Iterative Cone, SIScone),
- Sequential Recombination Algorithms (k_T , Cambridge/Aachen, Anti- k_T).

Cone algorithms are based on the concept of the parton showering and hadronisation dynamics and a jet is spatially restricted into a cone shaped region with an axis along the direction of the initial parton. On the other hand, the sequential recombination algorithms repeatedly combine the objects which are closest according to some distance measure and in this way reflect the process of parton showering.

Jet reconstruction algorithms apply a set of rules for combining particles into jets, usually by some distance measure to decide whether two particles belong to the same jet and usually satisfy these conditions (Salam, 2010):

- relatively simple to implement in an experimental analysis,
- relatively simple to implement in the theoretical calculation,
- defined at any order of perturbation theory,
- yielding finite cross sections at any order of perturbation theory,
- producing a cross section that is relatively insensitive to hadronisation,
- efficient at finding all physically relevant jets in an event and the same jets, should also be found at the parton level, particle level and calorimeter level,
- numerically efficient in identifying jets,
- collinear (IRC) and infrared safe.

Collinear (IRC) and Infrared safety are the fundamental requirements for jet algorithms.

Collinear safe: The jet finding methods should treat a collinear pair of particles likewise to a single particle with their combined momentum. From the theoretical perspective this means that the jet finding is independent of a particle splitting into two parallel travelling partons and should not change the results of the jet clustering. From the experimental perspective, such a feature means that the jet finding is mostly independent of the granularity of the detector.

Infrared safe: The jet reconstruction should be insensitive to the soft radiation in the event and theoretically consistent with pQCD calculations. Experimentally, cuts to compress the detector noise are applied to make the jet finding as independent as possible of low energy deposits.

The configurations of the infrared and collinear safe algorithm are shown separately in Figure 4.5. From the top figure we can see that adding a soft gluon should not change the jet clustering results (Infrared safety) and from the bottom figure splitting one parton into two collinear partons should not change the jet clustering results (Collinear safety).

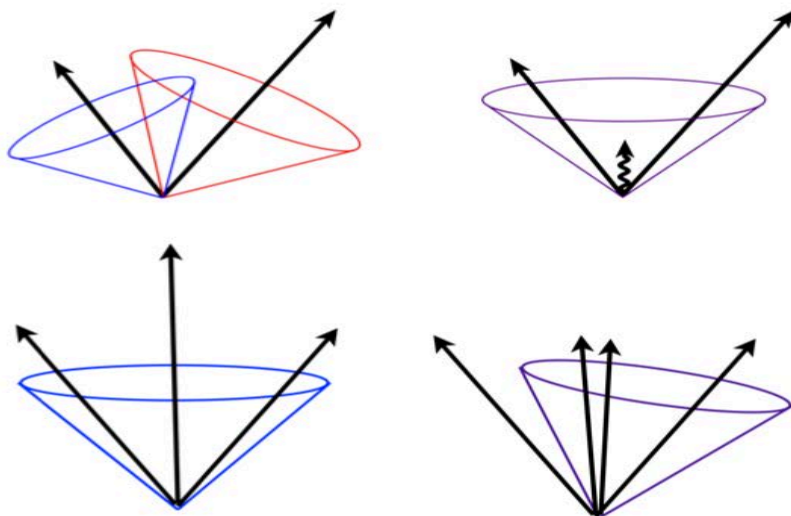


Figure 4.5. Configuration of Infrared (top) and Collinear (bottom) safe algorithm (Blazey et al., 2000).

Three jet clustering algorithms are currently implemented and supported in the CMS software. These are:

- k_T (cone size 0.4/0.6),
- seedless infrared safe (cone size 0.5/0.7),
- anti- k_T algorithm (cone size 0.5/0.7).

4.3.1. Iterative Cone Algorithm

It is a simple cone-based algorithm which has a fast response and is usually used for triggering purposes. This algorithm merges the energy deposits located in a cone around the most energetic calotowers and is applied to a list of input objects. Iterative cone algorithm is neither collinear nor infrared-safe but the CMS software has implemented iterative cone algorithm with cone size $R = 0.5$.

The steps taken to create the iterative cone jets can be summarized as below;

- an E_T -ordered list of input objects is created,
- a cone of size R (R is free parameter of the algorithm) in (η, ϕ) space is cast around the seed, the object with the largest E_T ,
- in order to calculate the feature of the protojet, the objects which are inside the cone are used to calculate:

$$E_T = \sum_i E_{Ti}, \eta = \frac{\sum_i (\eta_i x E_{Ti})}{E_T}, \phi = \frac{\sum_i (\phi_i x E_{Ti})}{E_T} \quad (4.8)$$

- the protojet is used to seed a new protojet,
- the procedure is repeated until the direction of the protojet is no longer changing and the jet is manifested stable,
- the stable protojet becomes a jet and the objects belonging to this jet are removed from the list of input particles and the procedure is repeated until the list is empty.

4.3.2. Seedless Infrared Safe Cone Algorithm

The Seedless Infrared-Safe Cone (SISCone) jet algorithm (Salam, 2007; Salam and Soyez, 2007) is another cone algorithm. It is both collinear and infrared safe in all orders of perturbation theory and uses a concept of a stable cone with a

circle of radius ΔR in the $\eta - \phi$ space and the sum of all the momenta of the particles. The algorithm attempts to identify all the stable cones as shown in Figure 4.6.

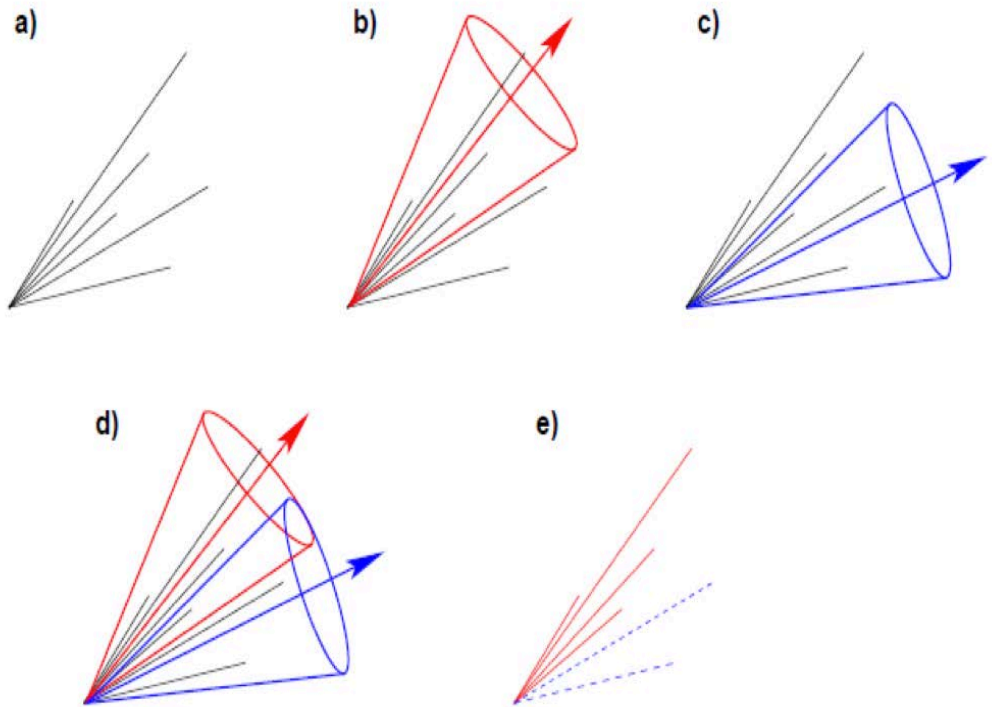


Figure 4.6. Cone-type Jet Algorithm: a) listing of initial 4-vectors, b) and c) finding stable cones, d) splitting/merging algorithm applied, e) final jets.

The algorithm does not use a seed as the iterative cone algorithm. It is acquired using pairs of particles with a distance smaller than twice the chosen jet radius. In the first step the algorithm finds all the stable cones, which are circles in $\eta - \phi$. When all stable cones are found, another step is applied in which the overlap of cones is either split between the two jets or the jets are merged. This step is called split merge procedure and another parameter is introduced that steers the behavior of the algorithm in such cases. Since the algorithm is both very CPU- time-consuming for events with many input objects and also does not work for the events with high pile-up activity, is not used as the standard jet finding algorithm in the CMS experiment.

4.3.3. Anti- k_T Algorithm

Anti- k_T algorithm (Salam, 2010) is an infrared and collinear safe algorithm and is highly recommended within the CMS experiment. The anti- k_T is a special form of k_T algorithm. The detailed description of the production of anti- k_T jets is listed below.

- Starting from an input list of objects, the algorithm defines d_i and d_{ij} . Here d_{ij} is distance between particle (or calorimeter tower) i and j .

$$d_i = \frac{1}{E_{Ti}^2} \quad (4.9)$$

$$d_{ij} = \min \left\{ \frac{1}{E_{Ti}^2}, \frac{1}{E_{Tj}^2} \right\} \times \left(\frac{\Delta R_{ij}}{R} \right)^2 \quad (4.10)$$

Here the dimensionless parameter R is the radius of jet and ΔR_{ij} is the distance (in y , ϕ space) between each pair of protojets. In a more general form distance equation can be written as (Salam, 2010);

$$d_{ij} = \min \left\{ p_{Ti}^{2p}, p_{Tj}^{2p} \right\} \times \left(\frac{\Delta R_{ij}}{R} \right)^2 \quad (4.11)$$

distance d_{iB} (between i and beam (B)) is defined as:

$$d_{iB} = p_{Ti}^{2p} \quad (4.12)$$

$$\Delta R_{ij}^2 = (y_i - y_j)^2 + (\phi_i - \phi_j)^2 \quad (4.13)$$

The parameter p governs the relative power of the energy versus geometrical (ΔR_{ij}) scales and can be positive, negative or zero.

- $p = 1$ for the k_T algorithm (firstly soft particles are clustered),
- $p = 0$ for the Cambridge-Aachen algorithm (an energy dependent clustering algorithm),
- $p = -1$ for the anti- k_T algorithm (firstly hard particles are clustered),
 - if the minimum value is a d_i , particle i is removed from the list of particles and called a jet,
 - if the minimum value is a d_{ij} , particles i and j are recombined into a single new particle according to Eq. (4.8),
 - the procedure is repeated until all particles are ended.

The behavior of different jet algorithms on parton level is illustrated in Figure 4.7. As it can be seen there, the anti- k_T jet algorithm produces the best results. CMS supports k_T algorithm with cone sizes $R = 0.4$ and $R = 0.6$ and supports anti- k_T algorithm with cone sizes $R = 0.5$ and $R = 0.7$. In this thesis, jets are reconstructed using anti- k_T algorithm with cone size parameter $R = 0.5$.

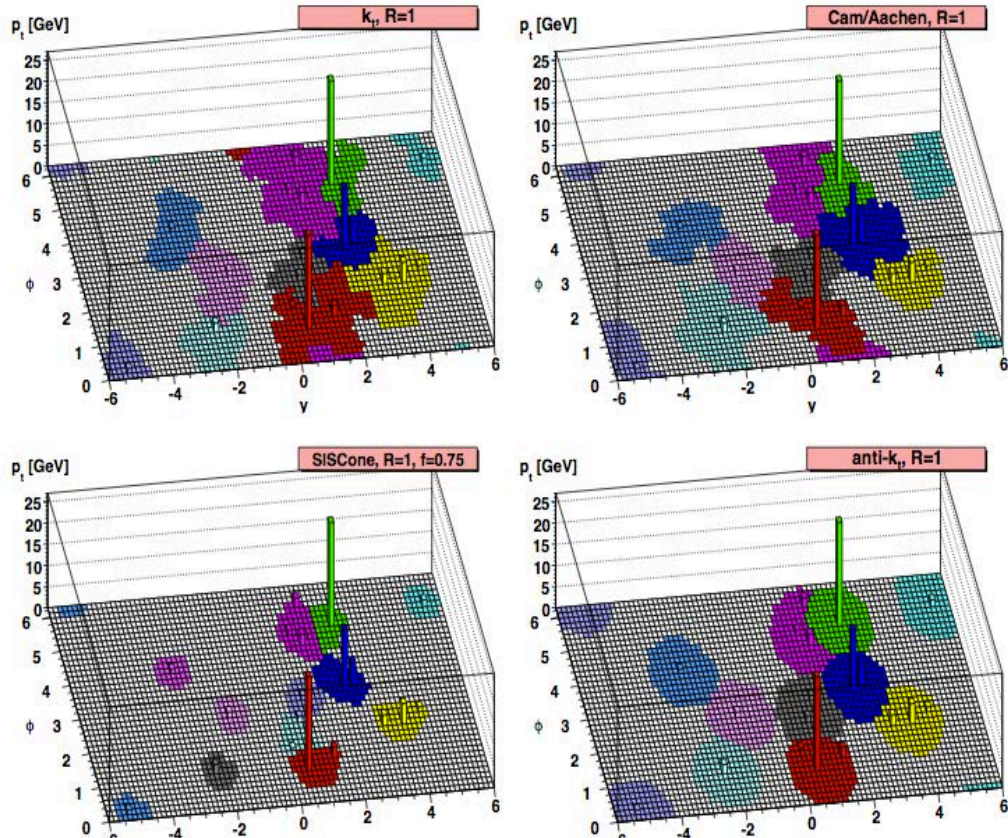


Figure 4.7. Illustration of different jet algorithms in parton level (Salam, 2010).

4.4. Jet Energy Corrections

The calorimeters have electronics noise and detect presence of pileup events from other pp collisions in the same bunch crossing. On the other hand calorimeters have non-linear response to the energy deposited by particles and they are not straightforward to translate the measured energy to the true energy of the particle. To mitigate this problem, a set of jet energy corrections (JEC) has been developed and is applied to the measured jet energy depositions in order to correct detected jets on average to an observable definition that is independent of the response of the CMS.

There are several levels of factorized corrections which are implemented in CMS as shown in Figure 4.8. Each of them has a different effect. The first three levels of corrections are required for any physics analysis, while the last four are

optional corrections. In Figure 4.8 required correction levels are shown with red color and optional correction levels are with orange.

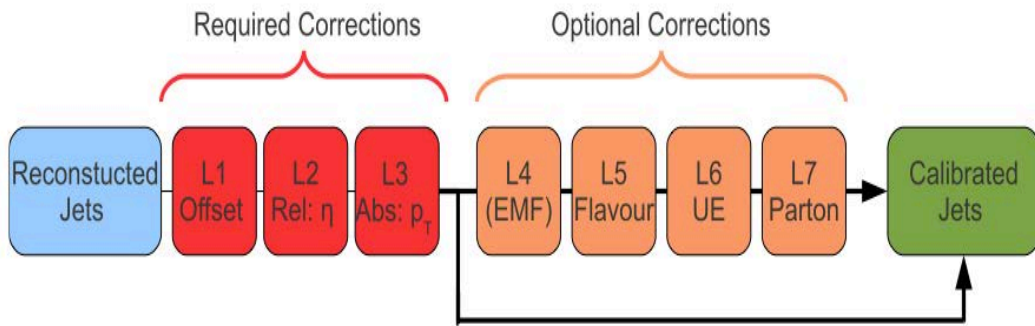


Figure 4.8. Factorized Jet Energy Corrections in CMS (Kirschenmann, 2010).

If only required jet corrections are included, a relation of the CaloJet energy and the uncorrected CaloJet energy is expressed mathematically as (Zielinski et al., 2010):

$$E_{Corrected} = (E_{Uncorrected} - E_{offset}) \times C_{Rel}(\eta, p_T'') \times C_{Abs}(p_T') \quad (4.14)$$

- where p_T'' is the transverse momentum of the jet corrected for offset,
- $p_T' = p_T'' \times C_{Rel}(\eta, p_T')$ is the transverse momentum of the jet corrected for offset and pseudorapidity dependence,
- C_{Rel} is the relative correction obtained by removing variations in the jet response relative to the central region,
- C_{Abs} is the absolute correction for variations in jet response versus p_T .

Equation 4.14 which includes the offset, relative and absolute corrections can be extended further by multiplying the right hand side with optional (EMF, Flavour, UE and Parton) correction factors.

4.4.1. Required Jet Energy Corrections

Level 1 (L1) (Pileup) Offset Correction: The offset correction is the first step in the chain of the corrections. The goal of the L1 correction is to remove the energy not associated with the high p_T collision which is undesirable energy coming from electronic noise in the calorimeter electronics, extra pp interactions within the same bunch crossing (“in-time pile-up”), additional energy integrated by the calorimeter read-out electronics from bunch crossings before and after the trigger event (“out-of-time pile-up”). This extra energy can be subtracted from the output and includes contributions by applying offset correction (Zielinski et al., 2010).

Level 2 (L2) (η dependence) Relative Jet Correction: This correction should be done after the offset correction. The aim of the L2 relative correction is to make the jet response flat as a function of η . The response of each position in η is related to the detector response averaged over $|\eta| < 1.3$. L2 correction is achieved by correcting a jet with the MC truth and a data driven dijet balancing method. The dijet balance method measures the energy response of a reconstructed jet at arbitrary pseudorapidity, relative to a control region. The control region is chosen to be the barrel ($|\eta| < 1.3$) because it is a uniform detector (Kousouris et al., 2010).

Level 3 (L3) (p_T dependence) Absolute Jet Correction: The goal of the L3 absolute correction is to make the jet response flat as a function of p_T . The parameters are obtained from MC simulations and are always applied on L2 corrected jets. The absolute scale only has to be fixed precisely in an arbitrary pseudorapidity region since the response is uniform in η after the relative correction.

4.4.2. Optional Jet Energy Corrections

Level 4 (L4) Electromagnetic Fraction Correction: The response of the detector as a function of the fraction of the jet energy deposited in the electromagnetic calorimeter (EMF) is described by L4 correction. Its aim is to improve the jet energy resolution by correcting dependence on the jet electromagnetic fraction (EMF) of the jet energy response.

Level 5 (L5) Jet Flavor Dependence Correction: Since the particle content for the various jet flavours is different, specific correction is needed to correct with respect to the flavour of the jet. L5 jet energy correction addresses the dependence of response on the jet flavor.

Level 6 (L6) Underlying Event Correction: The underlying event is dependent on the hard scattering in the proton collision therefore the energy contribution of the underlying event to the total energy of the jets in the event will be different for various physics processes. L6 correction aim is to remove underlying event energy from the jet due to soft interactions involving spectator partons. L6 correction is often part of the correction to the parton level.

Level 7 (L7) Parton Correction: The final jet energy correction aim is to correct the jet energy to the original parton energy in order to correct for the energy loss due to radiation. L7 correction translates back to the parton level, making the CaloJet (JPT or Particle Flow Jet) p_T equal to the average of the original parton p_T .

4.5. Jet Reconstruction and Performance in HF

General information on the jet reconstruction algorithms was given in the section 4.3. Jet reconstruction is a two-stage procedure. In the first stage, an input collection is processed as a set of Lorentz vectors. Every Lorentz vector fulfilling energy and/or p_T requirements is used by the jet-clustering algorithm. In the second stage, after jet clustering is finished, the jet type information is extracted from objects contributing to the jet and the corresponding values are related to the jet. In this part we will discuss MC jet studies, jet energy response (JER) and the jet reconstruction resolution in both energy and position. The goal of the analysis is to commission jet reconstruction at forward rapidities and to check the sensitivity for the future studies of low- x parton distributions. Jets are reconstructed with the anti- k_T ($R = 0.5$) algorithm in the HF calorimeter in the range $3.2 < |\eta| < 4.7$ and in the transverse momentum range $p_T \approx 20 - 120$ GeV/c.

4.5.1. Performance of the Forward Jet Reconstruction in Monte Carlo

In order to evaluate performance of the jet reconstruction algorithms, the created CaloJets are compared to the GenJets, which are independent of the response of the CMS detector. Applying the same jet reconstruction algorithm to the stable particles that are coming out of the hadronisation process makes GenJets. Since GenJets can only be accessed from the simulated information, they can not be observable jets. Equivalently, in the actual detected event are CaloJets which are in fact similar to GenJets right after they reached the detector. For MC studies the official Spring10 MC samples were used. They were reconstructed with CMSSW_3_5_6 software. The MC samples were;

- QCD Pt15/Spring10-START3X V26A 356ReReco-v1/GEN-SIM-RECO
- QCD Pt30/Spring10-START3X V26A 356ReReco-v1/GEN-SIM-RECO

The detailed MC simulation of the CMS detector response is based on GEANT4 (Agostinelli et al., 2003). Simulated events were processed and reconstructed in a similar way as collision data.

4.5.2. Jet Energy Response

JER describes how well a jet clustering algorithm works. For all passing GenJets the Corrected Jet Response is measured as below:

$$\text{Corrected Jet Response} = \frac{\text{CorrCaloJet } p_T}{\text{GenJet } p_T} \quad (4.15)$$

here, *CorrCaloJet* p_T is the transverse momentum of the reconstructed calorimeter jet and *GenJet* p_T is the transverse momentum of the jet reconstructed from all the generated stable particles. *CorrCaloJet* is produced from L1 (pedestal), L2 (η balancing) and L3 (p_T balancing) jet corrections, which correct the CaloJet to have the same p_T as the GenJet on average. In this study JER is plotted in bins of *GenJet* p_T listed in Table 4.2.

Table 4.2. Bin edges of *GenJet* p_T in GeV/c used for the studies of the jet response.

20	27	35	45	57	72	90	120
----	----	----	----	----	----	----	-----

All GenJets in the forward pseudorapidity range of $3.2 < |\eta_{\text{GenJet}}| < 4.7$ are selected and were matched with CaloJets in the (η, ϕ) space with $\Delta R=0.2$. The ΔR variable is defined as:

$$\Delta R = \sqrt{\Delta\phi^2 + \Delta\eta^2} \quad (4.16)$$

here $\Delta\eta$ and $\Delta\phi$ denote respectively the jet pseudorapidity and azimuthal angle separations. The ΔR distributions for two bins in p_T are given in Figure 4.9 and Figure 4.10. If the closest CaloJet is not within $\Delta R = 0.2$ the GenJet is discarded.

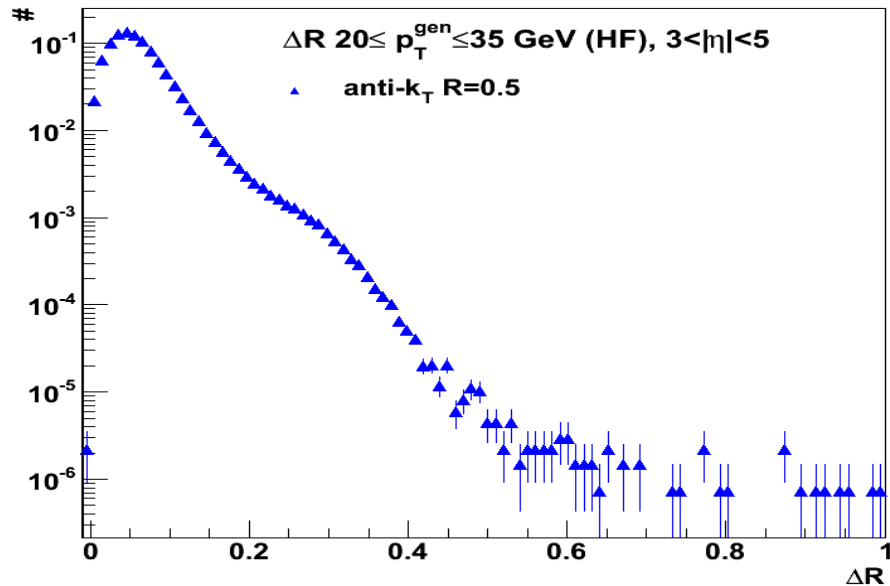


Figure 4.9. ΔR distributions for the jet p_T bin 20-35 GeV/c for the anti- k_T ($R = 0.5$) algorithm.

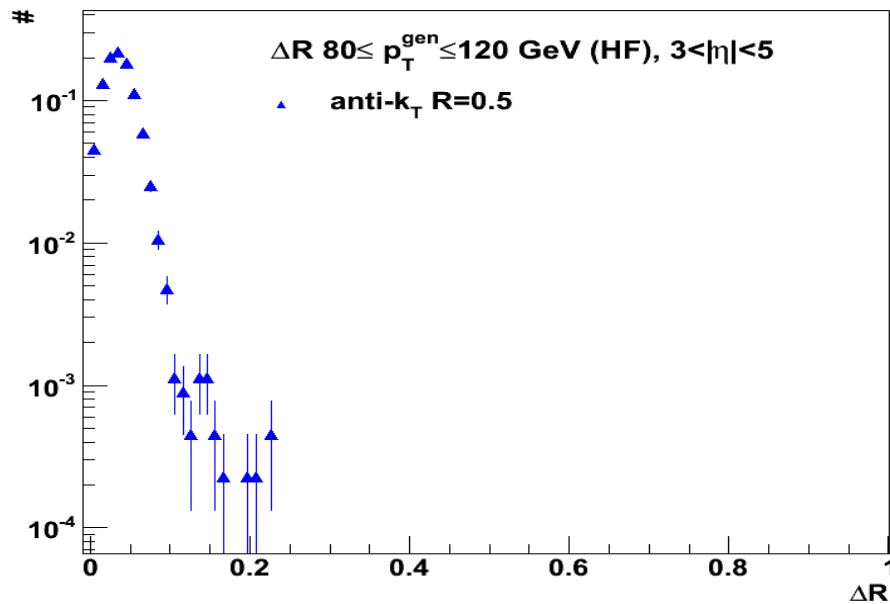


Figure 4.10. ΔR distributions for the jet p_T bin 80-120 GeV/c for the anti- k_T ($R = 0.5$) algorithm.

Corrected jet response histograms fitted with a Gaussian function in the interval $\pm 1.5 \sigma$ centered around the mean for the anti- k_T ($R = 0.5$) algorithm are shown in Figure 4.11. Each histogram corresponds to a different range in p_T^{GenJet} . The corrected jet response peaks near 1, showing a good performance of the applied corrections.

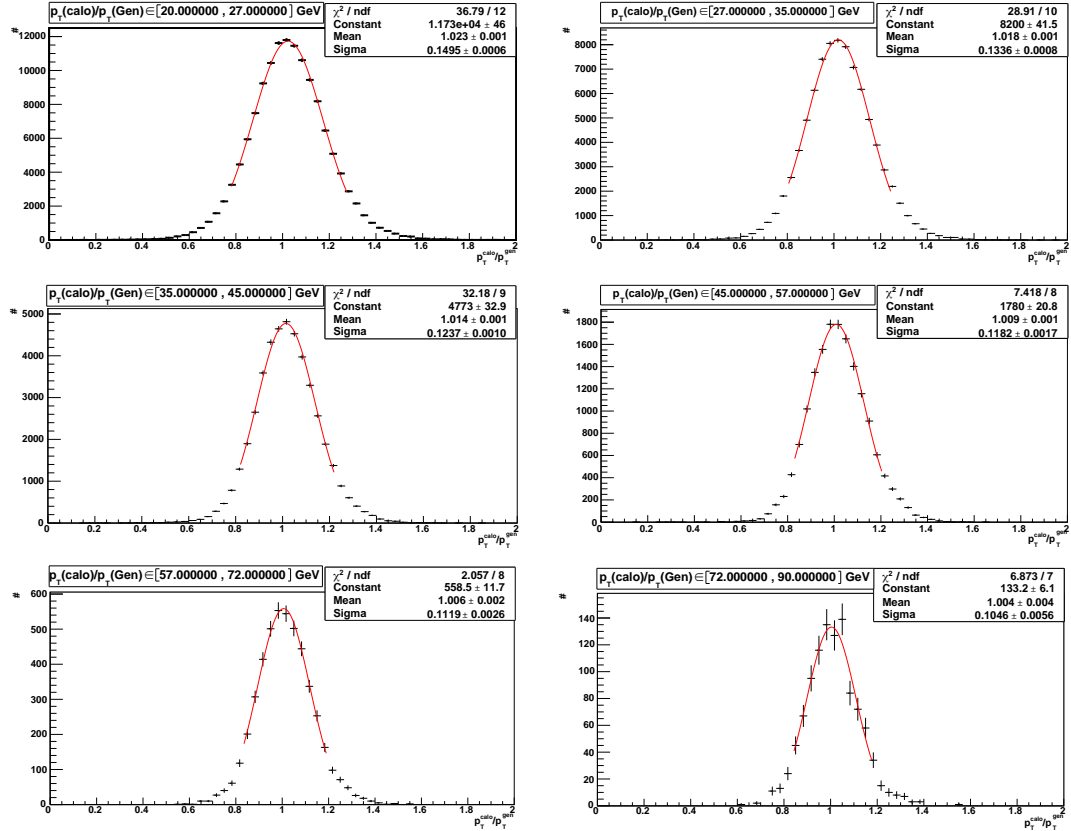


Figure 4.11. Corrected jet response distributions for different p_T bins and for anti- k_T ($R = 0.5$) algorithm.

The corrected jet response as a function of GenJet p_T and η are given in Figure 4.12 and Figure 4.13. The response curves for forward jets are flat within a few percent of the preferred value of 1 in the range $p_T^{GenJet} = 20\text{--}120 \text{ GeV}/c$.

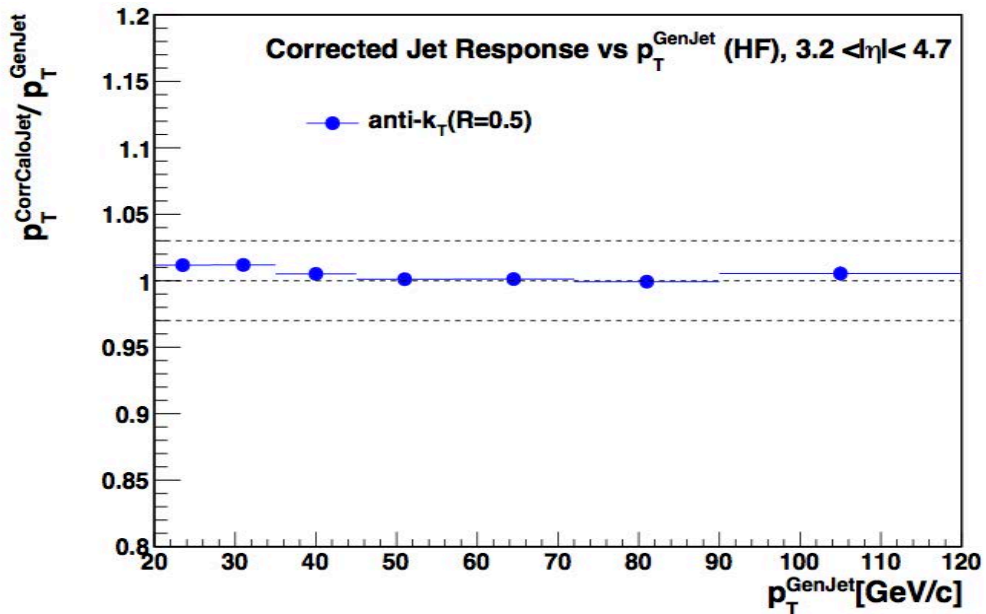


Figure 4.12. Corrected jet response as a function of p_T^{GenJet} for the anti- k_T ($R = 0.5$) algorithm.

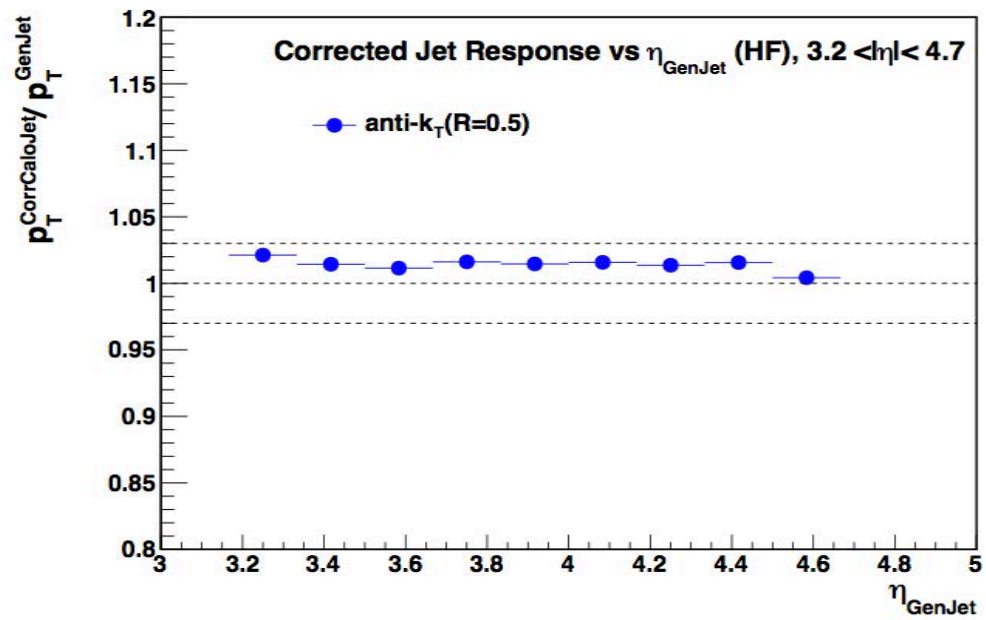


Figure 4.13. Corrected jet response as a function of η_{GenJet} for the anti- k_T ($R = 0.5$) algorithm.

In Figure 4.12 and Figure 4.13 the dashed lines indicate the desired response of 1 as well as $\pm 3\%$ deviations.

4.5.3. Jet Energy Resolution

Jet energy resolution (Brona, Cerci et al., 2010) is the uncertainty on the measured jet energy after applying the required corrections. The σ parameters of the Gaussian fits were extracted from Figure 4.11 and used as data points to identify the jet energy resolution curve as a function of p_T^{GenJet} as shown in Figure 4.14. The resolution curve was then fitted with the below function;

$$f_{(p_T)} = \sqrt{\left(\frac{a}{p_T^{GenJet}}\right)^2 + \left(\frac{b}{\sqrt{p_T^{GenJet}}}\right)^2 + c^2} \quad (4.17)$$

Here a, b, c values are fit parameters and these parameters are quoted in the legend of Figure 4.14. In this figure red line represents fit function of resolution curve.

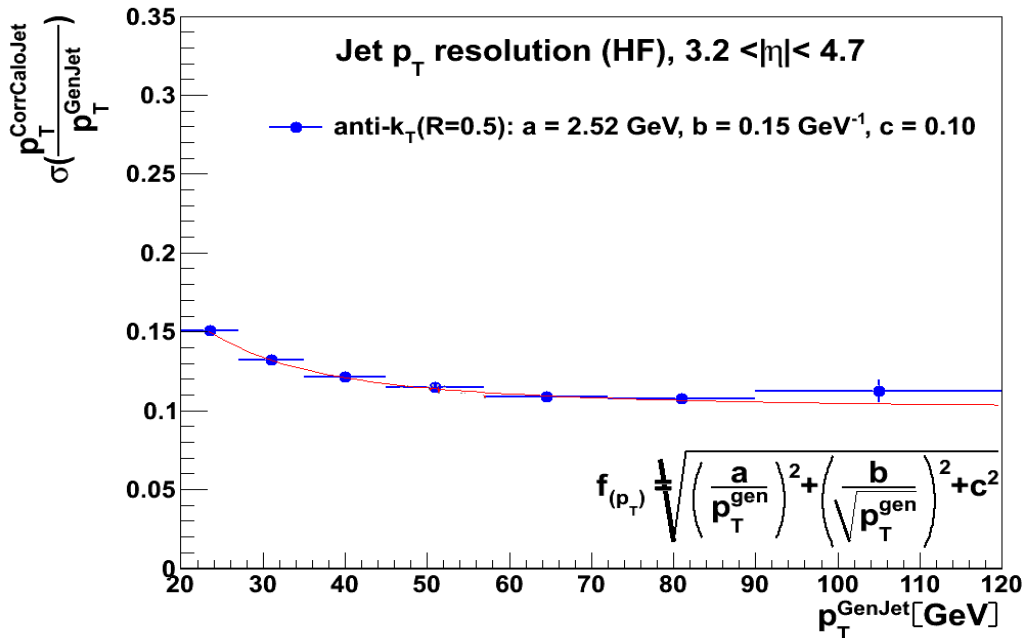


Figure 4.14. Energy resolution as a function of p_T^{GenJet} for the anti- k_T ($R = 0.5$) algorithm for jets reconstructed in $3.2 < |\eta| < 4.7$.

Figure 4.14 shows that the p_T resolution for forward jets reconstructed with the anti- k_T algorithm is $\sim 15\%$ at $p_T = 20$ GeV and decreases to $\sim 12\%$ for $p_T \gtrsim 100$ GeV.

4.5.4. Jet Position Resolution

The jet position resolutions in azimuth (ϕ) and pseudorapidity (η) are measured in HF calorimeter and determined from the distributions of the following variables for the matched jets.

$$\Delta\phi = \phi_{\text{CaloJet}} - \phi_{\text{GenJet}} \quad (4.18)$$

$$\Delta\eta = |\eta_{\text{CaloJet}}| - |\eta_{\text{GenJet}}| \quad (4.19)$$

The distributions of these variables for different p_T bins are presented in Figures 4.15 and 4.17. The distributions fitted with Gaussian functions are used to calculate the resolutions in ϕ and η as functions of p_T^{GenJet} given in Figures 4.16 and 4.18. The position (η, ϕ) resolutions for jets in HF are very good, the measured values are $\sigma_{\phi,\eta} = 0.035$ at $p_T = 20$ GeV and $\sigma_{\phi,\eta} \sim 0.02$ above 100 GeV.

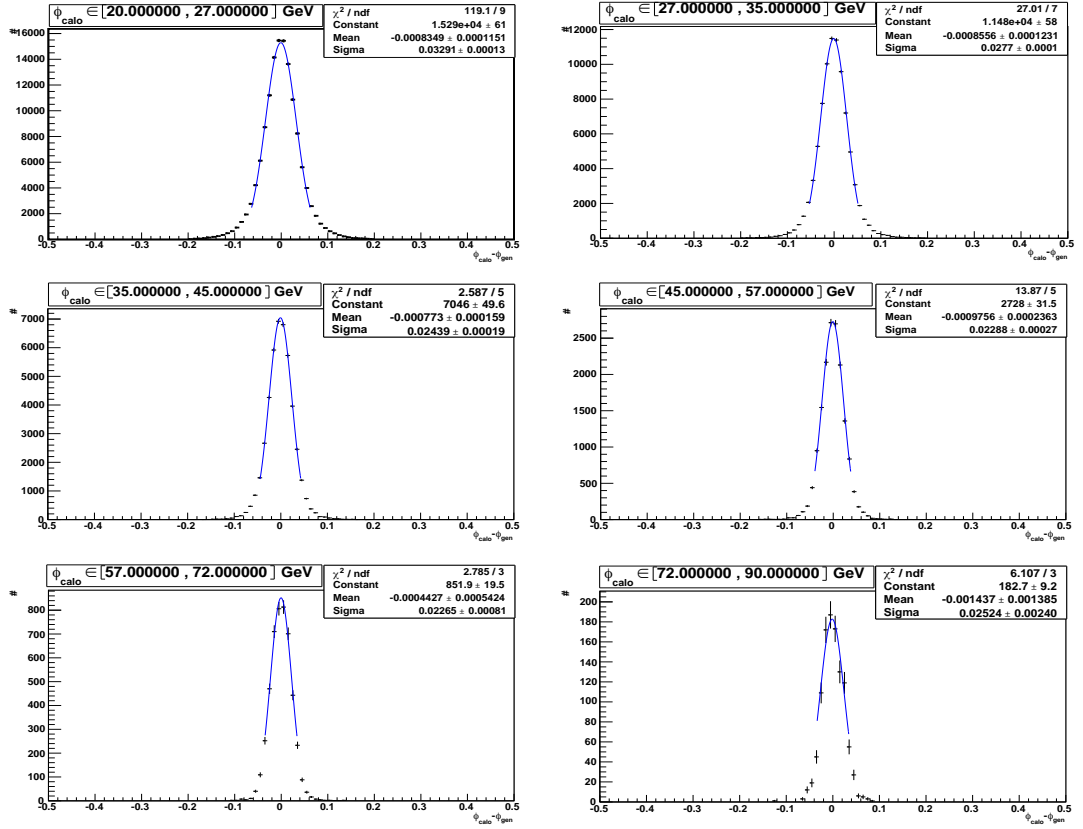


Figure 4.15. The $(\phi_{\text{CaloJet}} - \phi_{\text{GenJet}})$ distributions with Gaussian fits. Each histogram corresponds to a different range in p_T^{GenJet} .

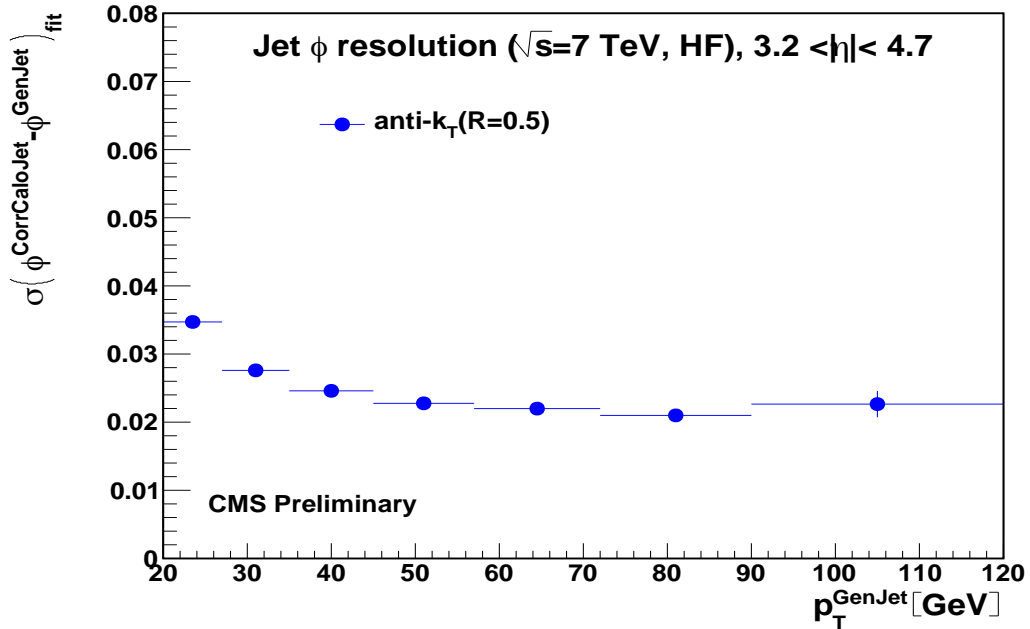


Figure 4.16. HF jet ϕ resolutions as a function of p_T^{GenJet} for the anti- k_T ($R = 0.5$) algorithm.

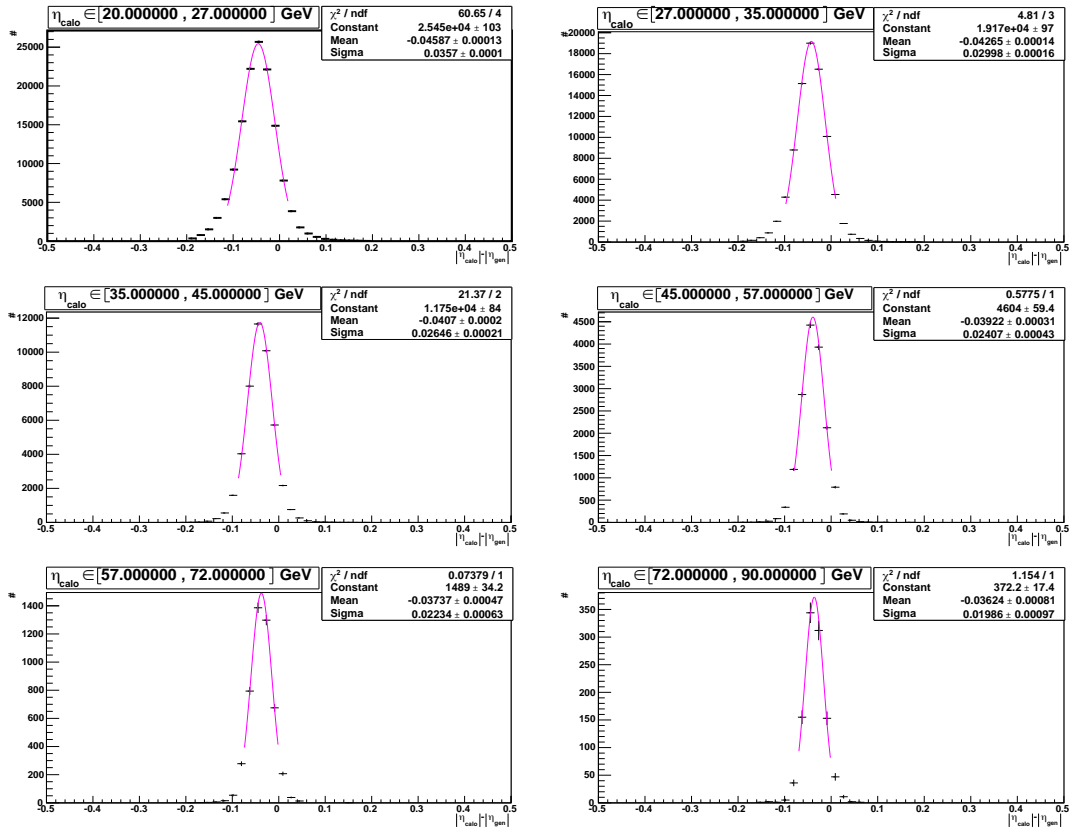


Figure 4.17. The $(|\eta_{\text{CaloJet}}| - |\eta_{\text{GenJet}}|)$ distributions with Gaussian fits. Each histogram corresponds to different range in p_T^{GenJet} .

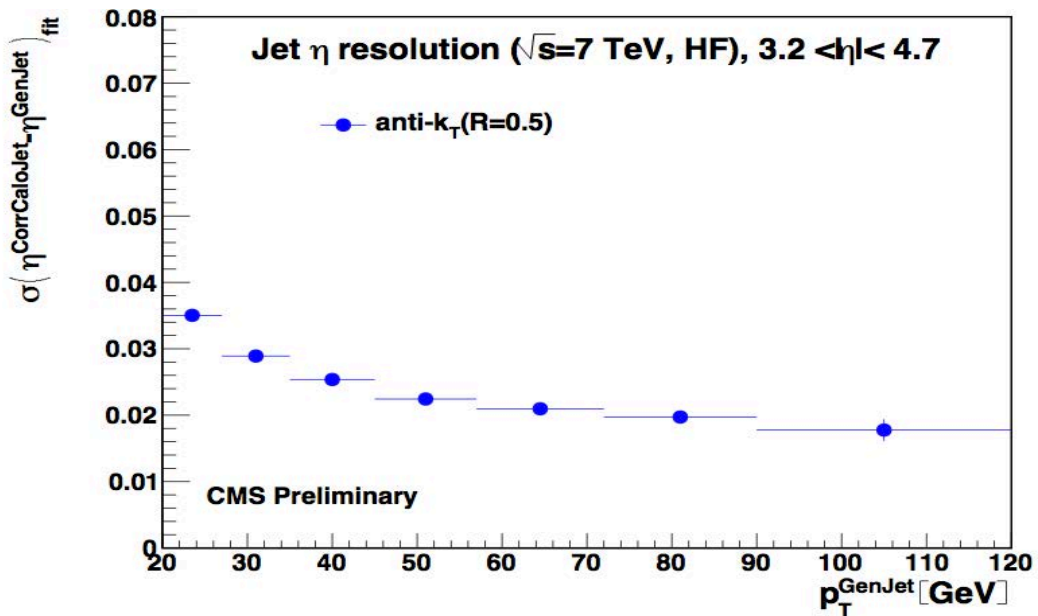


Figure 4.18. HF jet η resolutions as a function of p_T^{GenJet} for the anti- k_T ($R = 0.5$) algorithm.

5. INCLUSIVE FORWARD JET CROSS SECTION MEASUREMENT in PROTON-PROTON COLLISIONS at $\sqrt{s} = 7$ TeV

This chapter discusses measurements of the cross section of inclusive forward jets in pp collision, applied unfolding procedure that was used to translate reconstructed spectra into true spectra and finally, systematical uncertainties related to the measurements and theoretical uncertainties.

5.1. Forward Jet Production

First forward jet measurements were performed in pp collisions at $\sqrt{s} = 7$ TeV in CMS. The CMS experiment has detection capacity at forward rapidities ($|\eta| > 3$) which allows it to reconstruct jets in a kinematic range of interest for various Higgs and QCD physics studies in pp collisions at TeV energies.

Forward jet production gives important information on the underlying parton structure and its dynamical evolution in the proton. Especially, it provides valuable information on the gluon density $xG(x, Q^2)$ in a regime of low momentum fraction (d'Enterria, 2009) ;

$$x = p_{parton}/p_{hadron} < 10^{-2} \quad (5.1)$$

where p_{parton} is the momentum of parton and p_{hadron} is the momentum of hadron. In CMS calorimeter, jets in HF are sensitive to $x = 0.0004$. From leading-order (LO) kinematics, rapidities (y_1 and y_2) and momentum fractions of two colliding partons (x_1 and x_2) are related via:

$$x_1 = (p_T/\sqrt{s}) \cdot (e^{y_1} + e^{y_2}), \quad x_2 = (p_T/\sqrt{s}) \cdot (e^{-y_1} + e^{-y_2}) \quad (5.2)$$

In pp collisions, the minimum parton momentum fractions as probed in each proton in a $2 \rightarrow 2$ process with a jet of momentum p_T produced at pseudorapidity η are:

$$x_1^{\min} = \frac{x_2 x_T e^\eta}{2x_2 - x_T e^{-\eta}} \text{ and } x_2^{\min} = \frac{x_T e^{-\eta}}{2 - x_T e^\eta} \quad (5.3)$$

where $x_T = 2p_T/\sqrt{s}$ and x_2^{\min} decreases by a factor of ~ 10 every 2 units of rapidity. The extra e^η lever arm motivates the interest of forward jet production measurements to study the PDFs at small values of x from Equation (5.3) (Cerci et al., 2009). Figure 5.1 shows the $\log(x_{1,2})$ distribution for parton-parton scattering in pp collision at $\sqrt{s} = 7$ TeV in the HF acceptance.

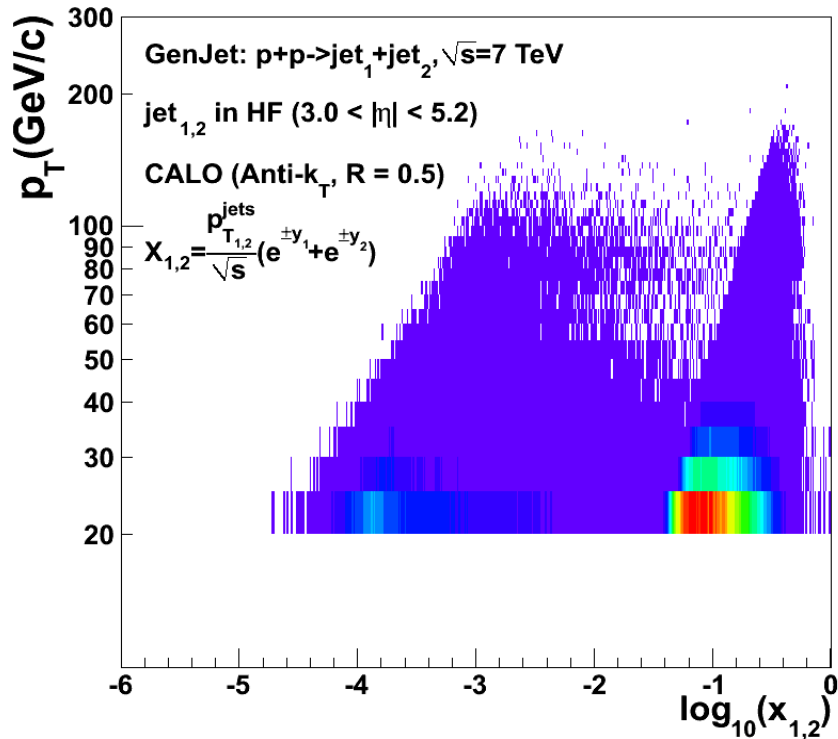


Figure 5.1. $\log(x_{1,2})$ distribution of two partons producing at least one jet above $p_T = 20$ GeV/c at forward rapidities in pp collision (Cerci et al., 2009).

The hadronic final state in charged current DIS can be characterized in terms of the production rate of jets, that is jet cross sections. The simplest cross section is the inclusive jet cross section. “Inclusive” means that all jets passing the relevant kinematic cuts are counted. Figure 5.2 shows the diagram for inclusive forward jet production. If more than one jet is present, the one with highest p_T is considered, as shown in Figure 5.2.

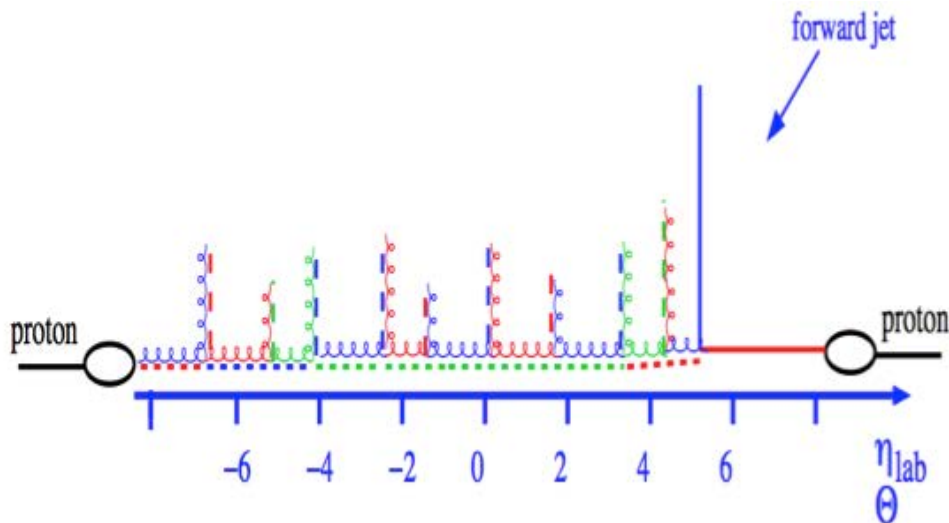


Figure 5.2. Feynman diagram for inclusive forward jet production (Cipriano, 2014).

Measurement of inclusive jet production is performed at the LHC over a kinematic range in transverse momentum and rapidity much larger than in any previous collider experiment (Rabbertz, 2012). Basic comparisons with SM theoretical predictions are based either on NLO QCD calculations, or on NLO matched parton shower event generators. NLO calculations are supplemented with nonperturbative (NP) corrections predicted from MC event generators (Hautmann, 2013).

5.2. Data and Monte Carlo Samples

The data set used in the analysis was reconstructed with CMSSW 3_8_X version. The kinematic range of this measurement is shown as a function of the jet p_T . MC samples from PYTHIA 6 (version 6.422), PYTHIA 8 (version 8.135), HERWIG 6 (version 6.510.3) + JIMMY and HERWIG++ (version 2.3) are reconstructed with CMSSW 3_7_X version. In this analysis the reconstructed data was prepared as ROOT ntuples using calorimeter cleaning and basic data quality cuts. The CMS standard relative (L2) and absolute (L3) corrections for η and p_T variation of the jets were applied using the official tag. A residual correction was also applied to account for differences between data and MC. Finally events that were affected by the HF PMT hits were removed. The good runs were selected based on official CMS JSON files. The data and MC samples used in the analysis were following.

Data Samples :

- JetMETTau / Run2010A-Nov4ReReco-v1 /RECO
- JetMET/Run2010A-Nov4ReReco-v1/RECO
- MinBias/Commissioning10-SD-JetMETTauMonitor-Jun9thSkim-v1/RECO
- JetMETTauMonitor/Run2010A-Jun9thReReco-v1/RECO

MC Samples:

- QCD-Pt-XtoY-TuneD6T-7TeV-pythia6/Summer10-START37-V6-v1/GEN-SIM-RECO
- QCD-Pt-XtoY-CTEQ6L1-7TeV-herwig6/Summer10-START37-V6-v2/GEN-SIM-RECO
- QCD-Pt-XtoY-7TeV-pythia8/Summer10-START36-V10-S09-v1/GEN-SIM-RECO

5.3. Event Selection and Analysis Cuts

For inclusive forward jet analysis (Cerci, Sunar Cerci et al., 2010), (Chatrchyan et al., 2010a) the HLTJet15U (uncorrected jet $p_T > 15$ GeV) trigger was used. All triggered events were required to have a good primary vertex (PV) and the PV is reconstructed from at least five tracks that lie within $|z_{\text{PV}}| < 24$ cm of the center of the detector. In order to filter away the beam scraping events, we require the fraction of high-purity tracks with respect to the total number of tracks to be at least 25% for events with more than 10 tracks. Jets were reconstructed using the anti- k_T algorithm with cone size 0.5 ($\Delta R = \sqrt{\Delta\phi^2 + \Delta\eta^2}$).

In data, large calorimetric signals arising from noise, beam halo energy deposits, or cosmic ray showers can be observed from the hard scattering of the beam protons. All these sources of noise and non-collision data can generate large amounts of transverse energy E_T . In order to remove all these unwanted effects some analysis cuts were applied for this study and are described in sections 5.3.1 and 5.3.2.

5.3.1. HF Noise Cut

A charged particle can produce fake signals when it travels over the window of PMT of the HF detector. Such particles are beam halo muons or late showering hadrons. The property of the PMT hit events is such that they are localised to a single PMT, i.e. only one of the channels in one readout tower register large signals. Events with exceptional noise due to charged particles directly hitting the window of the HF PMTs are flagged with different algorithms and removed from the inclusive jet analysis.

5.3.2. Jet Quality Criteria Cut

The Jet Quality Criteria (JetID) (Harel, 2009 and 2010) cuts were used to remove unphysical energy deposits in the HF calorimeter originating from the

detector such as calorimeter noise, hot cells and defects of the detector electronics or beam background noise: beam-pipe and beam-gas collisions.

The HF detector is divided into two regions: HFa ($3.8 > |\eta| \geq 3.0$) and HFb ($|\eta| \geq 3.8$) and the following jet quality criteria (loose) cuts are applied:

- $n^{hit} > 1 + 2.4(\ln p_T^{raw} - 1)$ in HFa,
- $n^{hit} > 1 + 3(\ln p_T^{raw} - 1)$ in HFb,
- $0.6 + 0.05(\max(0, 9 - \ln E^{raw}))^{1.5} > \alpha_{LS} > -0.2 - 0.041(\max(0, 7.5 - \ln E^{raw}))^{2.2}$.

The Jet ID cuts are based purely on the jet properties: $p_T^{CaloJet}$, $E^{CaloJet}$ and number of RecHits events clustered into jet n^{hit} and α_{LS} (a fraction of electromagnetic component of the total jet energy).

5.4. Inclusive Forward Jet Cross Section Measurement

The single jet cross section can be defined in several ways. Theoretically inclusive forward jet cross section calculations are described in the sense of the invariant cross section $E \frac{d^3\sigma}{d^3p}$. Experimentally, the measured variables are the transverse energy p_T , pseudorapidity η and azimuth angle ϕ . From the point of these variables, the triple-differential cross section is expressed as $\frac{d^3\sigma}{dp_T d\eta d\phi}$ where the two are related by:

$$E \frac{d^3\sigma}{d^3p} = \frac{d^3\sigma}{d^2p_T dy} \rightarrow \frac{1}{2\pi p_T} \frac{d^2\sigma}{dp_T d\eta} \quad (5.4)$$

where y is the rapidity of the jet and $1/2\pi$ is ϕ . In this analysis the differential inclusive jet cross section is measured simply using the number of jets N observed in

a given η and p_T interval normalized by the total luminosity L defined by the basic formula 5.5:

$$\frac{d^2\sigma}{dp_T d\eta} = \frac{C_{corr}}{L \cdot \varepsilon_t} \cdot \frac{N_{evts}}{\Delta p_T \cdot \Delta\eta} [\text{pb}/(\text{GeV}/c)]. \quad (5.5)$$

where:

- N_{evts} is the number of jets counted in a bin,
- L is the integrated luminosity,
- ε_t reflects the efficiency of the jet trigger,
- C_{corr} is the resolution unsmeared or MC correction factor,
- Δp_T and $\Delta\eta$ are the p_T and rapidity bin sizes, respectively.

The starting value of binning has been chosen to be 35 GeV because of the trigger limitations.

Table 5.1. Resolution based binning in jet transverse momentum p_T , (GeV/c).

35	45	57	72	90	120	150
-----------	-----------	-----------	-----------	-----------	------------	------------

5.5. Jet Trigger and Trigger Efficiency

The jet trigger uses the electromagnetic and hadronic transverse energy sums computed in calorimeter regions (4×4 trigger towers), except for the HF region where it is the trigger tower itself. The jets are characterized by the transverse energy E_T in 3×3 calorimeter regions. This region's sliding window technique spans the complete (η, ϕ) coverage of the CMS calorimeter as shown in Figure 5.3. The summation spans 12×12 trigger towers in barrel and endcap or 3×3 larger HF towers in the HF. Jets are labeled by (η, ϕ) indices of the central calorimeter region, while ϕ size of the jet window is the same everywhere. The η binning gets somewhat larger at high η because of the size of calorimeter and trigger tower segmentation (Bayatian, 2000a).

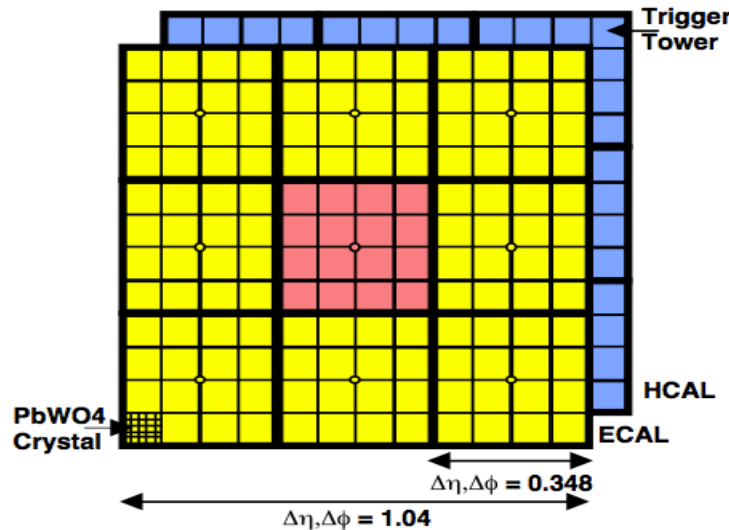


Figure 5.3. Jet Trigger Algorithm (Bayatian, 2000a).

In this analysis the highest non-prescaled trigger stream is considered for the trigger efficiency. For this reason, SD JetMETTauMonitor and JetMETTauMonitor data sets were used. In these datasets all events were recorded at 12 nb^{-1} low luminosity. On the other hand the prescale factors were also taken into account since the luminosity was increasing. The analysis was limited to the events selected by the “HLTJet15U” single jet trigger stream. The turn-on of the single jet trigger in data is specified as a ratio to the lower p_T trigger (“HLT L1Jet6U”). Table 5.2 lists features of the trigger that were included in this analysis.

Table 5.2. L1 and High Level Trigger jet descriptions.

Trigger name	L1 Seeds	Information
HLT_L1Jet6U	L1_SingleJet6U	A jet with $E_T > 6 \text{ GeV}$
HLT_Jet15U	L1_SingleJet6U	A single jet trigger, requiring ≥ 1 jet at HLT with $E_T > 15 \text{ GeV}$. The jet energy threshold is chosen based on uncorrected jets.

Figure 5.4 shows the jet p_T spectrum procured from the single-jet trigger

stream (left plot), alongside the corresponding trigger turn-on curve compared to the monitor trigger (right plot). The final spectrum will be used only from 35 GeV upwards. In this p_T cut (35 GeV) the selected trigger was 100% efficient. The trigger efficiency for jets with corrected $p_T > 35$ GeV as a function of η is shown in Figure 5.4 (bottom). It is flat, at the 100% level.

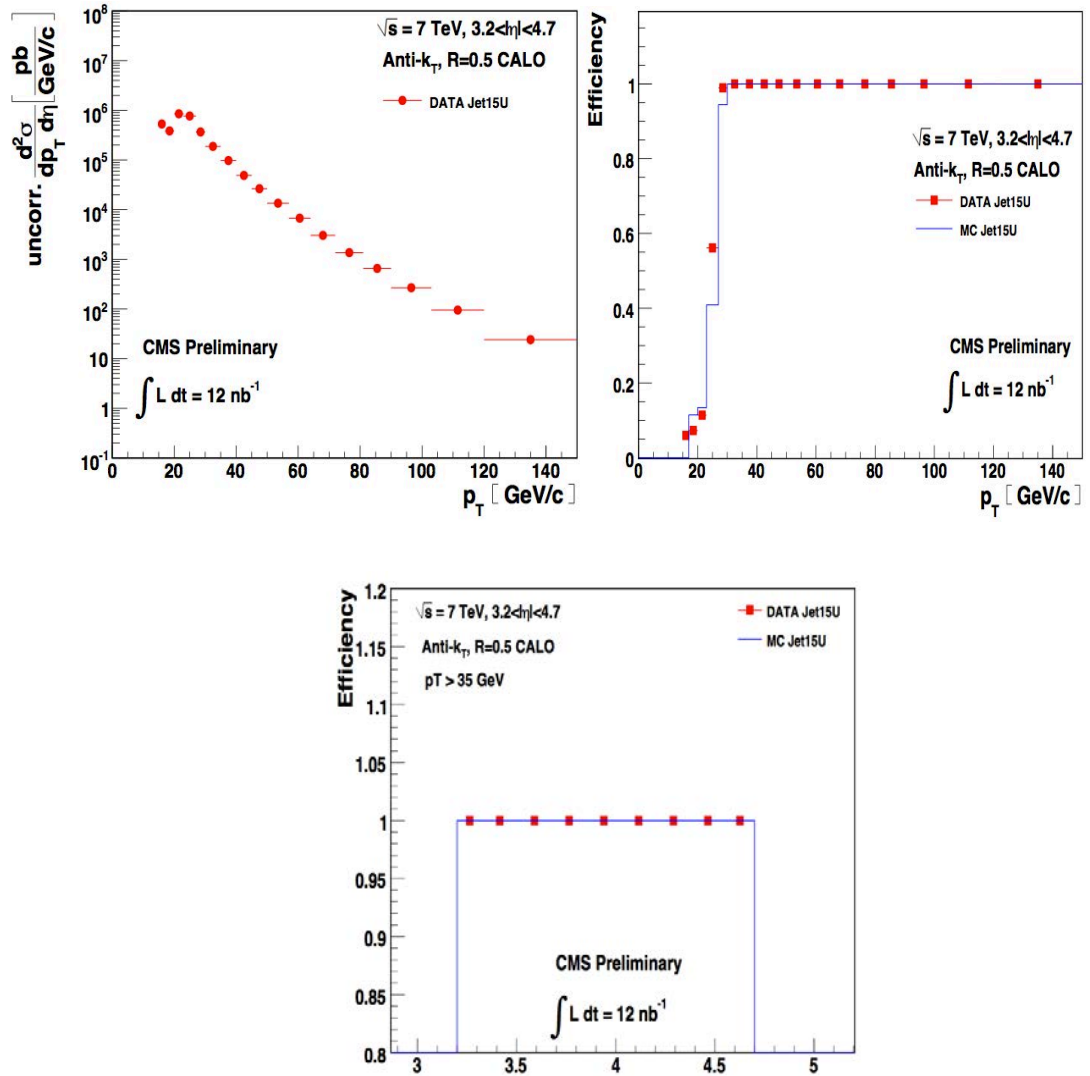


Figure 5.4. Jet p_T spectrum (before applying JEC) of the trigger stream used for forward jet analysis (left), jet trigger turn-on of the HLTJet15U stream vs. corrected jet p_T (after applying JEC) (right) and Jet trigger efficiency vs. jet η (bottom).

5.6. Luminosity Calculation

In this analysis the official luminosity measurement rules for CMS physics analysis recommended by the CMS luminosity group were applied. The luminosities for different trigger paths were directly calculated using `lumiCalc.py` script which generated JSON output file from the GRID (CRAB) root tuples. This file contained only the lumi sections (LS) that were later analyzed. Figure 5.5 shows the total (left) and effective (right) luminosity trigger and prescale factor (bottom) run by run for the HLT Jet15U trigger.

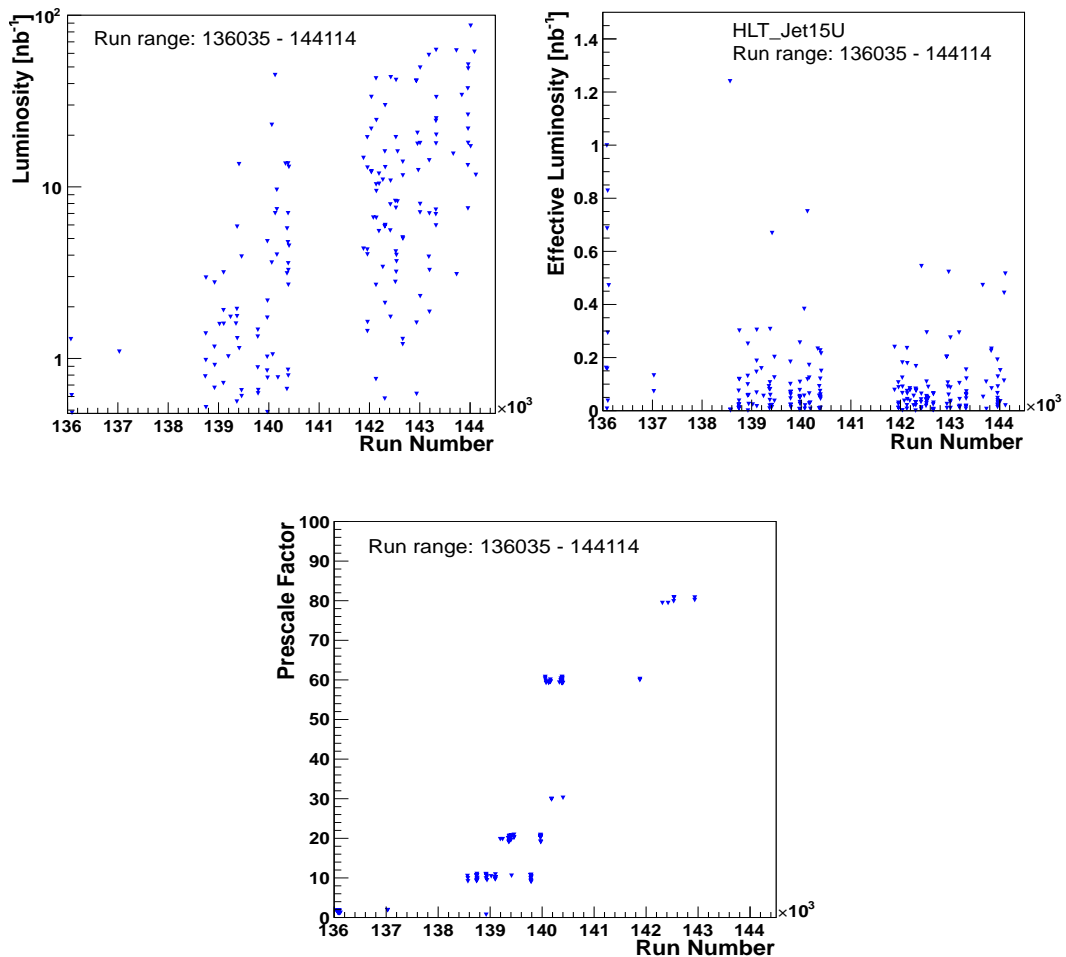


Figure 5.5. Total luminosity shown run-by-run (left), effective luminosity obtained from the trigger HLTJet15U shown by run number (right). The prescale factors of HLT Jet15U trigger is shown by run number (bottom).

5.7. Unfolding Method

Due to detection efficiency, measurement resolutions and systematic biases, the measured distribution can vary from the true distribution. Some events may never get reconstructed or migrate to neighbouring bins. To obtain precise measurements from the data, different effects of the detector need to be corrected. To correct for these effects, an unfolding procedure has been applied. There exist several alternative methods for unfolding of the measured distributions. Bin-to-Bin MC method and the Ansatz method were used in this analysis. Events from the PYTHIA 6.4 and HERWIG + JIMMY MC generators were compared before and after passing through the detector simulation, labeled generator (HAD) level and reconstructed (REC) level, respectively.

5.7.1. Bin-to-Bin Monte Carlo Method

The bin-to-bin MC method is used to perform the final results of the Inclusive Forward Jet analysis. To unfold the cross section by applying bin-by-bin correction factors, the MC sample has to be compatible with the data sample and the bin widths have to be chosen such that migrations between bins are small enough. When we look at a bin i on the detector level and the same bin i on the hadron level we should see the same results, but unfortunately because of some unwanted processes in the detector this is often not the case. For this reason a correction factor had to be found. We used two methods:

In the first method, the hadron level measurements were divided by the detector level measurements and correction factor was determined from MC samples generated by PYTHIA 6.4 and HERWIG + JIMMY MC event generators.

$$N_{all\ jets}^{data}(E_{had}^{data} \epsilon bin_i) = N_{all\ jets}^{data}(E_{det}^{data} \epsilon bin_i) \cdot C_{corr} \quad (5.6)$$

$$C_{corr} = \frac{N_{all\ jets}^{MC}(E_{had}^{MC}\epsilon bin_i)}{N_{all\ jets}^{MC}(E_{det}^{MC}\epsilon bin_i)} \quad (5.7)$$

where;

- $N_{all\ jets}^{MC}(E_{had}^{MC}\epsilon bin_i)$ is the number of jets on hadron level in bin i ,
- $N_{all\ jets}^{MC}(E_{det}^{MC}\epsilon bin_i)$ is the number of jets on detector level in bin i .

Figure 5.6 shows the reconstructed p_T spectrum for inclusive forward jets. This is compared to MC events passing through full detector simulation and analysed in the same way as the data. The data are calibrated through the JES normalisation, but not unfolded nor corrected to the stable-particle level. From the Figure 5.6 we can say that PYTHIA 6 (D6T) MC generator is more compatible with the data than the HERWIG 6.510 (+JIMMY). Only in the last bins this compatibility breaks.

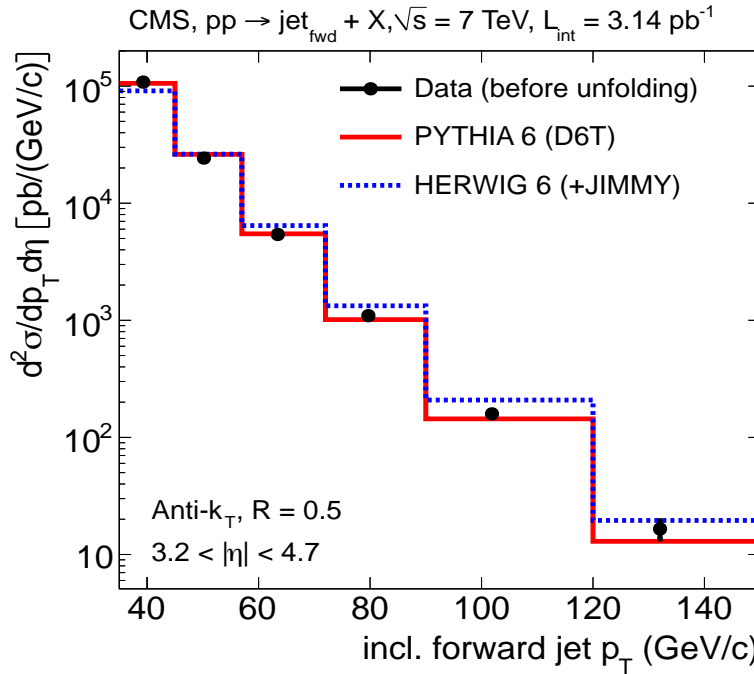


Figure 5.6. Measured differential cross sections for jets as a function of p_T before unfolding the energy resolution (black dots), compared to detector-level MC simulations generated with PYTHIA 6 and HERWIG 6.

Inclusive Forward CaloJets p_T and η cross section on detector level for DATA and MC simulations, PYTHIA 6.4 and HERWIG + JIMMY are shown in Appendix B.

In the second method the correction factor is calculated using acceptance (A), background (B), purity (P) and stability (S) terms as shown in Equation 5.8.

$$C_{corr} = \frac{(1 - B_i^{MC})}{A_i^{MC}} \cdot \frac{P_i^{MC}}{S_i^{MC}} \quad (5.8)$$

The acceptance is explained as the number of matched jets divided by number of all jets on hadron level as shown in Figure 5.7 (left).

$$\text{Acceptance } (A_i^{MC}) = \frac{N_{\text{matched jets}}^{MC} (pT_{\text{gen}}^{MC} \epsilon \text{bin}_i)}{N_{\text{all jets}}^{MC} (pT_{\text{gen}}^{MC} \epsilon \text{bin}_i)} \quad (5.9)$$

The background is defined as the number of jets on the detector level that can not be matched to a jet on the hadron level as shown in Figure 5.7 (right).

$$\text{Background } (B_i^{MC}) = 1 - \frac{N_{\text{matched jets}}^{MC} (pT_{\text{det}}^{MC} \epsilon \text{bin}_i)}{N_{\text{all jets}}^{MC} (pT_{\text{det}}^{MC} \epsilon \text{bin}_i)} \quad (5.10)$$

Since the detector has limited resolution, a jet in bin i on the hadron level can be reconstructed in another bin on the detector level. This is an undesirable situation. To measure these migrations into and out of a bin, the purity and stability are used respectively. Purity is defined by how many jets on the detector level really belong to this bin.

$$\text{Purity } (P_i^{MC}) = \frac{N_{\text{matched jets}}^{MC} (E_{\text{det}}^{MC} \epsilon \text{bin}_i \wedge E_{\text{had}}^{MC} \epsilon \text{bin}_i)}{N_{\text{matched jets}}^{MC} (E_{\text{det}}^{MC} \epsilon \text{bin}_i)} \quad (5.11)$$

Stability is defined by how many jets remain in the bin while going from the hadron to detector level.

$$\text{Stability } (S_i^{MC}) = \frac{N_{\text{matched jets}}^{MC} (E_{\text{had}}^{MC} \epsilon \text{bin}_i \wedge E_{\text{det}}^{MC} \epsilon \text{bin}_i)}{N_{\text{matched jets}}^{MC} (E_{\text{had}}^{MC} \epsilon \text{bin}_i)} \quad (5.12)$$

For CaloJets Purity was found to be 0.5 which means that 50% of the jets measured in one bin on the detector level are also in the same bin on the hadron level, 50% of the jets have migrated into that bin for CaloJets as shown in Figure 5.8 (left). And stability is found to be 0.6 for CaloJets which means that 60% of the jets in one bin on the hadron level are also found in that bin on the detector level. Figure 5.8 (right) shows the stability of jets. Acceptance, Background, Purity and Stability plots for PF jets are also shown in Appendix A.

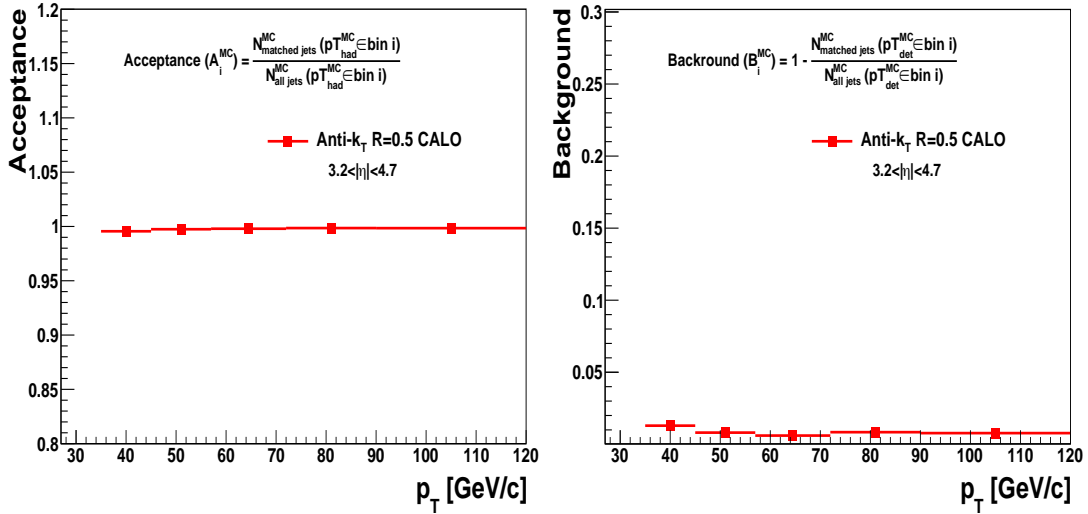


Figure 5.7. The acceptance (left) and background (right) as a function of corrected CaloJets p_T for PYTHIA 6.4

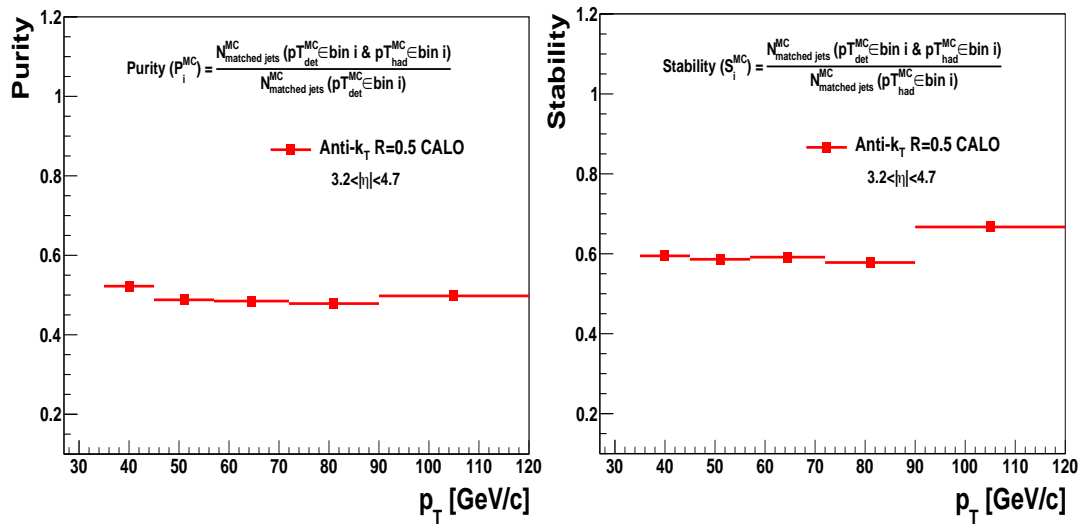


Figure 5.8. The purity (left) and stability (right) as a function of corrected CaloJets p_T for the bins in which cross section measurements are performed shown for PYTHIA 6.4.

Figure 5.9 shows the unfolding correction factor obtained for the PYTHIA 6 (D6T) and HERWIG 6.510 (+JIMMY) as event generators differ by < 5%. The hatched band in all panels represents the uncertainty of changing the jet p_T resolution by $\pm 10\%$. It is observed to cover the range of differences found for the two methods of unfolding the data.

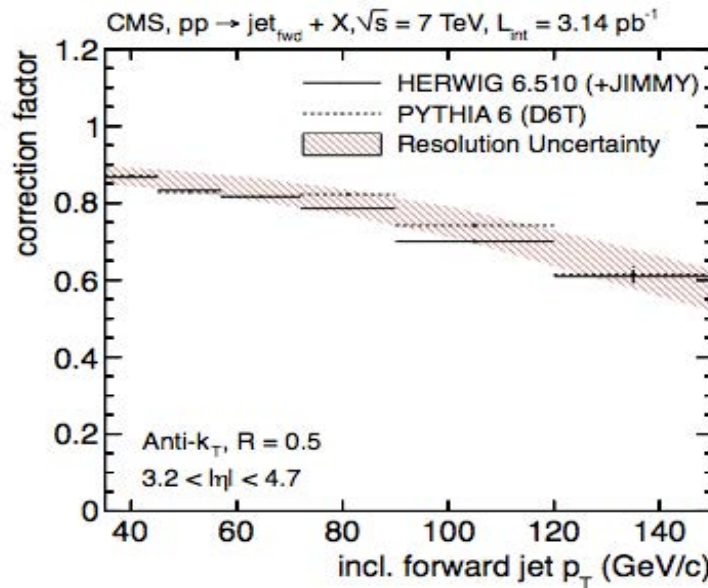


Figure 5.9. The bin-by-bin unfolding correction factors as a function of p_T for inclusive forward jets.

5.7.2. Ansatz Method

Inclusive jet cross section measurement as a function of p_T is the fold of the real particle jet spectrum convoluted with the detector finite p_T and y resolutions. While the p_T smearing effect must be corrected, the effect of the y resolution can be disregarded to the first order. The unsmeared corrections for the jet p_T spectra in these studies are derived from the Ansatz Method and are used for comparing the bin-to-bin MC method and obtaining the p_T resolution uncertainty. In this method a functional description of the unknown particle jet cross section was taken into account as expressed by Formula 5.13.

$$f(p_T) = N_0 \cdot p_T^{-\alpha} \left(1 - \frac{2 \cosh(y_{\min}) p_T}{\sqrt{s}}\right)^\beta \exp(-\gamma / p_T) \quad (5.13)$$

Here N_0 , α , β and γ are fit parameters, $p_T^{-\alpha}$ term defines the QCD matrix element and the term $\left(1 - \frac{2 \cosh(y_{\min}) p_T}{\sqrt{s}}\right)^\beta$ indicates the behavior of the parton densities at high proton momentum fractions x as well as its dependence on rapidity. The measured cross section is fitted with a smeared Ansatz function $F(p_T)$ as a fold of the particle jet spectrum with the detector resolution:

$$F(p_T) = \int_0^\infty f(p'_T) R(p'_T, p_T) dp'_T \quad (5.14)$$

$R(p'_T, p_T)$ is an area-normalized Gaussian centered at 0 and with a width equal to the jet p_T resolution. It can be formulated as:

$$R(p'_T, p_T) = \frac{1}{\sqrt{2\pi}\sigma(p'_T)} \exp\left[-\frac{(p'_T - p_T)^2}{2\sigma^2(p'_T)}\right] \quad (5.15)$$

$\sigma(p_T)$ is a parameterization of the relative σ dependence of p_T , it can be written as:

$$\frac{\sigma(p_T)}{p_T} = \sqrt{\text{sgn}(N) \cdot \left(\frac{N}{p_T} \right)^2 + S^2 \cdot p_T^{m-1} + C^2} \quad (5.16)$$

where N is a noise term while S is a stochastic term and C is a constant term. The fit for calorimeter jets is procured by limiting $N \geq 0$ and $m = 0$, see Figure 5.10.

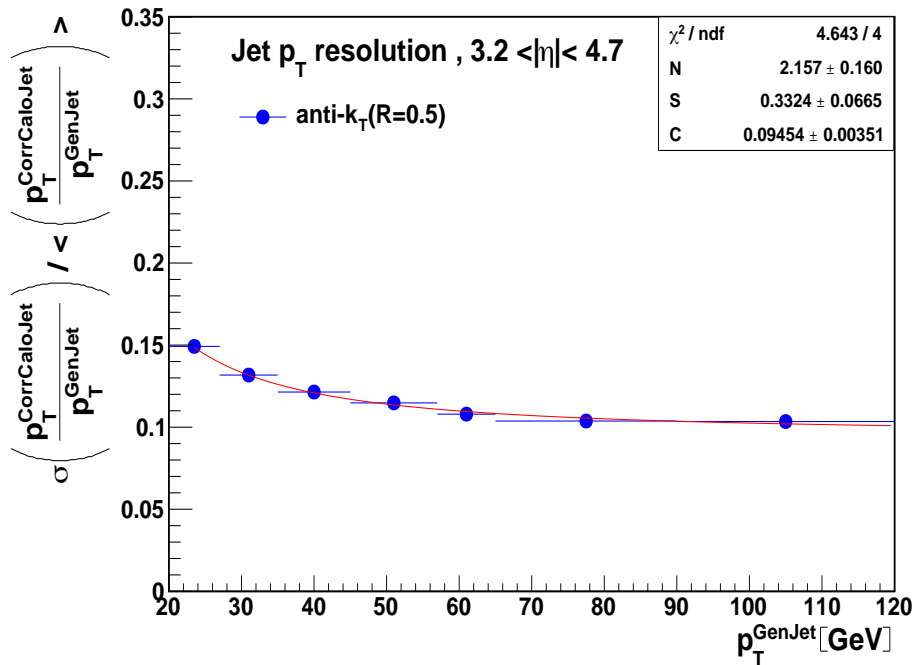


Figure 5.10. Inclusive forward CaloJets p_T resolution with CMS MC simulation PYTHIA 6.4.

Once the measured spectrum is fitted with the smeared Ansatz function, in the last step the correction factor is calculated for every bin as :

$$C_{bin} = \frac{\int_{bin} f(p_T) dp_T}{\int_{bin} F(p_T) dp_T} \quad (5.17)$$

5.7.3. Full Unfolding

When the detector level distribution is represented by a finite set of parameters y and the hadron level distribution is represented by x , we can write it as :

$$y = Rx, \quad (5.18)$$

where R is a response matrix. The response matrix R in the unfolding method is derived using simulated MC samples.

The matrix element r_{ij} is expressing the possibility to observe an entry in histogram bin i of the histogram y , if the true value is from histogram bin j of the histogram x . To perform the unfolding, matrix R has to be reversed and used only with the distribution that was measured in the experiment n :

$$\hat{x} = R^{-1}n \quad (5.19)$$

The procedure is acceptable if the statistical uncertainties on x , y and n can be ignored. If this is not the situation large fluctuations in the final unfolded spectrum may lead to random results. Statistics for response matrix is illustrated in Figure 5.11. In this figure each entry demonstrates the cross section of CaloJets and GenJets in a given p_T bin. To build the matrix, numbers involved in the dashed line box are matched pairs where the matching parameter is $\Delta R < 0.2$. The numbers outside of the dashed line box indicate the not matched CaloJets and GenJets.

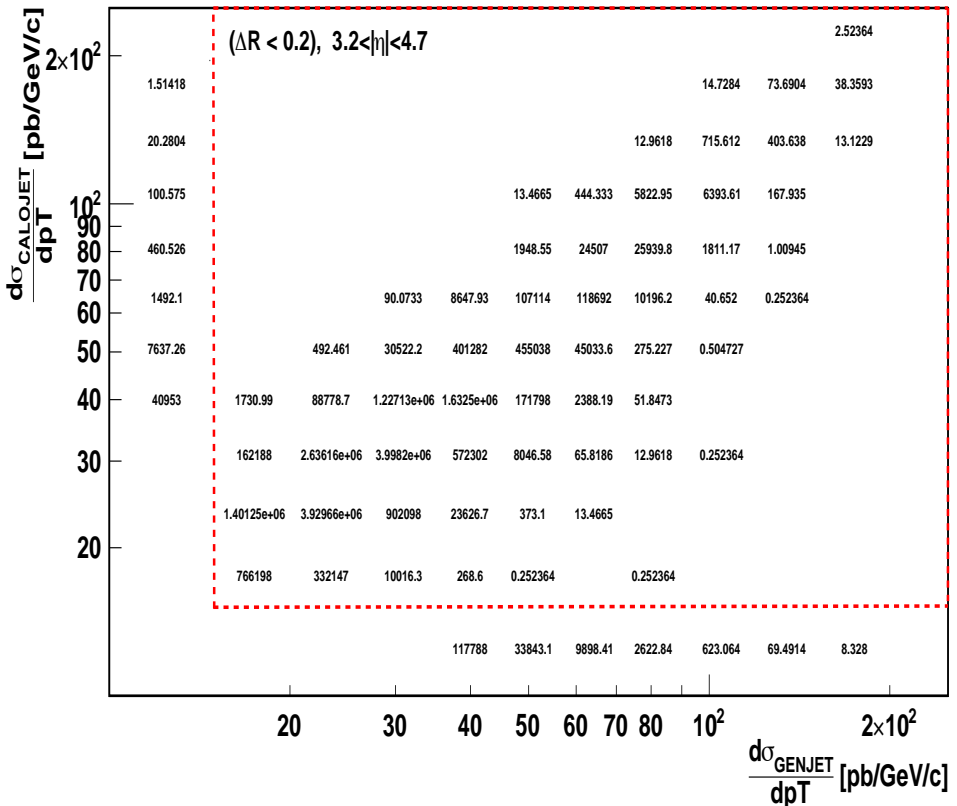


Figure 5.11. Matrix element between CaloJets and Generated jets.

The diagonal elements are large, whereas the non-diagonal elements are small and for this reason prone to statistical fluctuations. As a consequence the MC statistics with the full unfolding and response matrix inversion is not credible and therefore was not used.

5.7.4. RooUnfold Method

The RooUnfold package was designed to provide a framework for different unfolding algorithms. At present RooUnfold applies or interfaces to Iterative Bayes, Singular Value Decomposition (SVD), TUnfold, Bin-By-Bin correction factors and Unregularized Matrix Inversion methods.

The smearing matrix, as described in the Figure 5.11, has been used in RooUnfold to check the unfolding. As a control mechanism, the Bin-to-Bin method has been applied using the smearing matrix. The correction factors agree completely

with the ones procured in the previous section. To check the unfolding, PYTHIA event generator has been used and the results are presented in Figure 5.12.

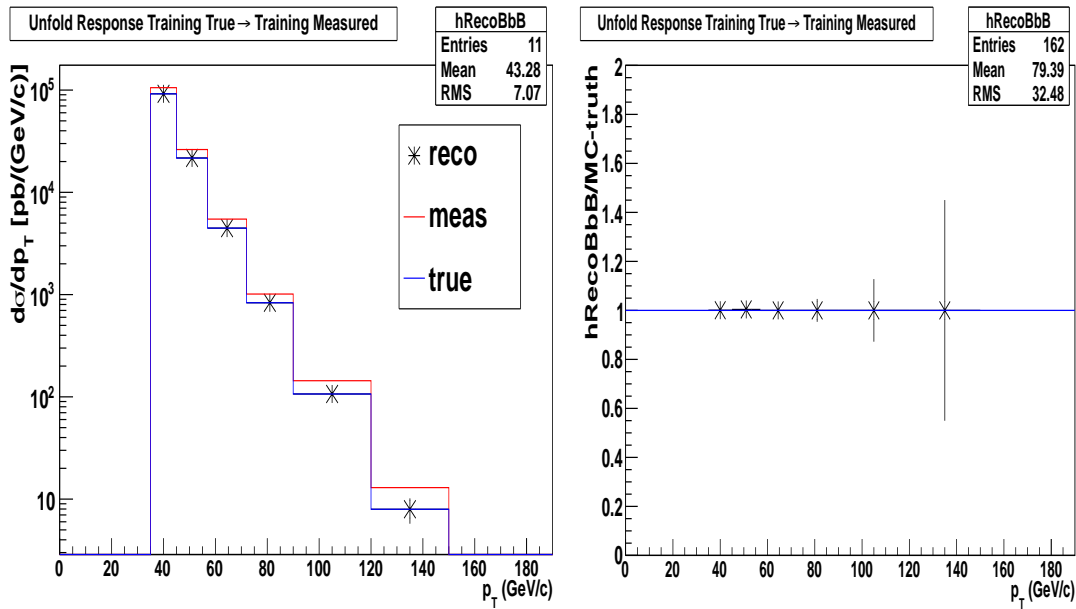


Figure 5.12. Bin-by-Bin unfolding using RooUnfold. The measured, MC true and unfolded cross section (left). Ratio of unfolded to MC true cross section (right).

While the left plot shows the cross section as a function of p_T at detector level (meas), after unfolding (reco) and the MC prediction at hadron level, the right plot shows the ratio of unfolded to hadron level prediction. As expected the ratio is exactly one. In this analysis another unfolding method called d'Agostini (Bayes unfolding) is also shown in the following Figures 5.13 – 5.17 for different number of iterations. When only 1 iteration is used at large p_T we saw agreement between the unfolded results and the prediction, on the other hand in the smaller p_T bins large fluctuations can be observed. With increasing number of iterations, the fluctuations become even more apparent.

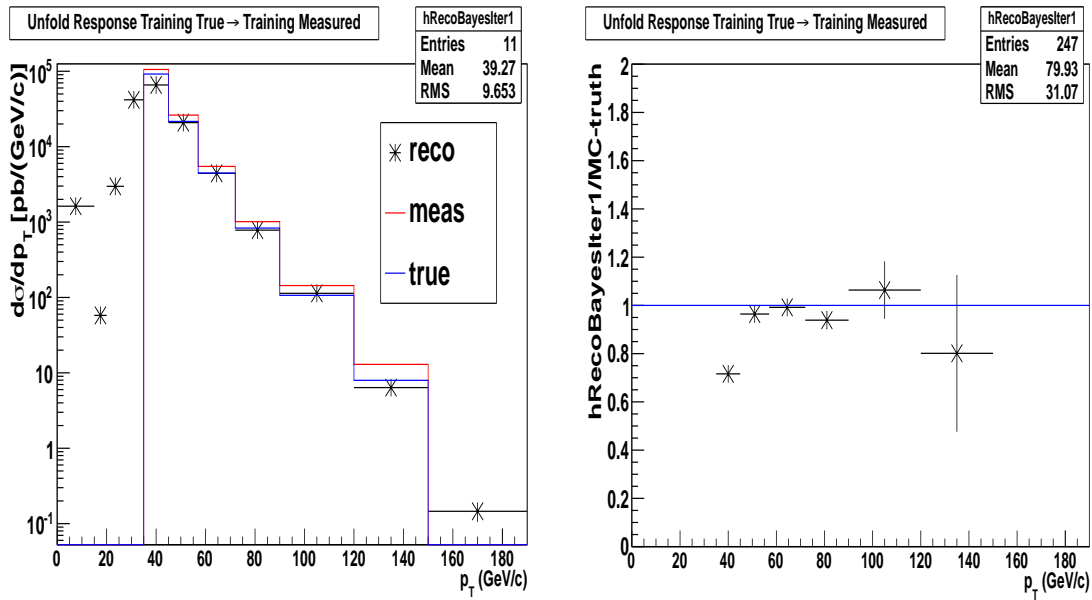


Figure 5.13. Bayes (D'Agostini with 1st iteration) unfolding using RooUnfold. The measured, MC true and unfolded x-section (left). Ratio of unfolded to MC true x-section (right).

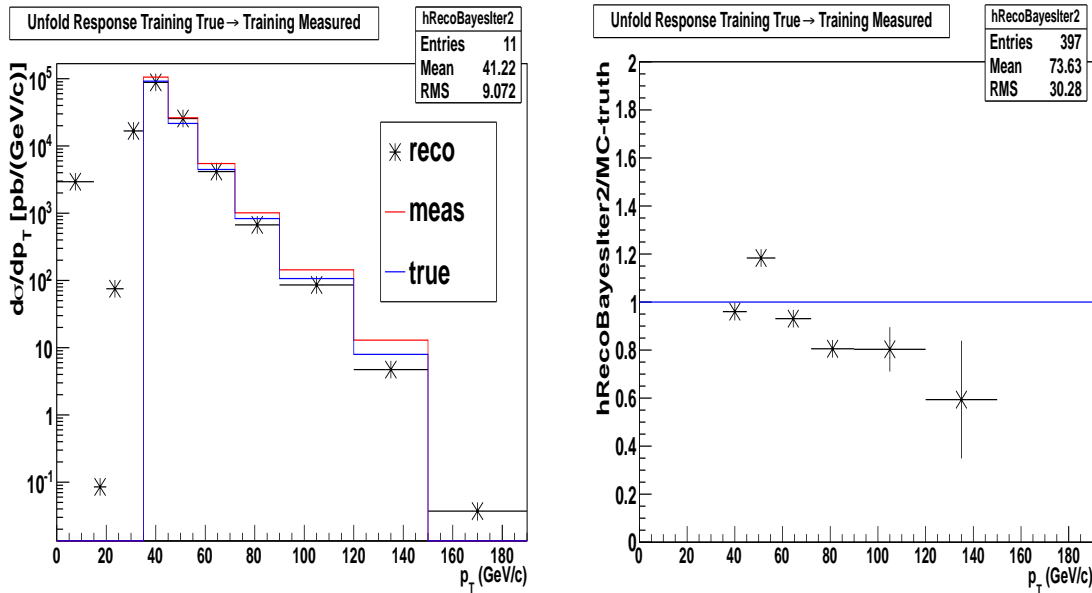


Figure 5.14. Bayes (D'Agostini with 2nd iteration) unfolding using RooUnfold. The measured, MC true and unfolded x-section (left). Ratio of unfolded to MC true x-section (right).

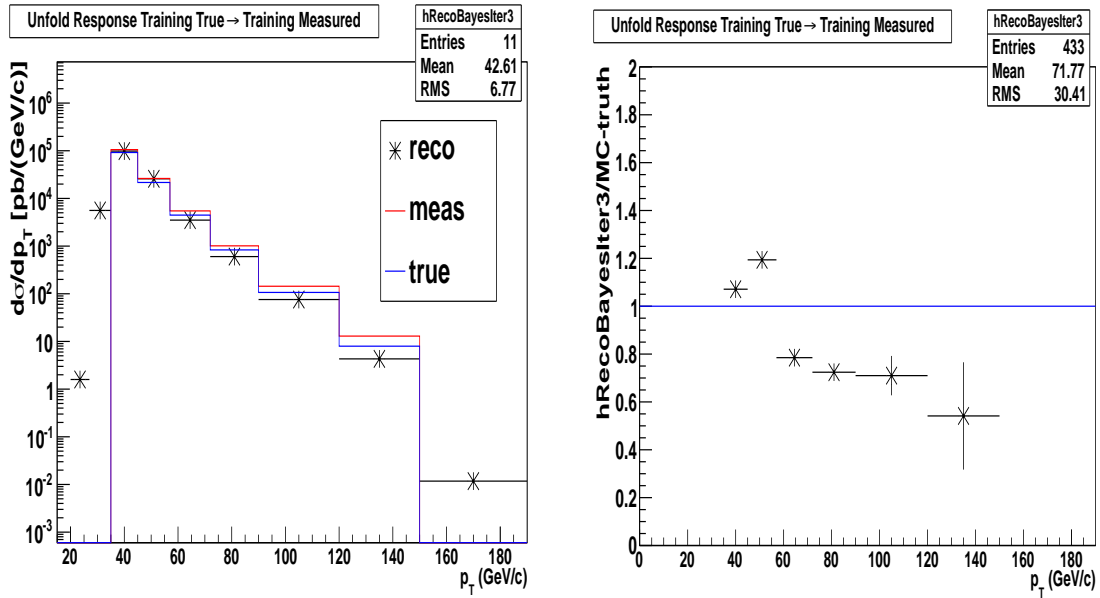


Figure 5.15. Bayes (D'Agostini with 3rd iteration) unfolding using RooUnfold. The measured, MC true and unfolded x-section (left). Ratio of unfolded to MC true x-section (right).

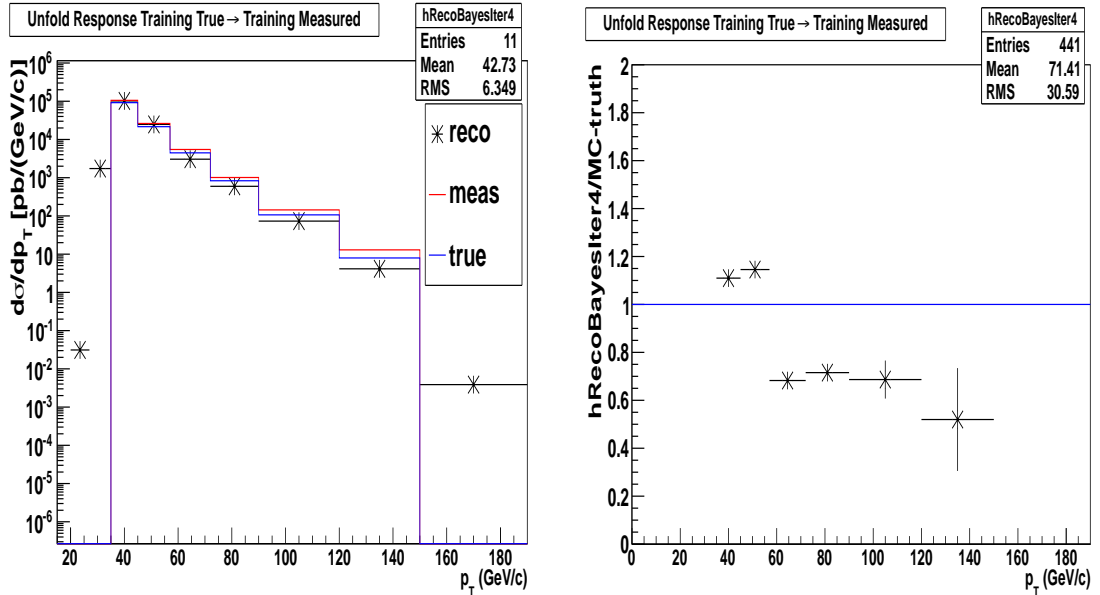


Figure 5.16. Bayes (D'Agostini with 4th iteration) unfolding using RooUnfold. The measured, MC true and unfolded x-section (left). Ratio of unfolded to MC true x-section (right).

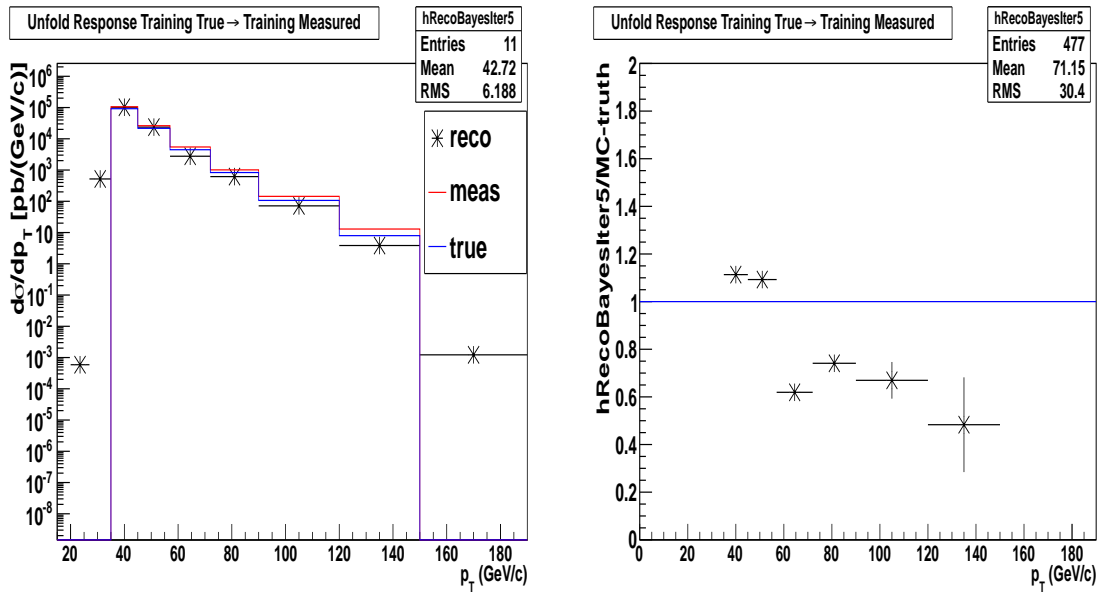


Figure 5.17. Bayes (D'Agostini with 5th iteration) unfolding using RooUnfold. The measured, MC true and unfolded x-section (left). Ratio of unfolded to MC true x-section (right).

The results of unfolding using Singular Values Decomposition (SVD) as a function of the regularisation parameter k_{term} are also demonstrated in Figures 5.18 – 5.22.

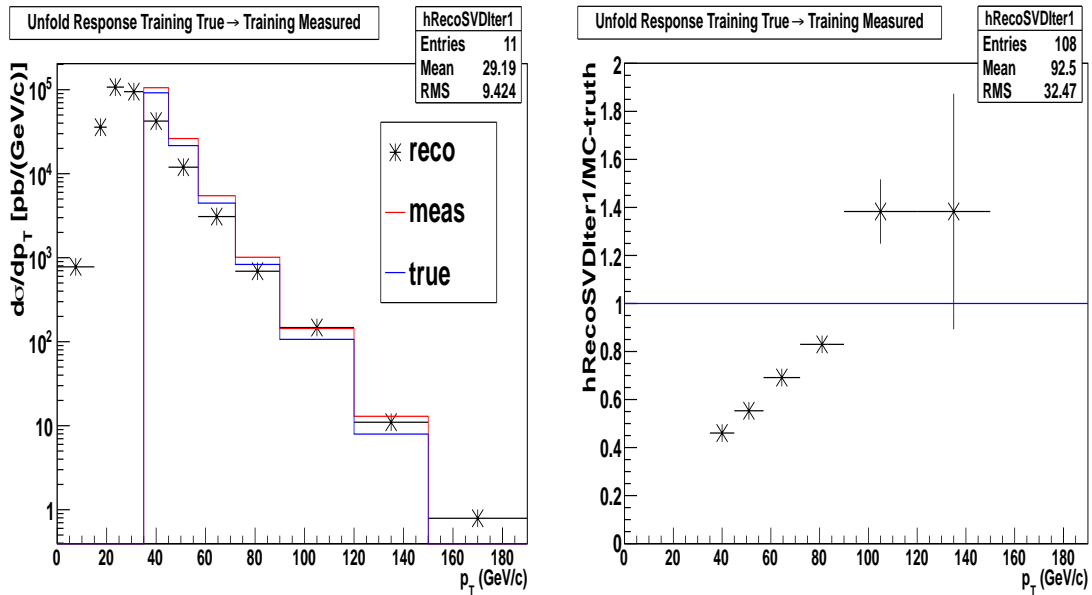


Figure 5.18. SVD (with $k_{term} = 1$) unfolding using RooUnfold. The measured, MC true and unfolded cross section (left). Ratio of unfolded to MC true cross section (right).

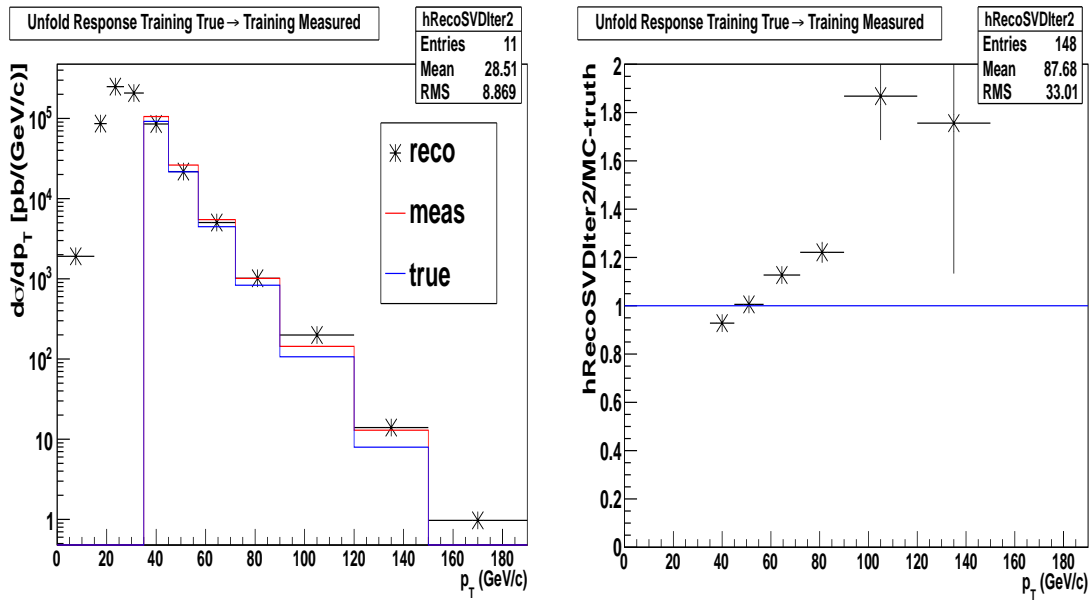


Figure 5.19 SVD (with $kterm = 2$) unfolding using RooUnfold. The measured, MC true and unfolded cross section (left). Ratio of unfolded to MC true cross section (right).

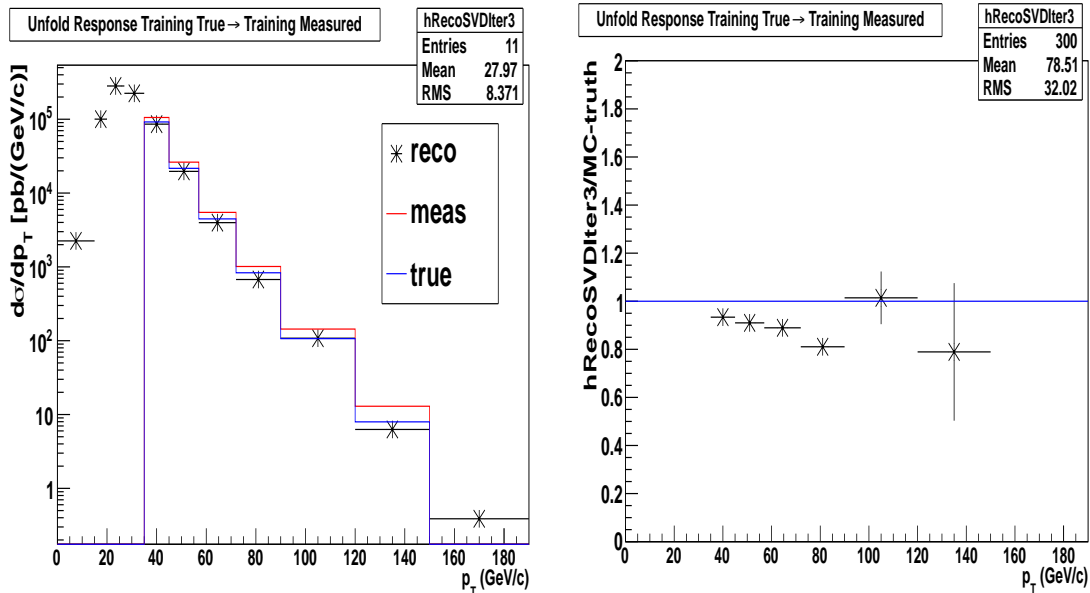


Figure 5.20. SVD (with $kterm = 3$) unfolding using RooUnfold. The measured, MC true and unfolded cross section (left). Ratio of unfolded to MC true cross section (right).

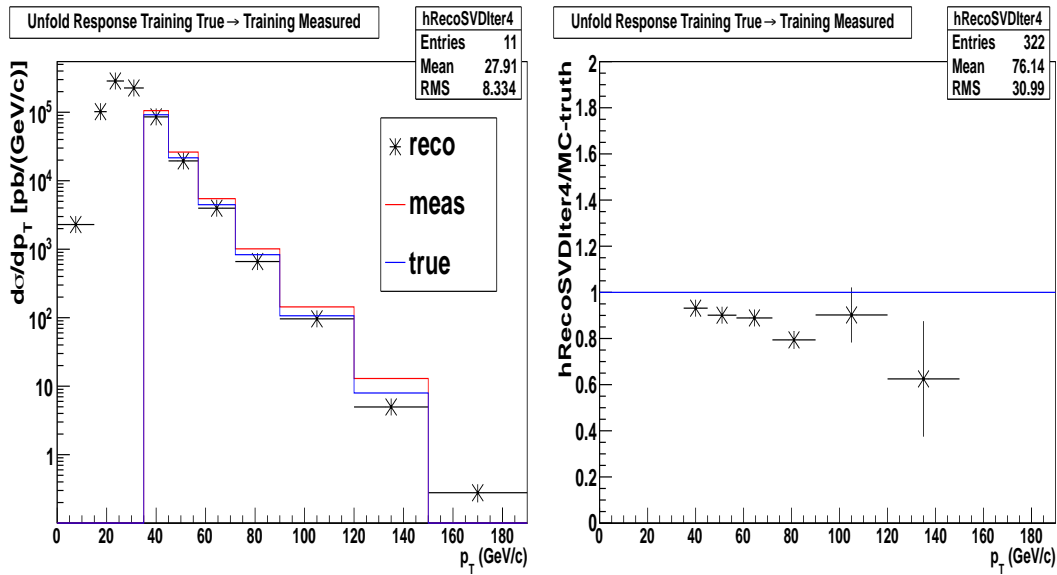


Figure 5.21. SVD (with $kterm = 4$) unfolding using RooUnfold. The measured, MC true and unfolded cross section (left). Ratio of unfolded to MC true cross section (right).

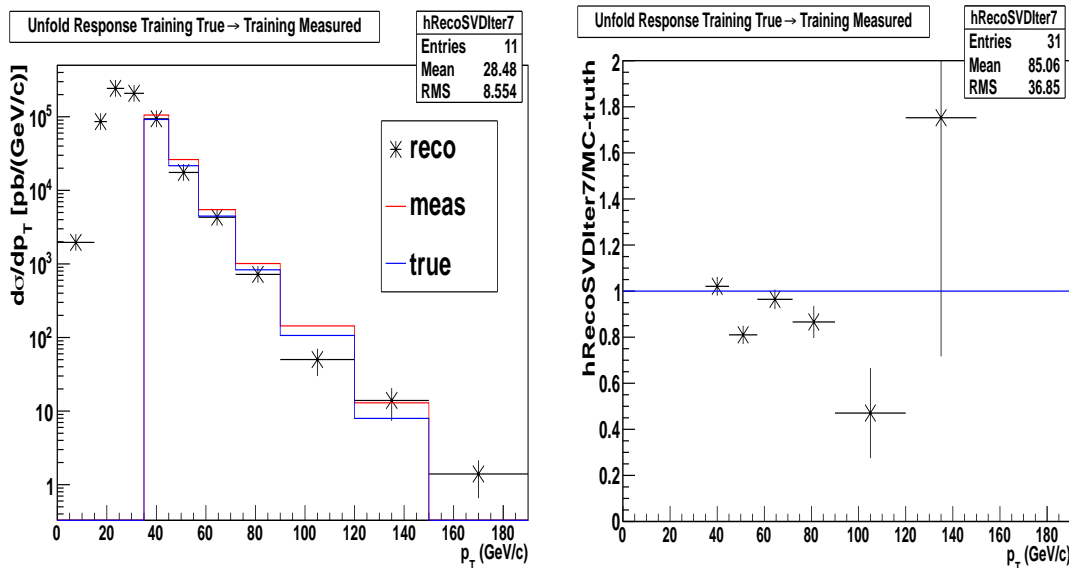


Figure 5.22. SVD (with $kterm \geq 7$) unfolding using RooUnfold. The measured, MC true and unfolded cross section (left). Ratio of unfolded to MC true cross section (right).

The fluctuations observed using d'Agostini and SVD methods are not appropriate for steeply falling distributions. For this reason we have applied corrections obtained from the Bin-to-Bin method, as described in the previous section.

5.7.5. Bin Centre Correction

The jet p_T cross section in each bin p_T is drawn at the bin center to avoid extensive and error-prone numerical integration in two dimensions. It is computed using an initial unsmeared Ansatz fit. Figures 5.23 (left) and 5.24 (left) present a smeared Ansatz fit to the corrected, normalized jet p_T spectrum obtained from data and PYTHIA 6.4 respectively. Figure 5.23 (right) and Figure 5.24 (right) shows the ratio of the measured distributions over Ansatz fits for data and PYTHIA 6.4.

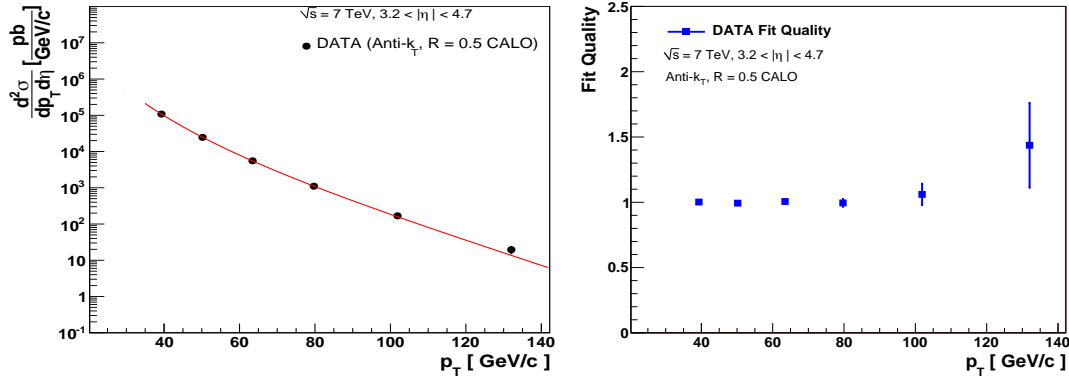


Figure 5.23. Smeared Ansatz fit to the jet p_T spectrum for DATA (left), Quality of the fit: fractional difference between the fitting curve and the "data" points. Error bars are statistical only (right).

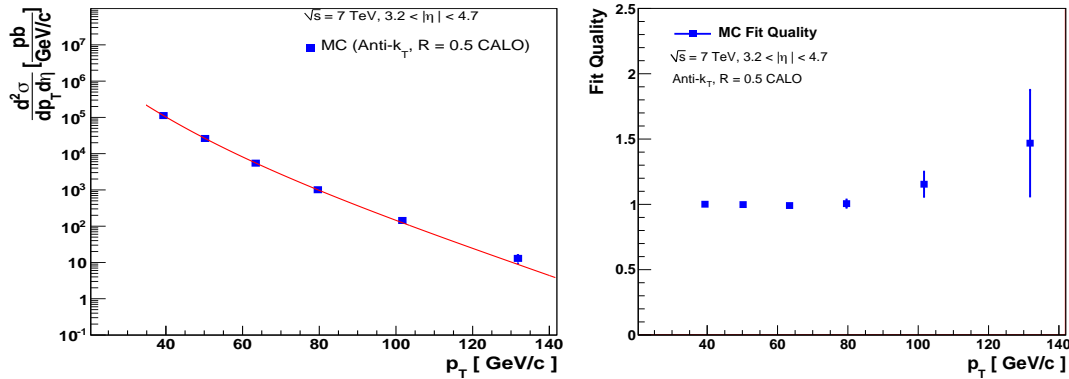


Figure 5.24. Smeared Ansatz fit to the jet p_T spectrum for MC (left), Quality of the fit: fractional difference between the fitting curve and the "data" points for MC (PYTHIA 6.4). Error bars are statistical only (right).

The fit parameters and individual χ^2/NDF are listed in Table 5.3.

Table 5.3. Smeared Ansatz fits to the inclusive jet cross section.

Rapidity bin	N_0	α	β	γ	χ^2/NDF
DATA	$4.04\text{e}+12 \pm 2.23\text{e}+12$	-4.48 ± 0.12	8 ± 0	1.612 ± 0.8	5.3/4
MC	$1.47\text{e}+15 \pm 2.8\text{e}+13$	-5.7 ± 0.044	8 ± 0	-51.312 ± 0.262	4.6/4

Comparison of the correction factors obtained from MC method (average PYTHIA 6.4 and HERWIG + JIMMY) and Ansatz method are also given in Figure 5.25. In this plot the black points show the correction factors obtained with the Ansatz method for the data spectrum while the blue squares for the PYTHIA 6.4 spectrum. Yellow band shows p_T resolution uncertainty for Ansatz method with fit to MC. More details can be found in Appendix C.

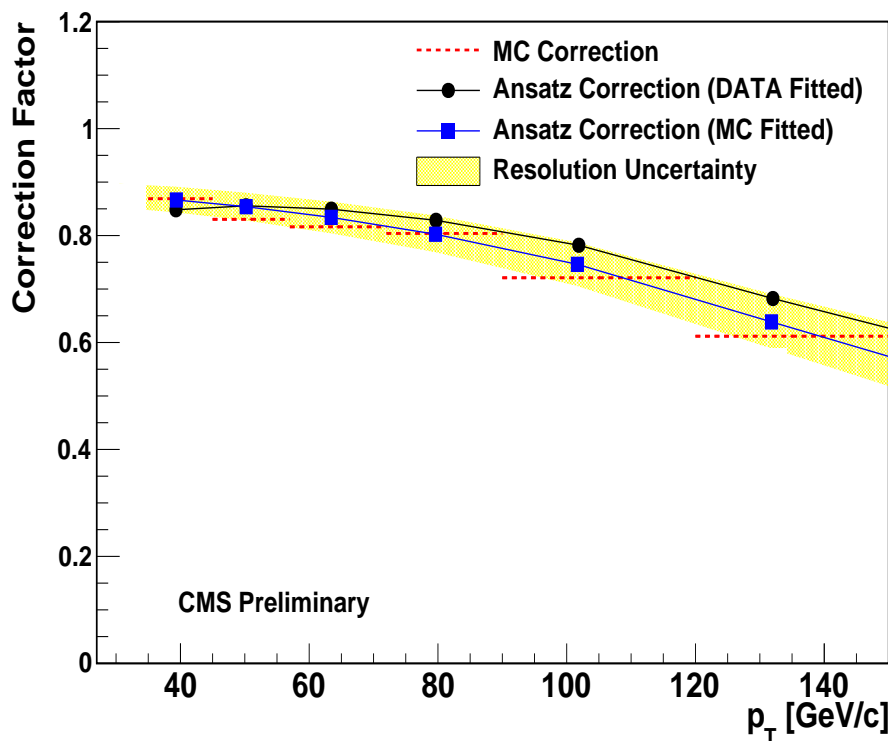
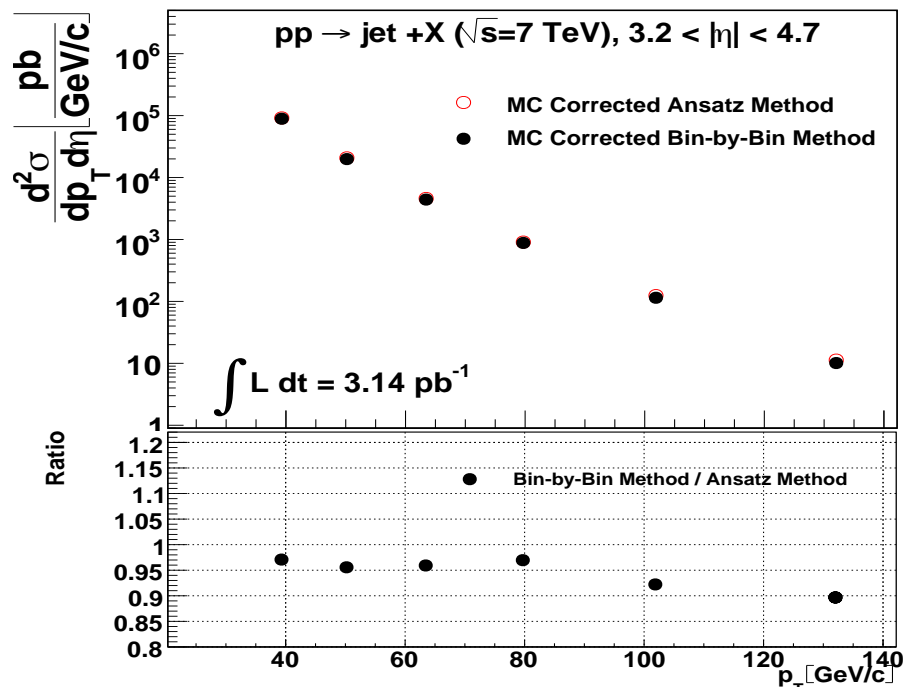


Figure 5.25. The comparison of the correction factors obtained from MC method and Ansatz method.

MC (average PYTHIA 6.4 and HERWIG + JIMMY) correction and Ansatz method correction for data was applied to the partly corrected spectrum (after JEC) and can be seen in Figure 5.26 (top). The comparison of corrected cross section is in Figure 5.26 (bottom).



5.26. The final unsmeared cross sections obtained after the application of correction factors from MC method and Ansatz method and their ratio of cross sections obtained from both methods (bottom).

Differences between these corrections obtained from MC and Ansatz method were in the range of 1% -10% when changing from bin to bin. For the further analysis the MC method was chosen for the unfolding. To account for differences between both MC models and between the Ansatz and MC methods, an uncertainty was attributed to the final unfolded results.

5.8. Systematic Uncertainties

Because of the non-perfect understanding and simulation of the physics and of detector effects the corrected observables can be systematically mismeasured. In this study all the systematic uncertainties were added to the statistical errors and are shown as error bars in figures. Systematic uncertainties are twofold:

- Experimental Uncertainties
- Theoretical Uncertainties

5.8.1. Experimental Uncertainties

These are some of the primary sources of experimental uncertainty in the jet cross sections measurements: Jet Energy Scale, Unfolding, Jet p_T Resolution and Luminosity uncertainties.

5.8.1.1. Jet Energy Scale

The inclusive jet cross section measurement is sensitive to the Jet Energy Scale (JES) because of the steeply falling nature of the spectrum with increasing jet p_T . The JES uncertainty comes mainly from the uncertainty on the single particle response and it is the dominant source of systematic uncertainty. It affects both the reconstruction of the transverse energy of the selected jets and also the reconstructed kinematic variables measured with the calorimeter. In this analysis jet energy corrections were applied to take into account inefficiencies, non-linearities and finite resolutions in energy and position of the reconstructed jets, energy loses in dead material besides event and jet selections. The jet energy correction (JEC) uncertainties are utilized according to the JetMET group recommendations (Chatrchyan et al., 2010b). The systematic uncertainty of the whole calibration factor is the sum in quadrature of the relative scale (η dependent) and the absolute (p_T dependent) scale uncertainties.

At forward rapidities, the HF calorimeter has a JES calibration uncertainty that differs between 3% and 6%, based on the p_T and η of the reconstructed jet. This uncertainty must be convoluted with that relevant to a ~ 0.8 GeV energy shift per pileup-event because of the existence of other hadrons around the forward jet axis. Jet-by-jet JEC uncertainty values were propagated. For this reason main p_T spectrum was obtained with JEC. JEC values were recalculated using the uncertainty of JEC which were used to correct the jet p_T . Then with new JEC, two jet p_T spectra were obtained as JES up and JES down and shown in Figure 5.27. JES uncertainty band were calculated using JES up, JES down and central spectra. The formulas below describe bin-by-bin computation of JES uncertainty bands.

$$\% JESUp = \frac{p_{T, JESUp} - p_{T, Central}}{p_{T, Central}} \cdot 100 \quad (5.20)$$

$$\% JESDown = \frac{p_{T, Central} - p_{T, JESDown}}{p_{T, Central}} \cdot 100 \quad (5.21)$$

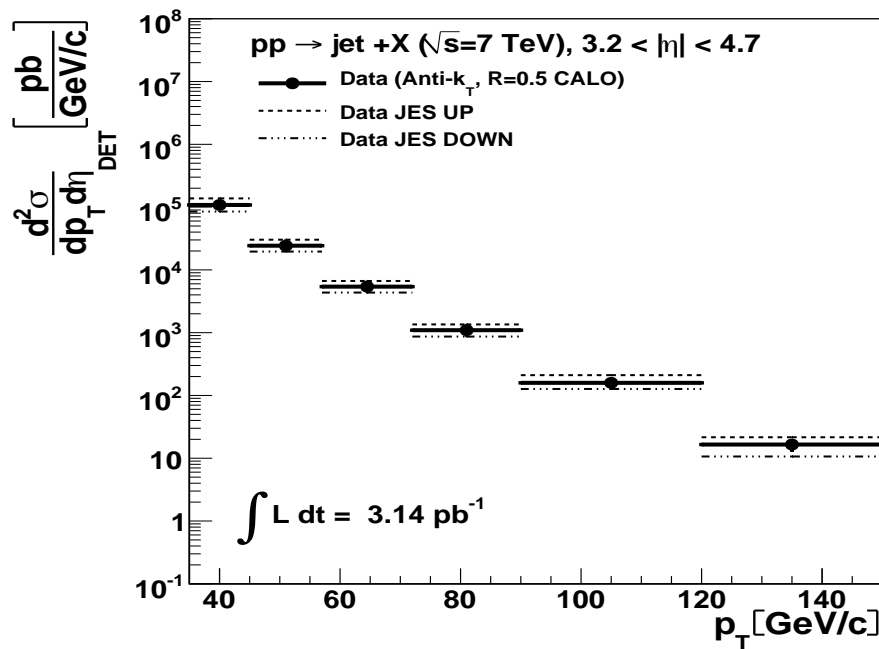


Figure 5.27. Corrected jet p_T spectrum with JEC.

In Figure 5.27 dashed lines represent corrected jet p_T spectrum with recalculated JEC. Here JEC are obtained using JEC uncertainty up (increased) and down (decreased) values.

5.8.1.2. Jet p_T Resolution

The JetMET group recommends a $\pm 10\%$ uncertainty on the jet p_T resolution. This amount translates into an uncertainty of 3 to 6% (with increasing p_T) on the final cross sections. The jet p_T resolution uncertainty is presumed by smearing the Ansatz with changing resolutions ($\pm 10\%$ within uncertainties) and comparing results to smeared central Ansatz. The uncertainty of the jet energy resolution is the ratio between the central smearing and the extreme values ($\pm 10\%$).

Additionally uncertainty of 3% was added in quadrature, because the model dependence of the correction factors described by the difference between the PYTHIA 6 and HERWIG 6 MC event generators was used to unfold the cross sections.

5.8.1.3. Jet Quality Criteria

In order to estimate the systematic uncertainties related to the jet quality criteria “Tight” cuts are applied in the following manner to the jet selection:

- $n^{hit} > 1 + 2.7(lnp_T^{raw} - 0.8)$ in HFa,
- $n^{hit} > 1 + 3.5(lnp_T^{raw} - 0.8)$ in HFb,
- $n_{90}^{hit} > 1.5 \max(0, lnp_T^{raw} - 1.5)$ in EF jets,
- $0.5 + 0.057(\max(0.9 - lnE^{raw}))^{1.5} > \alpha_{LS}$
 $\alpha_{LS} > \max(-0.6, -0.1 - 0.026 \max(0.8 - lnE^{raw}))^{2.2}$ in HF
 $\alpha_{LS} > \max(-0.9, -0.1 - 0.05 \max(0.5 - lnp_T^{raw}))^2$ in EF,
- $\sigma_{\eta\eta}$ and $\sigma_{\phi\phi}$ are both in the range $(10^{-10}, 0.12)$.

Here the EF jets are identified as jets with $2.6 \leq |\eta| < 3.4$ and $0.1 \leq f_{LS} < 0.9$.

Transverse momentum spectrum obtained with the “TIGHT” Jet ID cut was compared to the one obtained with “LOOSE” Jet ID cut. In Figure 5.28 the ratio between the p_T distribution obtained with the LOOSE and TIGHT Jet ID is shown. Here the average systematic error was estimated to be 0.5 %.

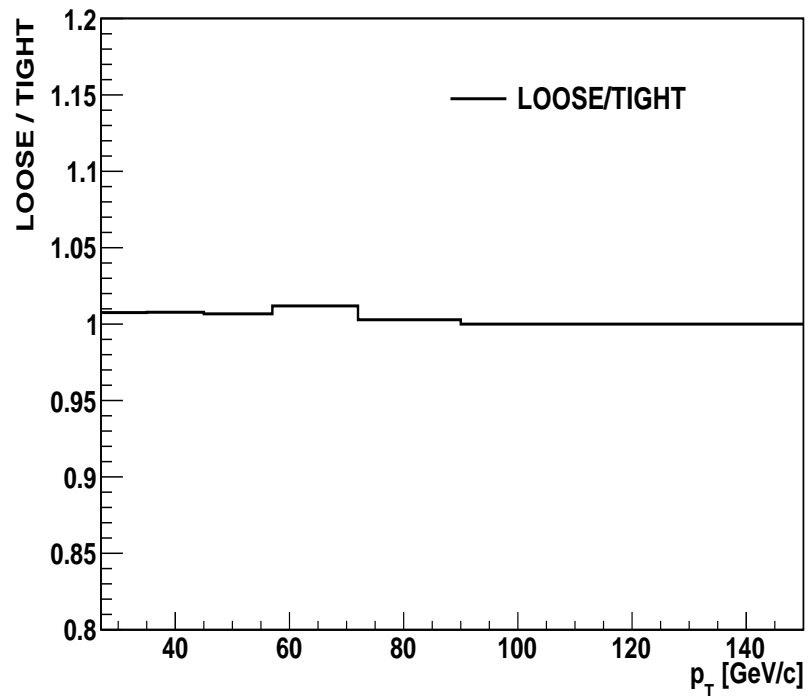


Figure 5.28. The ratio between the p_T distribution obtained with the “LOOSE” and “TIGHT” Jet ID.

5.8.1.4. HF Cleaning

In the CMSSW framework there are three versions of the HF cleaning called V1, V2 and V3. In this analysis all versions are used to estimate the effect of the choice of the cleaning method on the forward jet transverse momentum spectrum.

V1 cleaning:

- is developed using 0.9 TeV collision data,
- the short fiber RecHits are flagged using the Polynominal Energy Threshold (PET) algorithm (with energy $>$ PET and $R < 0.98$),
- the long fiber RecHits are flagged using the S9/S1 algorithm (with energy $>$ PET and $S9/S1 <$ energy-dependent S9/S1 cut). In this algorithm the noise hits are defined by calculating a ratio of the energy in a long fibre and a sum of energies in 9 of its neighbours. If this ratio is smaller than a threshold identified as a function of long fibre energy, the RecHit is flagged as a PMT hit,
- long fiber RecHits in $i\eta$ ring 29 are flagged using the PET cleaning algorithm (with $R > 0.98$).

V2 cleaning:

- is optimized on 7 TeV collision data,
- the short fiber RecHits are the same as V1 (here $R < -0.8$),
- long fiber RecHits are the same as in V1 cleaning.

V3 cleaning:

- is optimized on QCD FlatPt samples,
- the short fiber RecHits are the same as in the V2 cleaning,

- long fiber RecHits are flagged using the S9/S1 algorithm (with energy > PET and S9/S1 < energy-dependent S9/S1 cut),
- long fiber RecHits in $i\eta$ ring 29 are flagged using the PET cleaning algorithm (with $R > 0.8$).

These three versions of the HF cleaning were compared by analyzing the following data with CMSSW 3_6_1_patch2.

- /JetMETTau/Run2010A-Jun14thReReco_v2/RECO

Figure 5.29 shows the ratio between the p_T distribution obtained with the V1 and V2 (full line) and V3 and V2 (dashed line).

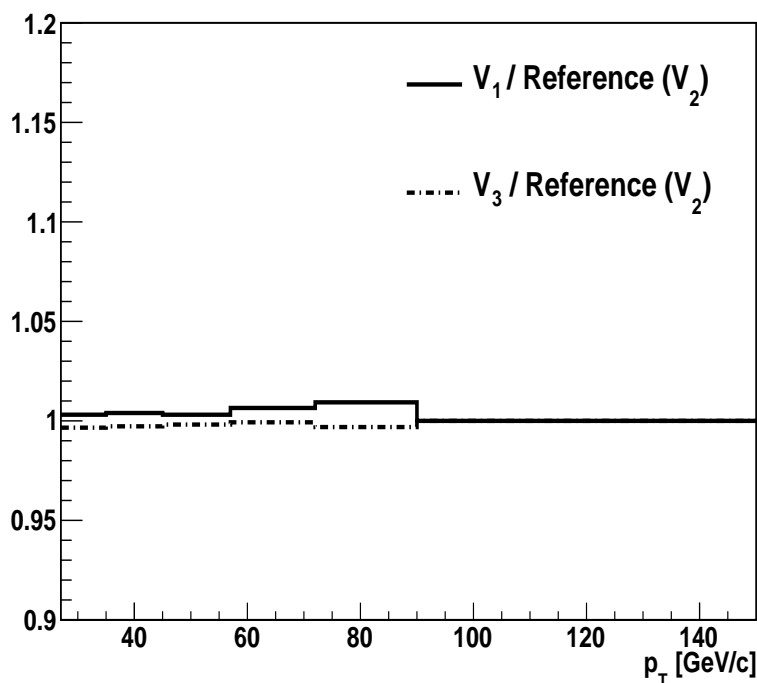


Figure 5.29. The ratio between the p_T distribution obtained with the V1, V2 and V3 of the HF cleaning.

We can infer from the Figure 5.29 that, as expected, the V2 is tighter than V1 but looser than V3. The average systematic uncertainty found with the selection of the HF cleaning method is of the order of 1.0 %.

5.8.1.5. Primary Vertex Cut ($|z|$)

In this analysis the primary vertex is reconstructed with $|z| < 15$ cm and influence of the $|z|$ cut is investigated by analyzing the data with $|z| < 24$ cm. Figure 5.30 shows the ratio between the p_T distribution obtained with the $|z| < 24$ cm and $|z| < 15$ cm. The systematic error due to the $|z|$ cut was found to be 0.5%.

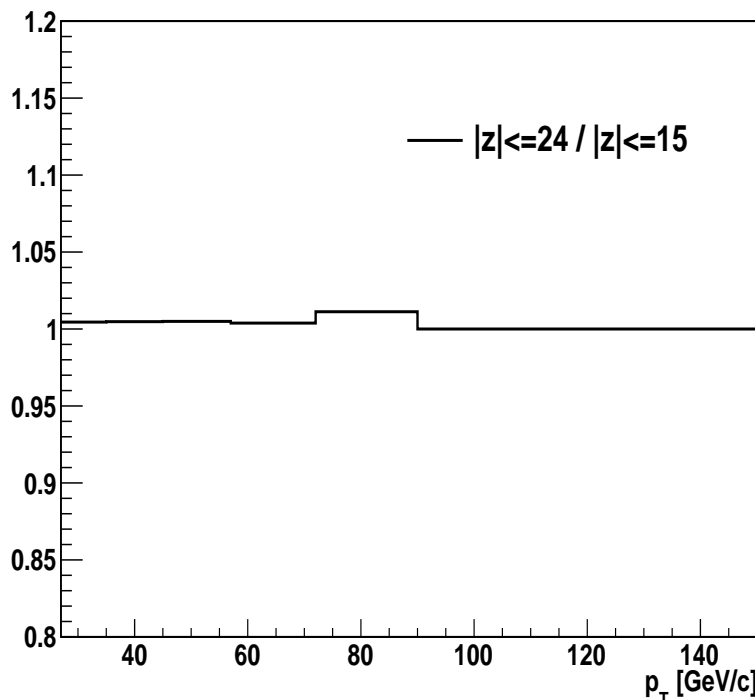


Figure 5.30. The ratio between the p_T distribution obtained with the $|z| < 24$ cm and $|z| < 15$ cm.

5.8.1.6. Pile-Up Effect

Multiple pp collisions during the same bunch crossing and electronic signals from previous bunch crossings that are still present in the detector cause a pileup problem. In order to remove this effect, pileup calculation needs to be performed. To estimate the pile-up of the instantaneous luminosity of each bunch crossing we considered for each luminosity section (LS) (23.3s). The pile up events expected rate, per second for the minimum bias cross section, was multiplied with the instantaneous

luminosity. Poisson distribution from the expected number of pile-up events was generated and weighted by its integrated luminosity for each LS and crossing. Results obtained using the official pile-up estimation script are given in Figure 5.31(left). In Figure 5.31(right), the change of pile-up is demonstrated with regard to the number of primary vertices in each run.

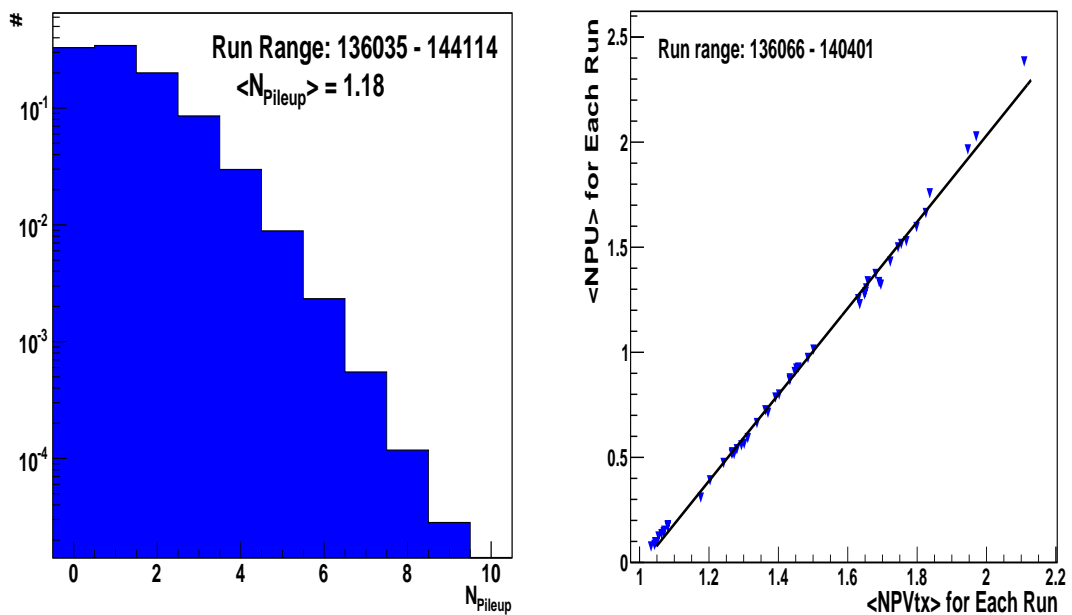


Figure 5.31. Average pile-up estimation obtained for the each run number used in the analysis (left). Average pile-up estimated per run with respect to number of primary vertices per run (right).

In the sample of events selected for the inclusive forward jets analysis the average pile-up was found to be 1.18.

5.8.1.7. Offset Correction

Offset correction is an important parameter used to evaluate the influence of pileup and calorimeter noise. The main goal of this study was to estimate the energy not related to high p_T scattering. For this reason the energy with contributions from calorimeter electronic noise and pileup effect was separated.

In order to calculate the only noise contribution, Zero Bias events were used. That means: without any pre-conditions (except a beam crossing), events from

random trigger were selected and in these events, a veto on the Minimum Bias trigger events was applied because vetoing the Minimum Bias trigger events gives a pure noise sample. As a result the contribution from noise is found to be less than 0.01 GeV in p_T over the whole η range covered by the HF calorimeter.

In order to calculate the offset from one additional interaction event, Minimum Bias trigger events in early runs were selected and $E_{offset}(\eta)$ were calculated. The measured energy can then be attributed to noise+one pile-up. This study shows that the contribution from noise + one pileup is large in the forward region up to 7 GeV in energy but it is small in p_T up to 0.35 GeV for $|\eta| = 3.5$ and decreasing to 0.1 GeV for $|\eta| = 5$. Earlier studies indicated that difference between the estimated and the true offset can be as large as factor 2 for the forward region. This factor is taken into account when calculating the possible systematic effect for forward jets. In section 5.8.1.6 for the inclusive forward jets analysis the average pile-up was found to be 1.18. Therefore the uncertainty in the present analysis is $0.35 \times 1.18 \times 2 = 0.80$ GeV.

In order to cross check the pile-up estimation, the ratio of the detector level p_T distributions obtained for forward jets, coming from events with only one good primary vertex reconstructed and for all forward jets are shown in Figure 5.32 (left). To calculate the ratio, both distributions were normalized to unity. Then same ratios were plotted for forward jets from events with single vertex and for forward jets from events with single vertex applying first a shift of 0.5, 1, 2 and 3 GeV to the p_T of each jet, Figure 5.32 (right). This shift shows the effect of pileup. Ratios shown in Figure 5.32 (right) differs from 1, while the ratio from Figure 5.32 (left) is compatible with 1. From this observation we can conclude that pile-up does not play an important role in the measurement and 0.80 GeV is rather a safe estimate for the possible shift of the spectrum.

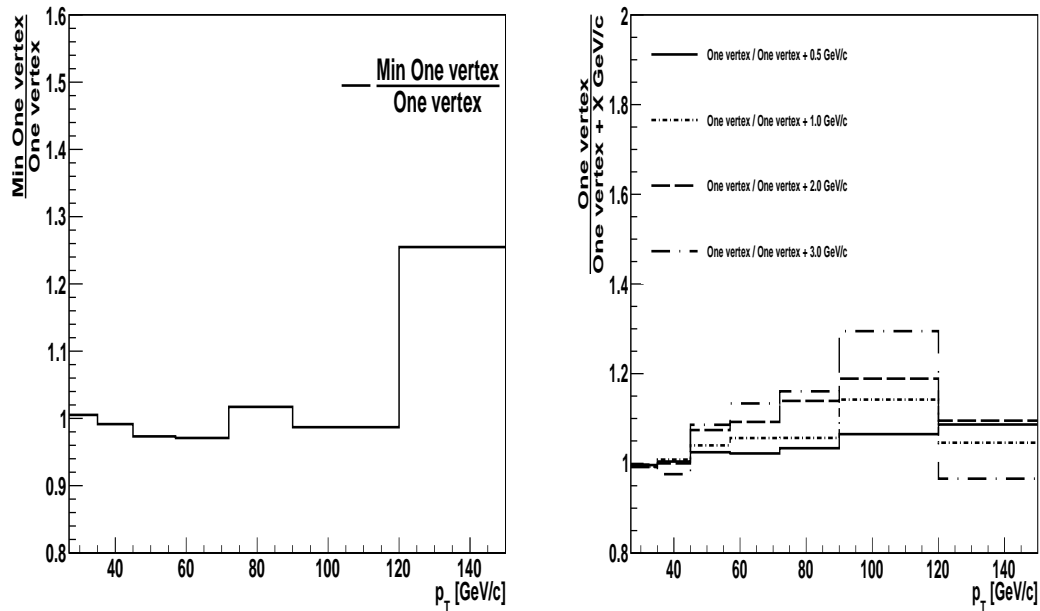


Figure 5.32. The p_T distributions for jets from events with exactly one vertex reconstructed and for jets from all events (left). The p_T distribution for jets from events with exactly one vertex reconstructed and the same distribution after applying to each jet a p_T shift of 0.5, 1, 2 and 3 GeV (right).

5.8.1.8 Summary of the Experimental Systematic Uncertainties

The different contributions to the experimental uncertainty are shown as a function of jet p_T in Figure 5.33. The grey areas represent the total uncertainty, while the two hatched areas indicate the uncertainties on the JES and the unfolding procedure.

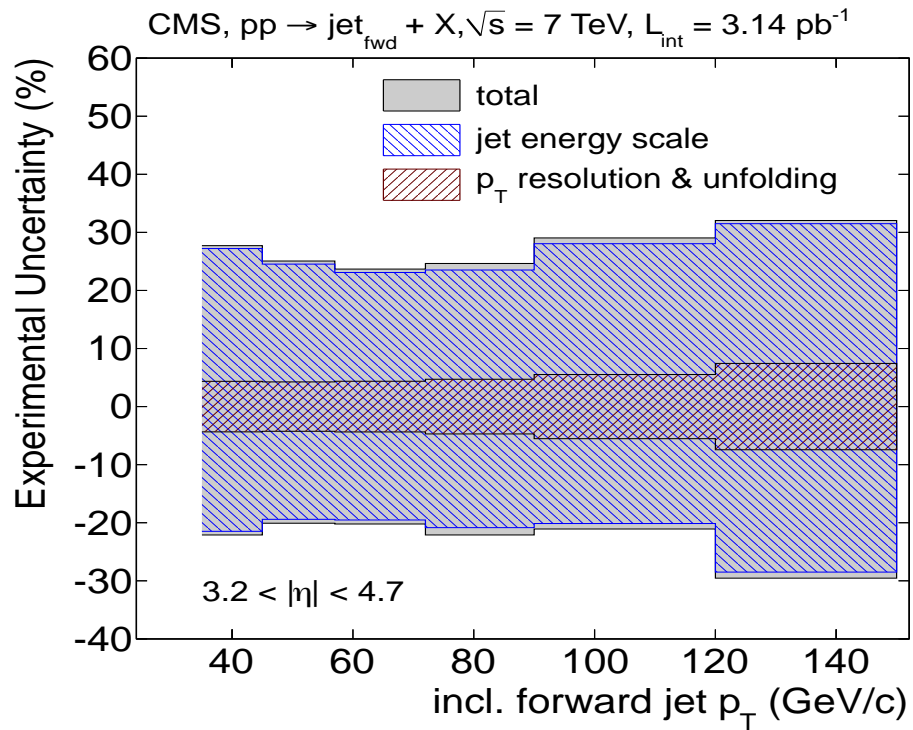


Figure 5.33. Experimental uncertainties as a function of jet p_T for inclusive forward production.

The experimental systematic uncertainties on the forward jets cross section measurement are summarized in Table 5.4.

Table 5.4. Summary of the systematic uncertainties.

Effect	Size of the effect
Jet energy scale	Energy scale shift $\pm 3\text{--}6\%$
Jet p_T resolution	Resolution changed by $\pm 10\%$
Model dependency (PYTHIA 6.4 +HERWIG+JIMMY)	1-5%
Jet quality criteria	0.5%
HF cleaning criteria	1.0%
Primary vertex selection	0.5%
Pileup and detector noises	0.80 GeV (3% at 30 GeV, 0.8 at 100 GeV)
Integrated luminosity	4%

5.8.2. Theoretical Predictions

The theoretical predictions consist of a next-to-leading-order (NLO) QCD calculation and a Non-Perturbative (NP) correction to account for the multiparton interactions and hadronisation effects. In this analysis, uncertainties of factorisation and renormalisation scales as well as PDFs uncertainties have been evaluated. For this reason the measured differential jet cross sections are compared to predictions from different pQCD approaches such as general purpose event generators PYTHIA 6 (version 6.422) with D6T and Z2 tunes, PYTHIA 8 (version 8.135) with Tune 1 HERWIG 6 (version 6.510.3) with underlying-event modelled with JIMMY and HERWIG++ (version 2.3).

5.8.2.1. Next to Leading Order (NLO) Calculations

Next-to-leading order pQCD theoretical predictions are calculated using NLOJET++ within the fastNLO (Kluge, Rabbertz and Wobisch, 2006) package with CT10 parton distribution functions (PDF) (Lai et al., 2010), as well as with the POWHEG framework matched to the PYTHIA 6.4 parton shower MC. Additionally, measured distributions are compared to results from the CASCADE (version 2.2.04) which includes parton radiation from QCD evolution in $1/x$ and to HEJ which includes extra contributions from wide-angle gluon radiation, that are not available in the other models.

The PYTHIA 6 and HERWIG 6 event generators use the CTEQ6L PDFs (Pumplin et al., 2002) while the PYTHIA 8 uses CTEQ5L PDFs (Lai et al., 2000) and Herwig++ uses MRST2001 PDFs (Martin et al., 2002). CASCADE MC includes Set-A unintegrated parton distributions and p_T cuts of the matrix-element partons of 14 GeV/c. The HEJ event generator uses the MSTW2008NLO PDFs (Martin et al., 2009). The default renormalisation and factorisation scales have been set to $\mu_r = \mu_f = p_T$ for both NLO calculations.

5.8.2.2. Non Perturbative (NP) Corrections

The NLO pQCD calculations give predictions at the parton level, while the experimental data are corrected to the particle level. For this reason the NP effects must be considered when a comparison between the data and the theoretical predictions is needed. pQCD predictions include initial state radiation which forms parton scattering from hadron-hadron interactions. It is very important to compare these predictions with experimental high energy physics data. The experimental data was corrected for detector and collider effects. NLO predictions of pQCD generated by MC events are corrected for non-perturbative (NP) effects which include hadronization and multiple parton interaction (MPI). Before comparing the data to parton-level theoretical predictions, NP uncertainties related to off-jet hadronisation and splash in UE within the jet area were also specified. NP effects were calculated by comparing the PYTHIA 6 and HERWIG 6 + JIMMY parton-level spectra with the corresponding particle-level predictions after hadronisation and UE activity. For this analysis the correction factors shown in Figure 5.34 are determined as the average between the predictions derived from the PYTHIA 6.4 and HERWIG + JIMMY event generators.

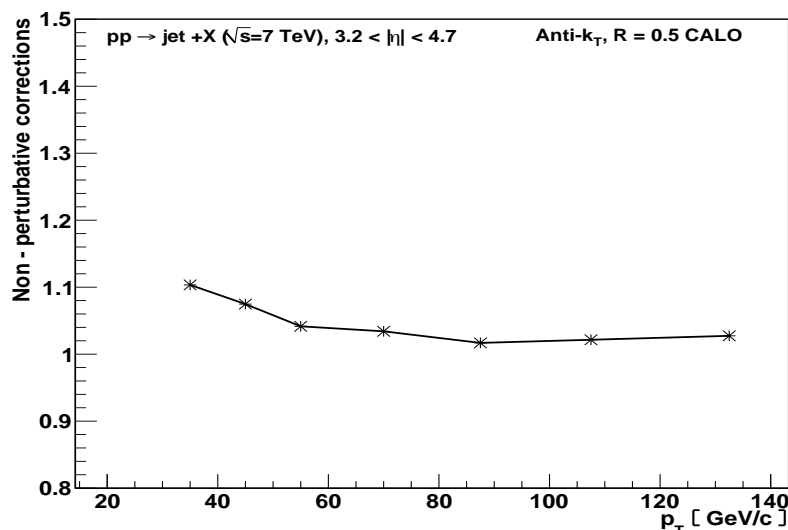


Figure 5.34. Non-perturbative corrections to NLO QCD calculations. The error bars correspond to half the spread between the predictions from PYTHIA 6.4 and HERWIG + JIMMY.

The NP correction factors amount to 1.10 (1.02) at the lowest (highest) p_T bin considered in this study. Half of the difference between these two predictions, shown as a function of forward jet p_T in Figure 5.35, is taken as an estimate of the total systematic uncertainty related to this NP effect.

For NLO predictions (NLOJET++ and POWHEG), the uncertainties relevant to the PDF and the strong coupling a_s can be estimated following the PDF4LHC interim recommendations (Alekhin et al., 2011). While the PDF uncertainty is estimated from the maximum envelope procured from the 68% confidence level eigenvectors (CL68) of the CT10, MSTW2008 and NNPDF2.1 (Ball et al., 2011) sets, the strong coupling a_s uncertainty is derived from separate fits using the CT10 PDF where $a_s(M_Z)$ is changed by ± 0.002 and is added in quadrature to the uncertainty on the PDF. At the end, the quality of the pQCD approach at NLO is appraised by varying the renormalization (μ_r) and factorization (μ_f) scales by factors in the following six combinations: $(\mu_r, \mu_f) = (p_T/2, p_T/2), (p_T/2, p_T), (p_T, p_T/2), (p_T, 2p_T), (2p_T, p_T)$ and $(2p_T, 2p_T)$. All the sources of theoretical uncertainties are shown in Figure 5.35 (left). The NP corrections dominate for $p_T < 60$ GeV/c, while PDF and a_s uncertainties dominate above that p_T . Scale uncertainties are less important at all transverse momenta. These three sources of uncertainty are added in quadrature into a single theoretical uncertainty band.

Figure 5.35 (right) shows the same NP and scale uncertainties, but different PDF obtained using the HERAPDF1.0 (Aaron et al., 2010) parton densities. We used 33 HERAPDF1.0 eigenvalues corresponding to 68% confidence-level uncertainties of this PDF set that account for experimental, model and parametrisation uncertainties of the HERA data fit. Two more HERAPDF1.0 fits, with a_s changed by ± 1 standard deviation of the world-average value (0.1176 ± 0.002), were also used and added in quadrature to the PDF uncertainty. HERAPDF1.0 sets have fewer constraints on the gluon density at high- x than other globally-fitted PDF and also HERAPDF includes extra uncertainties on the initial shape of the parton distributions. For this reason, at high p_T jets, HERAPDF1.0 uncertainty is larger than the PDF4LHC uncertainty.

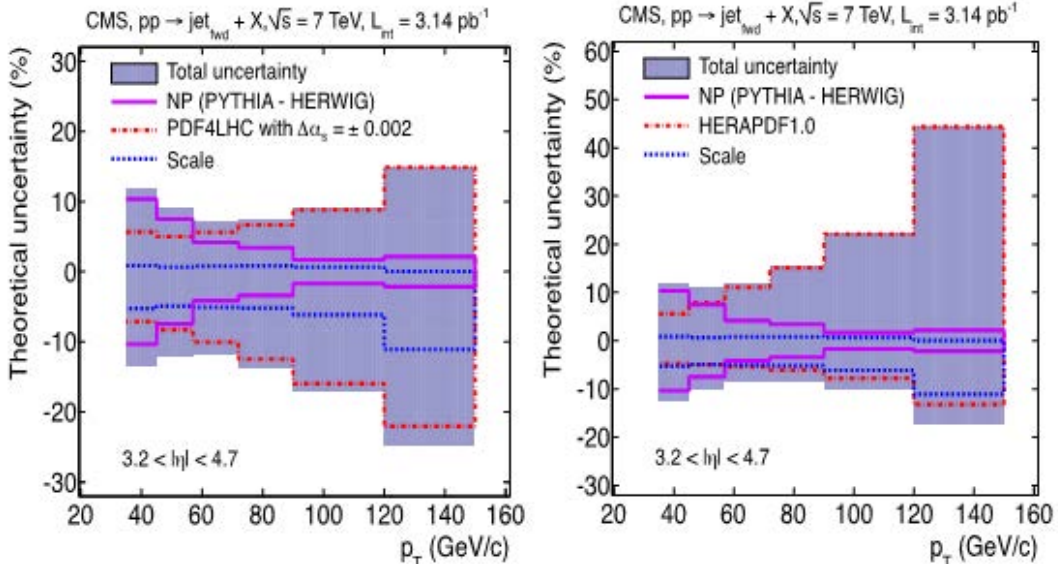


Figure 5.35. Uncertainties on the predicted NLO inclusive forward jet spectrum. The contributions from NP effects, choice of PDF and the value of the strong coupling α_s (computed with the PDF4LHC prescription) and uncertainties associated with the renormalization and fragmentation scales (left). The uncertainties from NP, PDF and α_s (obtained with HERAPDF1.0) and the theoretical scales (right). Total uncertainties are obtained by adding quadratically the uncertainties on NP, PDF and the scales.

The unfolded data cross section values, fNLO and various MC models on hadron level and differences between each other are tabulated in Appendix D.

5.8.3. Inclusive Forward Jet Spectrum

The fully corrected inclusive forward jet cross section as a function of p_T is shown in Fig. 5.36 (left) compared to the models discussed above. Figure 5.36 (right) shows the ratio of theoretical to experimental jet cross sections, including the NLO band of uncertainty. The error bars on all data points (which, in (left), are smaller than the size of the markers) reflect just statistical uncertainties, with systematic uncertainties plotted as grey bands. The dark band in 5.36 (right) shows the theoretical uncertainty on the NLO predictions. From the Figure 5.36 we can conclude that forward jet spectrum is consistent with all predictions within the

theoretical and experimental uncertainties. On the other hand POWHEG has a less steeper p_T spectrum than the data and CASCADE seems to have a more “concave” spectral form than the data in the intermediate p_T region. A diminution of the experimental uncertainties, mostly the jet energy scale, is needed in order to extract more certain conclusions from the data-theory comparison.

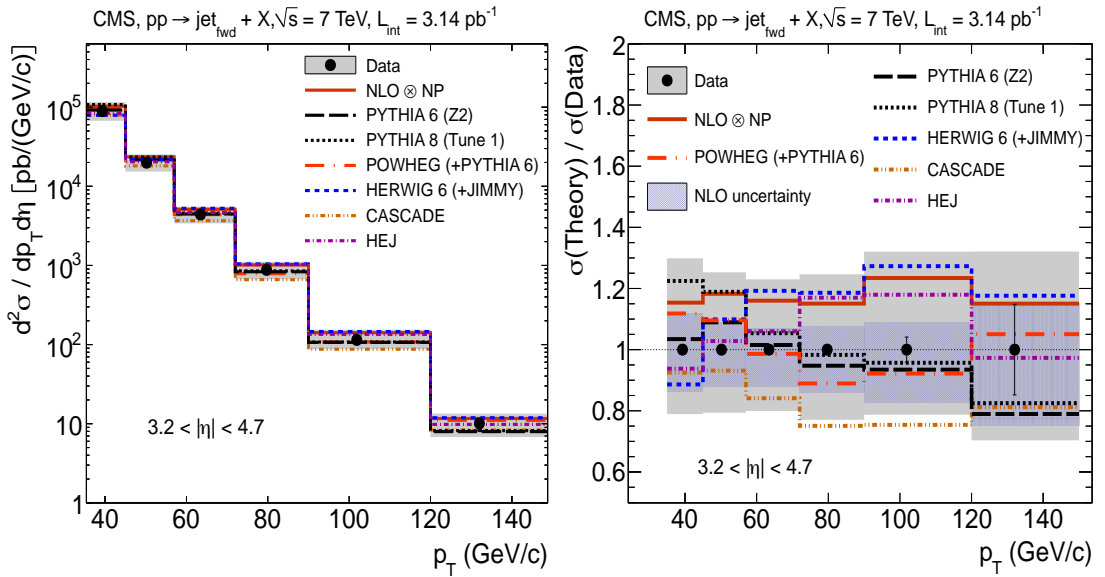


Figure 5.36. Inclusive jet cross section at forward pseudorapidities ($3.2 < |\eta| < 4.7$), fully corrected and unfolded, compared to particle-level predictions from PYTHIA 6, PYTHIA 8, HERWIG 6, NLOJET++ corrected for non-perturbative effects, POWHEG, CASCADE and HEJ (left). Ratio of theory/data for the forward jet spectrum (right).

The NLO predictions compared to the data in the form of bin-by-bin ratios of data to theory are displayed in Figure 5.37. Here, NP correction, renormalisation and factorisation scale uncertainties, common to all theoretical predictions, are added in quadrature and shown by the dashed (magenta) lines around the ratio at unity in Figures. 5.37 (left) and (right). Uncertainties on individual PDF sets are demonstrated as bands. To improve readability, comparisons to data are performed separately in panel (left) using the central values of all investigated PDF sets relative to CT10, in panel (right) for MSTW2008 and NNPDF2.1 and in panel (bottom) for HERAPDF1.0 and ABKM09.

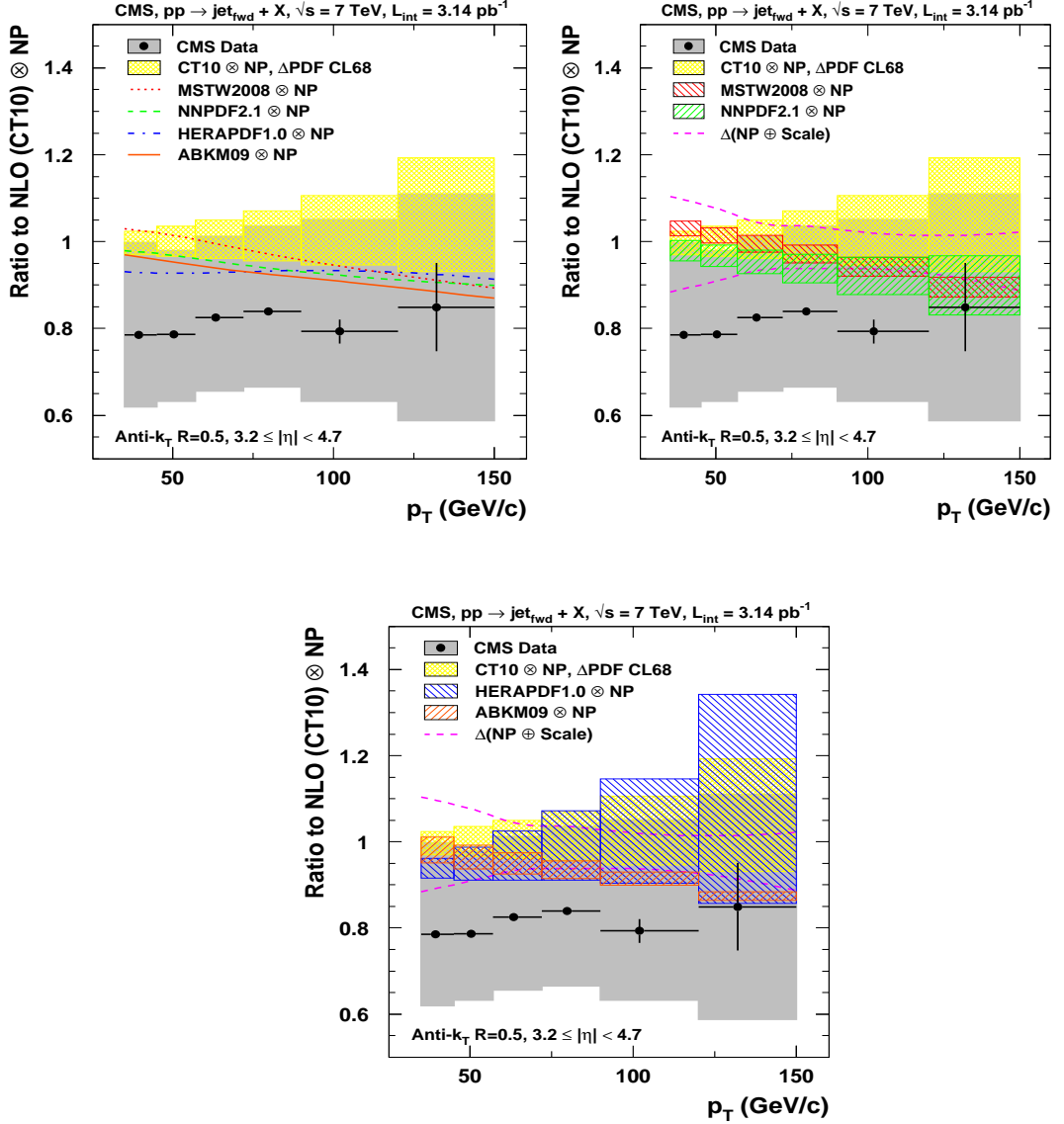


Figure 5.37. The NLO predictions compared to the data. For all the central PDF predictions (left), for the MSTW2008 and NNPDF2.1 sets (right) and for the HERAPDF1.0 and ABKM09 PDF (bottom). The corresponding PDF uncertainties are shown as colored bands around the ratios. Common theoretical uncertainties from choices of scale and non-perturbative corrections are indicated by dashed (magenta) curves in (right) and (bottom).

All NLO predictions for different PDFs are similar and compatible with the data, even though these predictions have tendency to systematically overestimate the central values of the measured forward jet cross sections by $\sim 20\%$ in all p_T bins.

5.9. Forward-Central Dijet Production

Forward-central jet cross section measurement (Chatrchyan et al., 2012) is sensitive to both the multiplicity of jets and also their p_T distribution. Understanding the dynamics of forward jet production, with/without accompanying central jets is also necessary for modeling multijet backgrounds at the LHC. The selection procedure for the forward–central dijet production shown in Figure 5.38 (Cipriano, 2014) is similar to the one for the inclusive forward jet production. Additively, a central jet within $|\eta| < 2.8$ pseudorapidity with a $p_T > 35$ GeV is necessary.

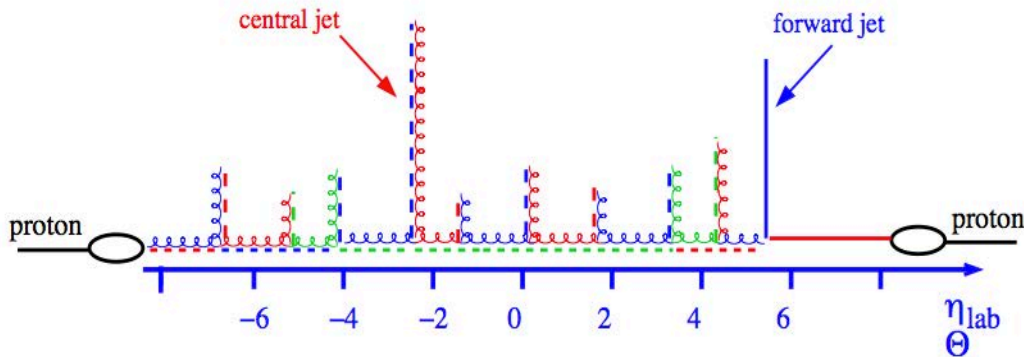


Figure 5.38. Feynman diagram for forward–central dijet production.

The associated production cross section of one central (c) jet and one forward (f) jet at $\sqrt{s} = 7$ TeV is given as (Zhu et al., 2011):

$$\frac{d^4\sigma}{dp_T^c dp_T^f d\eta^c d\eta^f} \quad (5.22)$$

The formula can be given for the forward (f) and central (c) regions separately:

$$\frac{d\sigma}{dp_T^f} = \frac{1}{\Delta\eta^f} \cdot \frac{d^4\sigma}{dp_T^c dp_T^f d\eta^c d\eta^f} \rightarrow p_T^c > 35 \text{ GeV} \wedge |\eta^c| < 2.8 \quad (5.23)$$

Dijet events were taken with the dijet trigger requiring two jets with p_T above 35 GeV. Trigger efficiencies were determined from the ratio of the yield of events involving forward-central jets that pass the HLT requirements. Figure 5.39 shows the reconstructed jet p_T spectrum for forward jets in dijet events. This is compared to MC events and analysed in the same way as the data. The data shown are calibrated through the JES normalisation, but not unfolded.

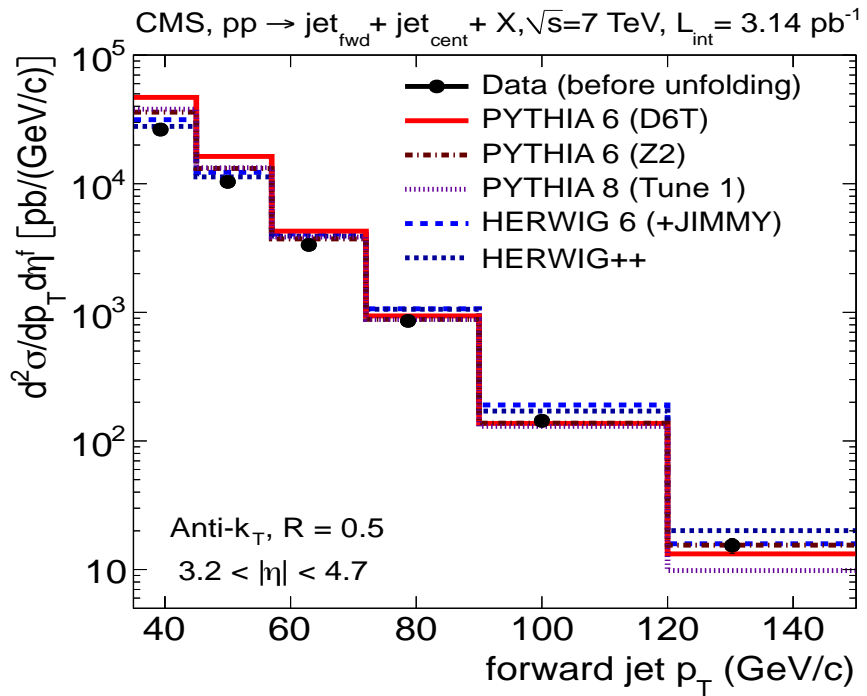


Figure 5.39. Measured differential cross sections for forward jets in dijet events as a function of p_T before unfolding the energy resolution (black dots), compared to detector-level MC simulations generated with different versions of PYTHIA and HERWIG for forward jets in dijet events.

The second correction (unfolding) of the measured jet spectrum was applied to determine the finite energy resolution of the calorimeters. For forward jets, the relative p_T resolution, obtained from full-simulation studies and verified by the momentum imbalance in dijet data is below 12% for $p_T > 35 \text{ GeV}/c$.

The JES uncertainties translate into uncertainties of the order of $\pm(20\text{--}30)\%$ in the final forward jet cross section. The $\pm 10\%$ uncertainty on the jet p_T resolution

(Fig. 5.39) translates into an uncertainty of 3 to 6% (increasing with p_T) on the final cross sections. Model dependence uncertainty which results from the difference between the PYTHIA 6 and HERWIG 6 event generators was found to be 3% and was added in quadrature. The uncertainty of the integrated luminosity was concluded to be 4% on the overall normalization of the spectra.

Different contributions to the systematic uncertainty were demonstrated as a function of jet p_T in Figure 5.40. In this figure the grey areas indicate the total uncertainty, whereas the two hatched areas show the uncertainties on the JES and the unfolding procedure. Here uncertainty on the calibration of the JES was calculated to be $\sim 30\%$. Statistical uncertainty was found to be 1-2% in the low p_T bin while this amount was 5-10 % for the highest bin. In consequence regarding systematic uncertainty, we can say that the statistical uncertainty is small and is calculated by adding individual contributions.

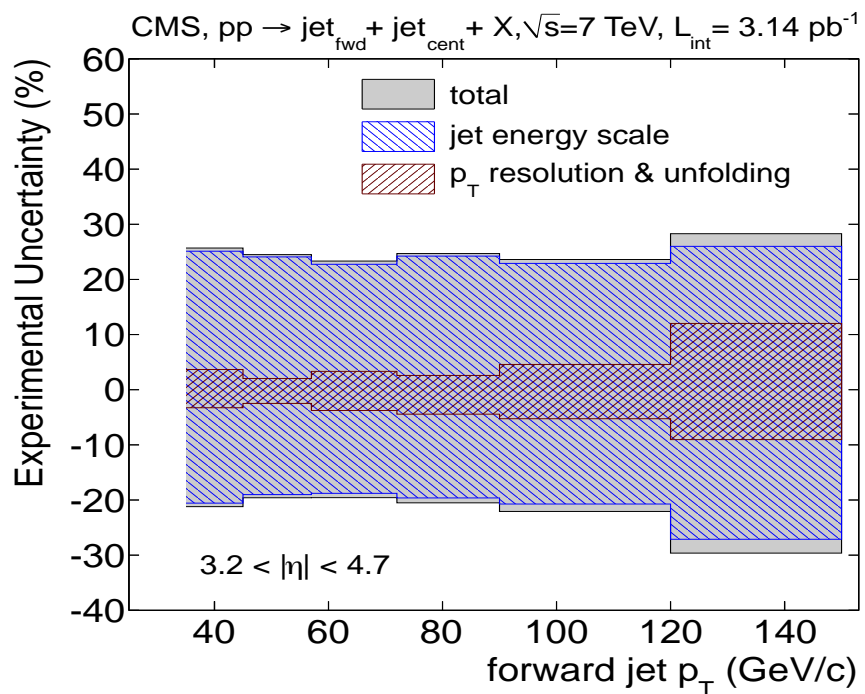


Figure 5.40. Systematic uncertainties as a function of jet p_T for forward jet spectra in dijet events. The outer limits of the grey areas show the overall uncertainties, from adding in quadrature uncertainties from the JES, the unfolding and the luminosity.

The fully corrected cross section for the production of at least one forward and at least one central jet is presented in Figure 5.41 for forward jets. In this figure the grey bands indicate the systematic uncertainties and the cross sections obtained with PYTHIA 6 for D6T and Z2 tunes, PYTHIA 8, POWHEG (using PYTHIA for parton showering and hadronisation) and CASCADE were superimposed on the data. On the other hand the cross sections obtained with HERWIG 6, HERWIG++, POWHEG (using HERWIG for parton showering and hadronisation) and HEJ were shown in the next Figure 5.42. The error bars on all data points reflect statistical uncertainties, with systematic uncertainties plotted as grey bands.

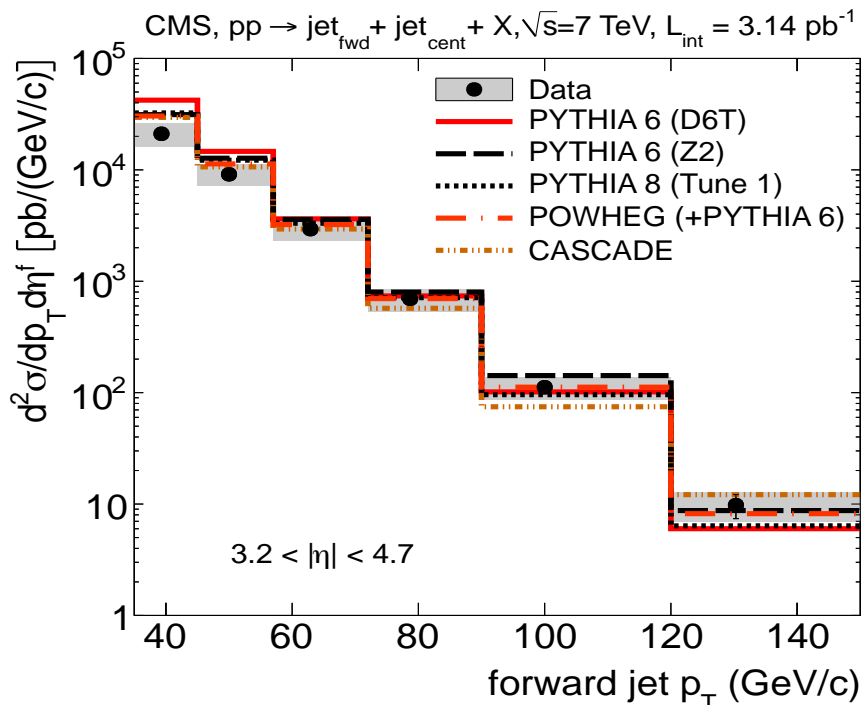


Figure 5.41. Differential cross sections as a function of jet p_T for dijet events with at least one forward jet for PYTHIA, POWHEG (+PYTHIA6), CASCADE.

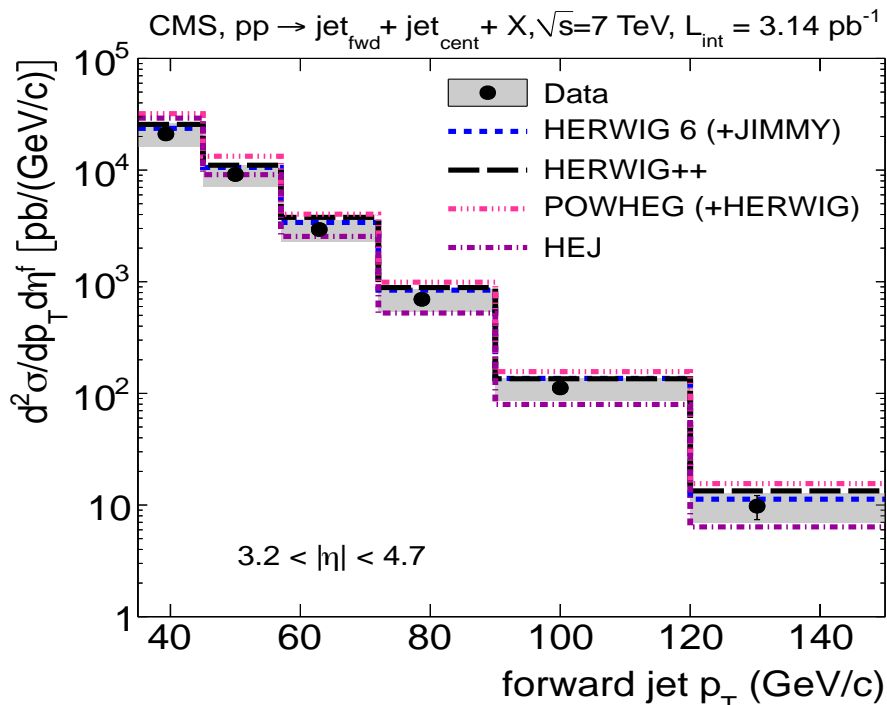


Figure 5.42. Differential cross sections as a function of jet p_T for dijet events with at least one forward jet for HERWIG, POWHEG (+HERWIG), HEJ.

Figure 5.43 and Figure 5.44 show the ratio of theory to data for differential cross sections as a function of p_T for forward jets produced in dijet events. Here the HERWIG 6 and HERWIG++ MC event generators appear to be consistent with the data. The other generators and different tunes, do not describe the data over the full range of p_T values. PYTHIA 8 with Tune 1 and PYTHIA 6 with Tune Z2 were more compatible with the data (but not tune D6T). Changes in the normalization of the underlying events and initial and final state radiation can only partially explain the inconstancy between PYTHIA and the data. The NLO MC POWHEG matched to the HERWIG parton shower reproduced well the dependence on p_T , however the normalization was overestimated by $\sim 40\%$. CASCADE predicts a different p_T -dependence which might come from the initial-state parton showers. The HEJ describes the data reasonably well but is used only at parton level here.

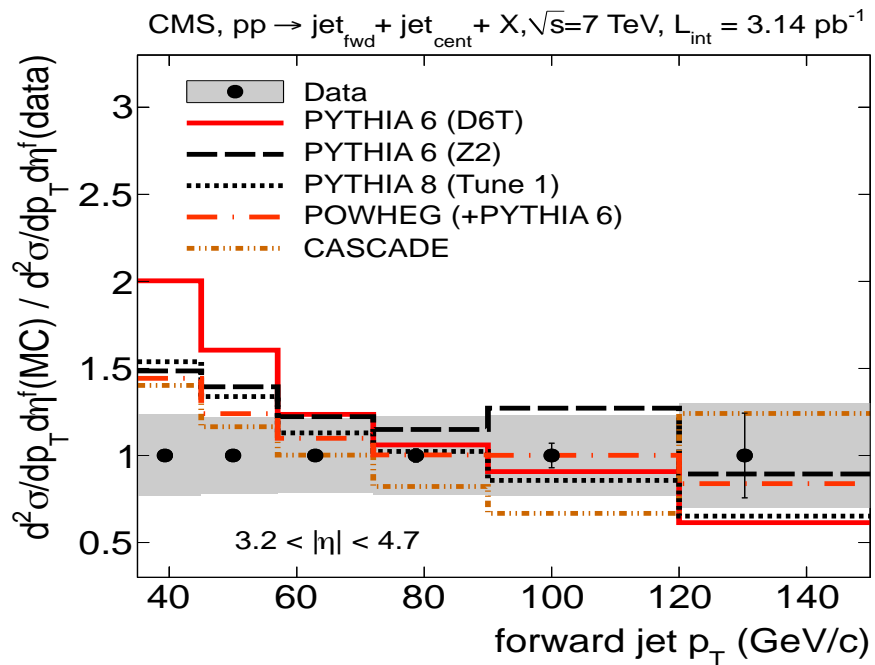


Figure 5.43. Ratio of theory to data for differential cross sections as a function of p_T , for forward jets produced in dijet events for PYTHIA, POWHEG (+PYTHIA6), CASCADE.

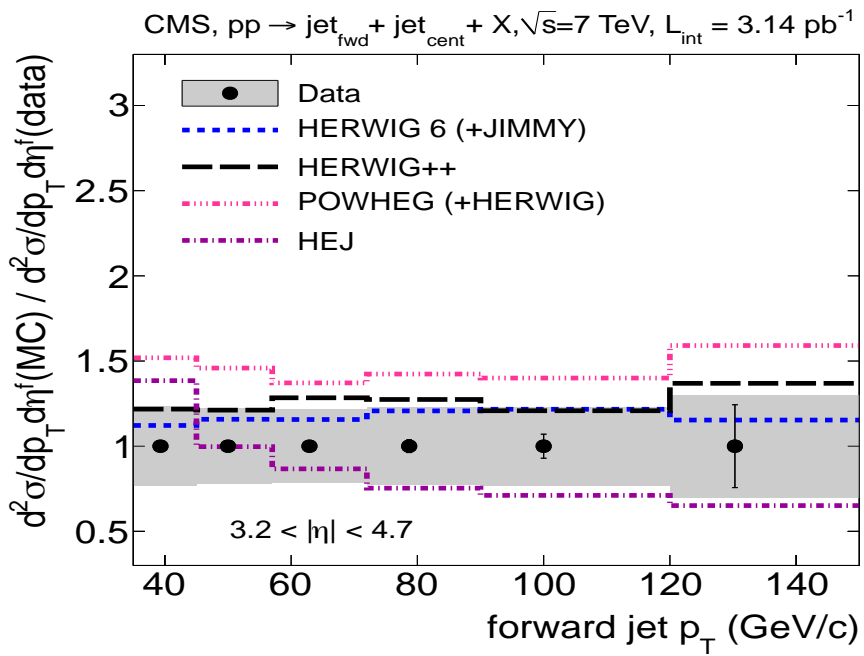


Figure 5.44. Ratio of theory to data for differential cross sections as a function of p_T , for forward jets produced in dijet events for HERWIG, POWHEG (+HERWIG), HEJ.

Summary of the p_T -dependent differential cross sections for inclusive forward jets (second column), and for forward (last column) jets in dijet events can be found in Table 5.5. The first (second) uncertainty reflects the statistical (systematic) contribution.

Table 5.5. The measured, fully corrected p_T differential jet cross sections and their associated uncertainties.

p_T bin (centre) GeV/c	$\frac{d^2\sigma}{dp_T d\eta}$ pb/(GeV/c)	$\frac{d^2\sigma}{dp_T^f d\eta^f}$ pb/(GeV/c)
35-45 (39.3)	$(89 \pm 0.2^{+24}_{-19}) \times 10^3$	$(21 \pm 0.2^{+5.4}_{-0.5}) \times 10^3$
45-57 (50.2)	$(20 \pm 0.1^{+4.9}_{-3.9}) \times 10^3$	$(9.2 \pm 0.1^{+2.2}_{-1.8}) \times 10^3$
57-72 (63.2)	$(4.4 \pm 0.04^{+1.0}_{-0.9}) \times 10^3$	$(2.9 \pm 0.06^{+0.7}_{-0.6}) \times 10^3$
72-90 (79.2)	$880 \pm 10^{+200}_{-180}$	$690 \pm 30^{+170}_{-140}$
90-120 (101.0)	$115 \pm 4^{+40}_{-25}$	$110 \pm 8^{+25}_{-25}$
120-150 (132.0)	$10 \pm 1.2^{+3}_{-3}$	$10 \pm 2.3^{+3}_{-3}$

6. CONCLUSIONS

The primary goal of the LHC is the search for new physics beyond the SM. Many models predict the production of new, coloured particles which eventually decay into quarks and gluons and observed as particle jets in the detector. Therefore, a certain understanding of the properties and production of jets in hadron-hadron collisions is necessary to study the underlying partonic QCD processes and parton density functions (PDFs) of the colliding hadrons. The large calorimetric coverage of CMS detector permits to perform a study of jet production for the first time in a region of pseudorapidity $|\eta| > 3$, which has never been investigated before (Cerci, Sunar Cerci et al., 2010). In this thesis three different measurements were presented. To find new physics, the detector first has to be understood completely by studying the detector response and resolution for known SM processes. For this reason in the first study using the official Spring10 PYTHIA MC QCD event samples, jet response, jet energy resolution and jet position resolution analyses have been performed. In order to reconstruct jets in the HF calorimeter anti- k_T jet algorithm in the $3.2 < |\eta| < 4.7$ pseudorapidity range were used. Jet reconstruction and performance studies indicate that the response curves for forward jets were flat in the range $p_T^{GenJet} = 20\text{-}120 \text{ GeV}/c$. On the other hand the p_T resolution for forward jets was found to be $\sim 15\%$ at $p_T = 20 \text{ GeV}$ and decreased to $\sim 12\%$ for $p_T \geq 100 \text{ GeV}$, while the jet position resolutions kept $\sigma_{\phi,\eta} = 0.035$ at $p_T = 20 \text{ GeV}$ and $\sigma_{\phi,\eta} \sim 0.02$ above 100 GeV.

The main part of this thesis was dedicated to the study of jet cross sections. The hadronic final state can be characterized from the point of the production rate of jets, in other words jet cross sections. In the second analysis, inclusive forward jets cross section have been measured as a function of p_T , in the $3.2 < |\eta| < 4.7$ pseudorapidity range with transverse momentum range of 35-150 GeV using 3.14 pb⁻¹ data. The jet transverse momentum spectrum was obtained with the anti- k_T algorithm ($R = 0.5$) in the HF calorimeter. Data was compared with the different MC samples as well as with the theoretical models, and certain models were found to

describe the data better within the uncertainty band. The results show that POWHEG + PYTHIA 6 gives the best description while PYTHIA 6 and PYTHIA 8 describe the data reasonably well. CASCADE underestimates the cross-section while HERWIG 6 + JIMMY overestimate it. Within the large theoretical and experimental uncertainties NLOJET++ overrate the data. The total uncertainties are around $\pm 25\text{--}30\%$ and the jet energy scale is the dominant systematic uncertainty. This measurement is important because it provides the first test of perturbative QCD calculations in the forward region at the highest energies, in addition, it is the first cross-check for QCD background.

In the third measurement, the single-jet cross section has been calculated using 3.14 pb^{-1} data in pp collisions at $\sqrt{s} = 7 \text{ TeV}$ for the two leading jets in inclusive dijet events including at least one forward ($3.2 < |\eta| < 4.7$) and one central ($|\eta| < 2.8$) jet. Jets were reconstructed using the anti- k_T algorithm ($R = 0.5$) in the p_T range $35\text{--}150 \text{ GeV}/c$. The total systematic uncertainties were found to be $\pm(20\text{--}30)\%$ and were dominated by the absolute JES. Within the experimental and theoretical uncertainties, pQCD calculations, as implemented in PYTHIA and HERWIG, as well as in the combined DGLAP+BFKL resummation of the CASCADE model and with the extra wide-angle gluon radiations added in the HEJ model, are in a good consistent with the measured inclusive single-jet forward cross section. NLO calculations using recent sets of PDF also describe the data, but on the contrary the predicted absolute cross sections are about 20% larger.

For the inclusive dijet events, in the forward regions, above $p_T = 35 \text{ GeV}/c$ all PYTHIA tunes were found to overestimate the absolute cross sections for the simultaneous production of jets. NLO contributions from POWHEG to both of these parton shower MC generators increase the cross sections at all p_T and are consequently responsible for the disagreement with data. POWHEG + PYTHIA 6, which was the best prediction for inclusive forward jet cross section, gives similar result as PYTHIA 6 alone. CCFM CASCADE have problem describing the data for low- p_T forward jets. Finally HEJ gives the best description being closely followed by HERWIG 6 and HERWIG ++.

The measurements presented in this thesis offer an important test of pQCD in the forward region of hadronic collisions at the highest available energies and also provide a first check of models for multijet production concerning other processes at the LHC, characterised by forward/backward jet production. The forward-central dijet analysis gives information on multiparton radiation, DGLAP and BFKL dynamics and can contribute to the study of the QCD background in the search of the Higgs boson produced via vector-boson fusion (Chatrchyan et al., 2012).

All the measurements presented in this thesis were approved by physics committee in the CMS and consequently published.

REFERENCES

AAD, G., et al., 2008, “The ATLAS Experiment at the CERN Large Hadron Collider”. *Journal of Instrumentation* 3, 08, p. S08003 (2008).

AAMODT, K., et al., 2008, “The ALICE experiment at the CERN LHC”. *Journal of Instrumentation* 3, 08, p. S08002 (2008).

AARON, F., et al., 2010, H1 and ZEUS Collaboration, “Combined Measurement and QCD Analysis of the Inclusive ep Scattering Cross Sections at HERA”. *JHEP* 01 (2010) 109, arXiv:0911.0884, doi:10.1007/JHEP01(2010)109.

ABDULLIN, S et al., 2009, CMS ECAL/HCAL Collaboration, “The CMS barrel calorimeter response to particle beams from 2 to 350 GeV/c”, *The European Physical Journal C - Particles and Fields* 60 (2009) 359–373. doi:10.1140/epjc/s10052-009-0959-5.

ADRIANI, O., et al., 2008, “The LHCf detector at the CERN Large Hadron Collider”. *Journal of Instrumentation* 3, 08, p. S08006 (2008).

AGOSTINELLI, S., et al., 2003, “GEANT4: A simulation toolkit”, *Nucl. Instrum. Meth.* A506 250-303 (2003).

AITCHISON, I. J. R., 2007, “Supersymmetry in Particle Physics – An Elementary Introduction”. Cambridge University Press, 2007. ISBN 978-0-521-88023-7.

AKGUN, U., 2003, “CMS HF Calorimeter PMTs and Xi Baryon(+)c Lifetime Measurement”, CERN THESIS.

ALEKHIN, S., et al., 2011, “The PDF4LHC Working Group Interim Report”, arXiv:1101.0536.
_____, 2010, *Phys. Rev.* D81, 014032 (2010) [arXiv:0908.2766].

ANDERSEN, J. R., LONNBLAD, L., SMILLIE, J. M., 2011, “A Parton Shower for High Energy Jets”, arXiv:1104.1316 [hep-ph].

ANDERSEN, J. R., and SMILLIE, J. M., 2011, “Multiple Jets at the LHC with High Energy Jets”, *JHEP* 06 (2011) 010, arXiv:1101.5394, doi:10.1007/JHEP06(2011)010.

ANELLI, G., et al., 2008, “The TOTEM Experiment at the CERN Large Hadron Collider”. *Journal of Instrumentation* 3, 08, p. S08007 (2008).

ASLANOGLU, X., et al., 2007, “First Performance Studies of a Prototype for the CASTOR Forward Calorimeter at the CMS Experiment”, arXiv:0706.2576v3.

AUGUSTO ALVES JR, A., et al., 2008, “The LHCb Detector at the LHC”. *Journal of Instrumentation* 3, 08, p. S08005 (2008).

BAHR, M., et al., 2008, “Herwig++ Physics and Manual,” *Eur. Phys. J.* C58 (2008) 639–707, arXiv:0803.0883, doi:10.1140/epjc/s10052-008-0798-9.

BALL, R. D., et al., 2011, “Impact of Heavy Quark Masses on Parton Distributions and LHC Phenomenology”, *Nucl. Phys.* B849 (2011) 296–363, arXiv:1101.1300, doi:10.1016/j.nuclphysb.2011.03.021.

_____, 2009, *Nucl. Phys.* B809, 1 (2009) [arXiv:0808.1231v4].

BAWA, H. S., 2007, “Some Aspects of High E_T jets in p-p collisions at LHC” CERN-THESIS-2009-022.

BAYATIAN, G.L., et al., 2006, CMS Physics, “Tehcnical Design Report, Volume I: Detector Performance and Software”, 2006-001, CMS TDR 8.1, CERN/LHCC.

_____, 2000a, CMS TriDAS Project Technical Design Report Volume 1.

_____, 2000b, CMS TriDAS Project Technical Design Report Volume 2: The Data Acquisition System, Technical Report 2002-26 CERN/LHCC.

_____, 1998, The Tracker Project Technical Design Report, CERN-LHCC-98-006 (1998).

_____, 1997a, CMS Electromagnetic Calorimeter Project Technical Design Report, CERN/LHCC-97-33.

_____, 1997b, CMS Hadronic Calorimeter Project Technical Design Report, CERN/LHCC-97-31.

_____, 1997c, CMS Magnet Technical Design Report, CERN/LHCC-97-10.

_____, 1997d, CMS Muons Technical Design Report, CERN/LHCC-97-32.

BERARDI, V., et al., 2004, TOTEM Technical Design Report, “Total Cross Section, Elastic Scattering and Diffraction Dissociation at the Large Hadron Collider at CERN”.

BERINGER, J., et al., 2012, “Review of Particle Physics”. Phys. Rev. D. 86, 010001 (2012) (available at [<http://pdg.lbl.gov/2012/reviews/rpp2012-rev-qcd.pdf>]).

BERNET, C., et al., 2009, “Particle-Flow Event Reconstruction in CMS and Performance for Jets, Taus, and MET”, CMS-PAS-PFT-09-001.

BHATTI, A., and LINCOLN, D., 2010, “Jet Physics at the Tevatron”, arXiv:1002.1708 [hep-ex].

BJORKEN, J. D., 1969, “Asymptotic sum rules at infinite momentum”, Phys. Rev. 179, 1547–1553 (1969).

BLAZEY, G. C., et al., 2000, Run II Jet Physics: Proceedings of the Run II QCD and Weak Boson Physics Workshop, [arXiv:hep-ex/0005012].

BOYARKIN, O. M., 2007, “Introduction to Physics of Elementary Particles”, 2007.

BRONA, G., CERCI, S., et al., 2010, “First Measurement of Forward Jets in proton–proton Collisions at $\sqrt{s} = 7$ TeV in CMS”, CMS AN-2010/102.

BRUNING, O. S., et al., 2004, LHC Design Report, Technical Report, CERN-2004-003.

BUTTERWORTH, J. M., FORSHAW, J. R., and SEYMOUR, M. H., 1996, “Multiparton interactions in photoproduction at HERA”, Z. Phys. C72 (1996) 637, arXiv:hep-ph/9601371, doi:10.1007/s002880050286.

CAMPBELL, J.M., HUSTON, J.W., STIRLING, W.J., 2006, <http://arxiv.org/pdf/hep-ph/0611148v1>.

CATANI, S., et al., 2000, arXiv:hep-ph/0005025v1.

_____, 1990, Nucl. Phys. B 336 18.

CERCI, S., et al., 2009, “Low-x QCD studies with forward jets in proton-proton collisions at $s = 14$ TeV”, AIP Conference Proceedings 1105, 28 (2009); DOI: 10.1063/1.3122196.

CERCI, S., SUNAR CERCI, D., et al., 2010, “Measurement of the Inclusive Forward Jet Cross Section in pp Collisions at $\sqrt{s} = 7$ TeV in CMS”, CMS AN-2010/243.

CHATRCHYAN, S., et al., 2012, “CMS Collaboration, “Measurement of the inclusive production cross sections for forward jets and for dijet events with one forward and one central jet in pp collisions at $\sqrt{s} = 7$ TeV”, 10.1007/JHEP06(2012)036, arXiv:1202.0704 [hep-ex]. Published in JHEP 1206 (2012) 036, CMS PAPER FWD-11/002.

_____, 2010a, “Inclusive forward jet production cross sections in proton–proton collisions at $\sqrt{s} = 7$ TeV”, CMS PAS FWD-10/003.

_____, 2010b, CMS Collaboration, “Jet Energy Corrections determination at $\sqrt{s} = 7$ TeV”, CMS PAS JME-10/010 (2010).

_____, 2008, “The CMS experiment at the CERN LHC”, The CMS Collaboration JINST 3 S08004.

CHEUNG, S.L., 2011, “Search for Dijet Resonances in $\sqrt{s} = 7$ TeV Proton-Proton Collisions with the ATLAS Detector at the LHC”, CERN-THESIS-2011-162.

CIPRIANO, P., 2014, “Small-x QCD physics probed with jets in CMS”, arXiv:1402.2100 [hep-ex].

DITTMAR, M., et al., 2005, in Proceeds. HERA-LHC Workshop, hep-ph/0511119.

DOKSHITZER, Y.L., et al., 1991, “Basics of Perturbative QCD”.

D’ENTERRIA, D., 2009, “Forward jets physics in ATLAS, CMS and LHCb”, arXiv:0911.1273v1 [hep-ex].

_____, 2006, “Low-x QCD Physics from RHIC and HERA to the LHC”, arXiv:hep-ex/0610061v2.

ELLIS, R. K., et al., 1996, “QCD and Collider Physics”, Cambridge University Press.

ELLIS, S. D., et al., 2007, “Jets in Hadron-Hadron Collisions”, arXiv:hep-ph/0712.2447v1.

EVANS, L., and P. B. (editors), 2008, LHC Machine, Journal of Instrumentation 3 (2008), no. 08 S08001.

GLEYZER, S., 2011, “Search for the Dark Matter Signature in the Lepton Jet Final State at $\sqrt{s} = 7$ TeV”, CERN-THESIS-2011-055, CMS-TS-2011-037.

GLUCK, M., et al., 2008, Phys. Lett. B664, 133 (2008), [arXiv:0801.3618].

GRACHOV, O. A et al., 2006, “Status of zero degree calorimeter for CMS experiment”, AIP Conf. Proc. 867 (2006) 258 [nucl-ex/0608052].

HAREL, A., 2010, “Forward jet quality criteria”, CMS Analysis Note 2010/067.

_____, 2009, ”Calorimeter Jet Quality Criteria for the First CMS Collision Data”, The CMS Collaboration CMS-PAS-JME-09-008.

HAUTMANN, F., 2013, “ Soft Gluons and Jets at the LHC”, arXiv:1304.8133v1 [hep-ph], 30 Apr 2013.

HEINRICH, M., 2011, “A Jet Based Approach to Measuring Soft Contributions to Proton-Proton Collisions with the CMS Experiment”, CERN-THESIS-2011-190.

HIGGS, P., 1964, Phys. Rev. Lett. 13 (1964) 508–509.

HOYER, E. H., TURNER. W. C., and MOKHOV, N. V., 1998. Absorbers for the High Luminosity Insertions of the LHC, in Proceedings of the 6th European Particle Accelerator Conference, Stockholm Sweden (1998), <http://accelconf.web.cern.ch/AccelConf/e98/PAPERS/MOP13C.PDF>.

JUNG, H., 2001, “The CCFM Monte Carlo Generator CASCADE”, (2001), [hep-ph/0109102].

JUNG, H., et al., 2010, “The CCFM Monte Carlo generator CASCADE 2.2.0”, Eur. Phys. J. C79 (2010) 1237, arXiv:1008.0152.

KARAGIORGI, G., et al., 2007, “Leptonic CP violation studies at MiniBooNE in the (3 + 2) sterile neutrino oscillation hypothesis”. Phys. Rev. D, 75(1):013011, Jan 2007.

KIRSCHENMANN, H., 2010, “Exploitation of Jet Properties for Energy Scale Corrections for the CMS Calorimeters”, DESY-THESIS-2011-006, CERN-THESIS-2010-293 CMS-TS-2011-002.

KLUGE, T., RABBERTZ, K., and M. Wobisch., 2008, “fastNLO-fast pQCD calculations for hadron induced processes”. <http://hepforge.cedar.ac.uk/fastnlo>.

_____, 2006 “Fast pQCD calculations for PDF fits”, in 14th International Workshop on Deep Inelastic Scattering (DIS 2006), 20-24 Apr 2006, p. 483. Tsukuba, Japan, April, 2006, arXiv:hep-ph/0609285.

KOUSOURIS, K., et al., 2010, “Measurement of the Relative Jet Energy Scale in CMS with pp Collisions at 7 TeV”, CMS AN-2010/139.

LAI, H. L., et al., 2010, “New parton distributions for collider physics”, *Phys.Rev. D82* (2010) 074024.
arXiv:1007.2241, doi:10.1103/PhysRevD.82.074024.

_____, 2000, CTEQ Collaboration, “Global QCD analysis of parton structure of the nucleon: CTEQ5 parton distributions”, *Eur. Phys. J. C12* (2000) 375–392, arXiv:hep-ph/9903282, doi:10.1007/s100529900196.

LASTOVICKA, T., 2004, “Measurement of the Inclusive Deep Inelastic Scattering Cross Section at low Q^2 ”, H1-Thesis.

LAZARIDIS, C., 2011, “Jets Produced in Association with z Bosons in CMS at the LHC”, CERN-THESIS-2011-105, CMS-TS-2011-044.

MARCHESINI, G., et al., 1992, “HERWIG: A Monte Carlo event generator for simulating hadron emission reactions with interfering gluons. Version 5.1, April 1991”, *Comput. Phys. Commun.* 67 (1992) 465. doi:10.1016/0010-4655(92)90055-4.

MARTIN, A. D., et al., 2009, “Parton distributions for the LHC”, *Eur. Phys. J. C63* (2009) 189–285, arXiv:0901.0002, doi:10.1140/epjc/s10052-009-1072-5.

_____, 2002, “MRST2001: Partons and a_s from precise deep inelastic scattering and Tevatron jet data”, *Eur. Phys. J. C23* (2002) 73–87, arXiv:hep-ph/0110215, doi:10.1007/s100520100842.

NADOLSKY, P. M., et al., 2008, *Phys. Rev. D78*, 013004 (2008), [arXiv:0802.0007].

NAGY, Z., 2003, “Next-to-leading order calculation of three jet observables in hadron hadron collision”, *Phys. Rev. D68* (2003) 094002, arXiv:hep-ph/0307268, doi:10.1103/PhysRevD.68.094002.

NASON, P., and WEBER, B., 2012, “Next-to-Leading-Order Event Generators”, arXiv:1202.1251 [hep-ph].

PETRUKHIN, A., 2010, “Structure Function Measurements at HERA”, arXiv-hep-ex:1005.5612v1.

PINFOLD, J. L., et al., 2009, Technical Design Report of the MoEDAL Experiment. Technical Report, CERN-LHCC-2009-006. MoEDAL-TDR-001, CERN, Geneva (2009).

PLACAKYTE, R., 2011, “Parton Distribution Functions”, arXiv:1111.5452v4 [hep-ph].

PUMPLIN, J., et al., 2002, “New generation of parton distributions with uncertainties from global QCD analysis”, JHEP 07 (2002) 012, arXiv:hep-ph/0201195, doi: 10.1088/1126-6708/2002/07/012.

RABBERTZ, K., 2012, review talk at ISMD 2012, Kielce, September 2012.

RALICH, R. M., 2009, “Study of b Quark Pair Production Mechanisms in pp Collisions with the CMS Experiment at LHC”, CERN-THESIS-2009-021, CMS-TS-2010-040.

SALAM, G. P., 2010, “Towards Jetography”, arXiv-hep-ph:0906.1833.

_____, 2007, “A Practical Seedless Infrared Safe Cone Algorithm”, arXiv-hep-ph:0705.2696.

SALAM, G.P., and SOYEZ, G., 2007, “A practical seedless infrared-safe cone jet algorithm”. JHEP, 05:086.

SANUDO, S., 2009, “CMS detector geometry reconstructed with the Link alignment system”, CERN-THESIS-2009-155, CMS-TS-2010-001.

SCHEURER, A., 2008, “Algorithms for the identification of b- Quarks Jets with First Data at CMS”, CERN-THESIS-2008-133, CMS-TS-2008-019.

SCHRODER, M., 2012, “Quality of Jet Measurements and Impact on a Search for New Physics at CMS”, CERN-THESIS-2012-176.

SJOSTRAND, T., MRENNA, S., and SKANDS, P., 2008, “A Brief Introduction to PYTHIA8.1”, Comput. Phys. Commun. 178 (2008) 852, arXiv:0710.3820, doi:10.1016/j.cpc.2008.01.036.

_____, 2006, “PYTHIA 6.4 Physics and Manual”, JHEP 0605:026,2006 and arXiv-hep-ph:0603175v2.

SOPER, D. E., 1997, “Basics of QCD Perturbative Theory”, arXiv:hep-ph/9702203v1.

STOBER, F. M., 2008, “Study of Three-Jet Topologies and first Event Simulation with the Event Generator Herwig++ for the CMS experiment at the LHC”, CERN-THESIS-2008-114, CMS-TS-2010-002, IEKP-KA-2008-28.

TRICOLI, A., 2006, Acta Physica Polonica B-37 No 3.

ZHU, B., et al., 2011, “Measurement of the cross section of a central and a forward jet associated production”, CMS AN-2011/36.

ZIELINSKI, M., et al., 2010, “Jet Performance in pp Collisions at 7 TeV”, CMS-PAS-JME-10-003.

<http://www.hep.phy.cam.ac.uk/theory/webber/MCatNLO/>

<http://www.lhc-closer.es/1/3/4/0>

<http://inspirehep.net/record/837874/plots>

<http://cms.web.cern.ch/news/resistive-plate-chambers>

<https://inspirehep.net/record/1120513/plots>

http://en.wikipedia.org/wiki/Higgs_boson

<http://lpc.web.cern.ch/lpc/>

CURRICULUM VITAE

Semiray was born on October 29, 1979, in Adana, Turkey. She finished her high school education in Adana, 1996. She received her Bachelor's degree in Physics in 2002 from Çukurova University and got the master degree in High Energy Physics from Çukurova University in 2007 and then started her PhD study at the same year.

APPENDIX

A. Unfolding to the Cross Section

Acceptance, background plots were shown as a function of corrected PF jets p_T for PYTHIA 6.4 MC generator in Figure A.1.

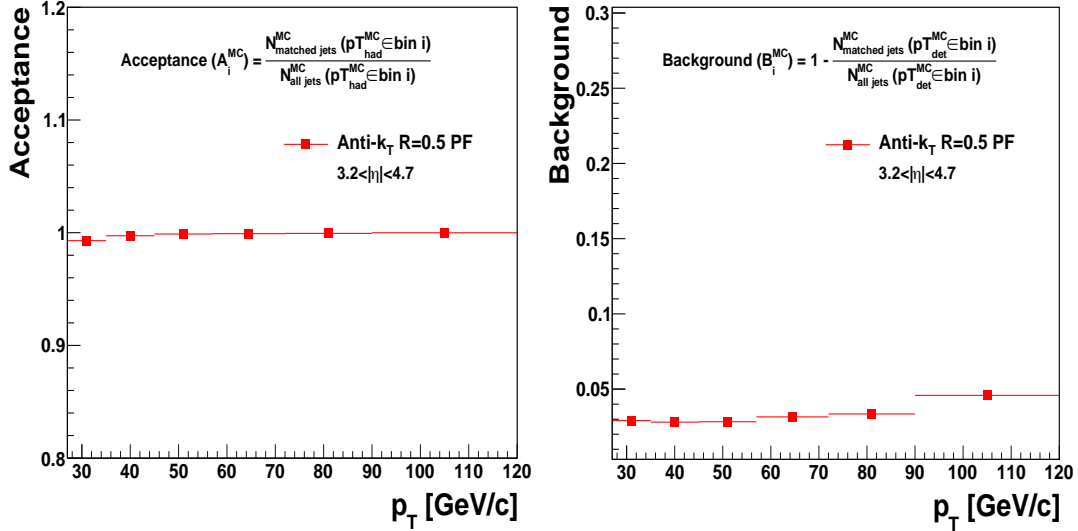


Figure A.1. The acceptance (left) and background (right) as a function of corrected PF jets p_T for PYTHIA 6.4.

Purity, stability plots were shown as a function of corrected PF jets p_T for PYTHIA 6.4 MC generator in Figure A.2.

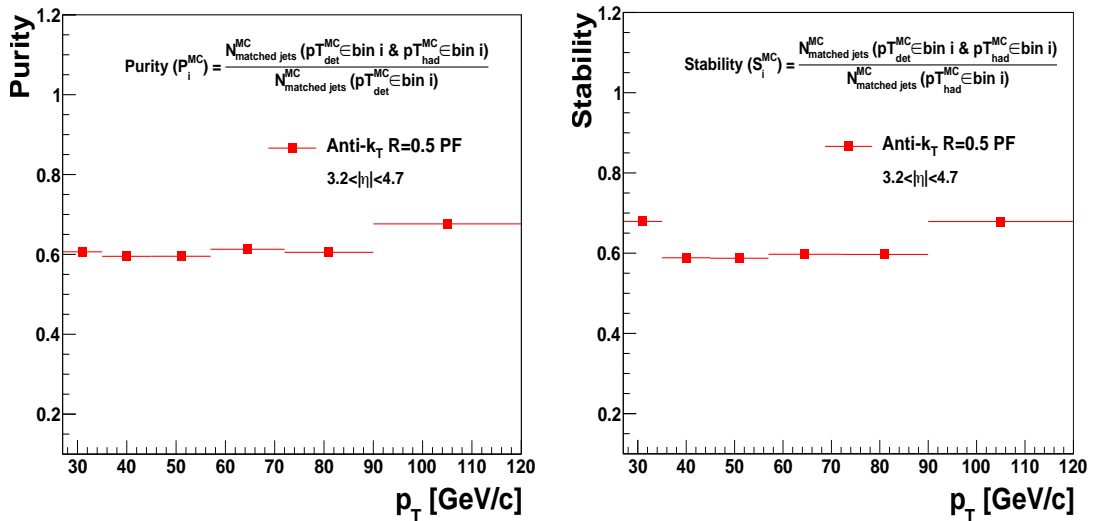


Figure A.2. The purity (left) and stability (right) as a function of corrected PF jets p_T for PYTHIA 6.4.

B. Inclusive Forward Jet Cross Section

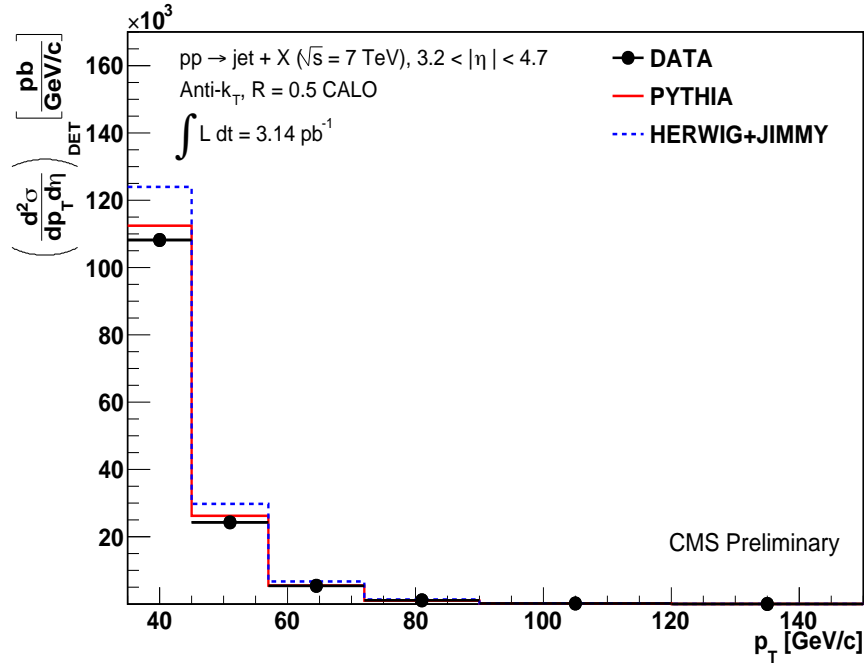


Figure B.1. Inclusive Forward Calo jets p_T cross section on detector level for DATA and MC simulations, PYTHIA 6.4 and HERWIG + JIMMY.

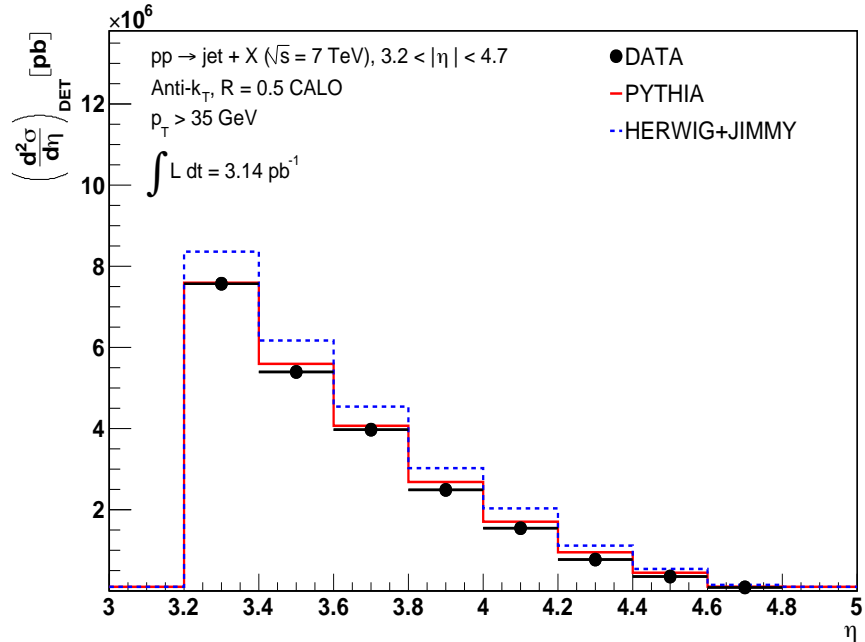


Figure B.2. Inclusive Forward CaloJets η cross section on detector level for DATA and MC simulations, PYTHIA 6.4 and HERWIG + JIMMY.

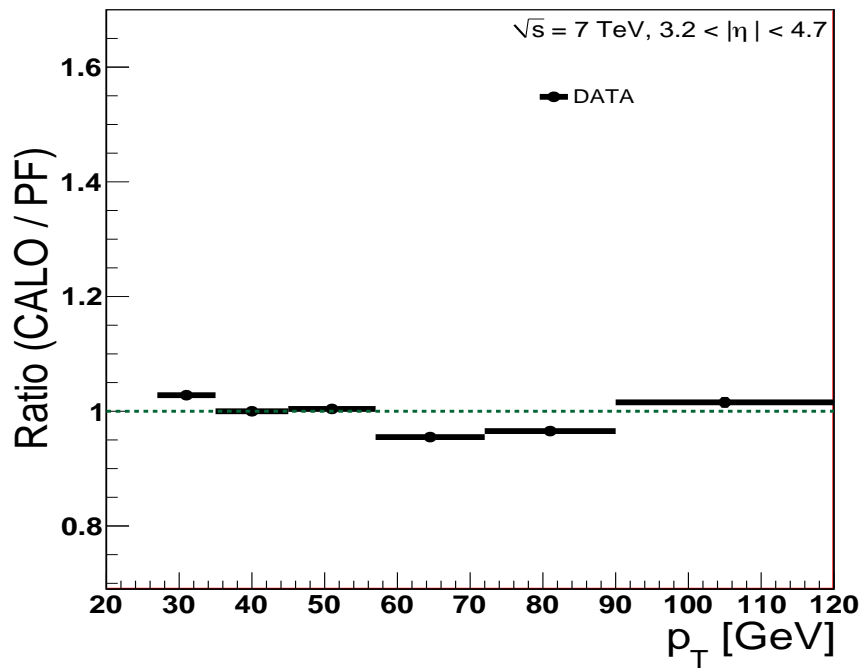


Figure B.3. Inclusive forward CaloJets vs. PF jets.

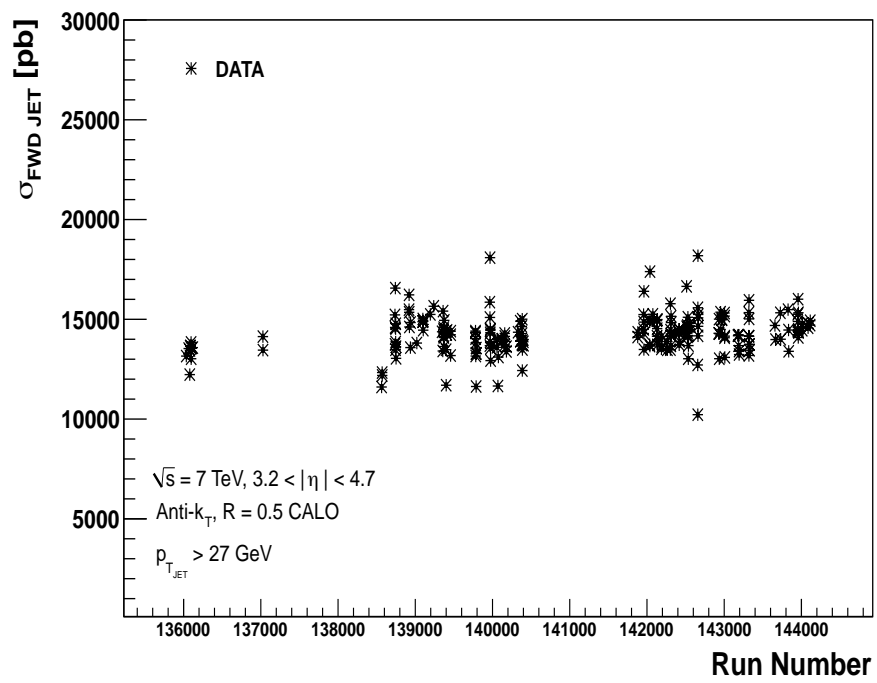


Figure B.4. Lumi yield plot.

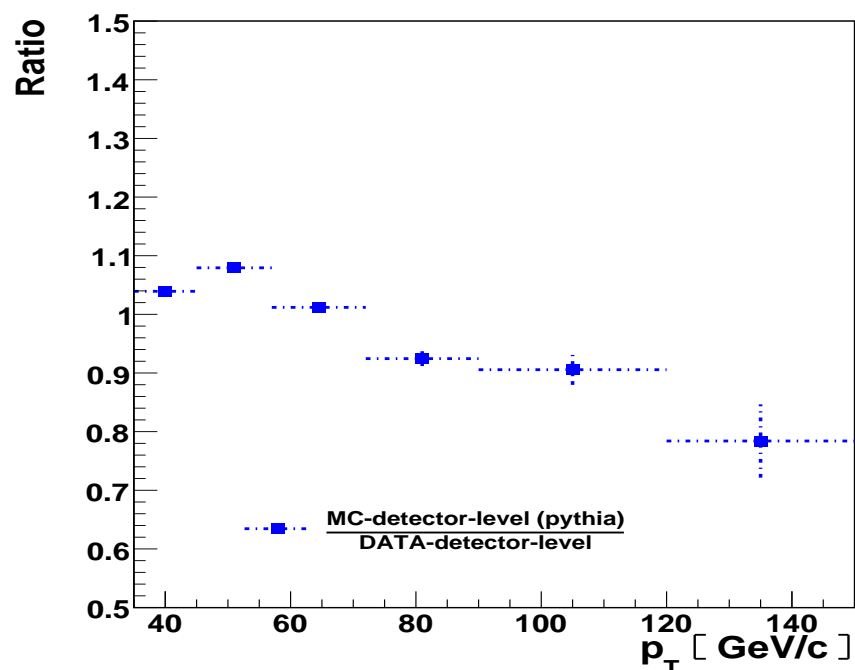


Figure B.5. Detector level comparison between data and MC (PYTHIA) simulation.

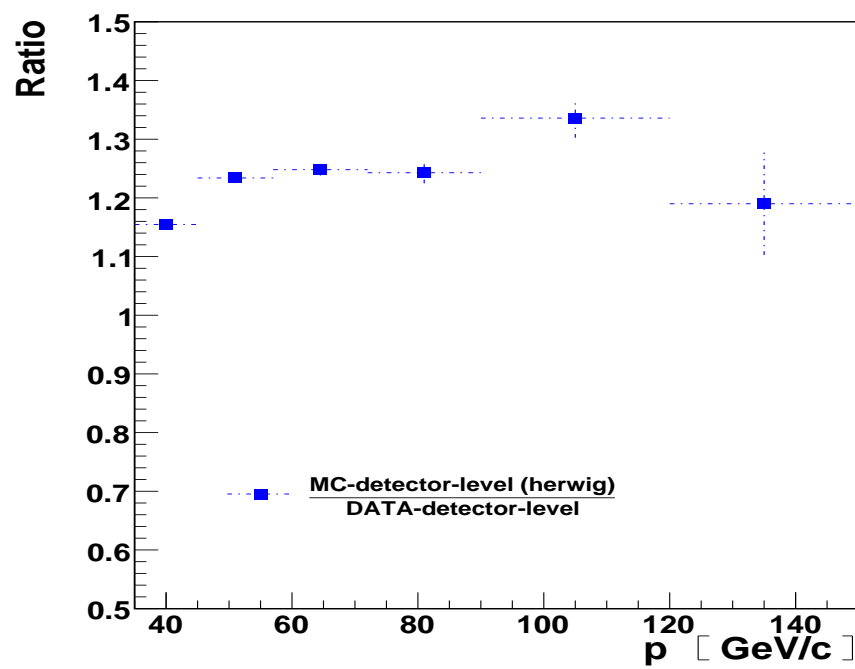


Figure B.6. Detector level comparison between data and MC (HERWIG) simulation.

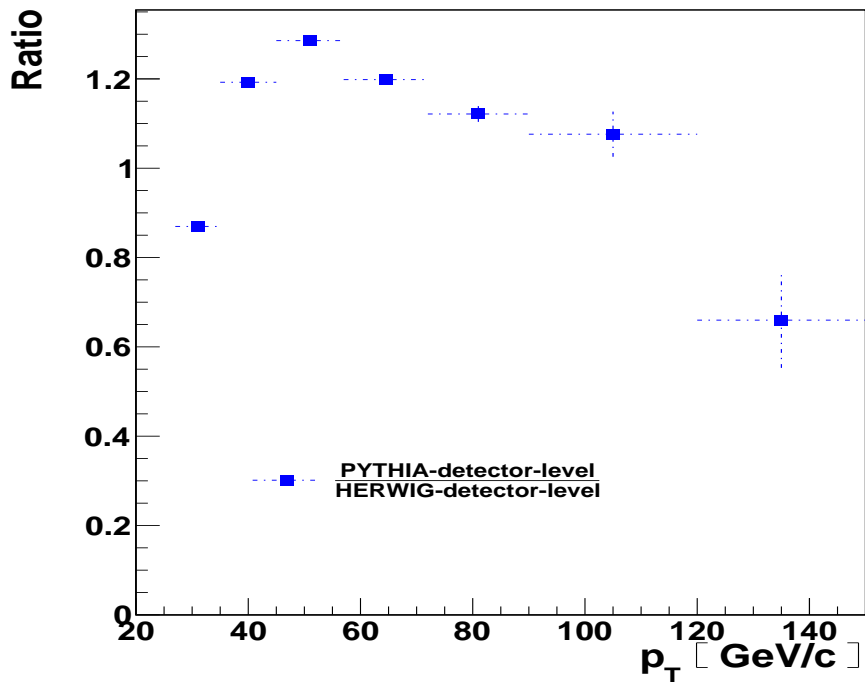


Figure B.7. Detector level comparison between PYTHIA and HERWIG.

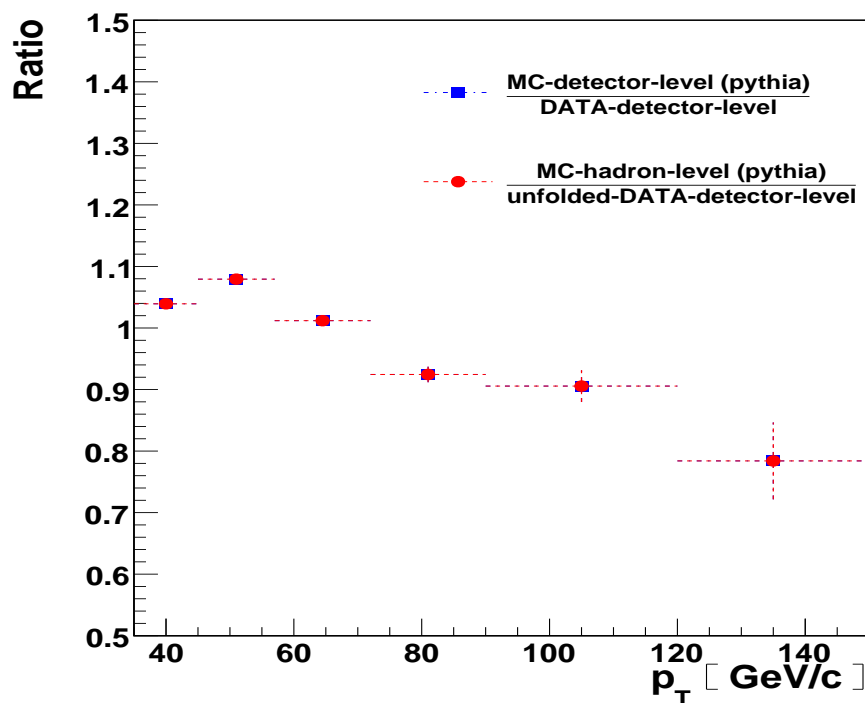


Figure B.8. Comparison between PYTHIA and DATA both detector level and hadron-level.

C. Bin-to-Bin Correction : Ansatz Method

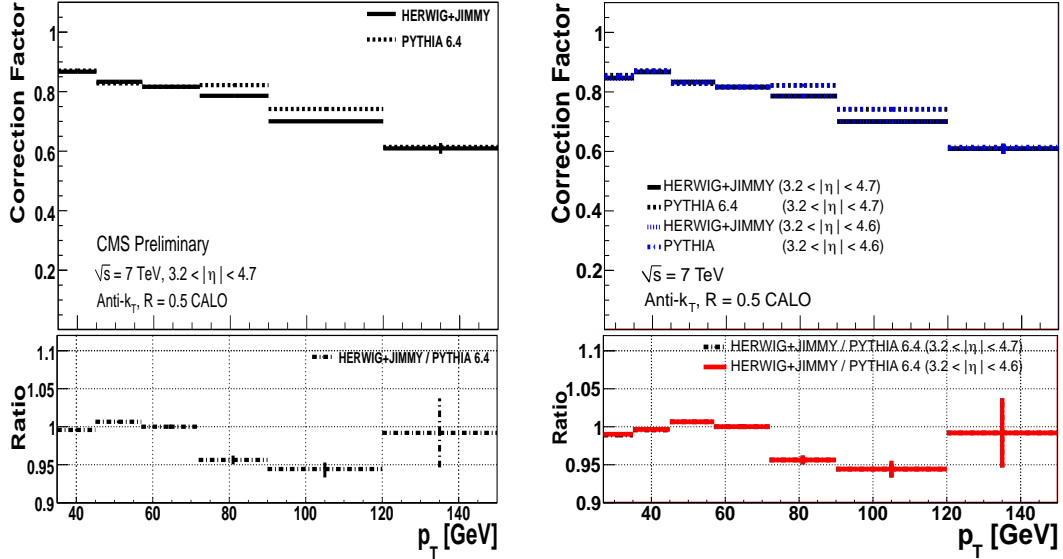


Figure C.1. Comparison of MC correction factor obtained from PYTHIA 6.4 and HERWIG + JIMMY MCs for CaloJets for $3.2 < |\eta| < 4.7$ (left), and a comparison of correction factor obtained within the range of $3.2 < |\eta| < 4.6$ (right).

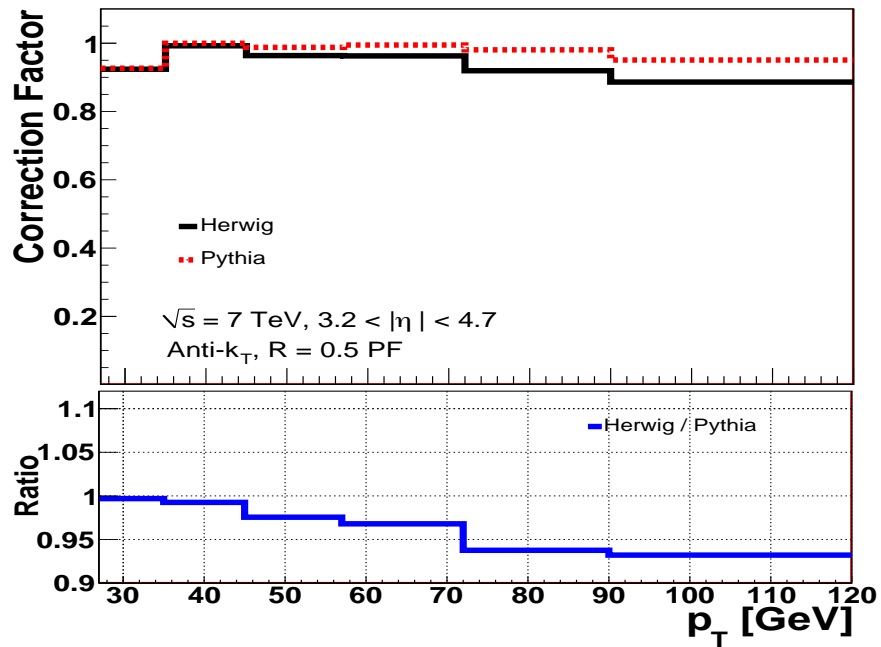


Figure C.2. A comparison of correction factor obtained within the range of $3.2 < |\eta| < 4.7$ for PF jets.

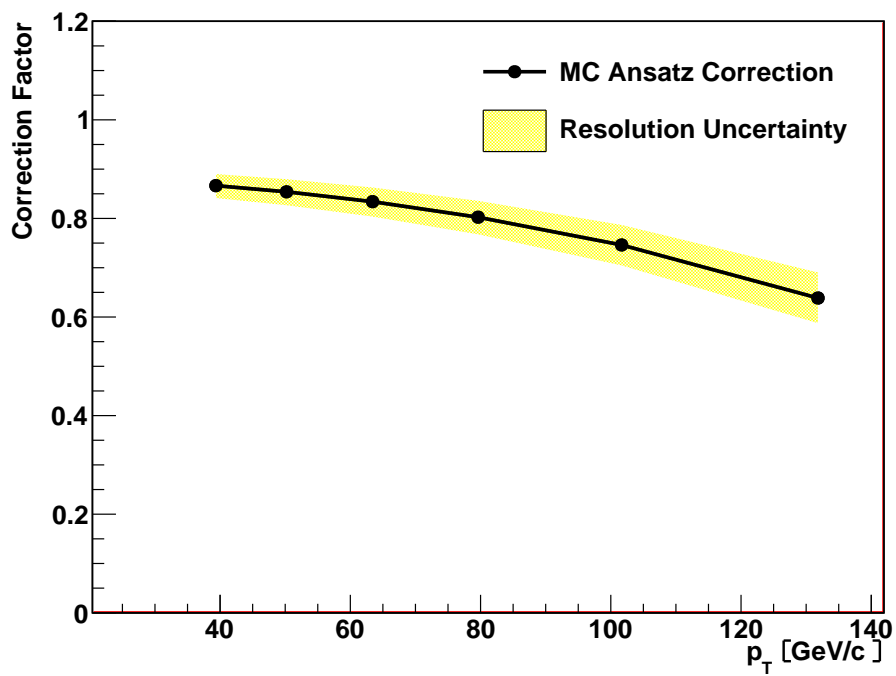
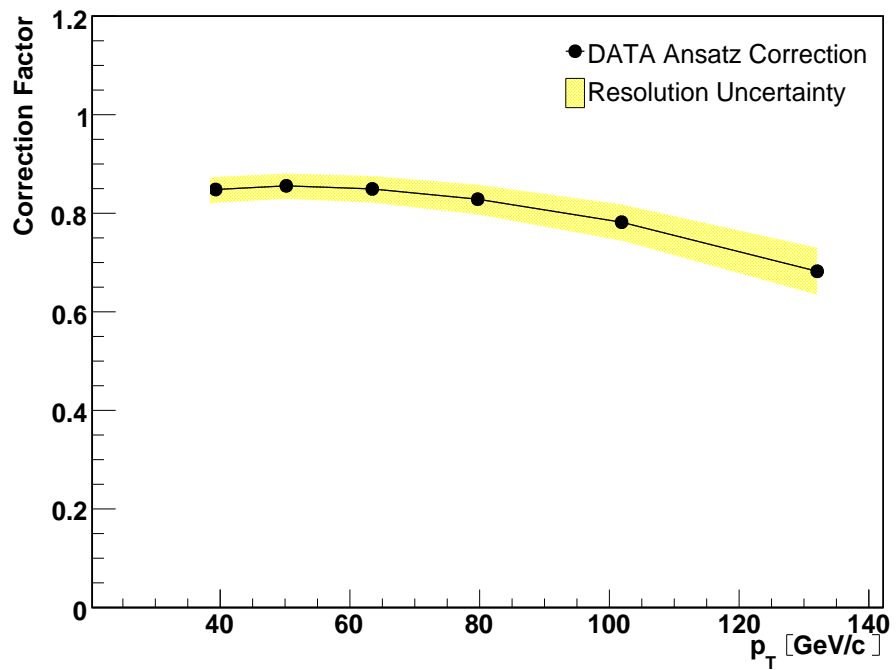


Figure C.3. Correction factor obtained from Ansatz method for data (top) and for PYTHIA 6.4 MC (bottom). Yellow band shows p_T resolution uncertainty.

D. Theoretical Uncertainties

Table D.1. Theoretical Uncertainty.

p_T [GeV]	NP	PDF	Scale	Total
35	10.35657 -10.23393	4.985139 -4.265666	1.105769 -5.608525	11.48909 -12.57816
45	7.521651 -7.399003	6.178792 -5.011699	0.8073563 -5.160905	9.657997 -10.47141
55	4.239107 -4.11646	7.372444 -5.757731	0.9565628 -5.160905	8.390071 -8.881421
70	3.493074 -3.370427	8.715303 -6.652971	0.9565628 -5.459318	9.310669 -9.286509
87	1.702596 -1.579948	10.9534 -7.99583	1.1057690 -5.608525	11.08057 -10.02776
107	2.299422 -2.027568	13.78833 -9.786308	0.8073563 -6.802177	13.86543 -12.23326
132	2.747041 -2.624394	17.96611 -12.17361	0.06132357 -10.23393	18.06582 -16.22889

Table D.2. The unfolded data cross section values, fNLO and various MC models on hadron level.

p_T [GeV]	σ (DATA)	σ (fNLO)	σ (CASCADE)	σ (PYTHIA 6)	σ PYTHIA 8	σ HERWIG	σ POWHEG
39.3047	89090.79	104199	79609.6	91886.9	107763	78968.8	95424.9
50.1909	19861.91	23875.3	18134.2	21615	23361.3	21867.9	21021.3
63.4487	4406.658	5205.31	3674.03	4467.78	4581.27	5257.13	4246.8
79.6988	879.768	1037.13	659.344	832.14	853.09	1044.98	781.401
101.879	114.4967	146.39	86.9074	106.662	107.807	145.91	109.086
132.027	10.10628	12.3279	8.25389	7.95577	8.17454	11.8949	11.401

Table D.3. Difference of the unfolded data cross section values with various MC samples on hadron level.

p_T (GeV)	$1 - \frac{\sigma(\text{DATA})}{\sigma(\text{PYTHIA6})}$	$1 - \frac{\sigma(\text{DATA})}{\sigma(\text{PYTHIA8})}$	$1 - \frac{\sigma(\text{DATA})}{\sigma(\text{HERWIG})}$
39.3047	0.0304301	0.173268	- 0.128177
50.1909	0.0811067	0.149794	0.0917307
63.4487	0.0136813	0.0381147	0.161774
79.6988	- 0.0572362	- 0.0312726	0.158099
101.879	- 0.073455	- 0.0620508	0.215292
132.027	- 0.270308	- 0.236311	0.150371

Table D.4. Difference of the unfolded data cross section values with fNLO and various MC samples on hadron level.

p_T (GeV)	$1 - \frac{\sigma(\text{DATA})}{\sigma(\text{fNLO})}$	$1 - \frac{\sigma(\text{DATA})}{\sigma(\text{CASCADE})}$	$1 - \frac{\sigma(\text{DATA})}{\sigma(\text{POWHEG})}$
39.3047	0.140159	- 0.119096	- 0.124447
50.1909	0.199043	- 0.0952747	- 0.0783708
63.4487	0.164583	- 0.199407	- 0.0432178
79.6988	0.114944	- 0.0334308	0.0680776
101.879	0.172159	- 0.317456	0.348142
132.027	0.274858	- 0.224426	0.628618